

8-2013

HYDROTHERMAL CHEMISTRY, CRYSTAL STRUCTURES, AND SPECTROSCOPY OF NOVEL FLUORIDES AND BORATES

Christopher Underwood
Clemson University, cunderw@clemson.edu

Follow this and additional works at: https://tigerprints.clemson.edu/all_dissertations

 Part of the [Chemistry Commons](#)

Recommended Citation

Underwood, Christopher, "HYDROTHERMAL CHEMISTRY, CRYSTAL STRUCTURES, AND SPECTROSCOPY OF NOVEL FLUORIDES AND BORATES" (2013). *All Dissertations*. 1145.
https://tigerprints.clemson.edu/all_dissertations/1145

This Dissertation is brought to you for free and open access by the Dissertations at TigerPrints. It has been accepted for inclusion in All Dissertations by an authorized administrator of TigerPrints. For more information, please contact kokeefe@clemson.edu.

HYDROTHERMAL CHEMISTRY, CRYSTAL STRUCTURES, AND
SPECTROSCOPY OF NOVEL FLUORIDES AND BORATES

A Dissertation
Presented to
the Graduate School of
Clemson University

In Partial Fulfillment
of the Requirements for the Degree
Doctor of Philosophy
Chemistry

by
Christopher Cole Underwood
August 2013

Accepted by:
Dr. Joseph W. Kolis, Committee Chair
Dr. William T. Pennington
Dr. Joseph S. Thrasher
Dr. Jeffery N. Anker

ABSTRACT

This dissertation is a two-part manuscript highlighting the utilities of the hydrothermal method for exploring phase space, then extending that to the targeted growth of potentially useful materials. Chapters 3 – 5 discuss the synthesis of Group 4 fluorides and oxyfluorides. The study of this class of compounds in regards to their single crystal structures is a rich, but neglected area. Among the Group 4 metals, compounds based on Zr and Ti have been extensively studied, while those based on Th and Hf are sparsely reported and those based on Ce(IV) are nearly completely neglected. Using the hydrothermal method, many new thorium, cerium(IV), and hafnium fluorides containing monovalent ions were synthesized and characterized. These systems exhibit great sensitivity toward both size and concentration of the monovalent metal in addition to experimental conditions such as temperature and reaction time. Interestingly, the descriptive and structural chemistries in the hafnium fluoride systems differ greatly from the thorium fluoride systems while showing no less structural variety. However, the structural chemistry in the cerium fluoride system acts as a bridge between thorium and hafnium fluoride systems. Crystal structures in these systems are introduced and discussed to describe the rich and varied chemistry. Several compounds exhibit luminescence from X-ray and UV-Vis excitations, and this interesting optical behavior is also discussed.

Chapters 6 and 7 focus on using the hydrothermal method to grow crystals having other sorts of optical functionality. A particularly rich system in this sense is the rare

earth (RE) borate system, which can be useful for nonlinear optical (NLO), lasing, and scintillator applications. In particular, YBO_3 appears to be an especially versatile host, as it has an acentric crystal structure and can accommodate a wide range of rare earth dopants such as Nd(III), Er(III), and Yb(III), which can be used to generate lasing activity. Surprisingly, few single crystals of RE-doped YBO_3 have been synthesized; in fact, recent work on RE-doped YBO_3 powders has focused primarily on Eu(III). The absorption and emission spectra of the dopants in YBO_3 show a definitive blue-shift of up to 10 nm as compared to the commonly-used laser hosts of yttrium aluminum garnet (YAG) and YVO_4 , and initial findings show comparable emissions to that of RE-doped YAG and YVO_4 . Another group of acentric borates, $\text{Na}_3(\text{RE})_9\text{O}_3(\text{BO}_3)_8$ (RE = Pr, Nd, Sm), were discovered in the process of synthesizing the RE-doped YBO_3 compounds. Absorption/emission spectroscopy and lifetime measurements of these borates will also be discussed.

DEDICATION

For Sonia and Cole - you are my world.

ACKNOWLEDGEMENTS

I would first like to thank Dr. Joe Kolis for allowing me the opportunity to learn about solid-state chemistry, particularly crystal growth using hydrothermal methods. The skills he taught me and the guidance he gave me are invaluable and will be an asset to me in my professional career. I would also like to thank him for bringing me into the fold in my time of crisis. For this, I am truly grateful.

I would also like to thank the members of the Kolis group, past and present. More specifically, I would like to thank Dr. Martin Kimani, Carla Heyward, Sara Comer, Rylan Terry, and Kyle Fulle. Without their help and the lengthy discussions we had about each other's ideas, this dissertation would not exist.

I would like to thank Dr. Matt Mann for passing the fluorides project on to me; I could not have gotten any luckier. I would especially like to thank Dr. Colin McMillen. Without his help, most of the crystallography and spectroscopy shown here would not have been possible.

I also thank my committee members, Dr. Bill Pennington, Dr. Joe Thrasher, and Dr. Andy Tennyson for their guidance in both the preparation of this dissertation and in my graduate work, and I also want to thank the staff of the chemistry department for their continued support. Lastly (but certainly not least), I want to thank my family and friends who have been there when I needed them and lifted me up when I was down.

TABLE OF CONTENTS

	Page
TITLE PAGE	i
ABSTRACT	ii
DEDICATION	iv
ACKNOWLEDGEMENTS	v
LIST OF TABLES	ix
LIST OF FIGURES	xi
CHAPTER	
I. CRYSTALS, CRYSTAL GROWTH, AND LASING: A BRIEF REVIEW	1
Introduction & History of Crystals	1
Solid-State Crystal Growth Techniques.....	3
History of Hydrothermal Techniques	5
Hydrothermal Crystal Growth	9
Crystal Growth and Lasing	11
Research Goals.....	14
References.....	16
II. EXPERIMENTAL TECHNIQUES.....	18
Hydrothermal Synthesis in Floating Liners	18
Powder X-ray Diffraction	22
Single Crystal X-ray Diffraction.....	23
Energy Dispersive X-ray Analysis (EDX).....	24
Differential Scanning Calorimetry (DSC) and Thermogravimetric Analysis (TGA).....	25
Infrared (IR) Spectroscopy	26
X-ray & Visible Fluorescence	26
UV-Vis-NIR Absorption Spectroscopy	27
Emission Spectroscopy	27
References.....	28

III.	HYDROTHERMAL SYNTHESIS AND CHARACTERIZATION OF NOVEL ALKALI THORIUM FLUORIDES	29
	Introduction.....	29
	Results and Discussion	31
	Conclusions.....	67
	References.....	70
IV.	HYDROTHERMAL SYNTHESIS AND CHARACTERIZATION OF NOVEL ALKALI CERIUM(IV) FLUORIDES.....	74
	Introduction.....	74
	Results and Discussion	75
	Conclusions.....	100
	References.....	102
V.	HYDROTHERMAL CHEMISTRY, STRUCTURES, AND LUMINESCENCE STUDIES OF HAFNIUM FLUORIDES CONTAINING MONOVALENT IONS	106
	Introduction.....	106
	Results and Discussion	108
	Conclusions.....	130
	References.....	133
VI.	HYDROTHERMAL GROWTH AND SPECTROSCOPY OF RARE EARTH DOPED ACENTRIC YTTRIUM ORTHOBORATES (Ln ³⁺ :YBO ₃ (Ln = Nd, Er, Yb).....	136
	Introduction.....	136
	Results and Discussion	139
	Conclusions.....	154
	References.....	155

Table of Contents (Continued)	Page
VII. HYDROTHERMAL CHEMISTRY, STRUCTURES, AND SPECTROSCOPY OF NON-CENTROSYMMETRIC LANTHANIDE BORATES OF FORMULA $\text{Na}_3\text{Ln}_9\text{B}_8\text{O}_{27}$ (Ln = Pr, Nd, Sm)	157
Introduction.....	157
Results and Discussion	158
Conclusions.....	168
References.....	168
VIII. SUMMARY AND PERSPECTIVE	170
APPENDICES	175
A: Copyright Releases	176
B: Crystallographic Data for Cs_2HfF_6 and Rb_2HfF_6	181
C: Tables of Fractional Coordinates	182

LIST OF TABLES

Table	Page
3.1 Crystallographic data for structures 1 - 4	32
3.2 Specific conditions for the syntheses of the cesium and rubidium compounds	33
3.3 Selected bond distances (Å) with esds for compounds 1 and 3	39
3.4 Selected bond distances (Å) with esds for compound 2 and 4	41
3.5 Specific reaction conditions for the syntheses of the title solids	46
3.6 Crystallographic data for CsThF ₅ structures 5 - 7	47
3.7 Selected bond distances (Å) with esds for compounds 5 - 7	51
3.8 Crystallographic data for structures 8 and 9	56
3.9 Selected bond distances (Å) with esds for compounds 8 and 9	57
3.10 Crystallographic data for structures 10 - 12	63
3.11 Selected bond distances (Å) with esds for compounds 10 - 12	65
4.1 Specific conditions for the syntheses of the monovalent metal cerium(IV) fluorides	77
4.2 Crystallographic data for compounds 1, 3, 5, and 8	78
4.3 Overview of reaction conditions for the syntheses of the monovalent metal cerium(IV) fluorides	79
4.4 Selected bond distances (Å) with esds for compounds 1, 3, 5, and 8	80
4.5 Crystallographic data for structures 2, 4, and 6	84
4.6 Selected bond distances (Å) with esds for compounds 2, 4, and 6	86
4.7 Crystallographic data for structures 9 and 11	90

List of Tables (Continued)

Table	Page
4.8 Selected bond distances (Å) with esds for compounds 9 and 11	90
4.9 Crystallographic data for structures 7 , 10 , and 12	92
4.10 Selected bond distances (Å) with esds for compounds 7 , 10 , and 12	93
4.11 Crystallographic data for structures 13 and 14	97
4.12 Selected bond distances (Å) with esds for compounds 13 and 14	98
5.1 Specific reaction conditions for the syntheses of some alkali hafnium fluorides	110
5.2 Crystallographic data for structures 1 - 5	112
5.3 Selected bond distances (Å) with esds for compounds 1 - 5	113
7.1 Crystallographic data for structures 1 - 3	162
7.2 Selected bond distances (Å) with esds for compounds 1 - 3	163

LIST OF FIGURES

Figure	Page
1.1 Diagram of a Czochralski furnace	5
1.2 Papin's digester as made for laboratory use	6
1.3 Schematic of a typical Morey-type vessel	8
1.4 Diagram relating space group to NLO property	14
2.1 Progressive steps to sealing a silver ampoule. (a) One end welded, ready for sample charging. (b) Fully welded sample ready for hydrothermal treatment. (c) Ampoule after hydrothermal treatment.....	19
2.2 Typical full setup of a floating-liner autoclave, complete with band heaters and cinder block pits.....	21
3.1 Overview of the reported monovalent alkali thorium fluorides single crystal structures.	30
3.2 Powder patterns of 1 (red) and the known pattern for CsTh ₃ F ₁₃ in a previously unidentified space group (black). The peaks around 38° is from the Al pan sample holder.....	34
3.3 Powder patterns of 3 (red) and the known pattern for CsTh ₃ F ₁₃ in a previously unidentified space group (black). The peaks around 38° is from the Al pan sample holder.....	34
3.4 A view of the channel structure of 1 projected down the <i>c</i> axis.	38
3.5 Perspective view of the channel structure of 2 down the <i>c</i> axis. The nine-coordinate thorium (shown as grey polyhedra) also run infinitely in the <i>c</i> direction and form hexagram-shaped channels where the Cs ⁺ (dark green) resides.....	40

List of Figures (Continued)

Figure	Page
3.6 Layered structure of 2 viewed along the [110] direction with a single unit cell shown with black edges. The two unique cesium sites occupy different layers in an alternating fashion. This also serves as a cross sectional view of the channel structure where only three of the six thorium polyhedra, participating in the channel construction, are currently displayed.....	41
3.7 Compound 4 viewed down the <i>c</i> axis, showing the zigzag nature of the thorium-containing layers. Layers are connected along the <i>b</i> axis through Th1-F5-Th1 bonding as well as Rb-F interactions.....	43
3.8 Channel structure in 4 viewed down the <i>a</i> axis. The nine-coordinate thorium atoms (shown as grey polyhedra) form elongated hexagon-shaped channels where the Rb ⁺ (dark green) can sit in a staggered formation.....	44
3.9 Section of the layers in 5 viewed down the <i>b</i> axis. The nine-coordinate thorium polyhedra run infinitely in the <i>ab</i> direction and alternate between the polyhedra and cesium atoms.....	49
3.10 Section of the layers in 5 viewed down the <i>c</i> axis. The cross-linked layers of polyhedra stacked along the [010] unit cell direction form bitrapezoidal-shaped channels infinitely in the <i>c</i> direction.....	49
3.11 Section of the layers in 6 (left) and 7 (right) viewed down the <i>b</i> axis.....	52
3.12 Section of the layers in 6 (left) and 7 (right) viewed down the <i>a</i> axis.....	52
3.13 DSC of compound 6 synthesized from condition 1. Each transition was investigated via PXRD... ..	54
3.14 PXRD of compound 6 at room temperature and after heating past each transition.... ..	54
3.15 (a) Compound 8 as viewed down the <i>ab</i> plane. (b) A layer of compound 8 as viewed down the <i>c</i> axis. Thorium polyhedra beneath the sheet are removed for clarity.....	58

List of Figures (Continued)

Figure	Page
3.16 (a) Compound 9 as viewed down the <i>ab</i> plane. (b) A layer of compound 9 as viewed down the <i>c</i> axis. Thorium polyhedra beneath the sheet are removed for clarity.....	60
3.17 (a) Cut away view of an ellipsoidal pore in compound 8 as viewed down the <i>ab</i> plane. The 12-coordinate cesium ion (shown uncoordinated) sits in the center of the pore. (b) Cut away view of the ellipsoidal pore in compound 9 as viewed down the <i>ab</i> plane. Two 5-coordinate sodium ions (Na-F bonds are bolded) are centered at the loci of the pore and are bridged by a corner-shared fluoride.....	62
3.18 The cage-like structure of compound 11 , as viewed down the <i>a</i> axis. The atoms are shown as thermal ellipsoids to demonstrate the large thermal parameter of F6. The thorium polyhedra are open-faced for clarity.....	64
3.19 Cut-away of the pores of compound 11 , as viewed down the <i>c</i> axis. The thorium polyhedra are open-faced for clarity.....	65
3.20 The cage-like structure of compound 12 , as viewed down the <i>b</i> axis. The polyhedra are shown as thermal ellipsoids to demonstrate the large thermal parameter of F6 orthogonal to the <i>c</i> axis. N1 and N2 are isotropic, and the thorium polyhedra are open-faced for clarity.....	68
3.21 Overview of the monovalent thorium fluorides synthesized using our hydrothermal method. The compounds in black are reported single crystal structures and the compounds in red are new structures. Any compounds in italics have previously-reported powder patterns that were used to confirm the identity of the new materials.....	69
4.1 Overview of the reported monovalent alkali cerium fluoride single crystals.....	75

List of Figures (Continued)

Figure	Page
4.2 (a) Compound 8 as seen down the <i>c</i> axis showing how the clusters join to form hexagram-shaped channels. (b) Compound 8 as seen down the <i>b</i> axis showing the layering that occurs with the clusters of cerium polyhedra. The oxygen atoms are enlarged to show their positions.....	82
4.3 (a) Compound 6 as seen down the <i>c</i> axis showing how the clusters join to form sheets that extend through [101] and result in ABAB stacking. (b) Compound 6 as seen down the <i>b</i> axis showing the unique channels that are formed as a result of the ABAB stacking.....	87
4.4 Compound 9 as seen down the <i>c</i> axis showing how the alkali polyhedra cluster to form hexagram-shaped channels where the Ce(IV) atoms sit.....	91
4.5 The cage-like structure of compound 5 , as viewed down the <i>a</i> axis. The atoms are shown as thermal ellipsoids to demonstrate the thermal parameter of F6. The thorium polyhedra are open-faced for clarity.....	94
4.6 (a) Helical building block of 13 as seen down the <i>b</i> axis. (b) Said helix as seen down the <i>c</i> axis, showing the square-shaped channel.....	99
4.7 The framework structure of 13 as seen down the <i>c</i> axis, showing two helical units per unit cell.....	99
4.8 (a) Compound 14 as seen down [001], showing the large triangular-shaped channels. The cerium(IV) polyhedral are open for clarity. (b) Compound 14 in the same viewpoint, only with the cerium(IV) polyhedra to show the smaller triangular-shaped channel that exists.....	100
4.9 Overview of the monovalent cerium(IV) fluorides synthesized using our hydrothermal method. The compounds in black are reported single crystal structures and the compounds in red are new structures. Any compounds in italics have previously-reported powder patterns that were used to confirm the identity of the new materials.....	101

List of Figures (Continued)

Figure	Page
5.1 Overview of the reported monovalent alkali and pseudo-alkali hafnium fluoride single crystals.	107
5.2 Structure of Li_2HfF_6 (a) as compared to Cs_2HfF_6 (b) viewed along [001], with some Cs polyhedra removed for clarity. Li atoms form $[\text{LiF}_6]^{5-}$ polyhedra, whereas Cs atoms form $[\text{CsF}_{12}]^{11-}$ polyhedra.....	114
5.3 Layers of hafnium atoms sandwiched between $[\text{LiF}_6]^{5-}$ polyhedra in Li_2HfF_6 (a) and $[\text{CsF}_{12}]^{11-}$ polyhedra in Cs_2HfF_6 (b) viewed off [010].....	114
5.4 (a) Structure of $\text{Na}_5\text{Hf}_2\text{F}_{13}$ viewed along [010]. (b) Space filling polyhedral view of an isolated $[\text{Hf}_2\text{F}_{13}]^{5-}$ unit surrounded by a channel of sodium fluoride polyhedra.....	117
5.5 Layered structure of $\text{K}_2\text{Hf}_3\text{OF}_{12}$ viewed along [010].	119
5.6 Staggered arrangement of $[\text{Hf}_3\text{OF}_{18}]$ clusters with gaps accommodating K3 atoms in $\text{K}_2\text{Hf}_3\text{OF}_{12}$	120
5.7 IR spectra of (a) Rb_2HfF_6 , (b) compound 2 , (c) compound 3 , and (d) compound 5	124
5.8 IR spectrum of $\text{Rb}_5\text{Hf}_4\text{F}_{21} \cdot 3\text{H}_2\text{O}$	125
5.9 Expanded IR spectrum of compound 5	125
5.10 X-ray luminescence of the title compounds. The compounds are listed in the order of intensity (most to least) from top to bottom. The spectra were displaced vertically to facilitate their comparison.....	127
5.11 Visible fluorescence spectra of the title compounds. The compounds are listed in the order of intensity (most to least) from top to bottom. Emission wavelengths less than 515 nm were cut off with a long pass emission filter. The spectra were displaced vertically to facilitate their comparison.....	129

List of Figures (Continued)

Figure	Page
5.12 Overview of the monovalent hafnium fluorides synthesized using our hydrothermal method. The compounds in black are reported single crystal structures and the compounds in red are new structures. Any compounds in italics have previously-reported powder patterns that were used to confirm the identity of the new materials.....	131
6.1 PXRD patterns for 0.5, 1, and 5% Nd:YBO ₃	140
6.2 PXRD patterns for 1, 3, and 5% Er:YBO ₃	141
6.3 PXRD patterns for 1, 5, and 10% Yb:YBO ₃	141
6.4 Crystal of 1% Nd:YBO ₃ grown from SN by hydrothermal treatment.....	143
6.5 Crystal of 5% Er:YBO ₃ grown from SN by hydrothermal treatment.....	144
6.6 Crystal of 1% Yb:YBO ₃ grown from SN by hydrothermal treatment.....	145
6.7 Crystal of 1% Yb:YBO ₃ shows the uneven plate “stacking” on the facets	146
6.8 Absorption spectra of 0.5, 1, and 5% Nd-doped YBO ₃ as compared to YBO ₃	147
6.9 Emission spectra of Nd:YBO ₃ , excitation at (a) 589, (b) 734, and (c) 803 nm	148
6.10 NIR emission spectra of 1% Nd:YBO ₃ excited at 589, 734, and 803 nm	149
6.11 Absorption spectra of 1, 3, and 5% Er-doped YBO ₃	150
6.12 NIR emission spectra of 5% Er:YBO ₃ excited at 957, 966, and 972 nm	151
6.13 Absorption spectra of 1, 5, and 10% Yb-doped YBO ₃	152

List of Figures (Continued)

Figure	Page
6.14 Emission spectra of Yb:YBO ₃ , excitation at (a) 925, (b) 941, and (c) 971 nm.....	153
6.15 NIR emission spectra of 5% Yb:YBO ₃ excited at 925, 941, and 971 nm	154
7.1 PXRD comparison of Na ₃ Nd ₉ B ₈ O ₂₇ flux to reported PXRD patterns for Na ₃ La ₂ (BO ₃) ₃ (left) and Na ₃ La ₉ B ₈ O ₂₇ (right).....	159
7.2 Photo depicting the trigonal prismatic and polyhedral morphologies of Na ₃ Nd ₉ B ₈ O ₂₇	160
7.3 (a) The fundamental building block (FBB) of compound 1 as seen down [001]. (b) The arrangement of the planar [BO ₃] ³⁻ units in compound 1 as seen down [001]. The sodium polyhedra are removed for clarity.....	163
7.4 (a) The layering of compound 1 as seen down [010]. (b) Off-axis view of the arrangement of the sodium polyhedra in compound 1 . The borate polyhedra are removed for clarity.....	164
7.5 Absorption spectrum of compound 1	166
7.6 Absorption spectrum of compound 2	166
7.7 Absorption spectrum of compound 3	167

CHAPTER ONE

CRYSTALS, CRYSTAL GROWTH, AND LASING: A BRIEF REVIEW

INTRODUCTION & HISTORY OF CRYSTALS

Crystals have existed in historical accounts from holding magical powers to annotating wealth. We are still amazed by the size and clarity of crystals that Mother Nature has made over billions of years. Even today, scientists ranging from physicists that study large naturally-occurring crystals for their spectroscopic properties, to geologists who study crystals to better understand their formation and the geology of the environment from which they originate. As chemists, we study crystals to understand how their atoms arrange to form such beautiful matter and how subjecting crystals to stressors (i.e. electromagnetic energy, pressure, temperature) affect their structure. This leads us to better understand how they are formed and what applications they may serve.

As early as the 19th century, scientists studied how to mimic Mother Nature by the advancement of man-made crystal growth and determining the best use of said crystals. It was in this time period where the possibility of preparing synthetic gemstones was first bolstered by research into the natural formation of crystals from magmatic lavas.^{1,2} Gaudin (1837) then used this research to synthesize small ruby rhombohedra in a eutectic melt of potassium alum and potassium chromate.³ Later, Verneuil (1904) grew rubies by perfecting Gaudin's technique, which is still practiced today to mass produce rubies for use as watch bearings and gemstones.⁴ Czochralski (1917) devised a method for growing large single crystals of metals that is also still used today to produce important semiconductors such as Si, Ge, and Ga.⁵ Shortly thereafter, Bridgman and Stockbarger

developed a variation of the Czochralski method (CZ) for growing single crystals of other semiconductors that are more difficult to grow using CZ due to their higher susceptibility to crystal defects (i.e., GaAs).⁶ Though growth of crystals using hydrothermal techniques had been known since Schafhäütl's contributions (1845),⁷ it was not used on an industrial scale until World War II for growing large α -quartz crystals to be used in SONAR technology.

A significant application was found for crystals in 1960 that would have a dramatic impact on their use in society. Using a synthetic ruby, Maiman noticed the first occurrence of light amplification by stimulated emission of radiation, more commonly referred to as the laser.⁸ Since the advent of the laser, optical crystalline devices for light manipulation have also emerged. Naturally occurring calcite (CaCO_3) and rutile (TiO_2) have become important optical crystals for birefringent applications.^{9,10} Non-linear optical crystals are useful for generating high energy photons from low energy laser light.¹¹ This was first observed using a quartz crystal; however, high efficient NLO crystals are not common in nature.¹²

These examples show how advances in crystal growth have provided scientists with a wide range of materials, each with different strong suits. Due to their technological importance, many synthetic crystals have been developed, including borates and fluoride crystals. This dissertation will focus on the man-made formation of fluoride and borate crystals and their study to better understand structure, formation, and potential applications.

SOLID-STATE CRYSTAL GROWTH TECHNIQUES

Many different solid-state techniques exist for growing crystals. In the interest of brevity, only three of the more widely-used growth methods will be discussed. One of the simplest techniques is the flux method, where the components are dissolved in a solvent (flux) in a Pt crucible, heated just above the melting point of the flux, and slowly cooled to encourage crystal growth via spontaneous nucleation (SN), meaning growth of relatively large single crystals without the addition of a preformed seed crystal. Some growth reactions use a seed crystal of the target material to induce SN. This method is particularly suitable for growing crystals free of thermal strain, and the crystals display natural facets so that they can be used for optical experiments without the need for further polishing. It is also favorable for use when the crystalline material has a high vapor pressure at its melting point, can undergo phase transitions at higher temperatures, or is an incongruent melting species.¹³ The disadvantages are that most flux method syntheses produce relatively small crystals, and impurities from the crucible and/or flux can become incorporated into the crystal.

Some of the typical low melting solvents are lead oxide, lead fluorides, bismuth oxide, alkali chlorides, alkali fluorides, borates, tungstates, molybdates, and vanadates.¹³ Many of these materials may be combined to form various eutectic fluxes with even lower melting points. The choice of solvent is based on the desired melting point, solubility of the crystalline material in the solvent, and probability of flux incorporation into the final product. Crystallization occurs from the solution when a region becomes supersaturated. This can be promoted by slow cooling or evaporation of the flux.¹³

However, for industrial scale growth the supersaturated solution is achieved by establishing zones with different temperatures. In this manner a seed could be placed in the cooler portion of the solvent to effectively grow large single crystals. When it comes time to retrieve the crystals, the flux is dissolved typically with hot water or nitric acid. The crystals then can be harvested from the platinum container and used for further growth.

In terms of technologically important materials, this growth technique is used for many magnetic materials including spinel ferrites, yttrium iron garnet, and hexaferrites.¹⁴ It has also become an important process for liquid-phase epitaxy of materials such as magnetic bubble materials.¹³ Comparatively, the industrial growth of crystals by the flux method is still eclipsed by the more favored CZ technique.

The CZ method involves a melt of the components in a crucible. A seed crystal attached to a wire is placed at the surface of the melt and slowly pulled away to a cooler region of the reactor. As the seed is pulled and rotated through this temperature gradient, growth occurs at the interface of the crystal and the melt to form one long ingot called a boule (see Figure 1.1). Only three variables exist by which to change the growth parameters: heating power, rotation rate, and pull rate. These factors can alter the diameter, quality, and growth rate of the boule. This method is widely used in manufacturing due to its ability to be scaled-up. However, the large thermal gradient between the seed crystal and the melt induces thermal strain in the boule, and inclusions of impurities from the crucible also hinder ideal crystal growth. This method is also limited to only congruently melting components.

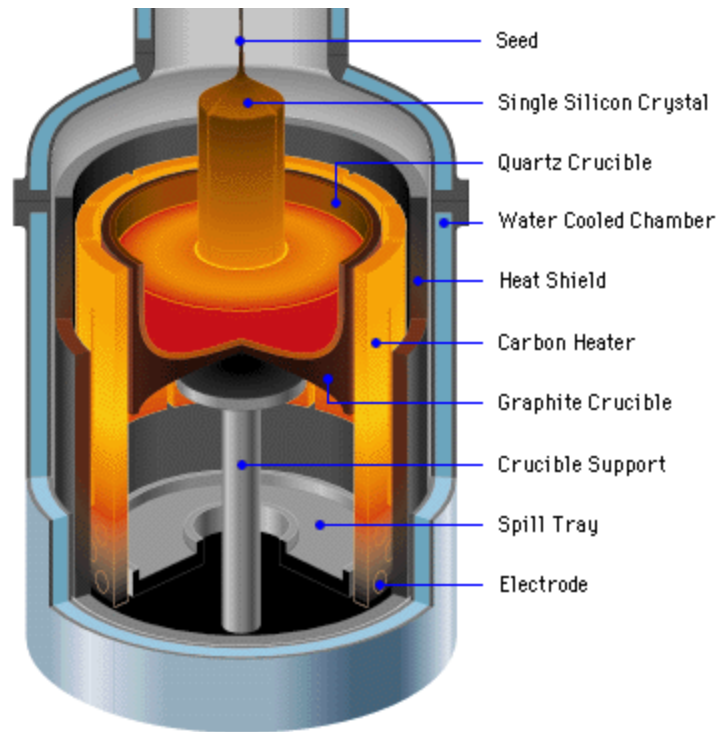


Figure 1.1. Diagram of a Czochralski furnace. Adapted from <http://meroli.web.cern.ch>

Despite its drawbacks, the CZ method is still a reliable means for growing crystals. Normal growth rates of boules from a CZ pull average 0.2 – 1.0 mm / min,¹⁵ and this method is used to produce semiconductor materials such as Ge and Si, as well as a number of optical and lasing crystals such as neodymium-doped yttrium aluminum garnet (Nd:YAG).

HISTORY OF HYDROTHERMAL TECHNIQUES

As mentioned earlier, the use of hydrothermal techniques for the purposes of crystal growth date back to Schafhäütl's successful synthesis in 1845 of microcrystalline

quartz using precipitated silicic acid in a Papin's digester (see Figure 1.2), the equivalent of a pressure cooker used to make sauces from leftover bones.^{7,16} Its ability to generate supercritical water from high pressures and temperatures due to the decrease in water viscosity (thus allowing for better diffusion through solid materials) allows for insoluble materials at supercritical temperature and pressure (STP) to become soluble in solution, thus illustrating a fundamental concept of the hydrothermal technique.



Figure 1.2. Papin's digester as made for laboratory use. Adapted from

<http://collectionsonline.nmsi.ac.uk>.

Shortly thereafter, Bunsen used thick walled glass tubes to successfully crystallize BaCO_3 and SrCO_3 in supercritical water in 1848.^{16,17} He used the temperature decrease method from 200 °C to allow for crystallization, allowing for the first documentation of visual reaction vessels. A few years later (1851), de Sénarmont developed the first

semblance of an autoclave for use in hydrothermal synthesis.^{16,18} He expounded on Bunsen's use of glass ampoules by placing them in gun barrels. The barrels were partially filled with water, welded shut, and heated in a furnace to a red glow. Using this process, de Sénarmont synthesized many sulfides, sulfates, carbonates, and fluorides making him a forefather of hydrothermal synthesis.

The technique introduced by de Sénarmont was used for many years until the introduction of Morey's vessel in 1914. Before this vessel, only acidic to neutral pH mineralizers could be used due to limitations of the glass ampoules; basic mineralizers would dissolve the glass in supercritical water. Morey devised a vessel that used a noble metal liner (gold in this case) that could withstand basic pH mineralizer dissolution (see Figure 1.3).^{16,19} Instead of welding the vessel shut, it made use of a flat plunger system that seals the vessel shut. Current commercially available Morey vessels only use Teflon liners and can only be heated to 200 °C. One improvement on this design was made by Bridgman; by changing the material that comprises the seal, higher pressure could be held, thus allowing for higher reaction temperatures to be used.²⁰ Another improvement was made by Tuttle, who simply beveled the plunger and autoclave to allow for a "cold seal" without the use of a fixed noble metal liner.²¹ These innovative designs are the bases for most modern autoclaves that are used for hydrothermal synthesis.

Despite the breakthroughs in hydrothermal crystal synthesis in the early 20th Century, these techniques fell by the wayside until World War II, when a shift occurred in hydrothermal synthesis from exploratory mineralogy to legitimate industrial application. Due to the Allied blockade of the Nazi Empire, Germany was unable to

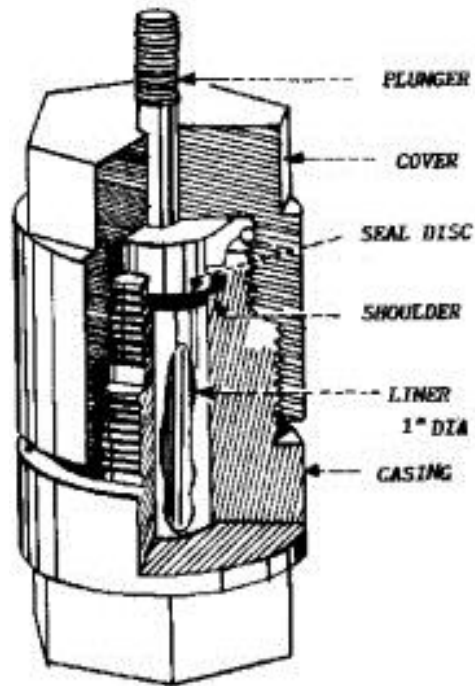


Figure 1.3. Schematic of a typical Morey-type vessel. Adapted from <http://origin-ars.els-cdn.com>.

obtain large amounts of α -quartz for use as a piezoelectric material in RADAR and SONAR devices.^{16,22} Since necessity is the mother of innovation, the Germans turned to hydrothermal crystal growth for manufacturing large amounts of α -quartz when Nacken successfully produced large amounts of the materials using cubic centimeter-sized seeds and silica feedstock.¹⁶ After the surrender of the Nazis, Allied scientists obtained this technology and began producing α -quartz of their own. By the 1980s between 600 – 700 tons of α -quartz was produced in this manner.¹⁶ Currently hydrothermal techniques are also commercially used to synthesize precious gems and magnetic oxides.²³⁻²⁶

HYDROTHERMAL CRYSTAL GROWTH

The hydrothermal method is a low-temperature, solution-growth method where crystals are grown in an autoclave from an aqueous solution at or above the boiling point of water. This aqueous solvent is both the growth medium and a pressure transmitting medium. The growth of large crystals generally occurs beyond the critical point of water (374 °C, 3204 psi). It is an attractive method because supercritical water has excellent dissolving and diffusion properties, both key steps in the crystal growth process.²⁷ The solvent may also contain mineralizers such as hydroxide, fluoride, or carbonate ions that assist in the dissolution of the starting materials, and their ions can also be incorporated into the structure of the growing crystals. In most cases, an inert metal liner is used to contain the reaction within the autoclave since the corrosive nature of the mineralizer precludes growth directly in the autoclave. These liners can either be floating sealed ampoules whose pressure is balanced externally by water or gas that occupies the remaining volume of the autoclave or can be fixed against the walls of the autoclave. Modern hydrothermal technology in our labs affords safe containment of pressures in excess of 1-3 kbar at 700 °C, permitting a number of different reaction conditions to be explored.

Crystal growth occurs by means of a solubility differential within the reaction vessel. The means by which a hydrothermal technique induces crystallization is through the use of a temperature gradient. In this case, one portion of the autoclave (typically the upper portion, see Chapter 2 for details) is held at a lower temperature than another portion of the vessel (typically the bottom portion). The solvent in the hot zone of the

autoclave becomes saturated with feedstock and is carried by convective flow to the cooler portion of the autoclave, where crystallization occurs. Using this technique, crystal growth can be allowed to proceed as spontaneous nucleation or directed onto a seed crystal.

Several reasons exist for why hydrothermal crystal growth is not as extensively studied as the melt techniques discussed previously. The most obvious reason is that it involves a highly specialized set of equipment and knowledge, requiring an extensive initial financial investment to obtain the necessary high-pressure equipment as well as a time investment to learn about its safe operation. The closed nature of the hydrothermal crystal growth system is also a disadvantage, for crystal growth cannot be observed *in situ*; that creates a certain amount of risk in these experiments, particularly prolonged growth experiments. This necessitates extensive preliminary studies to ensure full confidence in the growth conditions prior to attempting a long-term experiment. A related complication is the inability to easily identify intermediate species in hydrothermal solutions. Finally, hydrothermal growth results in lower observed average growth rates compared to melt techniques due to the nature of the supercritical solution.

Although hydrothermal techniques yield these lower growth rates, slower growth leads to crystals with fewer defects like in the case of hydrothermally grown potassium titanyl phosphate (KTP) versus flux grown crystals. Growth from a solution also makes it possible to grow materials that cannot be conveniently melted, including both refractory materials with very high melting points and materials that melt incongruently. The nature of supercritical solutions also provides for reduced solvent inclusions. Since

supercritical water is a much less viscous medium than melts, it is less likely to be trapped within a growing crystal and allows for better circulation within the reaction vessel, ensuring even distribution of components within the growth medium. The lower temperature of hydrothermal growth (typically under 700 °C) also leads to fewer problems with crystal cracking and thermal strain and less thermal defects than growth from a melt that typically exceeds 1000 °C. Likewise, kinetically stable products can be synthesized instead of those for which formation is strictly driven by thermodynamics. An aspect of hydrothermal growth that is appealing from an industrial standpoint is that the process is fully scalable, i.e., the commercial production of α -quartz. The principles of pressure containment, solubility, and mass transport remain the same regardless of the size of the reaction vessel. Finally, while managing temperature, pressure, gradient, and the concentration of the mineralizer can be a daunting task, each of these variables is fully under the control of the crystal grower, offering a potentially large matrix of combinations to optimize the chemistry of a crystal growth system. These advantages give hydrothermal techniques an appeal to scientists seeking to explore crystal chemistry.

CRYSTAL GROWTH AND LASING

One area of research conducted in this dissertation involves lanthanide-doped yttrium borates. These borate materials are important to many different applications, but my research was primarily confined to potential second harmonic generation. A brief summary of the past and current trends of lasing and second harmonic generation (SHG) will be provided in this section.

Over the past fifty years the laser field has greatly advanced in the industrial, medical, and scientific sectors. One area that has benefited from this progress is the field of non-linear optics (NLO). It is well known that light emitted from a laser system is constricted by the emission wavelength of the lasing ion. Despite the variety of lasing ions, many desirable wavelengths do not correspond with any known emissions. These wavelengths can only be reached by manipulating light through the use of non-linear materials, a phenomenon known as second harmonic generation (SHG) in which two photons of a longer wavelength are combined in a medium to form one photon of shorter wavelength.²⁸ A common example of this effect can be found in a Nd:YAG laser system. Light emitted from an Nd:YAG crystal generates 1064 nm photons, which then pass through a potassium titanyl phosphate (KTiOPO₄, or KTP) crystal. The second harmonic effects of KTP combine two 1064 nm photons into one 532 nm photon. The principles governing this phenomenon are presented in Equation 1.1.²⁹

$$\text{Equation 1.1} \quad P = \epsilon_0 \chi(1)E + \epsilon_0 \chi(2)EE + \epsilon_0 \chi(3)EEE + \dots$$

As light travels through a medium, it becomes polarized light, which is dependent on the permittivity of free space (ϵ_0), linear susceptibility $\chi(1)$, harmonic susceptibility $\chi(2,3,\dots)$ and the strength of the electric field (E). The harmonic susceptibility tensors are governed by the structural features of the medium. In particular, the second harmonic tensor, $\chi(2)$ is directly responsible for KTP's ability to generate 532 nm photons. One requirement for the harmonic susceptibility tensors is a lack of inversion symmetry in the

medium, or a crystal in this case.³⁰ For materials with a center of symmetry the harmonic tensors are equal to zero, which preclude any possible NLO properties.³¹

This indicates that materials that crystallize into a non-centrosymmetric space group will possess certain NLO properties, dependent on the nature of the acentricity. In a groundbreaking review relating the properties of commonly-used laser crystals to their space group, Halasyamani and Poppelmeier developed a visual correlation of these relations, which is shown in Figure 1.4.²⁸

As the search for better NLO crystals continue, most research focuses on structural building blocks that tend to crystallize in acentric space groups, such as the trigonal $[\text{BO}_3]^{3-}$ borate group. These groups can have small differences in the three boron oxygen bond distances, which leads to a distorted planar group. This distortion can lower the overall symmetry leading to acentric structures.³³ There is also interest in the octahedral environments of metals that can be exacerbated by their small radius and high charge due to Jahn-Teller effects, such as Ta^{5+} , Nb^{5+} , and Ti^{4+} . Those effects tend to distort these octahedral environments, thereby forming acentric structures.^{34,35} In extreme cases like KTP, the octahedral TiO_6 group distorts to the point that the Ti^{4+} adopts a square pyramidal TiO_5 geometry, which has been directly attributed to its excellent SHG properties.³⁶

Non-Centrosymmetric Crystal Classes

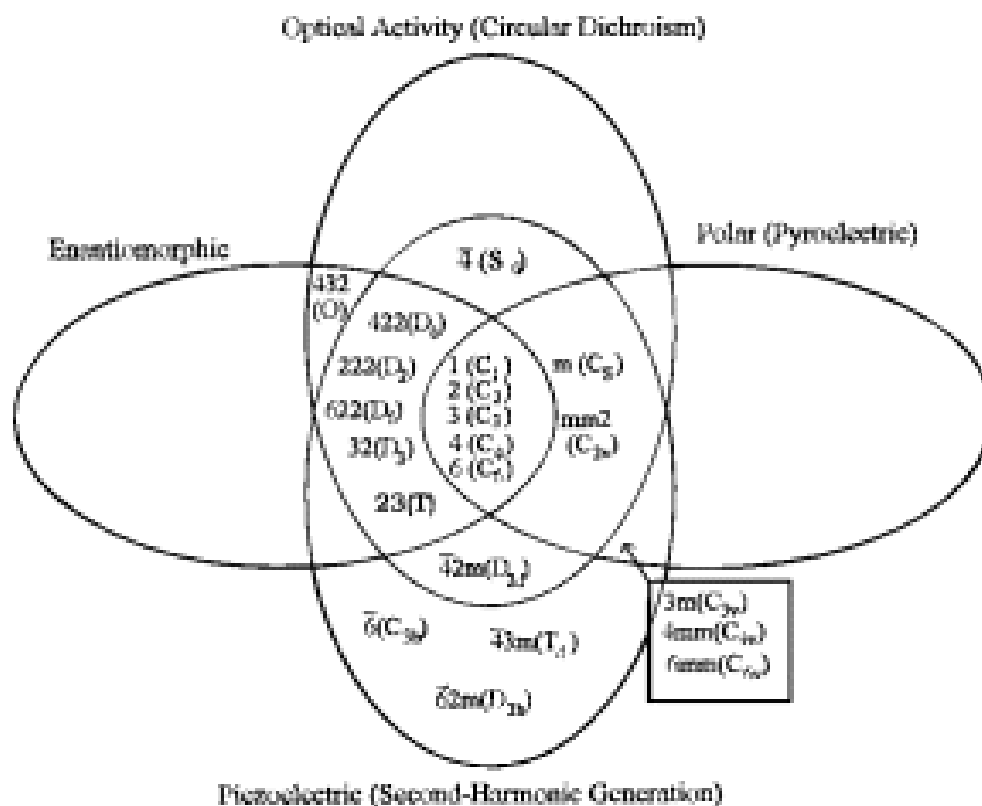


Figure 1.4. Diagram relating space group to NLO property.³²

RESEARCH GOALS

The first goal of this research was to determine the phases of alkali thorium, cerium(IV), and hafnium fluorides that could be synthesized utilizing the positive aspects of these hydrothermal techniques. Crystals of alkali thorium fluorides were previously found inside of molten fluoride salt reactors that utilized a thorium fuel source. Most of these crystals could not be fully characterized because they were either of poor quality or

the ability to collect single crystal X-ray data was not commercially available. Crystals of alkali ion thorium fluorides were synthesized to better characterize the phase space. Crystals of alkali ion hafnium fluorides were synthesized to both better characterize the phase space and to simulate the types of crystals that would be found in the same type of fluoride reactor if hafnium was the material used as the control rods in the reactor. Crystals of alkali ion cerium(IV) fluorides were synthesized to determine whether or not there were structural similarities between them and both the thorium and hafnium fluoride systems. With this being a descriptive study, it was a way to explore a wide area of phase space, elucidate new reaction chemistry and determine many unique crystal structures, and also gain valuable knowledge and experience in hydrothermal techniques that would be used in future projects that required more advance crystal growing skills.

The other goal of this research was to grow crystals of lanthanide-doped yttrium orthoborate (YBO_3). Since YBO_3 grows hydrothermally in an acentric space group and can be doped with a number of lanthanide ions, it may be possible to grow self frequency doubling laser crystals, namely crystals that both lase and frequency double the laser beam at the same time. Previous studies of this phase space have involved the synthesis of mostly microcrystalline powder; few single crystals have been grown, but they have not been large enough for suitable spectroscopic studies. Since it was determined to be a suitable laser host for SHG, I synthesized doped YBO_3 crystals using hydrothermal techniques with suitable size and clarity for absorption and emission studies.

REFERENCES

- (1) Hall, J. *Edin. Royal Soc. Trans.* **1805**, 5, 56.
- (2) Watt, G. *Phil. Trans. Royal Soc.* **1804**, 279.
- (3) Gaudin, A. *Comp. Rend.* **1837**, 4, 999.
- (4) Verneuil, A. *Ann. Chim. Phys.* **1904**, 3, 20-48.
- (5) Czochralski, J. *Z. Phys. Chem.* **1917**, 92, 219-221.
- (6) Bridgman, P. W. *Proc. Am. Acad. Arts Sci.* **1914**, 49, 627-643.
- (7) Schafhäütl, K. F. E. *Gelehrte Anzuigen Bayer. Akad.* **1845**, 20, 557, 561, 569, 593.
- (8) Maiman, T. H. *Nature* **1960**, 187, 493-494.
- (9) Smartt, R. N.; Steel, W. H. *J. Opt. Soc. Am.* **1959**, 49, 710-712.
- (10) DeVore, J. R. *J. Opt. Soc. Am.* **1951**, 41, 416-419.
- (11) Koechner, W. *Solid-State Laser Engineering*, 6th Ed. New York: Springer, 2006.
- (12) Franken, P. A.; Hill, A. E.; Peters, C. W.; Weinreich, G. *Phys. Rev. Lett.* **1961**, 7, 118.
- (13) Elwell, D.; Scheel, H. J. *Crystal Growth from High Temperature Solutions*. Academic Press, London-New York-San Francisco, 1975.
- (14) Görnert, P. *Prog. Cryst. Growth Char. Mater.* **1990**, 20, 263-284.
- (15) Müller, G. *Cryst. Res. Technol.* **2007**, 42, 1150-1161.
- (16) Rabenau, A. *Angew. Chem., Int. Ed. Engl.* **1985**, 24, 1026-1040.
- (17) Laszlo, T. S.; Sheehan, P. J.; Gannon, R. E. *J. Phys. Chem. Solids* **1967**, 28, 313-316.
- (18) Sakurai, T.; Kamada, O.; Ishigame, M. *J. Cryst. Growth* **1968**, 2, 326-327.
- (19) Vergnoux, A. M.; Giordano, J.; Foex, M. *Comp. Rend.* **1965**, 261, 3343-3345.

- (20) Tuttle, O. F. *Geol. Sci. Am. Bull.* **1949**, *60*, 1729.
- (21) Nacken, R. *Chem.-Zeitung* **1950**, *74*, 745-749.
- (22) Laudise, R. A. "Hydrothermal Growth" in *Crystal Growth: An Introduction*. Harmon, P., ed. New York: North Holland Publishing Co., 1973. pp. 162-197.
- (23) Laudise, R. A.; Kolb, E. D. *Endeavor* **1969**, *28*, 114-117.
- (24) Laudise, R. A.; Kolb, E. D.; Key, P. L. *Proc. Int. Symp. Hydrotherm. React.* **1983**, 527-530.
- (25) Laudise, R. A. *J. Cryst. Growth* **1983**, *65*, 3-23.
- (26) McMillen, C. D.; Kolis, J. W. *Phil. Mag.* **2012**, *92*, 2686-2711.
- (27) Kolis, J.W.; Korzenski, M.B. "Synthesis of Inorganic Solids" in *Chemical Synthesis Using Supercritical Fluids*, Jessop, P.G. and Leitner, W., eds. New York: Wiley-VCH, 1999. pp. 213-241.
- (28) Koechner, W. *Solid-State Laser Engineering*, 2nd Ed. Berlin, New York: Springer-Verlag, 1988.
- (29) Koechner, W. *Solid-State Laser Engineering*, 6th Ed. New York: Springer, 2006.
- (30) Nye, J. F. *Physical Properties of Crystals*. New York: Oxford University Press, 1985.
- (31) Boyd, R. W. *Nonlinear Optics*. San Diego: Academic Press, 2003.
- (32) Halasyamani, P.S.; Poepelmeier, K.R. *Chem. Mater.* **1998**, *10*, 2753-2769.
- (33) Becker, P. *Adv. Mater.* **1998**, *10*, 979-992.
- (34) Korotkov, A. S.; Atuchin, V. V. *Mater. Res. Bull.* **2006**, *41*, 1861-1867.
- (35) Korotkov, A. S.; Atuchin, V. V. *J. Solid St. Chem.* **2006**, *179*, 1177-1182.
- (36) Stucky, G. D.; Phillips, M. L. F.; Gier, T. E. *Chem. Mater.* **1989**, *1*, 492-509.

CHAPTER TWO

EXPERIMENTAL TECHNIQUES

HYDROTHERMAL SYNTHESIS IN FLOATING LINERS

Basic synthesis and recrystallization experiments were routinely performed in welded silver ampoules. The most important property of the ampoule is its inertness toward the reactants, since silver remained inert toward most basic mineralizers and fluorides under essentially all experimental conditions, and the reaction ampoules only showed reactivity toward oxidants or acidic mineralizers at temperatures above 450 °C. It is also much more cost effective than other inert metals such as gold or platinum. The ampoules were fashioned from 0.25" outer diameter fine silver tubing obtained from Leach-Garner, Inc. Tubing was cut from longer stock to 2.5" inch-long, and one end was crimped with a pair of needle-nose pliers. This crimped end was then welded using a CEA model TOP-165HF inert gas welder with a carbon or tungsten electrode under flowing argon (see Figure 2.1a for ampoule visual). Powdered starting materials were then weighed and added to the ampoule through the open end. Typically, 100-150 mg of solid starting material was used. The mineralizer was then added via disposable syringe. The mineralizer was either a previously prepared stock solution of known concentration or simply deionized water (that could dissolve a portion of the solid charge to form a mineralizer). A volume of 0.4 mL was chosen to ensure that the fluid would fill the reaction vessel upon heating.¹ Larger volumes made it difficult to seal the ampoules. It must also be noted that higher concentrations of basic mineralizers ($> 8 M$) and the acidic mineralizer KHF_2 at any concentration made it difficult to seal the ampoules. The open

end of the ampoule was then cleaned with a cotton swab to remove any residual powder or mineralizer that would also make the ampoule difficult to weld seal. The clean, open end was crimped and welded shut as described for the bottom of the ampoule (see Figure 2.1b).



Figure 2.1. Progressive steps to sealing a silver ampoule. (a) One end welded, ready for sample charging. (b) Fully welded sample ready for hydrothermal treatment. (c) Ampoule after hydrothermal treatment.

Sealed ampoules were thoroughly inspected for leaks under a microscope and placed in an autoclave of 27 mL internal volume with a bore diameter of 0.5". The autoclave effectively acts as the means by which temperature and pressure are transmitted to the floating silver ampoules. Autoclaves were typically constructed of a nickel-based superalloy such as Inconel 718, which offers containment of high pressures at temperatures up to 800 °C, and the internal bore could hold up to six vertically-positioned ampoules. These vessels were fabricated in the University machine shop. The ampoules were then counter-pressured with deionized water to prevent them from bursting when heated. The cap assembly (including a gauge, pressure relief valve, high pressure tubing (rated to 120 kpsi), sealing plunger, and cap nut) was then screwed onto the threaded portion of the autoclave. This assembly utilized the Tuttle sealing mechanism, where the cap nut drives the cone-shaped plunger against the circular autoclave opening, creating a line seal (see Figure 2.2).²

The sealed autoclave containing the ampoules was then heated using a ceramic band heater (Delta Mfg.) that is strapped to the outside of the autoclave and controlled by an electric temperature controller. Temperatures up to 675 °C could be reached in about two hours. The temperature of the autoclave was measured by thermocouples strapped to the outside using said band heaters. The ceramic band heaters provided a much more reliable means of controlling the temperature gradient than the vertical tube furnaces initially used by the Kolis group. The autoclave and heaters were then placed in a cinder block containment pit filled with vermiculite insulation. Gradients of 10 - 120 °C could be achieved and were exactly repeatable for subsequent experiments. Autoclaves



Figure 2.2. Typical full setup of a floating-liner autoclave, complete with band heaters and cinder block pits.

were held within 3 °C of their set temperatures for 3-14 days, depending on the demands of the experiment. Typical exploratory experiments lasted 3-5 days, while some recrystallization experiments lasted up to 2 weeks to encourage the formation of larger crystals. The pressure was monitored carefully and manually relieved for safety purposes if it exceeded 30 kpsi. At the conclusion of the experiment, the autoclave was allowed to cool to room temperature over a twelve-hour period, and the ampoules were removed.

Because the counter pressure exceeded the pressure generated by the contents of an ampoule, properly sealed ampoules were compressed upon heating (see Figure 2.1c). Thus, the pressure registered on the gauge provided a convenient reading of the pressure inside the ampoules. The ampoules were opened and their contents flushed onto filter paper with deionized water. The products were then washed, dried under vacuum filtration, and prepared for subsequent analysis.

The reactions were further scaled up to 0.375" O.D. silver ampoules when larger crystals or greater amounts of product were sought. These ampoules were six inches in length and typically contained 10 times the amount of starting charge and mineralizer than the 0.25" O.D. ampoules. Because of their size, only one of these larger ampoules could be placed in an autoclave. Autoclaves containing 0.375" ampoules were subjected to similar heating parameters as those containing 0.25" ampoules described earlier. In these cases, two band heaters were used to attain the proper temperature gradient.

POWDER X-RAY DIFFRACTION

Powder X-ray diffraction (PXRD) was used to characterize the bulk solids following a reaction via either a flux reaction or hydrothermal treatment. Crystals were ground using a mortar and pestle and powdered samples were placed on zero background Al sample holders for analysis. The data was collected using a Rigaku Ultima IV X-ray diffractometer with Cu K α radiation ($\lambda = 1.5418 \text{ \AA}$). Patterns were collected from 5 - 65° in 2 Θ at a scan speed of 1.0° / min. The collected data was processed using the *PXDL* software suite.³ Experimental powder patterns were compared to known patterns indexed

in the ICDD powder diffraction file database using the Card Information feature of *PXDL*.³

SINGLE CRYSTAL X-RAY DIFFRACTION

Single crystal X-ray diffraction was used to identify and structurally characterize new species. Diffraction was performed on clear, well-formed single crystals less than 0.75 mm in size that had been mounted on the tip of a glass fiber using a small amount of epoxy. Single crystal X-ray intensity data were collected using a Rigaku Mercury CCD detector and an AFC-8S diffractometer equipped with a graphite monochromator that emits Mo K α radiation ($\lambda = 0.71073 \text{ \AA}$). The *CrystalClear* software package was used to drive the instrument, collect data, and integrate reflections.⁴ The distance from the crystal to the detector was fixed at 27.9 mm for all experiments.

Preliminary crystal screening was performed using four scans where ω was varied (0, 30, 60 and 90°) while χ and Φ remained fixed at 0°. A five second exposure time was used for the screening images. A preliminary reduced cell was obtained from these scans, and the images were inspected for evidence of possible crystal twinning. If the crystal was deemed suitable, a full data set consisting of 480 total images was collected. The exposure time for scans in the full data set could be modified depending on the diffraction intensity observed in the screening images, but was most often set at 5 or 10 second exposure lengths. These 480 images were divided into two segments. For the first 360 images, ω was scanned from -90 to 90° in 0.5° increments while χ was held at 45° and Φ held at 0°. The final 120 images were collected by scanning ω from -30 to 30°

also in 0.5° increments while holding χ at 45° and Φ at 90° . After all data was collected, it was integrated and a high-resolution unit cell obtained. The integrated data was then converted into a usable form using the *REQAB* software package.⁵ The resulting hkl intensity file was then transferred to the *SHELXTL* 6.10 software package for structure determination and refinement.⁶

Data reduction including the application of Lorentz and polarization effects (Lp) and absorption corrections were performed using *CrystalClear*. The structures were solved by direct methods and refined using subsequent Fourier difference techniques, by full-matrix least squares, on F^2 using *SHELXTL* 6.10.⁶ The space groups were determined from the observed systematic absences and confirmed using the *MISSYM* algorithm within the *PLATON* program suite.⁷ All atoms were refined anisotropically except where specified.

ENERGY DISPERSIVE X-RAY ANALYSIS (EDX)

Elemental analysis data was obtained using a Hitachi S-3400N scanning electron microscope (SEM) equipped with an Oxford INCA energy dispersive X-ray analysis (EDX) detector. Samples were affixed to a carbon disc by means of double-sided carbon tape. The disc was then attached to a 51 mm stage that was placed in the SEM chamber. The chamber was evacuated, and the electron beam was activated, having an accelerating voltage of 20 kV. The stage was then brought to a working distance of 10 mm, suitable for electron imaging. Crystals with flat, clean faces were chosen for elemental analysis by EDX. Scattered X-rays were collected over a 30 second analysis period for each point

of interest. Typically, at least five different data points were collected for a given sample to obtain a reasonable standard deviation for the composition. The INCA analyzer was standardized using copper tape prior to analysis.

DIFFERENTIAL SCANNING CALORIMETRY (DSC) AND THERMOGRAVIMETRIC ANALYSIS (TGA)

Differential scanning calorimetry (DSC) and thermogravimetric analysis (TGA) were performed using TA Instruments SDT-2960 simultaneous DSC-TGA instrument. Clean alumina sample pans (90 μ L volume) were tared on the microbalance arms prior to use. For a typical DSC/TGA experiment, 5 – 20 mg of powdered sample was placed in the forward sample pan while the rear sample pan was left empty as a reference for DSC. The sample and reference were heated from room temperature to any desired temperature up to 1400 °C at a rate of 10 °C / min. Flowing nitrogen was used to purge the furnace. Measurements of mass, temperature, and heat flow were recorded by the *TA Instrument Control* software program every second.⁸ Data analysis was performed using the *TA Universal Analysis* software package.⁹ Thermal events were characterized according to the positions of endotherms and exotherms in relation to weight loss. Observed weight loss was compared to theoretical weight loss values calculated from the molecular weight of the compound analyzed. Baseline corrections were made using a sapphire standard weighing 50 mg.

INFRARED (IR) SPECTROSCOPY

Infrared spectra of powdered samples were obtained using the KBr pellet technique. Approximately 10 mg of analyte powder was mixed with about 60 mg of KBr (International Crystal Laboratories, 99.999%) using a mortar and pestle. This mixture was pressed into a transparent pellet under 10 kpsi pressure imparted by a Carver hydraulic press on an Aldrich macro-micro KBr die containing the mixture. The pellet was then dried at 80 °C to remove any surface water. Samples were analyzed using a Nicolet Magna 550 IR spectrometer. Data was collected using *OMNIC* 6.1a software suite¹⁰ by scanning from 400 – 4000 cm⁻¹ under flowing nitrogen. Background from the KBr matrix was subtracted by scanning a blank KBr pellet over the same range of wavenumbers. Absorption peaks were assigned to their proper vibrational modes using literature specific to the class of compounds being analyzed.

X-RAY & VISIBLE FLUORESCENCE

Both X-ray and visible fluorescence were conducted on the monovalent hafnium fluorides. The X-ray luminescent spectra and fluorescent spectra were performed on a DMI5000 epifluorescent microscope (Leica Microsystems), equipped with a xenon light source and a DeltaNu DNS300 spectrometer. To acquire X-ray excited optical luminescent spectra, the samples were irradiated by an X-ray beam from an Amptek Mini X-ray tube (Ag target) set at 40 kV and 99 μA, and a 3 s acquisition was used. Fluorescence spectra were acquired using a Xe light source with a 460-495 nm short pass excitation filter and 515 nm emission filter with an acquisition time of 0.1 s.

UV-Vis-NIR ABSORPTION SPECTROSCOPY

Absorption measurements on the doped YBO_3 crystals were performed on a Perkin Elmer Lambda 900 Spectrophotometer from 200 – 3000 nm. This spectrophotometer utilized a deuterium lamp source for wavelengths up to 360 nm, switching over to a WI halogen lamp for higher wavelengths. Detection was achieved using a PMT detector up to 830 nm and a Peltier-cooled PbS detector beyond 830 nm. Data were collected using the UV-WinLab 6.0 software program.¹¹

Absorption measurements on the other acentric borates were performed using a Shimadzu UV-3101 PC UV-vis NIR Scanning Spectrophotometer from 200 – 3000 nm. An integrating sphere was used to accommodate solid powder samples in diffuse reflectance mode. This spectrophotometer also utilized a deuterium lamp source for wavelengths up to 360 nm, switching over to a WI halogen lamp for higher wavelengths. Detection was achieved using a PMT up to 830 nm and a PbS detector beyond 830 nm. Powdered samples were measured against a BaSO_4 standard, and data was converted from reflectance to absorption units using a Kubelka-Munk function.¹²

EMISSION SPECTROSCOPY

Excitation and emission spectra for materials containing lanthanide ions were obtained using a Jobin Yvon Horiba FluoroLog Tau-3 Spectrofluorometer. The spectrofluorometer utilized a 450 W xenon arc lamp source and was equipped with a PMT detector for detection up to 850 nm and a Hamamatsu InGaAs NIR detector for higher wavelengths. Typical emission spectra were collected over a range of 700 – 1700

nm, depending on the active lanthanide ion. Data was collected in 10 nm steps with a step size of 1.0 sec / nm. Samples consisting of powder or crystalline material containing single crystals up to 1.5 mm in size were placed in square cuvettes for analysis.

REFERENCES

- (1) Kennedy, G. C. *Am. J. Sci.* **1950**, *248*, 540-564.
- (2) Tuttle, O. F. *Geol. Soc. Am. Bull.* **1949**, *60*, 1727-1729.
- (3) PDXL, Version 2.1.1, Rigaku Corp., 2010.
- (4) CrystalClear, Rigaku/MSC, The Woodlands, TX, 1999.
- (5) REQAB, Rigaku Corp., Tokyo, Japan, 2010.
- (6) Sheldrick, G. M. SHELXTL, Structure Determination Software Programs, Version 6.1, Bruker Analytical X-ray Systems Inc., Madison, WI, 2000.
- (7) Spek, A. L. PLATON - A Multipurpose Crystallographic Tool; Utrecht University: Utrecht, The Netherlands, 2003.
- (8) THERMAL ADVANTAGE Instrument Control Software, Version 1.1A, TA Instruments, 1999.
- (9) UNIVERSAL ANALYSIS for Windows 95/98, Version 3.6C, Build 3.6.0.17, TA Instruments and Waters LLC, 1998.
- (10) OMNIC IR Control Software, Version 6.1a, Thermo Nicolet Corp., 1997.
- (11) UV-WinLab Software Program, Version 6.0, PerkinElmer, Inc., 2008.
- (12) Wendlandt, W. W.; Hecht, H. G. *Reflectance Spectroscopy*, Interscience Publishing: New York, NY, 1966.

CHAPTER THREE

HYDROTHERMAL SYNTHESIS AND CHARACTERIZATION OF NOVEL ALKALI THORIUM FLUORIDES

INTRODUCTION

The descriptive chemistry of solid-state inorganic thorium compounds received considerable attention in the early era of atomic energy,¹ but has been somewhat neglected in the last several decades. However, it may be worthy of new interest because of the possible use of thorium as a safe nuclear fuel in the future. Unlike uranium or plutonium, thorium cannot be weaponized or undergo meltdown in a reactor. The U.S. has enormous amounts of extractable thorium ore on shore, making it an intriguing material for the next generation of nuclear energy.² As such, the fundamental descriptive chemistry of thorium is worthy of revisiting.

Recently, it was found that thorium oxide can be grown as large high-quality single crystals using fluoride mineralizers in hydrothermal fluids.³ The use of molten alkali thorium fluoride systems (such as molten $\text{LiF} - \text{BeF}_2 - \text{ThF}_4$) as a fuel source in modern reactors² suggest that further hydrothermal exploration of inorganic thorium fluorides may be fruitful. One class of compounds of particular interest is the alkali thorium fluorides. These compounds are of technological interest because the next generation of both fusion and fission reactors may employ molten alkali thorium fluorides as a fuel source.^{2a} Previous work was done primarily on molten alkali fluoride salts and led to a variety of alkali metal thorium fluorides in the tetravalent state. A considerable number of $\text{A}_x\text{Th}_y\text{F}_z$ compounds, where A = alkali metal, were characterized,

mostly by either powder or single crystal diffraction (see Figure 3.1).^{1,4-30} Most of these original phases are sodium and potassium thorium fluorides with, to our knowledge, only one rubidium thorium fluoride and no cesium-containing examples previously reported as single crystal structures.

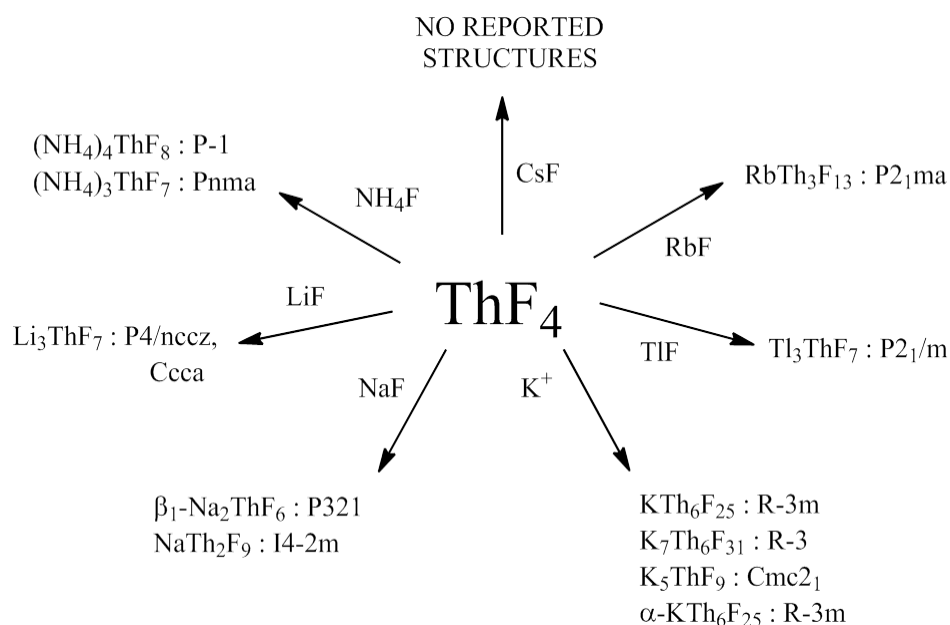


Figure 3.1. Overview of the reported monovalent alkali thorium fluoride single crystal structures.

Most of these early results are nearly 40 years old. Given the renewed technological interest in thorium chemistry and the interesting behavior of the oxides in hydrothermal fluids, a new study of thorium fluorides in hydrothermal fluids was undertaken. It was found that the chemistry of the thorium fluorides is much richer than anticipated. In general the reaction of ThF₄ with alkali fluorides in hydrothermal fluids

leads to a wide variety of new alkali metal thorium fluoride compounds. Systematic exploration of the phase space has uncovered a number of new species that typically reflect the size and stoichiometry of the alkali ion. Perhaps surprisingly, any hydrolysis of the Th-F bond, even in aqueous solution above 600 °C was rarely observed. Furthermore, inclusion of alkaline earth ions in the solution leads to ready formation of mixed alkali-alkaline earth thorium fluorides,³¹ suggesting that much of this phase space is still very rich. In this chapter, the chemistry and structures of a series of new alkali thorium fluorides grown from hydrothermal solution is described. Specifically, a series of new rubidium and cesium thorium fluorides including the first characterized cesium compound is reported and their structures correlated to other known metal fluorides.

RESULTS AND DISCUSSION

Initial Study: Cesium and Rubidium Thorium Fluorides³²

Descriptive Synthetic Chemistry

All the materials shown in this chapter have been synthesized hydrothermally from spontaneous nucleation (SN) of ThF₄ reacting with various concentrations of alkali fluoride mineralizers. Crystallographic data for this initial study are shown in Table 3.1, and detailed reaction conditions for the syntheses of cesium and rubidium thorium fluorides are shown in Table 3.2. Though synthesized in this initial study, the polymorphs of CsThF₅ and the structure Rb₇Th₆F₃₁ (**5**) will be discussed in detail in other sections.

Table 3.1. Crystallographic Data for Structures **1** – **4**

	1	2	3	4
Chemical Formula	F ₁₃ Th ₃ Cs	F ₁₃ Th ₃ Cs	F ₁₃ Th ₃ Rb	F ₉ Th ₂ Rb
F.W. (g/mol)	1076.03	1076.03	1028.59	720.55
Space group	<i>Pmc2₁</i>	<i>P6/mmm</i>	<i>Pmc2₁</i>	<i>Pnma</i>
Temp./K	293±2	293±2	293±2	293±2
Crystal system	Orthorhombic	Hexagonal	Orthorhombic	Orthorhombic
a, Å	8.1830 (16)	8.2607 (12)	8.1805 (16)	8.9101 (18)
b, Å	7.5780 (15)	8.2607 (12)	7.4378 (15)	11.829 (2)
c, Å	8.6244 (17)	8.6519 (17)	8.6594 (17)	7.1692 (14)
V, Å ³	534.81 (18)	511.30 (15)	526.88 (18)	755.6 (3)
Z	2	2	2	4
D _{cal} , Mg/m ³	6.682	6.989	6.483	6.334
Indices (min)	[-9, -9, -10]	[-10, -10, -10]	[-10, -9, -10]	[-11, -14, -8]
(max)	[9, 8, 10]	[10, 10, 10]	[10, 9, 10]	[11, 14, 8]
Parameters	89	26	89	59
F(000)	884	875	848	1192
μ, mm ⁻¹	45.119	47.193	46.982	45.824
2θ range, °	3.58 – 25.01	2.85 – 26.34	2.49 – 26.31	3.32 – 26.44
Collected reflections	4235	4870	4896	6376
Unique reflections	1008	250	1149	813
Final R (obs. data), ^a R ₁	0.0327	0.0393	0.0301	0.0797
wR ₂	0.0687	0.0976	0.0550	0.2327
Final R (all data), R ₁	0.0379	0.0394	0.0364	0.0829
wR ₂	0.071	0.0977	0.0576	0.2370
Goodness of fit (S)	1.020	1.187	1.093	1.079
Extinction coefficient	0.0078 (3)	0.0018 (4)	0.0064 (2)	0.0069 (11)
Largest diff. peak	4.002	7.777	4.170	10.005
Largest diff. hole	-2.120	-3.179	-2.287	-14.235

$$^a R_1 = [\sum ||F_o| - |F_c||] / \sum |F_o|; wR_2 = \{[\sum w[(F_o)^2 - (F_c)^2]^2]^{1/2}\}$$

Reactions were investigated by differing pressure, reaction time, and ratios of A:Th (A = Cs, Rb) as a means to explore this phase space and identify any trends in compound formation. Crystals of **1** and **2** seem to most commonly form as a mixture of phases over a wide range of Cs:Th ratios and reaction conditions. Phase pure yields were not common, but could be obtained from specific reaction conditions outlined in Table 3.1. Selected PXRD patterns for these products are shown in Figures 3.2 and 3.3,

Table 3.2. Specific conditions for the syntheses of the cesium and rubidium compounds

Condition*	Mineralizer	Alkali:Th Ratio	Pressure (kbar)	Time (days)	Crystal Shape(s)	Compound
1	CsF, 9 M	7.4:1	1	3	Polyhedra	CsTh ₃ F ₁₃ (<i>Pmc</i> 2 ₁) (1)
2	CsF, 0.5 M	0.41:1	1	6	Polyhedra	1
3	CsF, 1 M	0.82:1	1	3	Hexagonal rods	CsTh ₃ F ₁₃ (<i>P6/mmm</i>) (2)
4	CsF, 2 M	1.6:1	1	4	Square rods, polyhedra	1, 2 , CsThF ₅ **
5	CsF, 1 M	0.82:1	1	12	Square rods, polyhedra, hexagonal plates	1, 2 , CsThF ₅ **
6	RbF, 0.5 M	0.41:1	1	4	Polyhedra	RbTh ₃ F ₁₃ (<i>Pmc</i> 2 ₁) (3)
7	RbF, 1 M	0.82:1	1	7	Polyhedra	3
8	RbF, 1 M	0.82:1	1.67	6	Polyhedra, plates	3 , RbTh ₂ F ₉ (<i>Pnma</i>) (4)
9	RbF, 2 M	1.6:1	1.5	1	Polyhedra	Rb ₇ Th ₆ F ₃₁ (<i>R</i> $\bar{3}$)
10	RbF, 9 M	7.4:1	1	3	Polyhedra	Rb ₇ Th ₆ F ₃₁ (<i>R</i> $\bar{3}$)

*All condition temperatures are 575 °C

**These products will be described in the next section

showing the potential for phase purity. It is interesting that formation of the CsTh₃F₁₃ phases is not limited to the lowest Cs:Th ratios as one may expect based on the chemical formula, with these crystals forming from even 9 M CsF solutions. Also of note is that only the shortest reaction using 1 M CsF concentrations afforded a phase-pure yield of

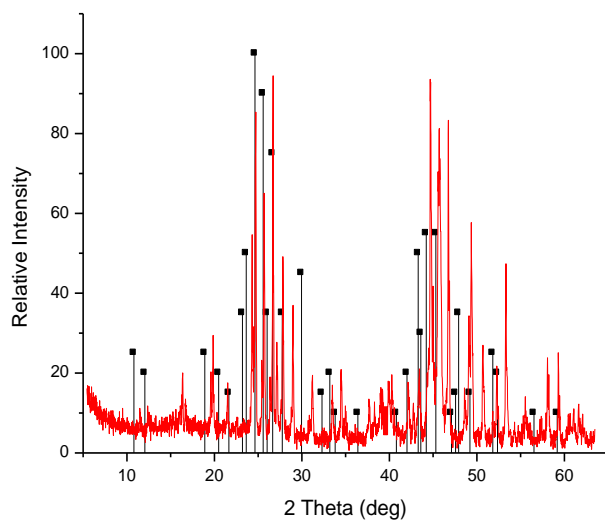


Figure 3.2. Powder patterns of **1** (red) and the known pattern for CsTh₃F₁₃ in a previously unidentified space group (black). The peaks around 38° is from the Al pan sample holder.

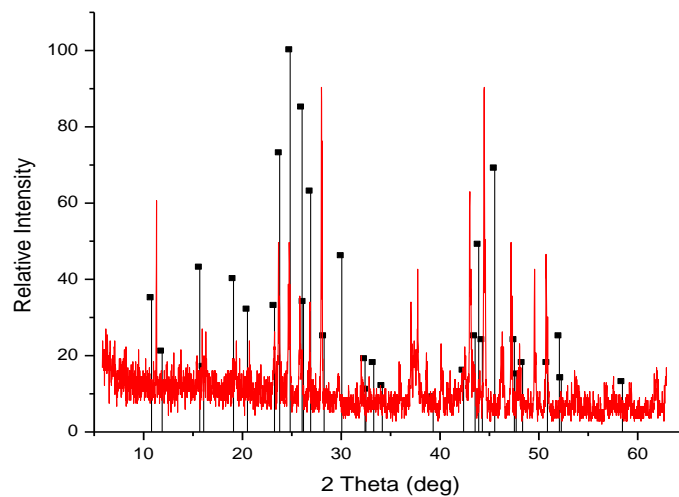


Figure 3.3. Powder patterns of **3** (red) and the known pattern for RbTh₃F₁₃ in a previously unidentified space group (black). The peaks around 38° is from the Al pan sample holder.

hexagonal CsTh₃F₁₃, suggesting that longer reaction time may cause conversion of **2** to **1**. Conditions 4 and 5 also support this conclusion, as a mixture of the phases is obtained from these longer experiments.

A variety of rubidium thorium fluorides resulted from similar reactions (conditions 6 - 10) in Table 3.2. In these cases, the products seem to be fairly sensitive toward the Rb:Th ratio in the reaction. This sensitivity is in fact reflected in the chemical formulae of the products, with RbTh₃F₁₃ forming from the lowest RbF concentrations (Rb:Th ~ 0.4:1 to 0.8:1), RbTh₂F₉ from Rb:Th ~ 0.8:1 and Rb₇Th₆F₃₁ from Rb:Th above 1.6:1. It is especially interesting that while both **3** and **4** formed from 1 *M* RbF, compound **4** only formed as a minor product in the reaction occurring at higher pressures suggesting there may be pressure dependence in its formation. Also note that unlike the cesium thorium fluoride system, a hexagonal modification of RbTh₃F₁₃ has not been observed in this study.

Attempts using nearly the exact conditions that form the Cs analog **2** do not lead to the hexagonal rubidium thorium fluoride. Similarly, the formation of **5** is unique to the rubidium thorium fluoride system. The very short reaction time and somewhat elevated pressure of this reaction have been applied to cesium thorium fluoride experiments with no evidence of a Cs analog of **5**. Powder XRD from conditions 7 and 9 was compared to known powder patterns of **3** and **5**, confirming these products were phase pure. The presence of RbTh₂F₉ was not apparent from the powder pattern of the material obtained via condition 8, thus compound **4** must be a very minor product identified only by selection of an appropriate single crystal for structure analysis. A shift to higher 2 θ

angles is observed for compound **3** relative to compound **1** accounting for the smaller unit cell volume of the Rb-containing isomorph.

*Crystal Structures of Orthorhombic (A)Th₃F₁₃ (A = Cs, Rb, **1** and **3** respectively)*

Solids **1** and **3** both crystallize in the acentric orthorhombic space group $Pmc2_1$ (No. 26), confirmed by PXRD comparisons to previously reported powder patterns (for which no space group was determined) and those simulated from our own single crystal structure determinations.^{4,8,12} Single crystals of suitable quality have not previously been synthesized for compound **1**; however, SXRD data for compound **3** was reported by Brunton¹² in the space group $P2_1ma$, a non-standard but identical variation of $Pmc2_1$ (No. 26).³³ We were able to obtain a somewhat better structure solution for (**3**) ($R = 0.0297$) in this study than previously reported by Brunton ($R = 0.0710$). Atoms F1, F2, F5, F6, and F8 in compound **1** were refined using an ISOR restraint to prevent their principal mean square atomic displacements from being non-positive definite. Both crystallographically unique thorium atoms are slightly distorted antiprisms with average Th-F distances of 2.385 (8) and 2.381 (9) for Th1 and Th2, respectively in **1** and 2.377 (12) and 2.373 (9) Å for Th1 and Th2, respectively, in **3**. These correlate well with both the expected values predicted by Shannon³⁴ and the values found by Brunton.¹² This phase contains Th1, A1, F1, F2, F5, F6, and F9 atoms in special positions, with all having m symmetry.

The isostructural compounds consist of alternating edge-shared nine-coordinate thorium atoms that conform to both monocapped square antiprisms (Th1) and tricapped

trigonal prisms (Th2). Unique Th atoms are edge sharing through F2 and F3 and corner sharing with separate connections through F7 and F8. Th1 is corner sharing with itself through F9, while Th2 is corner sharing with itself through F4 and F5 as well as edge sharing with itself through F1 and F6. This results in a layered framework based on triangular clusters of thorium fluoride polyhedra with channels in the framework oriented along [010] that accommodate the Cs or Rb cations (see Figure 3.4). This accounts for the observed cell parameters where the a and c axes are nearly equivalent for both the Cs and Rb compounds whereas the expected elongation associated with the presence of Cs in these channels is primarily apparent (albeit modestly) in the b axis length. Only a small difference in the average nine-coordinate alkali metal to fluoride bond distances (3.103 (3) in **1** and 3.036 (3) Å in **3**) is observed, as these appear to be largely governed by the diameter of the channels formed by the Th-F framework. It is reasonable to assume that smaller alkali cations Na^+ and K^+ would be very weakly bound in the channels of this structure type and would perhaps adopt a different structure type for an $\text{ATh}_3\text{F}_{13}$ formulation. As such, the $\text{KTh}_3\text{F}_{13}$ formulation had previously only been proposed in a hexagonal crystal system based on crystal morphology and thermal analysis data,⁶ and no space group or unit cell parameters were reported.

*Crystal Structures of Hexagonal $\text{CsTh}_3\text{F}_{13}$ (**2**)*

Solid **2** crystallizes in the hexagonal space group $\text{P6}/mmm$ (No. 191). This hexagonal polymorph of $\text{CsTh}_3\text{F}_{13}$ has not been previously reported, and its structure is notably different from the orthorhombic phase **1**. Owing to its high symmetry, every

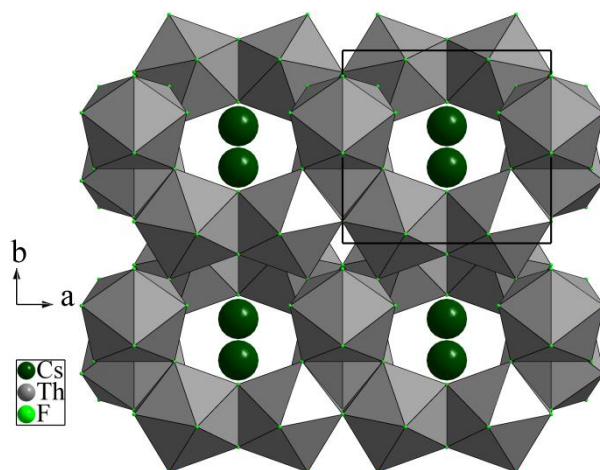


Figure 3.4. A view of the channel structure of **1** projected down the c axis.

atom save F3 sits on a special position. Cs1 and Cs2 both have $6/mmm$ symmetry, Th1 has $2mm$ symmetry, and F1, F2 and F4 have $m2m$, $3m$, and mmm symmetry, respectively. The single unique thorium atom in **2** adopts a slightly distorted monocapped square antiprismatic geometry. The thorium fluoride polyhedron is considered only slightly distorted as compared to previously reported calculations for standard monocapped square antiprisms³⁵ due to small variations in the Th-F bond lengths (Table 3.3). The apices of these polyhedra (formed by F4) are aligned along the c axis and are corner shared by neighboring Th atoms. Further connectivity of the polyhedra along the c axis occurs via edge sharing of F1 atoms as well as along the a and b axes through edge sharing of F2 and F3. Th-F bonds range from 2.301 (1) Å to the apical F4 to a somewhat elongated 2.481 (7) Å to F2 (see Table 3.3), but having an average of 2.379 Å, correlating well with the expected values predicted by Shannon.³⁴

Table 3.3. Selected Bond Distances (Å) with esds for Compounds **1** and **3**

Compound 1		Compound 3	
Bond Distances (Å)		Bond Distances (Å)	
Th1—F2	2.482 (19)	Th1—F2	2.445 (16)
Th1—F3 (x2)	2.463 (12)	Th1—F3 (x2)	2.466 (9)
Th1—F7 (x2)	2.360 (12)	Th1—F7 (x2)	2.348 (9)
Th1—F8 (x2)	2.350 (12)	Th1—F8 (x2)	2.344 (9)
Th1—F9 (x2)	2.32 (2)	Th1—F9 (x2)	2.314 (18)
Th2—F1	2.384 (8)	Th2—F1	2.366 (6)
Th2—F2 ⁱ	2.480 (11)	Th2—F2 ⁱ	2.486 (9)
Th2—F3	2.348 (13)	Th2—F3	2.347 (10)
Th2—F4 ⁱⁱ	2.340 (12)	Th2—F4 ⁱⁱ	2.352 (10)
Th2—F4 ⁱⁱⁱ	2.390(12)	Th2—F4 ⁱⁱⁱ	2.369 (10)
Th2—F5	2.355 (8)	Th2—F5	2.346 (7)
Th2—F6	2.388 (9)	Th2—F6	2.386 (7)
Th2—F7	2.333 (13)	Th2—F7	2.319 (9)
Th2—F8 ^{iv}	2.408 (11)	Th2—F8 ^{iv}	2.382 (9)
Cs1—F1	2.835(16)	Rb1—F1	2.826 (13)
Cs1—F3 (x2)	3.005 (12)	Rb1—F3 (x2)	2.921 (9)
Cs1—F4 (x2)	3.222 (12)	Rb1—F4 (x2)	3.162 (9)
Cs1—F6	2.911 (16)	Rb1—F6	2.889 (13)
Cs1—F6	3.097 (14)	Rb1—F6	3.002 (15)
Cs1—F8 (x2)	3.315 (16)	Rb1—F8 (x2)	3.220 (9)

Symmetry codes: (i) $x, -y, z+1/2$; (ii) $x, -y+1, z+1/2$; (iii) $x, -y, z-1/2$; (iv) $x, y-1, z$.

The resulting network of thorium fluoride polyhedra form hexagonally shaped channels along the c direction. The boundaries of the channel are formed by alternating F1 and F3 atoms so the channel varies in diameter from the base of each point in the hexagon, measuring 5.26 (2) Å in diameter for F3 boundaries and 5.79 (1) Å for F1 boundaries. Opposing Th atoms are separated by 8.261 (1) Å across the channel. This leaves ample space for the cesium ions to occupy the channel (see Figure 3.5). Cesium(1) exhibits a six-coordinate trigonal prismatic geometry and is fairly tightly bound in this channel to F1 atoms (Cs1-F1 = 2.890 (12) Å). Cesium(2) is held in place

by much weaker interactions, having 12 long bonds to F3 (3.131 (13) Å). The unique Cs atoms alternate along [001]. Thus the structure is layered along [001] with a layer of thorium polyhedra followed by a layer of Cs2 atoms, then a second layer of thorium polyhedra followed by a layer of Cs1 atoms as shown in Figure 3.6. Layers are also evident along [100] an [010]. Here only a two-layer repeat pattern of Th polyhedra exists followed by a layer containing Cs1, Cs2 and Th atoms.

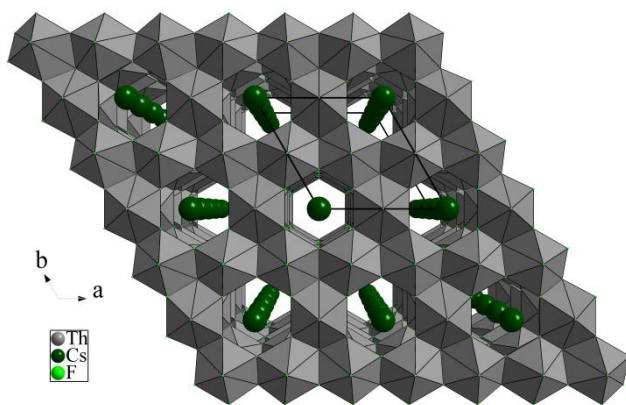


Figure 3.5. Perspective view of the channel structure of **2** down the *c* axis. The nine-coordinate thorium (shown as grey polyhedra) also run infinitely in the *c* direction and form hexagram-shaped channels where the Cs⁺ (dark green) resides.

The structural feature distinguishing structures **1** and **2** is most obviously the shape of the channels and the direction in which they run. This is certainly dependent on the differences in thorium geometries in each, and the simpler Th-F network of **2** is

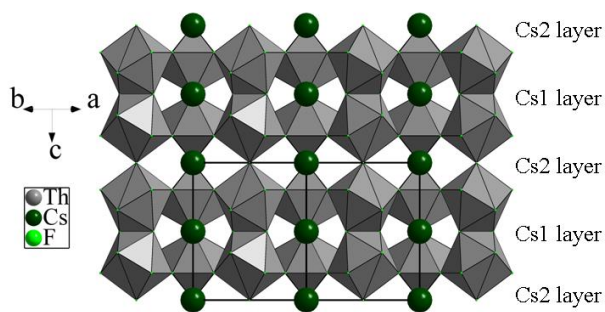


Figure 3.6. Layered structure of **2** viewed along the [110] direction with a single unit cell shown with black edges. The two unique cesium sites occupy different layers in an alternating fashion. This also serves as a cross sectional view of the channel structure where only three of the six thorium polyhedra, participating in the channel construction, are currently displayed.

Table 3.4. Selected Bond Distances (Å) with esds for Compound **2** and **4**

Compound 2		Compound 4	
Bond Distances (Å)		Bond Distances (Å)	
Th1—F1 (x2)	2.375 (6)	Th1—F1	2.367 (9)
Th1—F2 (x2)	2.481 (7)	Th1—F1	2.346 (9)
Th1—F3 (x4)	2.350 (6)	Th1—F2	2.338 (9)
Th1—F4	2.3006 (9)	Th1—F2	2.381 (9)
Cs1—F1 (x6)	2.890 (12)	Th1—F3	2.364 (10)
Cs2—F3 (x12)	3.131 (13)	Th1—F3	2.417 (8)
		Th1—F4	2.385 (9)
		Th1—F4	2.406 (9)
		Th1—F5	2.3531 (9)
		Rb1—F1 (x2)	2.772 (9)
		Rb1—F2 (x2)	2.744 (10)
		Rb1—F3 (x2)	2.857 (12)
		Rb1—F3 (x2)	3.182 (10)
		Rb1—F4 (x2)	3.248 (10)

Symmetry codes: (i) $-x+y+2/3, -x+1/3, z+1/3$; (ii) $-x+2/3, -y+1/3, -z+1/3$; (iii) $x-y-1/3, x-2/3, -z+1/3$; (iv) $y+1/3, -x+y+2/3, -z+2/3$; (v) $x-2/3, y-1/3, z+2/3$; (vi) $-y+1/3, x-y-1/3, z-1/3$.

reflected in its higher symmetry space group. It is interesting that in comparing compounds **1** and **2** when two types of thorium polyhedra are present the resulting structure is not only of lower orthorhombic symmetry, but it is also acentric. It can be postulated that the larger channel diameter of **2** may factor in why an analogous hexagonal $\text{RbTh}_3\text{F}_{13}$ phase has not been obtained, as the channel present in this structure type may be too wide to support Rb at the A2 alkali metal sites.

*Crystal Structure of RbTh_2F_9 (**4**)*

Compound **4** crystallizes in the orthorhombic space group $Pnma$ (No. 62). Unfortunately, due to relatively poor crystal quality in the numerous samples tested, the best final R_1 value is somewhat high at 0.0768, and all of the atoms had to be refined using an ISOR restraint to prevent their principal mean square atomic displacements from being non-positive definite (though Th1 still remained a non-positive definite and was refined isotropically). However, the structure makes good chemical sense, since Brunton characterized potassium uranium fluoride, KU_2F_9 , in the same space group and the atomic positions for each atom closely resembles this structure solution.³⁶ This new compound consists of alternating layers (along [010]) of nine-coordinate thorium atoms and rubidium atoms. The thorium atoms adopt a highly distorted tricapped trigonal prismatic geometry similar to that of Th2 in **1** and **3**. These polyhedra exhibit a preferential alignment of Th-F5 bonds along the b axis, which directly connect the thorium layers. The thorium fluoride polyhedron is highly distorted as compared to previously reported calculations for more typical tricapped trigonal prisms³⁷ due to

observed variations in the Th-F bond lengths (Table 3.4). The Th-F bond lengths vary from 2.338 (9) Å to 2.417 (8) Å with an average Th-F distance of 2.373 Å.

Thorium fluoride polyhedra are edge sharing through pairs of F1 atoms and through F2 and F3, and corner sharing through F4 and F5 to form the layered framework. Thorium atoms connect in a zigzag fashion along [100] and [001] within their layers, as shown in Figure 3.4. Channels in the Th-F framework running along the [100] direction accommodate the Rb cations. These channels are shaped as hexagons elongated along the *c* axis, and Rb atoms are staggered within the channels due to the zigzag nature of the thorium fluoride framework (Figures 3.7 and 3.8). The Rb cation exhibits six typical bonds to F atoms (F2, F3 and F5) ranging from 2.744 (10) Å to 2.857 (12) Å and two pairs of very weak interactions to each of F3 (3.182 (10) Å) and F4 (3.248 (10) Å) atoms. Thus, the channels here are much smaller than those in which the Rb resides in **3**.

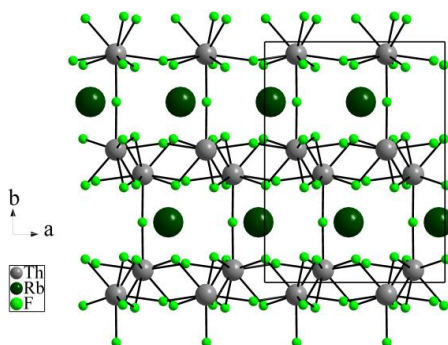


Figure 3.7. Compound **4** viewed down the *c* axis, showing the zigzag nature of the thorium-containing layers. Layers are connected along the *b* axis through Th1-F5-Th1 bonding as well as Rb-F interactions.

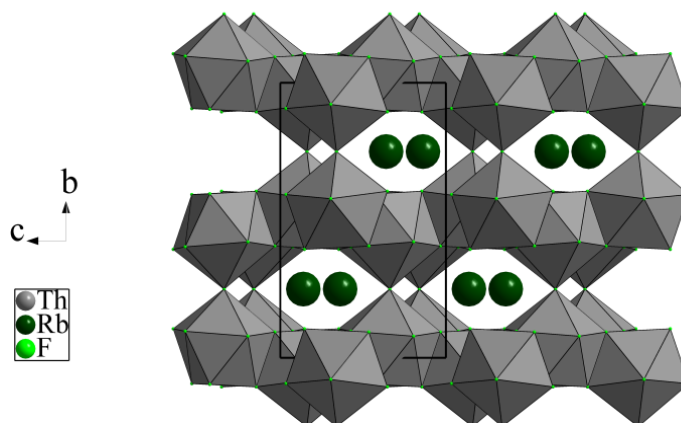


Figure 3.8. Channel structure in **4** viewed down the a axis. The nine-coordinate thorium atoms (shown as grey polyhedra) form elongated hexagon-shaped channels where the Rb^+ (dark green) can sit in a staggered formation.

Based on the observed Rb-F bond distances in this compound (and given a comparison of the bond lengths in the compounds $\text{K}_7\text{Th}_6\text{F}_{31}$ and $\text{Rb}_7\text{Th}_6\text{F}_{31}$ discussed below) it is not surprising that powders of previously reported KTh_2F_9 phase have been indexed in an orthorhombic crystal system ($Pnam$) with related cell parameters $a = 8.85 \text{ \AA}$, $b = 7.16 \text{ \AA}$ and $c = 11.62 \text{ \AA}$.¹⁶ Previously reported NaTh_2F_9 crystallizes in an entirely different structure type (s.g. $\bar{I}42m$).¹⁹ However, the single crystal structure determination of KU_2F_9 ⁴⁰ shows that it is similar to the structure reported herein. In the single crystal structure determination of the present study, only two atoms, Rb1 and F5, sit on special positions, and both have m symmetry.

The Polymorphism of CsThF₅³⁸

Descriptive Synthetic Chemistry

Crystallographic data for this study is shown in Table 3.5, and Table 3.6 summarizes the various reactions highlighted in this study. The reaction of CsF with ThF₄ in nearly a 1:1 ratio leads to formation of three different polymorphs of the formula CsThF₅, depending on subtle changes in the reaction time, temperature, and pressure. Many of the reactions generated mixtures of one or more products, but it was possible to obtain phase pure yields of polymorph **2** and **3** in some instances, as shown in Table 3.6. Attempts at synthesizing phase pure yields of **1** met with no success. However, it was interesting to observe the different products that were obtained in these attempts by changing the reaction conditions, as seen in conditions 1 – 4. Using condition 1, compound **2** was obtained as a phase-pure product. When the time was extended (condition 2) both **2** and the tetragonal polymorph **1** were formed, with the majority of the product being a mixture of the CsTh₃F₁₃ polymorphs discussed in the previous section. Increased pressure in the system (condition 3) results in an improved yield of **1** with less of the CsTh₃F₁₃ phases, with the lower-symmetry polymorphs not present. Using a somewhat increased reaction temperature (condition 4) resulted in phase-pure yields of **3**.

Comparing conditions 1 and 5 – 8, it is evident that compound **2** could be synthesized from a wide range of mineralizer concentration (and thus Cs:Th ratio). Mixtures of products were only observed when the CsF mineralizer concentration was between 2 – 3 M, and polymorph **3** was only observed at CsF concentrations above 3 M.

Table 3.5. Specific reaction conditions for the syntheses of the title solids

Condition*	Mineralizer	Alkali:Th Ratio	Pressure (kbar)	Time (days)	Compound
1	CsF, 1 M	0.82:1	1	3	CsThF ₅ (P2 _{1/c}) (6)
2	CsF, 1 M	0.82:1	1	12	CsThF ₅ (P4/nmm) (5), 6 , CsTh ₃ F ₁₃ **
3	CsF, 1 M	0.82:1	1.76	2	5 , CsTh ₃ F ₁₃ **
4 (625 °C)	CsF, 1 M	0.82:1	1	7	CsThF ₅ (P2 _{1/c}) (7)
5	CsF, 0.5 M	0.41:1	1	3	6
6	CsF, 2 M	1.6:1	1	4	6 , CsTh ₃ F ₁₃ **
7	CsF, 3 M	2.5:1	1	4	6 , 7 , CsTh ₃ F ₁₃ **
8	CsF, 10 M	8:1	1	5	6 , 7 , CsTh ₃ F ₁₃ **

*All condition temperatures are 575 °C unless otherwise specified

**This product has been described in the previous section

Phases of CsTh₃F₁₃ were always present in any reactions that yielded mixtures of various products. The propensity for formation of compound **2** over a variety of conditions compared to the somewhat limited conditions in which compounds **1** and **3** were obtained suggest that polymorph **2** is the more stable AThF₅ phase in cesium thorium fluoride systems, and that polymorphs **1** and **3** are observed in more specific reaction conditions. This theory was tested using DSC experiments as described below (*vide infra*).

Table 3.6. Crystallographic Data for CsThF₅ Structures **5** - **7**

	5	6	7
Chemical Formula	F ₅ ThCs	F ₅ ThCs	F ₅ ThCs
Color	Colorless	Colorless	Colorless
F.W. (g/mol)	459.95	459.95	459.95
Space group	P4/ <i>mmm</i>	P2 ₁ / <i>c</i>	P2 ₁ / <i>c</i>
Temp./K	293±2	293±2	293±2
Crystal system	Tetragonal	Monoclinic	Monoclinic
a, Å	5.7358 (8)	8.3600 (17)	8.4196 (17)
b, Å	5.7358 (8)	7.2870 (15)	14.645 (3)
c, Å	7.4048 (15)	8.9912 (18)	8.5017 (17)
α, °	90	90	90
β, °	90	116.69 (3)	102.67 (3)
γ, °	90	90	90
V, Å ³	243.61 (7)	489.37 (17)	1022.8 (4)
Z	2	4	8
D _{cal} , Mg/m ³	6.270	6.243	5.974
Indices (min)	[-6, -6, -8]	[-10, -9, -11]	[-10, -18, -10]
(max)	[6, 6, 8]	[9, 8, 11]	[10, 17, 9]
Parameters	18	65	128
F(000)	380	760	1520
μ, mm ⁻¹	37.960	37.791	36.165
2θ range, °	2.75 – 25.02	2.73 – 26.38	2.48 – 26.36
Collected reflections	1918	4040	8536
Unique reflections	149	1002	2097
Final R (obs. data), ^a R ₁	0.0435	0.0399	0.0621
wR ₂	0.1078	0.0913	0.1659
Final R (all data), R ₁	0.0450	0.0439	0.0762
wR ₂	0.1086	0.0942	0.1885
Goodness of fit (S)	1.159	1.084	1.135
Extinction coefficient	0.0000	0.0350 (14)	0.0039 (4)
Largest diff. peak	2.738	3.181	3.882
Largest diff. hole	-2.528	-4.155	-9.835

$$^a R_1 = [\sum ||F_o| - |F_c||] / \sum |F_o|; wR_2 = \{[\sum w[(F_o)^2 - (F_c)^2]^2]\}^{1/2}$$

Crystal Structure of CsThF₅ (**5**)

Compound **5** was found to crystallize into the tetragonal space group P4/*mmm* (No. 129). Its calculated powder pattern is similar to a previously reported powder pattern obtained on a melt grown sample of nominal composition CsThF₅;⁷ however, no

structural investigation or analysis was performed on that material. An equivalent solution was also obtained in space group $P4/n$, but $P4/nmm$ was preferred as it considered fewer parameters to reach the statistically equivalent solution.³⁹ The thorium atoms form slightly distorted square antiprisms with fluoride ions, having an average Th-F distance of 2.381 (17) Å, which correlates well with the expected values predicted by Shannon.³⁴ There are unique atoms that lie on special positions: Th1 and F1 have a mirror plane about the c axis and Cs1 has $2/m$ symmetry about the c axis, while F2 half occupies a general position.

This compound consists of layers alternating along the c axis between nine-coordinate thorium polyhedra and cesium atoms. The thorium atoms adopt a slightly distorted monocapped square antiprism geometry formed by two unique fluoride sites (Figure 3.9). F1 comprises the apex of the prism cap and is also bound to four Cs atoms. Its bond with thorium is shorter than the other bonds in the antiprism and runs exactly parallel with the c axis, dictating the polyhedral alignment. The F2 site (Wyckoff 16k) is half-occupied to complete the geometry about Th and to improve an abnormally high thermal parameter when fully occupied, and also to provide a sensible charge balance. The orientation of the apices of neighboring thorium fluoride polyhedra alternates by a 180° relative to the c axis. These polyhedra edge-share through two F2 atoms on four edges with one another. The thorium fluoride layers run infinitely in the ab plane to create bitrapezoidal-shaped channels along [001] (Figure 3.10). Cesium atoms fill these channels in the alternating layered fashion. Cesium is 12-coordinate with fluoride having an average bond distance of 3.036 (15) Å and the Cs-F polyhedra are edge sharing.

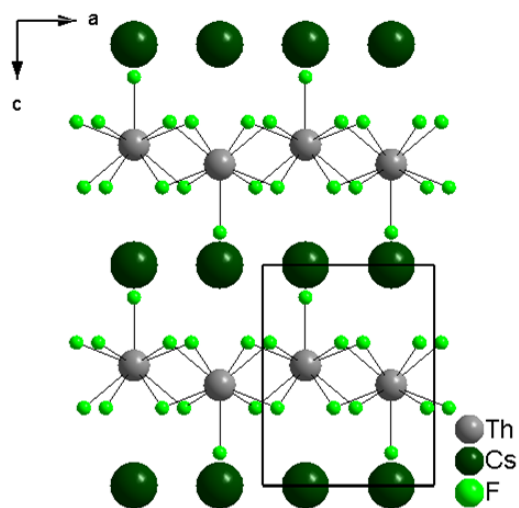


Figure 3.9. Section of the layers in **5** viewed down the b axis. The nine-coordinate thorium polyhedra run infinitely in the ab direction and alternate between the polyhedra and cesium atoms.

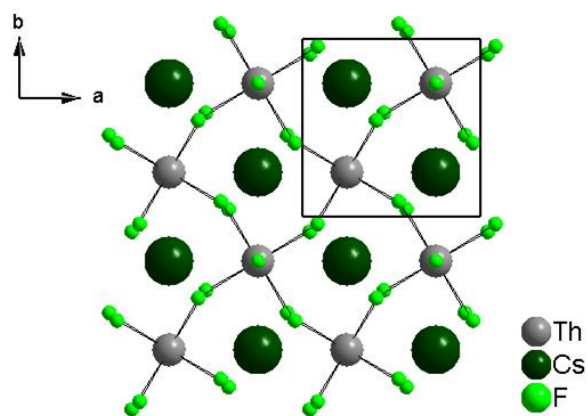


Figure 3.10. Section of the layers in **5** viewed down the c axis. The cross-linked layers of polyhedra stacked along the $[010]$ unit cell direction form bitrapezoidal-shaped channels infinitely in the c direction.

Crystal Structures of Unique CsThF₅ (6 and 7)

Solids **6** and **7** were shown to both crystallize into the monoclinic space group $P2_1/c$ (No. 14) upon structural refinement. These solids are isostructural to previously reported hafnium analogs RbHfF_5 ⁴⁰ and $(\text{NH}_4)\text{HfF}_5$,⁴¹ respectively. Though both **6** and **7** are the same formulation in the same space group, their crystallography is quite different both in terms of polyhedra orientation and their thorium layers. Notable differences are also observed in their axis lengths and β angles (Table 3.7). The thorium metal centers in both **6** and **7** are nine-coordinate with a tricapped trigonal prismatic geometry. They are slightly distorted with an average Th-F distance of 2.413 (7) for Th1 in **6**, and 2.403 (11) and 2.398 (11) Å in Th1 and Th2 in **7**, respectively, which correlate well with the expected values predicted by Shannon.³⁴

The long-range structure of **6** consists of chains of corner sharing thorium fluoride polyhedra propagating along the c axis (Figure 3.11, left). As shown in Figure 3.9, left, the Th-F chains are isolated from one another along $[010]$. Parallel chains are connected along $[100]$ and $[010]$ only through Cs-F interactions, as the Cs-F network forms a sheet in the bc plane in the center of the unit cell. Cs is surrounded by six fluorine ions with bonds ranging from 2.891 (7) to 3.275 (8) Å, and maintains two longer fluoride interactions of 3.417 (7) and 3.434 (8) Å. Interestingly, the short Th-F interaction (2.219 (8) Å) points directly toward this Cs-F sheet, similar to what is observed in the structure of **5**. In **7**, the thorium fluoride polyhedra group together in chains that propagate along $[001]$ by edge sharing, and link along $[100]$ through Th1-F8-Th2 corner sharing, resulting in a sheet of Th-F polyhedra in the ac plane (Figure 3.11, right). Sheets are separated

Table 3.7. Selected Bond Distances (Å) with esds for Compounds **5** - **7**

Compound 5		Compound 6		Compound 7	
Bond Distances (Å)		Bond Distances (Å)		Bond Distances (Å)	
Th1—F1	2.28 (3)	Th1—F1	2.395 (7)	Th1—F1	2.206 (10)
Th1—F2 (x4)	2.390 (17)	Th1—F1 ⁱ	2.387 (7)	Th1—F3	2.205 (11)
Th1—F2 (x4)	2.392 (17)	Th1—F2	2.441 (7)	Th1—F5	2.314 (11)
Cs1—F1 (x4)	3.070 (10)	Th1—F2 ⁱⁱ	2.364 (7)	Th1—F5 ⁱ	2.369 (12)
Cs1—F2 (x8)	3.019 (17)	Th1—F3	2.393 (6)	Th1—F7	2.422 (10)
		Th1—F3 ⁱⁱⁱ	2.429 (7)	Th1—F8	2.381 (12)
		Th1—F4	2.388 (7)	Th1—F9	2.428 (9)
		Th1—F4 ⁱⁱ	2.400 (7)	Th1—F10 ⁱ	2.524 (10)
		Th1—F5 ⁱⁱ	2.219 (8)	Th1—F10	2.779 (11)
		Cs1—F1 ^{iv}	3.129 (7)	Th2—F2	2.227 (11)
		Cs1—F1 ⁱ	3.417 (7)	Th2—F4	2.201 (11)
		Cs1—F2 ^v	2.938 (7)	Th2—F6	2.345 (10)
		Cs1—F3 ^v	3.275 (8)	Th2—F6 ⁱⁱ	2.365 (10)
		Cs1—F4 ^{vi}	2.891 (7)	Th2—F7	2.394 (10)
		Cs1—F5 ⁱⁱ	2.932 (8)	Th2—F8 ⁱⁱⁱ	2.335 (12)
		Cs1—F5 ⁱ	2.959 (8)	Th2—F9 ⁱⁱ	2.550 (9)
		Cs1—F5 ^{vi}	3.434 (8)	Th2—F9	2.720 (10)
				Th2—F10	2.443 (10)
				Cs1—F1	2.949 (12)
				Cs1—F2 ^{iv}	3.153 (12)
				Cs1—F2 ^v	3.398 (12)
				Cs1—F3 ⁱ	3.136 (11)
				Cs1—F3 ^v	3.144 (10)
				Cs1—F4 ^{vi}	3.062 (11)
				Cs1—F4 ^{vii}	3.337 (11)
				Cs1—F6 ^{vii}	3.071 (12)
				Cs1—F9 ^v	3.089 (10)
				Cs2—F1 ^{viii}	3.181 (10)
				Cs2—F1 ^{vii}	3.052 (10)
				Cs2—F2 ^v	3.160 (11)
				Cs2—F2 ^{iv}	3.266 (12)
				Cs2—F3 ^x	3.060 (12)
				Cs2—F4 ^{vi}	2.957 (11)
				Cs2—F5 ^{viii}	3.079 (12)
				Cs2—F7 ^{vii}	3.216 (10)
				Cs2—F10 ^{iv}	3.219 (10)

Symmetry codes: 2: (i) $-x+2, -y, -z$; (ii) $-x+2, y+1/2, -z+1/2$; (iii) $x, -y+1/2, z-1/2$; (iv) $x-1, -y+1/2, z-1/2$; (v) $-x+1, -y, -z$; (vi) $x-1, y, z-1$. 3: (i) $x, -y+1/2, z+1/2$; (ii) $x, -y+1/2, z-1/2$; (iii) $x+1, y, z$; (iv) $x-1, -y+1/2, z+1/2$; (v) $-x, y-1/2, -z+1/2$; (vi) $-x, -y, -z$; (vii) $x-1, y, z$; (viii) $-x-1, -y, -z$; (ix) $-x-1, y-1/2, -z+1/2$.

along [010] by layers of Cs atoms (Figure 3.12, right). It was also noted that a difference in the coordination environment of the two unique Cs atoms in this polymorph versus **6**, where Cs is nine-coordinate with bond distances to fluoride ranging from 2.949 (12) to 3.398 (12) Å. All unique atoms in both compounds lie on general positions.

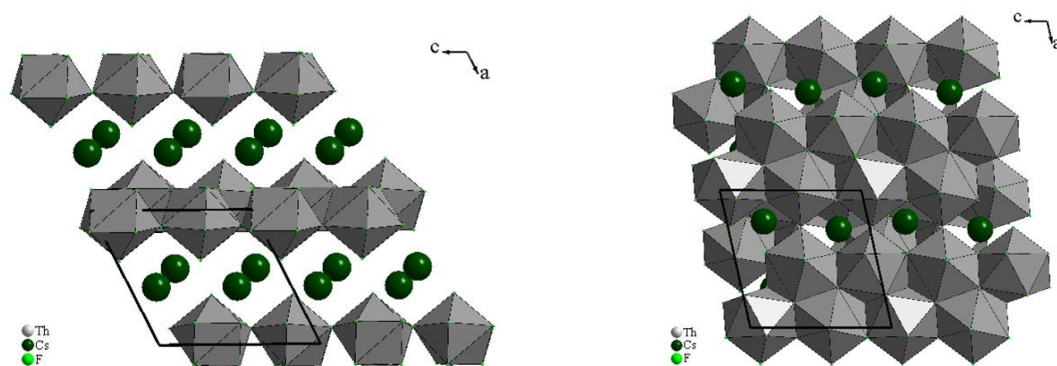


Figure 3.11. Section of the layers in **6** (left) and **7** (right) viewed down the b axis.

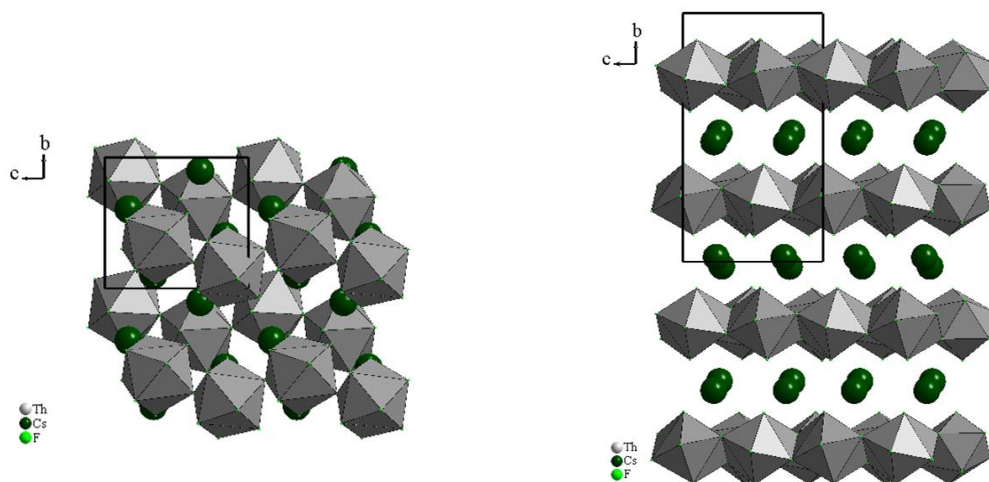


Figure 3.12. Section of the layers in **6** (left) and **7** (right) viewed down the a axis.

DSC Studies of CsThF₅ Polymorphs

In an effort to obtain some insight regarding the relative stabilities of the various Cs-Th-F polymorphs, DSC studies were conducted on phase pure samples of **6**. As can be seen in Figure 3.13, the DSC plot contains sharp endotherms around 500, 650, and 770 °C in addition to the large endotherm around 850 °C. It must be noted that each sample was heated under argon to prevent decomposition of the samples to ThO₂, as we have seen when heated in air. After heating another pure sample of **6** for one hour at 550 °C, past the first transition temperature, PXRD comparisons show that this sample was completely converted into compound **7** (Figure 3.14, red graph). This not only confirms that **6** and **7** are structurally different compounds but suggests that **7** is the higher temperature phase. This is consistent with our observation that **7** formed in its highest yield from hydrothermal reactions performed at more elevated temperatures. Upon further heating this sample to 700 °C for another hour, PXRD revealed another structural transition, this time to the hexagonal modification (*P6/mmm*) of CsTh₃F₁₃ (Figure 3.14, green graph). After one more heating cycle, the final observed transition results from the conversion of hexagonal CsTh₃F₁₃ to orthorhombic CsTh₃F₁₃ (Figure 3.14, blue graph). Thus it appears the hexagonal CsTh₃F₁₃ of our previous study may be a metastable phase in hydrothermal reaction conditions. Further heating to 925 °C results in the melting and subsequent decomposition of orthorhombic CsTh₃F₁₃ to CsF and ThF₄. The position of this endotherm is consistent with previous observations.^{4,7} Unfortunately, the inability to produce useful amounts of pure samples of polymorph **5** precludes any conclusions about its relative stability.

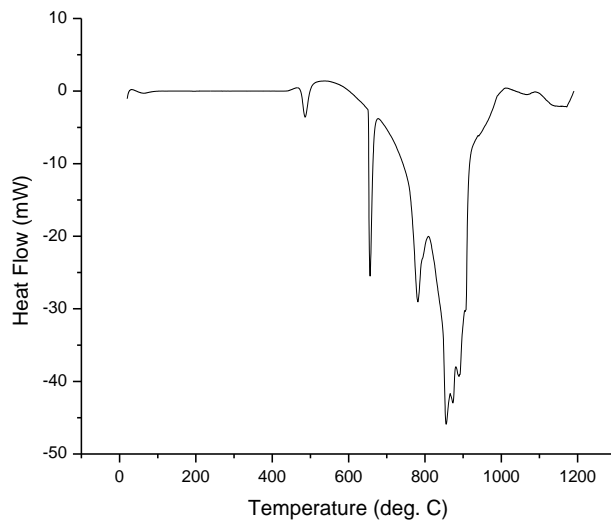


Figure 3.13. DSC of compound **6** synthesized from condition 1. Each transition was investigated via PXRD.

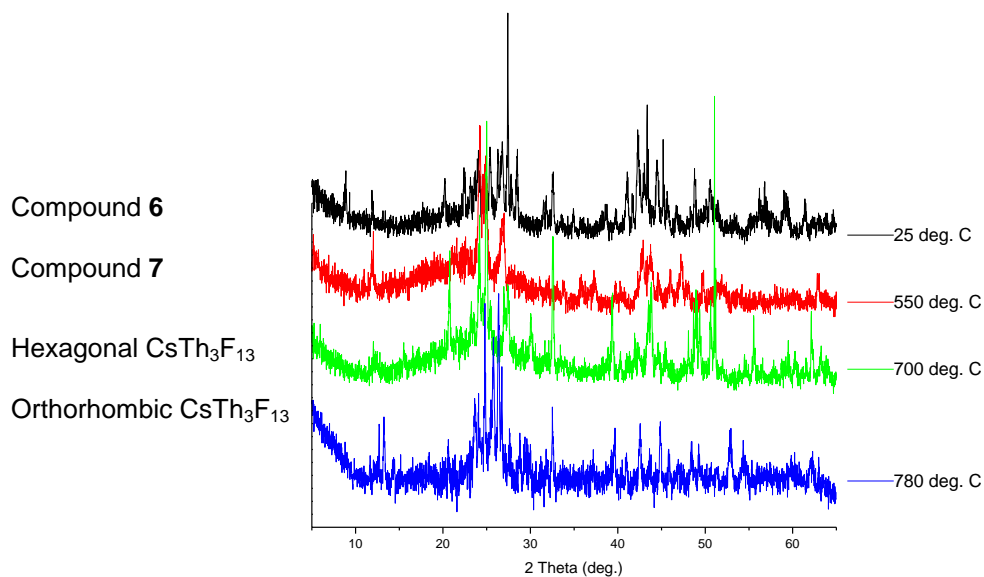


Figure 3.14. PXRD of compound **6** at room temperature and after heating past each transition.

The Crystal Structures of CsTh₆F₂₅ and NaTh₃F₁₃⁴²

Crystal Structure of CsTh₆F₂₅ (8)

Crystallographic data for this initial study is shown in Table 3.8. Compound **8** was found to crystallize into the hexagonal space group P6₃/mmc (No. 194). Atoms F3 and F5 in this solution had to be refined using an ISOR restraint to prevent their principal mean square atomic displacements from being non-positive definite. This compound is isostructural to the CsU₆F₂₅ formulation previously structurally characterized by Brunton.⁴³ Similar phases of **8**, RbTh₆F₂₅ and KTh₆F₂₅, were proposed to crystallize in P6₃/mmc via powder diffraction data.⁷ However, the only single crystal data available for this phase of alkali thorium fluoride is for α-KTh₆F₂₅, a polymorph that was found to crystallize in R $\bar{3}m$.¹⁵ Although it forms a framework system that contains pores, its thorium polyhedra stack in an ABCABC order, as compared to a structure that stacks in an ABAB order, similar to CsU₆F₂₅. The powder pattern for **1** is similar to a previously-reported powder pattern for a melt of nominal composition CsTh₆F₂₅ which was not otherwise characterized or structurally analyzed.⁴ The thorium atoms form slightly distorted tricapped trigonal prisms with fluoride ions, having an average Th-F distance of 2.391(7) Å, which correlates well with the expected values predicted by Shannon.³⁴ All the unique atoms in **8** lie on special positions. Th1, F2, and F4 have *m* symmetry along the *b* axis, F3 has a two-fold rotation along the *b* axis, F1 has *mm*2 symmetry, F5 and F6 has a three-fold rotation along the *a* axis and a mirror plane on the *b* axis, and Cs1 has 6*m*2 symmetry.

Table 3.8. Crystallographic Data for Structures **8** and **9**

	8	9
Chemical Formula	F ₂₅ Th ₆ Cs	F ₁₃ Th ₃ Na
F.W. (g/mol)	2000.15	966.11
Space group	P6 ₃ /mmc	P6 ₃ /mmc
Temp./K	293±2	293±2
Crystal system	Hexagonal	Hexagonal
a, Å	8.3507 (12)	8.2570 (12)
c, Å	16.914 (3)	16.891 (3)
V, Å ³	1021.5 (3)	997.3 (3)
Z	2	4
D _{cal} , Mg/m ³	6.503	6.434
Indices (min)	[-10, -10, -21]	[-10, -10, -21]
(max)	[10, 10, 19]	[10, 10, 20]
Parameters	37	40
F(000)	1640	1592
μ, mm ⁻¹	45.478	44.836
2θ range, °	2.41 – 26.35	2.41 – 26.36
Collected reflections	9073	8785
Unique reflections	435	433
Final R (obs. data), ^a	0.0403	0.0422
wR ₂	0.0962	0.1110
Final R (all data), R ₁	0.0457	0.0454
wR ₂	0.1008	0.1140
Goodness of fit (S)	1.222	1.212
Extinction coefficient	0.00032 (12)	0.00056 (19)
Largest diff. peak	8.324	2.949
Largest diff. hole	-2.953	-2.842

$$^a R_1 = [\sum ||F_o| - |F_c||] / \sum |F_o|; wR_2 = \{[\sum w[(F_o)^2 - (F_c)^2]^2]\}^{1/2}$$

The new compound consists of a framework of extended bilayers, using nine-coordinate thorium polyhedra as its principle building block (Figure 3.15). The thorium atoms adopt a slightly distorted tricapped trigonal prism. F4 comprises the apex of the prism and is also bound to neighboring Cs atoms. This Th-F bond (2.566 (8) Å) is longer than the other bonds in the prism and dictates the polyhedral alignment due to is corner-sharing by the thorium polyhedra in the next layer along the *c* axis. The apices of the neighboring thorium polyhedra in a given layer also alternate by 180° relative to the *c*

Table 3.9. Selected bond distances (Å) with esd's for compounds **8** and **9**

Compound 8		Compound 9	
Bond Distances (Å)		Bond Distances (Å)	
Th1—F1 (x2)	2.376 (5)	Th1—F1 (x2)	2.420 (5)
Th1—F2 (x2)	2.347 (5)	Th1—F2 (x2)	2.348 (4)
Th1—F3 (x2)	2.336 (3)	Th1—F3 (x2)	2.343 (3)
Th1—F4	2.3304 (16)	Th1—F4	2.334 (2)
Th1—F5	2.503 (4)	Th1—F5	2.357 (5)
Th1—F6	2.566 (8)	Th1—F6	2.663 (7)
Cs1—F1 (x6)	3.170 (11)	Na1—F1 (x3)	2.473 (11)
Cs1—F2 (x6)	3.268 (12)	Na1—F6 ⁱ	2.58 (2)
		Na1—F7	2.511 (19)

Symmetry codes: (i) $-x+1, -y+1, -z$.

axis. Within a common layer, the thorium polyhedra form clusters along the *ab* plane by two edge-sharing pairs, F1-F5 and F2-F6. These clusters form hexagonal-shaped ellipsoidal pores that run lengthwise along [001] where a single cesium ion sits in the center of the pore (Figure 3.15). When viewed down the *c* axis, it can be seen that the pore is distorted; measuring across the *a* axis, the pore is 5.008 (1) Å at its longest point and 4.620 (1) at its shortest point. The length of the pore along the *c* axis is 10.483 (31) Å.

Crystal Structure of NaTh₃F₁₃ (9)

Compound **9** was also found to crystallize into the hexagonal space group $P6_3/mmc$ (No. 194). It has the same space group and unit cell parameters as **8** but contains several different structural differences as highlighted below. This compound is isostructural to the $\text{NaNp}_3\text{F}_{13}$ formulation made previously by Cousson.⁴⁴ However,

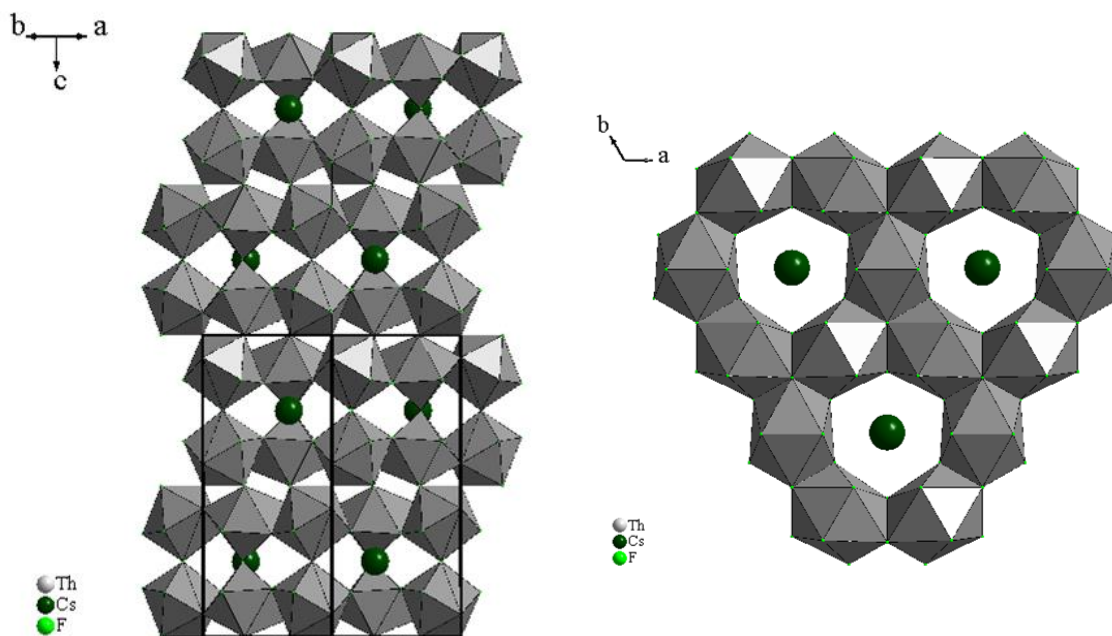


Figure 3.15. (a) Compound **8** as viewed down the ab plane. (b) A layer of compound **8** as viewed down the c axis. Thorium polyhedra beneath the sheet are removed for clarity.

similar phases of the formula $A\text{Th}_3\text{F}_{13}$ ($A = \text{Cs}, \text{Rb}$) have been identified by either single crystal (previous section) or powder diffraction,⁶ but having different structures. The structure of **9** differs greatly from these isoformulaic phases. For example, $\text{CsTh}_3\text{F}_{13}$ exists in two modifications: as $P6/mmm$ and $Pmc2_1$, both having channel structures. Although the hexagonal modification crystallizes in the same space group, the cell parameters are clearly much different and their channels extend infinitely and are not capped to form pores. The calculated powder pattern of **9** is generally similar to a previously reported powder pattern for $\text{CsTh}_6\text{F}_{25}$ ⁴ in that its peaks are shifted in comparison to **8** to account for the slightly smaller unit cell volume. The powder pattern

for **9** also contains a few additional peaks that account for the subtle structural differences. The thorium atoms are slightly distorted tricapped trigonal prisms with an average Th-F distance of 2.397 (6) Å, which correlates well with the expected values predicted by Shannon.³⁴ As in **8**, all the unique atoms in **9** also lie on special positions. Th1, F1, and F2 have a mirror plane along the *b* axis, F3 has a two-fold rotation along the *b* axis, F4 has *mm2* symmetry, Na1, F5, and F6 have a three-fold rotation along the *a* axis and a mirror plane along the *b* axis, and F7 has *6m2* symmetry. F7 occupies the same crystallographic site as Cs1 in **8**.

The new compound **9** exhibits the same framework as **8**, but with some slight differences. The thorium polyhedra also form clusters along the *ab* plane, but also edge-share with F1-F5 and F2-F6 pairs (Figure 3.16). These clusters also form similar hexagonal-shaped pores that run along [001], but in this case two sodium ions and one fluoride ion atom sit in the pore (Figure 3.16). The pore is also more distorted than in **8**; viewed down the *c* axis and measuring across the *a* axis, the pore measures 5.096 (1) Å at its longest point and 4.093 (1) Å at its shortest point. The contents of the pore are in a linear Na-F-Na arrangement along [001], as was observed by Cousson in the neptunium analog.⁴⁴

The Coordination of Cs⁺ in 8 Compared to Na⁺ in 9

The pores in both **8** and **9** are ellipsoidal shaped, but have hexagonal sides. In **8**, they measure 10.483 (31) Å long and the width measures 5.008 (1) Å at its longest point and 4.620 (1) at its shortest point, indicating that the very large cesium ion (3.76 Å ionic

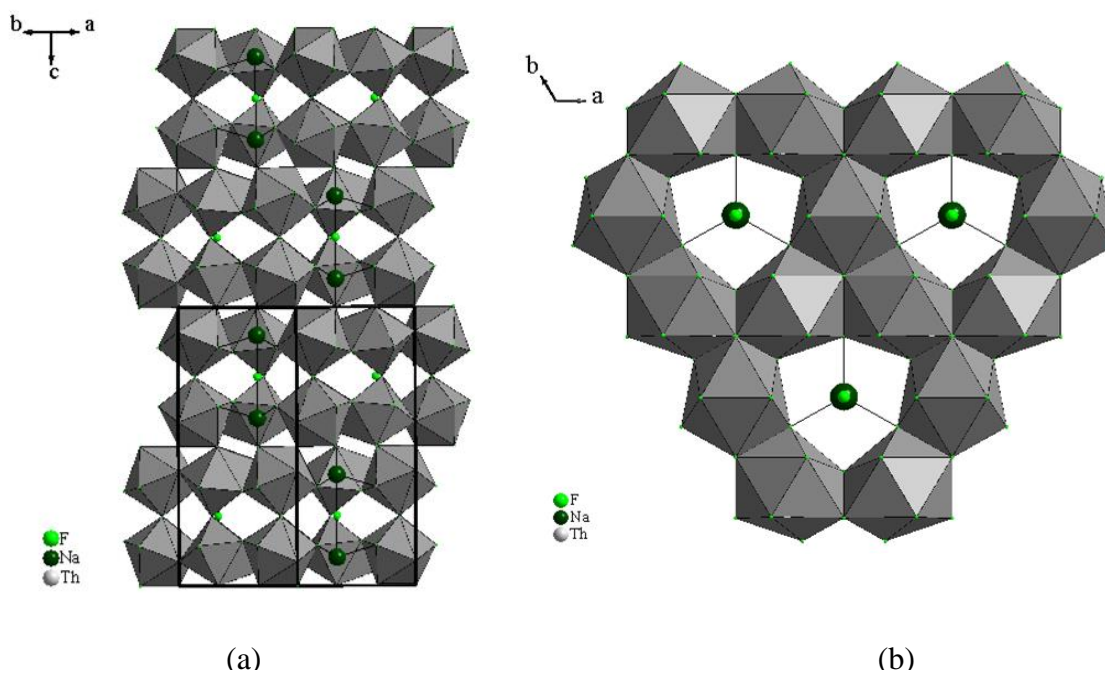


Figure 3.16. (a) Compound **9** as viewed down the *ab* plane. (b) A layer of compound **9** as viewed down the *c* axis. Thorium polyhedra beneath the sheet are removed for clarity.

diameter as 12-coordinate Cs(I)^{34}) sits in the center of the ellipsoid. There it is coordinated to 12 fluoride ions within the pore (Figure 3.17), with interactions of 3.170 (11) at the narrower part of the pore and 3.268 (12) Å at the wider part of the pore. The Cs-F polyhedra are edge-sharing with the thorium polyhedra surrounding the pore. Due to its much smaller size, it appears Na^+ would be too weakly bound to reside in the center of this pore. In **9**, the pores measure 10.185 (24) Å long and the width measures 5.096 (1) Å at its longest point and 4.093 (1) Å at its shortest point, leaving ample space for two much smaller sodium atoms (2.00 Å ionic diameter as five-coordinate Na(I)^{34}) and a fluoride ion, F7, to reside. Ion F7 is a linear bridging atom between the two sodium ions to create two sodium polyhedra that are five-coordinate centered at the loci of the

ellipsoid, thus yielding corner-sharing sodium polyhedra in the structure (Figure 3.17). The marginally wider pore size measured for compound **8** appears to account for its larger unit cell, particularly the lengthening of the *a* and *b* axes. However, the shorter length of the pore in **9** along the *c* axis does not seem to result in *c* axis contraction. In this case the Th1-F6 bond that is the boundary of the pore in this direction is elongated for **9** to form a shorter pore. Meanwhile the Th1-Th1 distance associated with this boundary is essentially unchanged between the two compounds to account for the similar *c* axis parameter. It is interesting to note that similar differences were mentioned by Cousson when comparing the aforementioned structures of $\text{NaNp}_3\text{F}_{13}$ to $\text{CsU}_6\text{F}_{25}$ in $P6_3/mmc$.^{43,44}

Structure-Type $\text{A}_7\text{Th}_6\text{F}_{31}$ (A = Rb, Tl, NH_4)

Crystallographic data for this study is shown in Table 3.10. This structure type crystallizes in the trigonal space group $R\bar{3}$ (No. 148); PXRD data of the bulk samples and simulated powder patterns from the single crystal structures in the present study are identical to a previously-reported powder pattern for $\text{Rb}_7\text{Th}_6\text{F}_{31}$ (**10**) for which no single crystal structure was reported.⁵ Only a few isostructural analogs of this class of compounds have previously been reported, including $\text{Na}_7\text{Th}_6\text{F}_{31}$ as a powder,¹⁰ and $\text{K}_7\text{Th}_6\text{F}_{31}$,¹³ and $\text{Na}_7\text{Zr}_6\text{F}_{31}$ ³⁷ as single crystals. For this set of compounds A2 (A = Rb, Tl, N) sits on a $\bar{3}$ symmetry site, and the other atom in a special position, F6, happens to sit on a 3-fold rotation symmetry site.

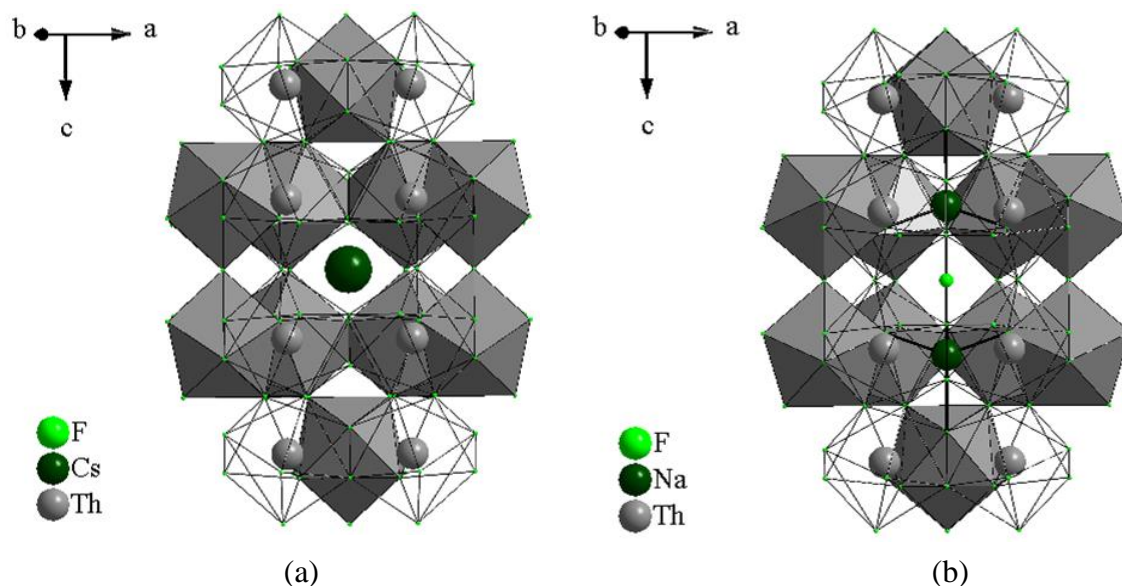


Figure 3.17. (a) Cut away view of an ellipsoidal pore in compound **8** as viewed down the ab plane. The 12-coordinate cesium ion (shown uncoordinated) sits in the center of the pore. (b) Cut away view of the ellipsoidal pore in compound **9** as viewed down the ab plane. Two 5-coordinate sodium ions (Na-F bonds are bolded) are centered at the loci of the pore and are bridged by a corner-shared fluoride.

*Crystal Structures of $Rb_7Th_6F_{31}$ (**10**) and $Tl_7Th_6F_{31}$ (**11**)*

Crystallographic data for compounds **10** – **12** are shown in Table 3.10. Compounds **10** and **11** consist of clusters of eight-coordinate thorium atoms in a pseudo-square antiprismatic geometry. Thorium polyhedra are edge sharing with one another through F3 pairs and corner sharing through F4 and F5. Thorium polyhedra are edge sharing with A1 (A = Rb, Tl) polyhedra through F3 and F2 as well as F1 and F2, with additional corner sharing through F3. Thorium(1) is only corner sharing with six-

coordinate A2 through F2 in this structure. A2 is sandwiched between A1 atoms by edge sharing of F2 atoms, isolating A2 from itself. The resulting framework forms a pore where F6 sits with very long interactions to Th1 (2.618(5) and 2.5986(4) Å for **10** and **11**, respectively) and A2 (3.698 (5) and 3.631 (1) Å). Fluoride(6) “rattles” significantly in this pore resulting in especially large thermal parameters (Figure 3.18).

Table 3.10. Crystallographic Data for Structures **10 - 12**

	10	11	12
Chemical Formula	F ₃₁ Th ₆ Rb ₇	F ₃₁ Th ₆ Tl ₇	F ₃₁ Th ₆ (NH ₄) ₇
F.W. (g/mol)	2598.45	3411.90	2079.31
Space group	R $\bar{3}$	R $\bar{3}$	R $\bar{3}$
Temp./K	293±2	293±2	293±2
Crystal system	Trigonal	Trigonal	Trigonal
a, Å	15.609 (2)	15.598 (2)	15.597 (2)
c, Å	10.823 (2)	10.893 (2)	10.952 (2)
V, Å ³	2283.6 (7)	2295.1 (7)	2307.5 (7)
Z	3	3	3
D _{cal} , Mg/m ³	5.668	7.405	4.489
Indices (min)	[-19, -19, -13]	[-18, -18, -12]	[-19, -19, -13]
(max)	[19, 19, 13]	[18, 18, 12]	[18, 19, 13]
Parameters	70	70	70
F(000)	3261	4158	2604
μ, mm ⁻¹	40.508	65.917	29.090
2θ range, °	2.41 – 26.03	2.40 – 24.97	2.39 – 26.34
Collected reflections	7061	6503	7350
Unique reflections	996	906	1047
Final R (obs. data), ^a	0.0357	0.0700	0.0275
wR ₂	0.0818	0.1736	0.0686
Final R (all data), R ₁	0.0461	0.0759	0.0288
wR ₂	0.0869	0.1828	0.0695
Goodness of fit (S)	1.119	1.092	1.142
Extinction coefficient	0.00085 (4)	0.0001101 (8)	0.000773 (5)
Largest diff. peak	1.393	7.438	2.284
Largest diff. hole	-2.834	-5.390	-2.357

$$^a R_1 = [\sum |F_o| - |F_c|] / \sum |F_o|; wR_2 = \{[\sum w[(F_o)^2 - (F_c)^2]^2]\}^{1/2}$$

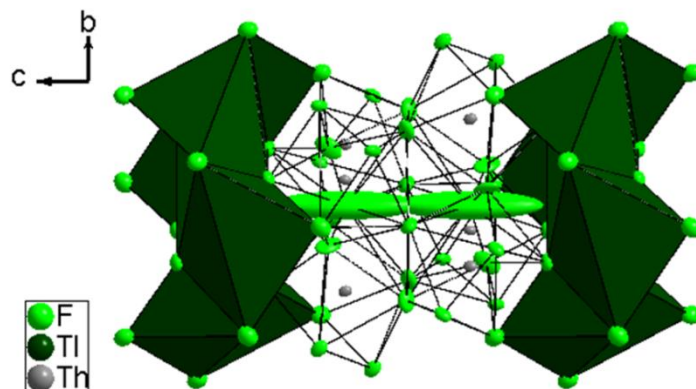


Figure 3.18. The cage-like structure of compound **11**, as viewed down the *a* axis. The atoms are shown as thermal ellipsoids to demonstrate the large thermal parameter of F6.

The thorium polyhedra are open-faced for clarity.

This phenomenon was also observed in the potassium analog of this compound.¹³ The pore measures 10.823 (2) Å for **10** and 10.893 (2) Å for **11** in length down the *c* axis between two A2 (running the entire length of the unit cell), by 5.615 (1) for **10** and 5.626 (1) Å for **11** at its widest point across the *ab* plane (dictated by their Th1-F5 bond distances, see Table 3.11). This spacing leaves ample room for two F6 to distribute its electron density throughout the pore. Two of these pores exist per unit cell (Figure 3.19). This structure type differs slightly from the others in this study in that channels are formed by a Th-F-A-F network, where the alkali metal not only resides in the channel (along with the F6 atom), but also contributes to determining the size of that channel (A1

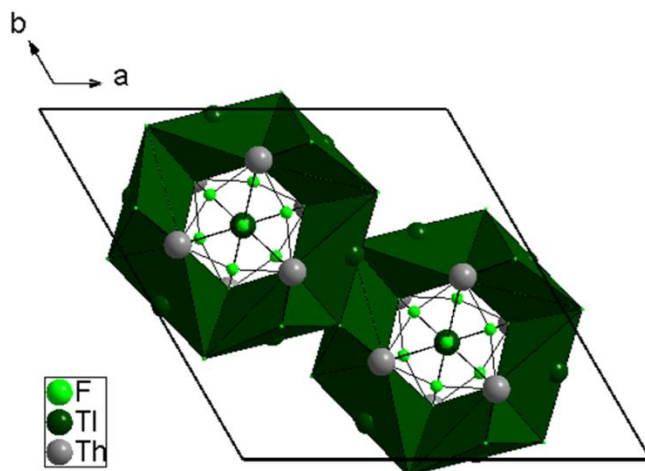


Figure 3.19. Cut-away of the pores of compound **11**, as viewed down the *c* axis. The thorium polyhedra are open-faced for clarity.

Table 3.11. Selected Bond Distances (Å) with esds for Compounds **10** - **12**

Compound 10		Compound 11		Compound 12	
Bond Distances (Å)		Bond Distances (Å)		Bond Distances (Å)	
Th1—F1	2.230 (7)	Th1—F1	2.2491 (5)	Th1—F1	2.2422 (8)
Th1—F2	2.232 (6)	Th1—F2	2.2727 (6)	Th1—F2	2.2524 (8)
Th1—F3	2.398 (6)	Th1—F3	2.4014 (5)	Th1—F3	2.3949 (5)
Th1—F3	2.435 (6)	Th1—F3	2.4354 (4)	Th1—F3	2.4109 (6)
Th1—F4	2.357 (6)	Th1—F4	2.3467 (5)	Th1—F4	2.3541 (8)
Th1—F4	2.376 (6)	Th1—F4	2.3721 (5)	Th1—F4	2.3641 (8)
Th1—F5	2.358 (7)	Th1—F5	2.3371 (5)	Th1—F5	2.3387 (6)
Th1—F5	2.339 (7)	Th1—F5	2.3473 (6)	Th1—F5	2.3419 (7)
Rb1—F1	2.846 (7)	Tl1—F1	2.7147 (5)		
Rb1—F2	2.895 (7)	Tl1—F1	2.833 (1)		
Rb1—F2	2.792 (6)	Tl1—F1	2.869 (1)		
Rb1—F3	3.339 (7)	Tl1—F2	2.838 (0)		
Rb2—F2 (x6)	2.815 (6)	Tl1—F2	2.7759 (5)		
		Tl2—F2 (x6)	2.814 (0)		

participates in the network and A2 sits in the channel).

This structure type enjoys an added aspect of flexibility that could also account for the variety of different chemical formulas that accommodate this structure type. For example, the Rb-F bond distances are 2.815 (6) Å for Rb2 (within the channel) and average of 2.840 Å for the nearest seven fluorides to Rb1 for **10**. Based on reference 13, the K-F bond distances are 2.736 (4) Å for K2 and an average of 2.698 (2) Å for K1. In addition to the flexibility afforded by having the monovalent metal as a component of the channel-forming network, adjustments in the size of the tetravalent ion (such as Zr⁴⁺ in Na₇Zr₆F₃₁) can be useful in creating channels of other sizes for alkali ions.⁴⁵ However, structure types flexible enough to accommodate K, Rb, and Cs have not yet observed an alkali thorium fluoride when the channels are formed by only thorium fluoride bonding.

*Crystal Structure of (NH₄)₇Th₆F₃₁ (**12**)*

Unlike **10** and **11**, the fundamental building block of compound **12** consist of clusters of three eight-coordinate thorium atoms in a pseudo-square antiprismatic geometry. Due to the change in coordination, the thorium polyhedra within each cluster corner share with one another through F5, and the clusters connect to each other by edge sharing through F4 pairs. Two thorium clusters are sandwiched between layers of ammonium ions (N1 and N2), with each layer consisting of six N1 surrounding one N2. Unfortunately, N1 and N2 had to be refined using an ISOR restraint to prevent their principal mean square atomic displacements from being non-positive definite (though N1 still remained a non-positive definite and was refined isotropically). The hydrogen atoms

on N1 and N2 could not be properly isolated for either compound from the remaining available Q-peaks during refinement. Similarly to the previously mentioned compounds, two of these pores exist per unit cell.

The resulting framework still forms a cage-like pore structure, in this instance measuring 10.952 (2) Å in length by 4.350 (1) Å in width. The two F6 ions also “rattle” significantly in this cage, but the thermal parameter of F6 behaves differently compared to the compounds discussed previously. Other compounds of the $A_7B_6F_{31}$ family possess F6 that spread their thermal parameters across the length of the pore (along the *c* axis). However, compound **12** possesses F6 that spread their thermal parameters *orthogonal* to the *c* axis, along the *ab* plane (Figure 3.20). This change could be explained due to possible hydrogen bonding between F6 and the hydrogen atoms from the ammonium ions. Because of this phenomenon, the thorium polyhedra could be considered “extremely distorted” nine-coordinate polyhedra with very long interactions to F6 (3.049 (11) Å).

CONCLUSIONS

The hydrothermal synthesis of monovalent thorium fluorides using ThF_4 and monovalent fluoride mineralizers yielded a wide variety of products, including the first fully characterized cesium thorium fluorides (Figure 3.21). Many of the formulations reported earlier were not previously characterized by single crystal diffraction due to the lack of suitably high quality crystals. Some of the compounds reported herein can be prepared as phase pure materials, opening the door for comparative studies of alkali metal

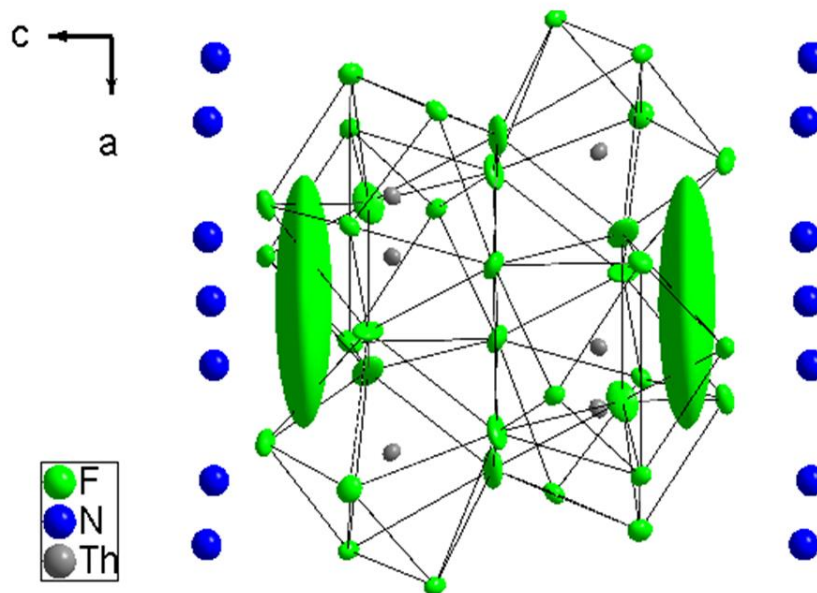


Figure 3.20. The cage-like structure of compound **12**, as viewed down the b axis. The polyhedra are shown as thermal ellipsoids to demonstrate the large thermal parameter of F6 orthogonal to the c axis. N1 and N2 are isotropic, and the thorium polyhedra are open-faced for clarity.

cerium(IV) and hafnium fluorides. Many of the compounds grow in a variety of polymorphs indicating the richness of this phase space. The identity of the species seems to be primarily dependent on the concentration of the fluoride mineralizer used in their syntheses. The resulting structures exhibit Th-F frameworks that form distinct channels in which the monovalent cations reside. Given the more rigid nature of the Th-F bond (compared to A-F) the results of the present study suggest there may be some value to using the size of these channels as a predictive measure as to which other monovalent thorium fluorides may crystallize in a particular structure type. Especially interesting is

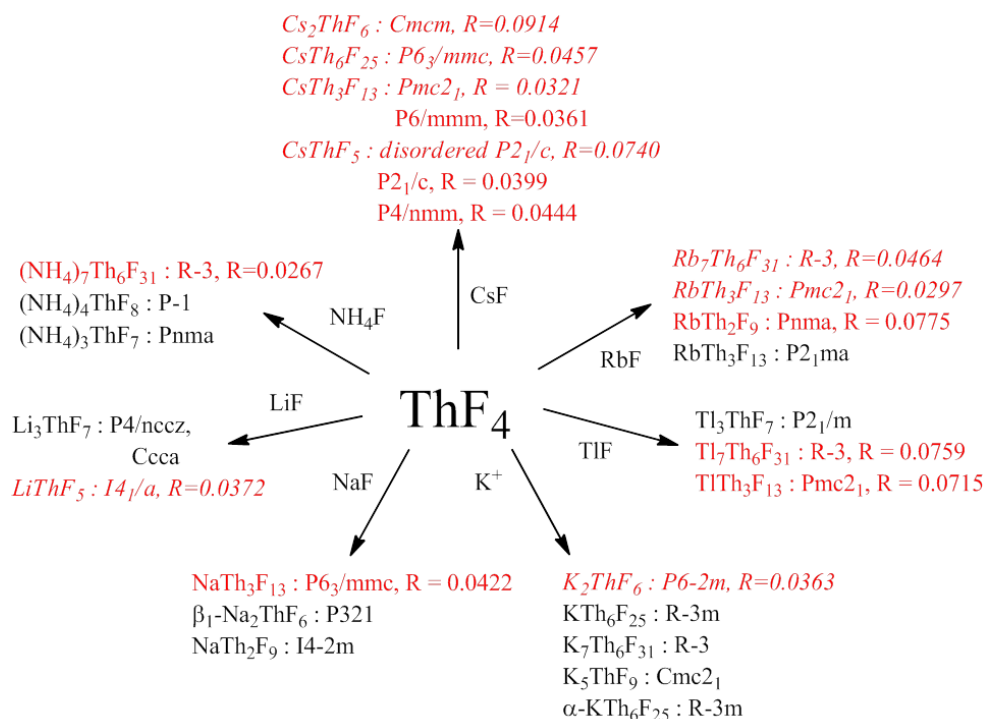


Figure 3.21. Overview of the monovalent thorium fluorides synthesized using our hydrothermal method. The compounds in black are reported single crystal structures and the compounds in red are new structures. Any compounds in italics have previously-reported powder patterns that were used to confirm the identity of the new materials.

that alkali thorium fluorides that are isostructural for all three K, Rb, and Cs phases have not yet been identified. For other monovalent thorium fluorides where multiple compounds are reported in the literature with the same formulation, the structures of the entire series are not sufficiently characterized. The facile growth of these stable monovalent thorium fluorides is an encouraging sign, and may be useful if thorium is to be developed as a safe alternative nuclear fuel source in the future.

REFERENCES

- (1) Brunton, G. D.; Insley, H.; McVay, T. N.; Thoma, R. E. *Crystallographic Data for Some Metal Fluorides, Chlorides, and Oxides*; ORNL-3761; U.S. Government Printing Office: Washington, DC, 1965.
- (2) (a) Jacoby, M. *Chemical and Engineering News* **2009**, November 16, vol. 87, no.46, 44-46. (b) "The Truth About Thorium and Nuclear Power" By Elizabeth Svoboda, *Popular Mechanics*, October 20, 2010. (c) "Thorium Fuel for Nuclear Energy" By Mujid Kazimi, *American Scientist*, September-October 2003, 91(5), 408-412. (d) Bagla, P. *Science* **2005**, 309, 1174-1175. (e) "China Syndrome: Going Nuclear to Cut Down on Coal Burning" By David Biello. *Scientific American*, March 28, 2011.
- (3) Mann, M.; Thompson, D.; Serivalsatit, K.; Tritt, T. M.; Ballato, J.; Kolis, J. *Cryst. Growth Des.* **2010**, 10, 2146-2151.
- (4) Thoma, R. E.; Carlton, T. S. *J. Inorg. Nucl. Chem.* **1961**, 17, 88-95.
- (5) Harris, L. A.; White, G. D.; Thoma, R. E. *J. Phys. Chem.* **1959**, 63, 1974-1975.
- (6) Asker, W. J.; Segnit, E. R.; Wylie, A. W. *J. Chem. Soc.* **1952**, 4470-4479.
- (7) Thoma, R. E. *Phase Diagrams of Nuclear Reactor Materials*; ORNL-2548; U.S. Government Printing Office: Washington, DC, 1959.
- (8) Derganov, E. P.; Bergman, A. G. *Dokl. Akad. Nauk.* **1948**, 60, 391.
- (9) Thoma, R. E.; Insley, H.; Landau, B. S.; Friedman, H. A.; Grimes, W. R. *J. Phys. Chem.* **1959**, 63, 1266-1274.
- (10) Thoma, R. E.; Insley, H.; Herbert, G. M.; Friedman, H. A.; Weaver, C. F. *J. Am. Ceram. Soc.* **1963**, 46, 37-42.
- (11) Harris, L. A. *Acta Crystallogr.* **1960**, 13, 502.
- (12) Brunton, G. D. *Acta Crystallogr., Sect. B: Struct. Cryst. Cryst. Chem.* **1971**, B27, 1823-1826.
- (13) Brunton, G. D. *Acta Crystallogr., Sect. B: Struct. Cryst. Cryst. Chem.* **1971**, B27, 2290-2292.

- (14) Ryan, R. R.; Penneman, R. A. *Acta Crystallogr., Sect. B: Struct. Cryst. Cryst. Chem.* **1971**, *B27*, 829-833.
- (15) Brunton, G. D. *Acta Crystallogr., Sect. B: Struct. Cryst. Cryst. Chem.* **1972**, *B28*, 144-147.
- (16) Zachariasen, W. H. *J. Am. Chem. Soc.* **1948**, *70*, 2147-2151.
- (17) Grzechnik, A.; Fechtelkord, M.; Morgenroth, W.; Posse, J. M.; Friese, K. *J. Phys. Condens. Matter* **2007**, *19*, 266219.
- (18) Zachariasen, W. H. *Acta Crystallogr.* **1949**, *2*, 390-393.
- (19) Grzechnik, A.; Morgenroth, W.; Friese, K. *J. Solid State Chem.* **2008**, *181*, 971-975.
- (20) Cousson, A.; Pagès, M. *Acta Crystallogr., Sect. B: Struct. Cryst. Cryst. Chem.* **1978**, *B34*, 1776-1778.
- (21) Pulcinelli, S. H.; de Almeida Santos, R. H.; Senegas, J. *J. Fluorine Chem.* **1989**, *42*, 41-50.
- (22) Laligant, Y.; LeBail, A.; Avignat, D.; Cousseins, J. C.; Ferey, G. *J. Solid State Chem.* **1989**, *80*, 206-212.
- (23) Laligant, Y.; Ferey, G.; El Ghoszi, M.; Avignat, D. *Eur. J. Solid State Inorg. Chem.* **1992**, *29*, 497-504.
- (24) Ryan, R. R.; Penneman, R. A.; Rosenzweig, A. *Acta Crystallogr., Sect. B: Struct. Cryst. Cryst. Chem.* **1969**, *B25*, 1958-1962.
- (25) Penneman, R. A.; Ryan, R. R.; Kressin, I. K. *Acta Crystallogr., Sect. B: Struct. Cryst. Cryst. Chem.* **1971**, *B27*, 2279-2283.
- (26) Gaumet, V.; El Ghoszi, M.; Avignat, D. *Eur. J. Solid State Inorg. Chem.* **1995**, *32*, 893-905.
- (27) Brunton, G. D. *Acta Crystallogr., Sect. B: Struct. Cryst. Cryst. Chem.* **1970**, *B26*, 1185-1187.

- (28) Brunton, G. D.; Sears, D. R. *Acta Crystallogr., Sect. B: Struct. Cryst. Cryst. Chem.* **1969**, *B25*, 2519-2527.
- (29) Zachariasen, W. H. *Acta Crystallogr.* **1948**, *1*, 265-269.
- (30) Zachariasen, W. H. *Acta Crystallogr.* **1949**, *2*, 388-391.
- (31) Stritzinger, J.; McMillen, C. D.; Kolis, J. *J. Chem. Crystallogr.* **2012**, *42*, 366-371.
- (32) Underwood, C. C.; Mann, M.; McMillen, C. D.; Kolis, J. W., *Inorg. Chem.* **2011**, *50*, 11825-11831.
- (33) *International Tables for Crystallography*; T. Hahn Ed.; Kluwer Publishers: Dordrecht, 1996; Vol.1.
- (34) Shannon, R. D. *Acta Crystallogr.* **1976**, *A32*, 751.
- (35) Robertson, B. E. *Inorg. Chem.* **1977**, *16*, 2735-2742.
- (36) Brunton, G. *Acta Crystallogr., Sect. B: Struct. Cryst. and Cryst. Chem.* **1969**, *B25*, 1919-1921.
- (37) Burns, J. H.; Ellison, R. D.; Levy, H. A. *Acta Crystallogr. Sect. B: Struct. Cryst. Cryst. Chem.* **1968**, *B24*, 230-237.
- (38) Underwood, C. C.; Mann, M.; McMillen, C. D.; Musgraves, J. D.; Kolis, J. W., *Solid St. Sci.* **2012**, *14*, 574-579.
- (39) Hamilton, W. C. *Acta Crystallogr.* **1965**, *18*, 502-510.
- (40) Koller, D.; Müller, B. G. *Z. Anorg. Allg. Chem.* **2002**, *628*, 575-579.
- (41) Plitzko, C.; Meyer, G. *Z. Anorg. Allg. Chem.* **1998**, *624*, 169-170.
- (42) Underwood, C. C.; McMillen, C.; Kolis, J. *J. Chem. Crystallogr.* **2012**, *42*, 606-610.
- (43) Brunton, G. *Acta Crystallogr., Sect. B: Struct. Cryst. Cryst. Chem.* **1971**, *B27*, 245-247.

- (44) Cousson, A.; Abazli, H.; Pagès, M.; Gasparin, M. *Acta Crystallogr., Sect. C: Cryst. Struct. Comm.* **1983**, C39, 318-320.
- (45) Rouse, J.; Weller, M. T. *Dalton Trans.* **2009**, 10330-10337.

CHAPTER FOUR

HYDROTHERMAL SYNTHESIS AND CHARACTERIZATION OF NOVEL MONOVALENT CERIUM(IV) FLUORIDES

INTRODUCTION

In the continued investigation into the descriptive chemistry of solid-state inorganic lanthanide and actinide compounds, more monovalent metal thorium fluorides have been discovered and advances in the synthesis and structure determination of monovalent metal cerium(IV) fluorides have been made. Recent successful use of fluoride mineralizers in the hydrothermal crystal growth of thorium oxide¹ and alkali thorium fluorides²⁻⁴ suggests that additional investigations into inorganic cerium(IV) fluorides may be fruitful.

Previous work was done primarily in molten alkali fluoride salts with thorium fluoride salts and showed that the chemistry of alkali metal thorium(IV) fluorides is quite extensive,⁵⁻³² with most of these early results coming from powder diffraction. Some work on single crystals was conducted (see Figure 3.1), with the predominant focus on potassium thorium fluorides with few other alkali metal examples. Surprisingly little work has been done on the chemistry of alkali cerium fluorides,³¹⁻³⁷ with most of the results coming from powder diffraction (see Figure 4.1). What is more surprising is that only one single crystal structure of an alkali cerium(IV) fluoride has ever been reported.³⁷

The chemistry of monovalent metal cerium(IV) fluorides in hydrothermal fluids was examined and it was found that it is considerably richer than anticipated. The structural chemistry is both complex and subtle. Hydrolysis of the Ce-F bond in

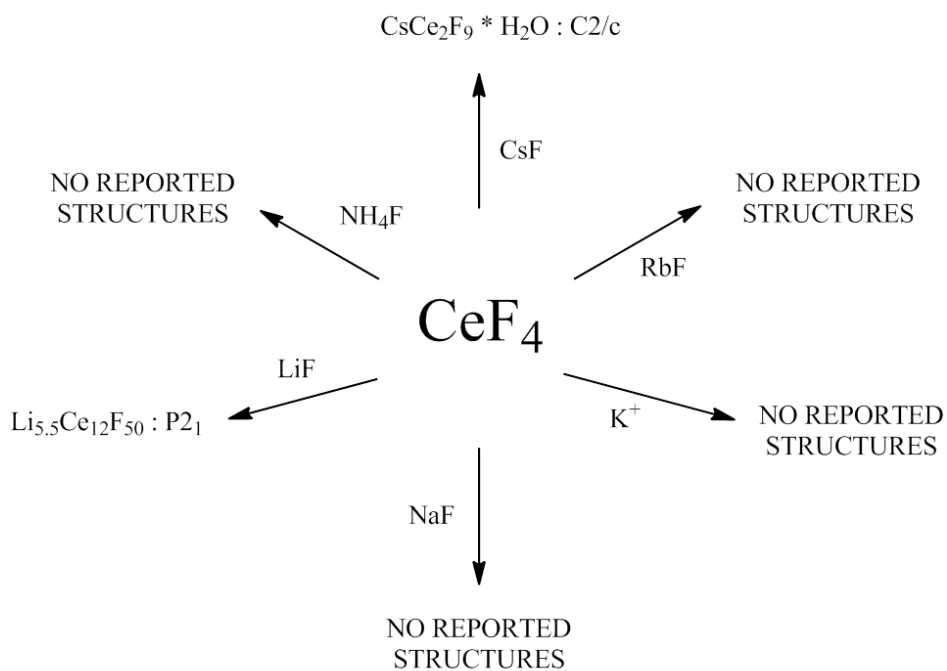


Figure 4.1. Overview of the reported monovalent alkali cerium fluoride single crystals.

aqueous solutions above 200 °C were rarely observed but the products are very sensitive to monovalent ion and reaction conditions, as well as reduction of cerium(IV) to cerium(III). In this Chapter, the chemistry and structures of a series of new monovalent metal cerium(IV) fluorides grown from hydrothermal solution are described, and compare their structures to other known metal fluorides.

RESULTS AND DISCUSSION

Descriptive Synthetic Chemistry

Reactions were investigated by differing ratios of A:Ce (A = Cs – Li, NH₄) as a means to explore this phase space and identify any trends in compound formation.

Detailed reaction conditions for the synthesis of monovalent metal cerium fluorides are shown in Table 4.1. A variety of monovalent metal cerium fluorides resulted from lower temperature reactions using lower mineralizer concentrations as shown in Table 4.1. Previous attempts were made at synthesizing monovalent cerium fluorides using similar conditions to that of the syntheses of the univalent thorium fluorides (see Chapter 3) with no success, yielding mostly CeF_3 powder as confirmed by PXRD. It must be noted that all the reactions of the alkali cerium fluoride systems using lower temperatures still contained CeF_3 powder, so phase pure materials could only be obtained through physical separation of single crystals from the samples.

Unlike in the case of the monovalent thorium fluorides (see Chapter 3), the products seem to be fairly sensitive toward the A:Ce ratio in the reaction. This sensitivity is in fact reflected in the chemical formulae of the products except in the cesium fluoride system. In this case, $\text{Cs}_2\text{Ce}_3\text{OF}_{12}$ is the only solid formed when Cs:Ce is less than 2:1. It is only when Cs:Ce ratios approach 5:1 when another solid, CsCeF_5 , is observed. The rubidium fluoride system shows more sensitivity toward A:Ce; $\text{RbCe}_3\text{OF}_{11}$ forms when the Rb:Ce ratio is less than 1:3, but forms RbCeF_5 when Rb:Ce ratio surpasses 1:1. In the ammonium and potassium fluoride systems, $\text{ACe}_3\text{OF}_{11}$ forms when the A:Ce ratio is lower than 1:3. Higher A:Ce ratios yield $(\text{NH}_4)\text{CeF}_5$ and $(\text{NH}_4)_7\text{Ce}_6\text{F}_{31}$ in their respective systems. It is interesting to note that the same results were obtained in the potassium cerium fluoride system when using either KF or KHF_2 as the mineralizer. In the case of the sodium cerium fluoride system, $\text{Na}_7\text{Ce}_6\text{F}_{31}$ only forms when the A:Ce ratio is between 1:3 and 2:1, unlike what is seen for the other reported systems ($\text{A:Ce} \geq 1:1$). Curiously,

Table 4.1. Specific reaction conditions for the syntheses of the monovalent metal cerium(IV) fluorides

Condition	Mineralizer	Monovalent:Ce Ratio	Crystal Shape(s)	Crystal(s)
1	CsF, 0.015 <i>M</i>	1:6	Polyhedra	Cs ₂ Ce ₃ OF ₁₂ (1)
2	CsF, 0.031 <i>M</i>	1:3	Polyhedra	1
3	CsF, 0.093 <i>M</i>	1:1	Polyhedra	1
4	CsF, 0.185 <i>M</i>	2:1	Polyhedra	1
5	CsF, 0.463 <i>M</i>	5:1	Square Rods	CsCeF ₅ (2)
6	RbF, 0.015 <i>M</i>	1:6	Plates	RbCe ₃ OF ₁₁ (3)
7	RbF, 0.031 <i>M</i>	1:3	Hex. Plates	3
8	RbF, 0.093 <i>M</i>	1:1	Square Rods	RbCeF ₅ (4)
9	RbF, 0.185 <i>M</i>	2:1	Square Rods	4
10	RbF, 0.463 <i>M</i>	5:1	Square Rods	4
11	NH ₄ F, 0.015 <i>M</i>	1:6	Plates	(NH ₄)Ce ₃ OF ₁₁ (5)
12	NH ₄ F, 0.031 <i>M</i>	1:3	Plates	5
13	NH ₄ F, 0.093 <i>M</i>	1:1	Rods	(NH ₄)CeF ₅ (6)
14	NH ₄ F, 0.185 <i>M</i>	2:1	Polyhedra	(NH ₄) ₇ Ce ₆ F ₃₁ (7)
15	NH ₄ F, 0.463 <i>M</i>	5:1	Polyhedra	7
16	KF, 0.015 <i>M</i>	1:6	Square Rods, Plates	KCe ₃ OF ₁₁ (8), K ₂ CeF ₆ (9)
17	KF, 0.031 <i>M</i>	1:3	Square Rods, Plates	8, 9
18	KF, 0.093 <i>M</i>	1:1	Plates, Polyhedra	9 , K ₇ Ce ₆ F ₃₁ (10)
19	KF, 0.185 <i>M</i>	2:1	Plates, Polyhedra	9, 10
20	KF, 0.463 <i>M</i>	5:1	Plates, Polyhedra	9, 10
21	KHF ₂ , 0.015 <i>M</i>	1:6	Square Rods, Plates	8, 9
22	KHF ₂ , 0.031 <i>M</i>	1:3	Square Rods, Plates	8, 9
23	KHF ₂ , 0.093 <i>M</i>	1:1	Plates, Polyhedra	9, 10
24	KHF ₂ , 0.185 <i>M</i>	2:1	Polyhedra	9, 10
25	KHF ₂ , 0.463 <i>M</i>	5:1	Polyhedra	9, 10
26	NaF, 0.015 <i>M</i>	1:6	Plates	Na ₂ CeF ₆ (11)
27	NaF, 0.031 <i>M</i>	1:3	Plates, Polyhedra	11 , Na ₇ Ce ₆ F ₃₁ (12)
28	NaF, 0.093 <i>M</i>	1:1	Plates, Polyhedra	11, 12
29	NaF, 0.185 <i>M</i>	2:1	Plates	12
30	NaF, 0.463 <i>M</i>	5:1	Plates	12
31	LiF, 0.015 <i>M</i>	1:6	Polyhedra	LiCe ₃ F ₁₃ **
32	LiF, 0.031 <i>M</i>	1:3	Polyhedra, Square Rods	LiCe ₃ F ₁₃ **, LiCeF ₅ (13)
33	LiF, 0.093 <i>M</i>	1:1	Square Rods	13
34	LiF, 0.185 <i>M</i>	2:1	Square Rods	13
35	LiF, 0.463 <i>M</i>	5:1	Plates	Li ₄ CeF ₈ (14)

*All condition temperatures are 250 °C. All conditions also contain CeF₃.

**Possible solution with high R₁ value.

Table 4.2. Crystallographic Data for Compounds **1**, **3**, **5**, and **8**

	1	3	5	8
Chemical Formula	Cs ₂ Ce ₃ OF ₁₂	RbCe ₃ OF ₁₁	(NH ₄)Ce ₃ OF ₁₁	KCe ₃ OF ₁₁
F.W. (g/mol)	930.18	737.33	659.37	690.95
Space group	R $\bar{3}m$	P $\bar{6}m2$	P $\bar{6}m2$	P $\bar{6}m2$
Temp./K	293±2	293±2	293±2	293±2
Crystal system	Trigonal	Hexagonal	Hexagonal	Hexagonal
a, Å	8.2663 (12)	8.0351 (11)	8.0457 (11)	7.9794 (11)
c, Å	31.851 (6)	8.3077 (17)	8.2918 (17)	8.2513 (17)
V, Å ³	1884.8 (5)	464.51 (13)	464.84 (13)	454.98 (13)
Z	6	2	2	2
D _{cal} , Mg/m ³	4.917	5.272	4.711	5.044
Indices (min)	[-9, -10, -39]	[-9, -9, -9]	[-9, -9, -10]	[-9, -8, -9]
(max)	[10, 10, 38]	[9, 9, 9]	[9, 9, 9]	[9, 9, 9]
Parameters	41	41	40	40
F(000)	2400	643	576	607
μ, mm ⁻¹	16.525	19.808	14.594	15.366
2θ range, °	2.92 – 26.01	2.45 – 24.96	2.46 – 25.97	2.47 – 25.03
Collected reflections	5765	3958	4179	3662
Unique reflections	510	366	400	362
Final R (obs. data), ^a	0.0212	0.0291	0.0400	0.0446
wR ₂	0.0451	0.0686	0.1004	0.1004
Final R (all data), R ₁	0.0213	0.0291	0.0401	0.0465
wR ₂	0.0451	0.0687	0.1005	0.1020
Goodness of fit (S)	1.266	1.215	1.194	1.193
Extinction coefficient	0.00017 (3)	0.0032 (6)	0.0065 (15)	0.0018 (6)
Largest diff. peak	0.824	2.060	2.825	3.263
Largest diff. hole	-1.438	-1.404	-1.740	-2.256

$$^a R_1 = [\sum ||F_o| - |F_c||] / \sum |F_o|; wR_2 = \{[\sum w[(F_o)^2 - (F_c)^2]^2]\}^{1/2}$$

Na₂CeF₆ forms over the entire range of Na:Ce ratios, a phenomenon that was not observed for any other phase in this study. The lithium fluoride system shows the most diversity; when the Li:Ce ratio is less than 1:3, LiCe₃F₁₃ is observed. When Li:Ce ratios reach 1:3, LiCeF₅ is observed and is the only solid observed at ratios between 1:1 and 2:1. At ratios greater than 2:1, Li₄CeF₈ become the only compound that is observed. Refer to Table 4.3 for a visual overview of this discussion.

Table 4.3. Overview of reaction conditions for the syntheses of the monovalent metal cerium(IV) fluorides

Alkali : Ce	Li	Na	NH ₄	K	Rb	Cs
1:6	LiCe ₃ F ₁₃	Na ₂ CeF ₆	(NH ₄)Ce ₃ OF ₁₁	KCe ₃ OF ₁₁ , K ₂ CeF ₆	RbCe ₃ OF ₁₁	Cs ₂ Ce ₃ OF ₁₂
1:3	LiCe ₃ F ₁₃ , LiCeF ₅	Na ₂ CeF ₆ , Na ₇ Ce ₆ F ₃₁	(NH ₄)Ce ₃ OF ₁₁	KCe ₃ OF ₁₁ , K ₂ CeF ₆	RbCe ₃ OF ₁₁	Cs ₂ Ce ₃ OF ₁₂
1:1	LiCeF ₅	Na ₂ CeF ₆ , Na ₇ Ce ₆ F ₃₁	(NH ₄)CeF ₅	K ₇ Ce ₆ F ₃₁ , K ₂ CeF ₆	RbCeF ₅	Cs ₂ Ce ₃ OF ₁₂
7:6	LiCeF ₅	Na ₂ CeF ₆ , Na ₇ Ce ₆ F ₃₁	(NH ₄)CeF ₅	K ₇ Ce ₆ F ₃₁ , K ₂ CeF ₆	RbCeF ₅	Cs ₂ Ce ₃ OF ₁₂
2:1	LiCeF ₅	Na ₂ CeF ₆	(NH ₄) ₇ Ce ₆ F ₃₁	K ₇ Ce ₆ F ₃₁ , K ₂ CeF ₆	RbCeF ₅	Cs ₂ Ce ₃ OF ₁₂
5:1	Li ₄ CeF ₈	Na ₂ CeF ₆	(NH ₄) ₇ Ce ₆ F ₃₁	K ₇ Ce ₆ F ₃₁ , K ₂ CeF ₆	RbCeF ₅	CsCeF ₅

Monovalent Cerium(IV) Oxyfluorides

Crystal Structure of (A)Ce₃OF₁₁ (A = Rb, NH₄, K)

Crystallographic data for compounds **1**, **3**, **5**, and **8** are shown in Table 4.2 and selected bond distances are shown in Table 4.3. Cerium(IV) oxyfluorides RbCe₃OF₁₁ (**3**), (NH₄)Ce₃OF₁₁ (**5**), and KCe₃OF₁₁ (**8**) all crystallize in space group $P\bar{6}m2$ (No. 187). This set of compounds is the first known with this formulation. The crystallographically unique sites consist of nine-coordinate cerium(IV) atoms as [CeOF₈]⁵⁻ units conforming to a distorted monocapped square antiprism geometry. Average Ce-F distances are 2.277 (4), 2.283 (5), and 2.268 (7) Å for **3**, **5**, and **8**, respectively, and average Ce-O distances 2.61 Å for Ce1 are observed (see Table 4.4). It must be noted that disordering occurs between F5 and O2; each atom shares the same coordinate position through half

occupation. All the crystallographically unique atoms are in special positions; Ce1, F2, and F3 have a mirror plane on the *b* axis, F1 has *mm*2 symmetry, F4 has a mirror plane on the *a* axis, O1 and F5/O2 have both three-fold rotational symmetry about the *a* axis and a mirror plane on the *b* axis, and A1 and A2 have $\bar{6}m2$ symmetry.

Table 4.4. Selected Bond Distances (Å) with esds for Compounds **1**, **3**, **5**, and **8**

Cs ₂ Ce ₃ OF ₁₂ (1)		RbCe ₃ OF ₁₁ (3)	
Bond Distances (Å)		Bond Distances (Å)	
Ce1—F1 (x2)	2.333 (2)	Ce1—F1	2.2439 (12)
Ce1—F2 (x2)	2.292 (2)	Ce1—F2 (x2)	2.338 (5)
Ce1—F3 (x2)	2.306 (3)	Ce1—F3 (x2)	2.263 (4)
Ce1—F4	2.110 (4)	Ce1—F4 (x2)	2.279 (3)
Ce1—O1	2.2084 (15)	Ce1—F5	2.211 (2)
Cs1—F1 (x3)	3.083 (4)	Ce1—O1	2.610 (10)
Cs1—F4 (x3)	3.035 (4)	Rb1—F2 (x6)	2.869 (8)
Cs2—F3 (x6)	3.380 (4)	Rb1—F3 (x6)	3.362 (12)
Cs2—F4 (x6)	2.995 (5)	Rb2—F4 (x6)	2.808 (5)
Cs3—F1 (x6)	3.348 (4)	Rb2—F2 (x6)	3.265 (9)
Cs3—F2 (x6)	2.932 (4)		
(NH ₄)Ce ₃ OF ₁₁ (5)		KCe ₃ OF ₁₁ (8)	
Bond Distances (Å)		Bond Distances (Å)	
Ce1—F1	2.2421 (15)	Ce1—F1	2.228 (3)
Ce1—F2 (x2)	2.341 (6)	Ce1—F2 (x2)	2.331 (8)
Ce1—F3 (x2)	2.273 (6)	Ce1—F3 (x2)	2.234 (8)
Ce1—F4 (x2)	2.284 (3)	Ce1—F4 (x2)	2.286 (6)
Ce1—F5	2.224 (6)	Ce1—F5	2.212 (5)
Ce1—O1	2.606 (19)	Ce1—O1	2.61 (2)
		K1—F2 (x6)	2.842 (14)
		K1—F3 (x6)	3.35 (2)
		K2—F4 (x6)	2.756 (10)
		K2—F2 (x6)	3.240 (15)

Three $[\text{CeOF}_8]^{6-}$ polyhedra share F2-F5 edges to form $[\text{Ce}_3\text{O}_3\text{F}_{22}]^{16-}$ clusters. All three polyhedra in the cluster share the central disordered F5/O2 atom, and thus the observed Ce-F/Ce-O bond distance is slightly shorter (average of 2.216 (4) Å) than one may expect due to this geometrical restriction by comparison to bond lengths reported by Shannon.³⁸ The central disordered atom is just slightly out of plane with the cerium atoms allowing Ce-F/O-Ce angles to be slightly distorted at 117.74 (2)°. These clusters join to each other by F3-O1 edge sharing to form cerium oxyfluoride layers in the *ab* plane (see Figure 4.2a). A second series of hafnium oxyfluoride clusters is joined to this first series along the *c* axis in repeating fashion by edge sharing pairs of F4 atoms, making the cerium oxyfluoride layer two polyhedra thick along [001] (see Figure 4.2b). The repeating arrangement creates distorted hexagram-shaped channels. The channels measure an average of 5.109 (11) Å along the *a* axis and 5.190 (14) Å along the *b* axis, ample room for the monovalent species to sit (i.e. six-coordinate Rb with a size of 3.04 Å according to Shannon, see Figure 4.2a).³⁸ Due to the large channel size, the coordination environment around A1 and A2 in compounds **3** and **8** each exhibit six longer bonds (3.362 (12) and 3.35 (2) Å for A1-F3 in **3** and **8**, and 3.265 (9) and 3.240 (15) Å for A2-F2, respectively) and six shorter bonds (2.869 (8) and 2.842 (14) Å for A1-F2 in **3** and **8**, and 2.808 (5) and 2.756 (10) Å for A2-F4, respectively).

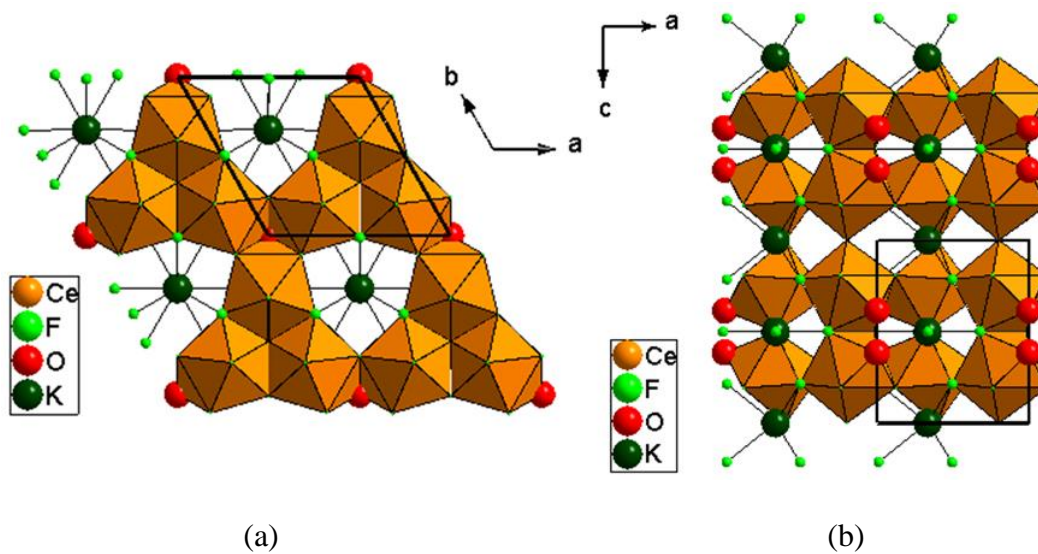


Figure 4.2. (a) Compound **8** as seen down the c axis showing how the clusters join to form hexagram-shaped channels. (b) Compound **8** as seen down the b axis showing the layering that occurs with the clusters of cerium polyhedra. The oxygen atoms are enlarged to show their positions.

*Crystal Structure of $Cs_2Ce_3OF_{12}$ (**1**)*

Compound **1** crystallizes in the trigonal space group $R\bar{3}m$ (No. 166). It is also isostructural to $Rb_2Zr_3OF_{12}$ and $Rb_2Hf_3OF_{12}$ previously found to grow from fluxes of RbF and HfF₄ in an atmosphere of Ar/HF,³⁹ as well as $Tl_2Zr_3OF_{12}$ grown from a melt of TlF, ZrF₄, and ZrO₂⁴⁰ and $K_2Zr_3OF_{12}$ grown by microwave-assisted hydrothermal synthesis from ZrF₄ and KOH.⁴¹ Most notably, I recently synthesized $K_2Hf_3OF_{12}$ by hydrothermal method.⁴² The crystallographically unique sites consist of eight-coordinate cerium atoms as $[CeOF_7]^{5-}$ units conforming to a distorted tricapped trigonal prism geometry, with average Ce-F distances of 2.282 (3) Å and a Ce-O distance of 2.2084 (15)

Å for Ce1. All the crystallographically unique atoms are in special positions; Ce1, F1, F3, and F4 have a mirror plane on the c axis, Cs1 and O1 have $3m$ symmetry, Cs2 and Cs3 have $\bar{3}m$ symmetry, and F2 has two-fold rotational symmetry about the c axis. The crystallography closely resembles that of $K_2Hf_3OF_{12}$, which is discussed in detail (see Chapter 5, compound **3**).

There are some major differences between compound **1** and the other oxyfluorides (compounds **3**, **5**, and **8**) that must be noted. Firstly, there is no half occupation by any of the atoms in compound **1**, which would account for the subtle difference in the formulation. Next, the cerium(IV) atoms in **1** are eight-coordinate whereas the cerium(IV) atoms in the other oxyfluorides are nine-coordinate. The three polyhedra in **1** that forms clusters are joined by a fully occupied oxygen atom (O1) instead of half occupied atoms (O2 and F5). Lastly, the clusters in **1** are joined through corner-sharing (via F3 atoms) instead of edge sharing (via O1 and F3 atoms) and formed staggered layers of cerium(IV) polyhedra with pores and very small triangular-shaped channels instead of repeating layers that form large hexagon-shaped channels.

Structures Having Formula (A)CeF₅

*Crystal Structure of (NH₄)CeF₅ (**6**)*

Crystallographic data for compounds **2**, **4**, and **6** are shown in Table 4.5 and selected bond distances are shown in Table 4.6. Compound **6** was shown to crystallize into the monoclinic space group $C2/m$ (No. 12). This is the first report of both this formulation and space group for this class of compounds. Attempts were made to obtain

a solution in space group $P2_1/c$, but $C2/m$ was preferred as it considered fewer parameters to reach the statistically equivalent solution⁴³ as well as gave a better R_1 value. Considering its hafnium analog, $(NH_4)HfF_5$,⁴⁴ crystallizes in $P2_1/c$, it must be noted that perhaps this is a polymorph that is only formed at lower reaction temperatures (refer to Chapter 2).

Table 4.5. Crystallographic Data for Structures **2**, **4**, and **6**

	2	4	6
Chemical Formula	CsCeF ₅	RbCeF ₅	(NH ₄)CeF ₅
F.W. (g/mol)	736.06	641.18	277.16
Space group	$P2_1/c$	$P2_1/c$	$C2/m$
Temp./K	293±2	293±2	293±2
Crystal system	Monoclinic	Monoclinic	Monoclinic
a, Å	8.3015 (17)	8.2091 (16)	8.1186 (16)
b, Å	14.221 (3)	13.527 (3)	13.831 (3)
c, Å	8.4515 (17)	8.3556 (17)	4.1286 (8)
β, °	104.47 (3)	103.78 (3)	102.65 (3)
V, Å ³	966.1 (3)	901.1 (3)	464.84 (13)
Z	4	4	4
D _{cal} , Mg/m ³	5.061	4.507	4.070
Indices (min)	[-9, -16, -10]	[-10, -16, -9]	[-10, -17, -4]
(max)	[9, 16, 9]	[10, 16, 10]	[10, 16, 5]
Parameters	128	128	48
F(000)	1264	1040	504
μ, mm ⁻¹	16.841	25.803	10.106
2θ range, °	2.53 – 25.10	2.55 – 26.41	2.96 – 26.05
Collected reflections	6990	8262	2015
Unique reflections	1713	1855	461
Final R (obs. data), ^a	0.0821	0.0602	0.0267
wR ₂	0.2472	0.1602	0.0699
Final R (all data), R ₁	0.0868	0.0617	0.0280
wR ₂	0.2496	0.1624	0.0702
Goodness of fit (S)	1.156	1.213	1.145
Extinction coefficient	0.00206 (3)	0.0203 (12)	0.0065 (13)
Largest diff. peak	5.164	3.677	1.039
Largest diff. hole	-3.959	-4.470	-1.532

$$^a R_1 = [\sum ||F_o| - |F_c||] / \sum |F_o|; wR_2 = \{[\sum w[(F_o)^2 - (F_c)^2]^2]^{1/2}\}$$

The crystallographically unique sites consist of eight-coordinate cerium atoms as $[\text{CeF}_8]^{4-}$ units conforming to a distorted monocapped square prismatic geometry, with average Ce-F distances of 2.2565 (17) Å for Ce1, which agrees with the Ce-F bond distance calculations by Shannon.³⁸ Some crystallographically unique atoms are in special positions; Ce1 has m symmetry, F1 has $2/m$ symmetry, and both F2 and N1 have two-fold rotational symmetry about the b axis. Compound **6** initially appears to contain 11-coordinate cerium(IV) atoms. Taking into account the half-occupancies of F2, F4, and F5, where F2 and F5 split occupancy and F4 splits with itself, the cerium(IV) atoms are actually eight-coordinate. Four cerium(IV) polyhedra form clusters by both edge-sharing of a pair of F2 atoms and a pair of F4 atoms. The clusters connect to each other through corner sharing of an F1 atom, forming a sheet that extends throughout the ac plane. The sheets are staggered and allow for the ammonium ions (represented by N1) to sit between the layers resulting in ABAB stacking (see Figure 4.3a). The nature of the stacking also allows for unique zigzag-shaped channels to form that run through the b axis. The channels are formed by a combination of diamond-shaped openings and zigzag-shaped openings overlapping each other (see Figure 4.3b).

Crystal Structures of CsCeF₅ (2) and RbCeF₅ (4)

Compounds **2** and **4** were shown to both crystallize into the monoclinic space group $P2_1/c$ (No. 14) upon structural refinement. Unfortunately due to relatively poor crystal quality in the numerous samples tested, the best final R_1 value is somewhat high

Table 4.6. Selected Bond Distances (Å) with esds for Compounds **2**, **4**, and **6**

CsCeF ₅ (2)		RbCeF ₅ (4)		(NH ₄)CeF ₅ (6)	
Bond Distances (Å)		Bond Distances (Å)		Bond Distances (Å)	
Ce1—F1	2.1196 (15)	Ce1—F1	2.126 (2)	Ce1—F1	2.264 (7)
Ce1—F3	2.0994 (16)	Ce1—F3	2.125 (2)	Ce1—F2 (x2)	2.344 (6)
Ce1—F5 ⁱ	2.221 (2)	Ce1—F5 ⁱ	2.256 (3)	Ce1—F3 (x2)	2.104 (5)
Ce1—F5	2.3136 (19)	Ce1—F5	2.246 (2)	Ce1—F4 (x2)	2.252 (7)
Ce1—F7	2.3552 (17)	Ce1—F7	2.325 (2)	Ce1—F4	2.271 (8)
Ce1—F8	2.3036 (17)	Ce1—F8	2.298 (2)	Ce1—F5 (x2)	2.308 (7)
Ce1—F9	2.2969 (15)	Ce1—F9	2.307 (2)	Ce1—F5 ^x	2.491 (7)
Ce1—F10 ⁱ	2.3982 (17)	Ce1—F10 ⁱ	2.391 (2)		
Ce2—F2	2.1315 (15)	Ce2—F2	2.115 (2)		
Ce2—F4	2.1091 (16)	Ce2—F4	2.099 (2)		
Ce2—F6	2.2605 (15)	Ce2—F6	2.295 (2)		
Ce2—F6 ⁱⁱ	2.2953 (17)	Ce2—F6 ⁱⁱⁱ	2.295 (2)		
Ce2—F7	2.2991 (16)	Ce2—F7	2.312 (2)		
Ce2—F8 ⁱⁱⁱ	2.3235 (17)	Ce2—F8 ⁱⁱ	2.282 (2)		
Ce2—F9 ⁱⁱ	2.4827 (17)	Ce2—F9 ⁱⁱⁱ	2.509 (2)		
Ce2—F9	2.8884 (19)	Ce2—F9	2.742 (2)		
Ce2—F10	2.3251 (16)	Ce2—F10	2.337 (2)		
Cs1—F1	2.9099 (19)	Rb1—F1	2.783 (3)		
Cs1—F2 ^{vii}	3.1870 (19)	Rb1—F2 ^{iv}	3.046 (3)		
Cs1—F2 ^{iv}	3.2562 (18)	Rb1—F2 ^{vii}	3.148 (3)		
Cs1—F3 ⁱ	3.0056 (17)	Rb1—F3 ⁱ	2.880 (2)		
Cs1—F3 ^{iv}	3.1262 (16)	Rb1—F3 ^{iv}	3.019 (2)		
Cs1—F4 ^{vi}	3.1137 (17)	Rb1—F4 ^{vi}	2.955 (2)		
Cs1—F4 ^v	3.2029 (18)	Rb1—F4 ^v	3.320 (2)		
Cs1—F6 ^v	3.1097 (16)	Rb1—F6 ^v	2.873 (2)		
Cs1—F9 ^{iv}	2.9731 (16)	Rb1—F9 ^{iv}	2.803 (2)		
Cs2—F1 ^v	2.9854 (16)	Rb2—F1 ^v	2.900 (2)		
Cs2—F1 ^{viii}	3.0359 (17)	Rb2—F1 ^{ix}	2.921 (2)		
Cs2—F2 ^{iv}	2.9934 (17)	Rb2—F2 ^{iv}	2.884 (2)		
Cs2—F2 ^{vii}	3.4146 (17)	Rb2—F2 ^{vii}	3.424 (2)		
Cs2—F3 ^{ix}	3.0679 (19)	Rb2—F3 ^{viii}	2.915 (3)		
Cs2—F4 ^{vi}	2.9807 (19)	Rb2—F4 ^{vi}	2.802 (3)		
Cs2—F5 ^{viii}	3.1291 (19)	Rb2—F5 ^{ix}	2.947 (3)		
Cs2—F7 ^v	3.1298 (17)	Rb2—F7 ^v	2.940 (2)		
Cs2—F10 ^{vii}	3.1316 (17)	Rb2—F10 ^{vii}	2.974 (2)		

Symmetry codes: (i) $x, -y+1/2, z+1/2$; (ii) $x, -y+1/2, z-1/2$; (iii) $x+1, y, z$; (iv) $-x, y-1/2, -z+1/2$; (v) $x-1, y, z$; (vi) $-x, -y, -z$; (vii) $x-1, -y+1/2, z+1/2$; (viii) $-x-1, -y, -z$; (ix) $-x-1, y-1/2, -z+1/2$; (x) $x, y, z-1$.

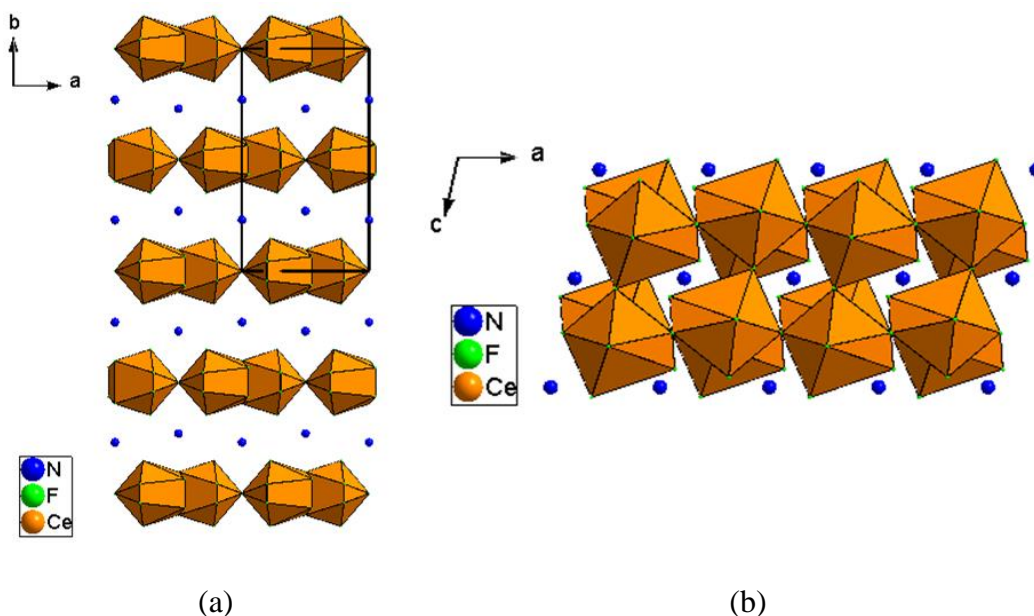


Figure 4.3. (a) Compound **6** as seen down the c axis showing how the clusters join to form sheets that extend through $[101]$ and result in ABAB stacking. (b) Compound **6** as seen down the b axis showing the unique channels that are formed as a result of the ABAB stacking.

for both **2** and **4** at 0.0821 and 0.0617, respectively. Attempts were made to obtain a solution in $C2/m$, but $P2_1/c$ was preferred as it gave a better R_1 value. Some atoms in both compounds (F5 and F6 for **2** and Ce1 and Ce2 for **4**) had to be refined using an ISOR restraint to prevent their principal mean square atomic displacements from being non-positive definite. However, the structure makes good chemical sense, since these solids are isostructural to previously-reported hafnium analogs $RbHfF_5$ ⁴⁵ and $(NH_4)HfF_5$ ⁴⁴, as well as a version of $CsThF_5$ that were prepared via hydrothermal method

(see Chapter 3, compound **7**). Both **2** and **4** have both eight-coordinate (Ce1) centers with monocapped square prismatic geometry and nine-coordinate (Ce2) centers with tricapped trigonal prismatic geometry. They are slightly distorted with an average Ce-F distance of 2.263 (2) and 2.346 (2) Å for Ce1 and Ce2 in **4**, and 2.259 (2) and 2.332 (2) Å in Ce1 and Ce2 in **6**, respectively, which correlate well with the expected values predicted by Shannon.³⁸ The crystallography closely resembles that of CsThF₅, which is discussed in detail (see Chapter 3, compound **7**).

Crystal Structures of Hexagonal (A)₂CeF₆ (A = K and Na, **9 and **11**, respectively)**

Crystallographic data for compounds **9** and **11** are shown in Table 4.6 and selected bond distances are shown in Table 4.7. Compounds **9** and **11** were shown to crystallize into the hexagonal space group $P\bar{6}2m$ (No. 189). They are isostructural with β -K₂UF₆ and β -Na₂ThF₆ synthesized by Zachariasen,³¹ as well as the recently reported single crystal structure of K₂ThF₆.⁴⁶ They are also isostructural with reported powder patterns for both K₂ThF₆³¹ and Rb₂ThF₆;¹³ however, these data were reported in the space group $C\bar{6}2m$, a non-standard but identical variation of $P\bar{6}2m$. Belonging to a hexagonal space group, compounds **9** and **11** solved comparatively in hexagonal space groups $P\bar{3}1m$ (No. 164, $R_1 = 0.0302$), $P6/mmm$ (No. 191, $R_1 = 0.0273$), and $P321$ (No. 150, $R_1 = 0.0124$), as well as the orthorhombic space group $Ibam$ (No. 72, $R_1 = 0.0416$). The space group $P\bar{6}2m$ was preferred as it considered fewer parameters to reach the statistically equivalent solution⁴³ as well as gave a better R_1 value and had literature precedence. The crystallographically unique sites consist of nine-coordinate cerium atoms as $[CeF_9]^{5-}$ units

conforming to a distorted tricapped trigonal prism geometry, with average Ce-F distances of 2.310 (3) and 2.306 (3) Å for Ce1 in **9** and **11**, respectively, which agrees with the Ce-F bond distance calculations by Shannon.³⁸ All of the crystallographically unique atoms are in special positions; Ce1 has $\bar{6}2m$ symmetry, A1 has $\bar{6}$ symmetry, and both F1 and F2 have $m2m$ symmetry.

Unlike most cases, the framework is formed by the alkali metal. The nine-coordinate alkali polyhedra join in groups of two through sharing a trigonal face formed by an F1 atom and two F2 atoms. These groups of polyhedra join to other groups through edge sharing of an F1 atom and an F2 atom, forming sheets that run throughout the *ab* plane. The sheets of alkali polyhedra also join to each other through sharing a trigonal face formed by two F1 atoms and an F2 atom and stack evenly throughout the *c* axis, forming distorted hexagram-shaped channels where the cerium(IV) atoms sit (see Figure 4.3). The channel measures 4.108 (6) Å for **9** and 4.100 (3) Å for **11** at their widest points, leaving ample room for the cerium(IV) atoms (2.22 Å diameter for Ce(IV) based on calculations by Shannon)³⁸ to sit.

When comparing the unit cell parameters of **9** and **11** to their associated bond distances (see Tables 4.7 and 4.8), it can be noted that the difference in the *a* and *b* axes arises from the A-F bond distance that make up the alkali polyhedra in the network, namely A1-F2 (2.600 (3) Å for **9** versus 2.274 (2) Å for **11**). As expected, the minimal difference in the *c* axis is credited to the cerium(IV) atoms in the channels running through the *c* axis with minimal difference in the Ce-F bonding between **9** and **11**, the largest difference being Ce1-F1 (2.195 (4) Å for **9** versus 2.179 (4) Å for **11**).

Table 4.7. Crystallographic Data for Structures **9** and **11**

	9	11
Chemical Formula	K ₂ CeF ₆	Na ₂ CeF ₆
F.W. (g/mol)	332.32	300.10
Space group	P $\bar{6}2m$	P $\bar{6}2m$
Temp./K	293±2	293±2
Crystal system	Hexagonal	Hexagonal
a, Å	6.5266 (9)	5.9431 (8)
c, Å	3.7064 (9)	3.7007 (7)
V, Å ³	136.73 (5)	113.20 (4)
Z	1	1
D _{cal} , Mg/m ³	4.036	4.402
Indices (min)	[-8, -8, -4]	[-7, -7, -4]
(max)	[8, 7, 4]	[7, 6, 4]
Parameters	14	15
F(000)	150	1040
μ, mm ⁻¹	9.880	10.284
2θ range, °	3.60 – 26.17	3.96 – 25.87
Collected reflections	1176	1040
Unique reflections	125	103
Final R (obs. data), ^a R ₁	0.0167	0.0098
wR ₂	0.0349	0.0218
Final R (all data), R ₁	0.0167	0.0098
wR ₂	0.0349	0.0218
Goodness of fit (S)	1.197	1.176
Extinction coefficient	0.27 (2)	0.050 (8)
Largest diff. peak	0.473	0.271
Largest diff. hole	-1.557	-0.554

$$^a R_1 = [\sum ||F_o| - |F_c||] / \sum |F_o|; wR_2 = \{[\sum w[(F_o)^2 - (F_c)^2]^2]\}^{1/2}$$

Table 4.8. Selected Bond Distances (Å) with esds for Compounds **9** and **11**

K ₂ CeF ₆ (9)		Na ₂ CeF ₆ (11)	
Bond Distances (Å)		Bond Distances (Å)	
Ce1—F1 (x3)	2.195 (4)	Ce1—F1 (x3)	2.179 (4)
Ce1—F2 (x6)	2.367 (3)	Ce1—F2 (x6)	2.369 (2)
K1—F1 (x6)	2.851 (4)	Na1—F1 (x6)	2.645 (4)
K1—F2 (x3)	2.600 (3)	Na1—F2 (x3)	2.274 (2)

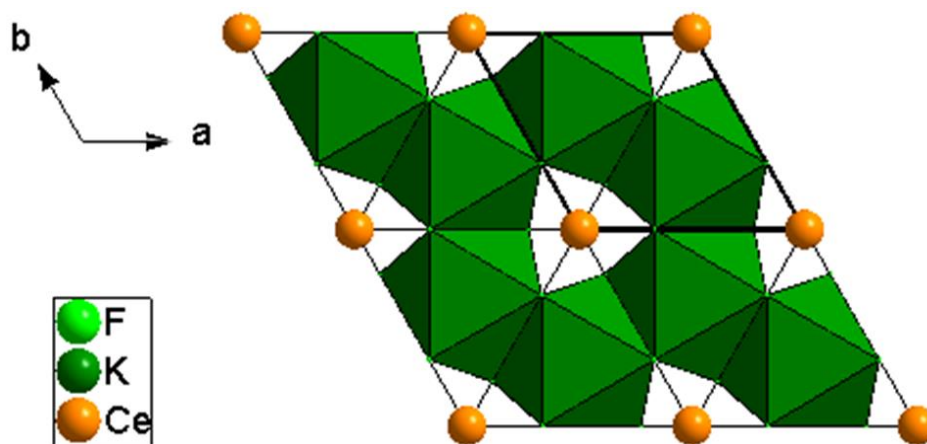


Figure 4.4. Compound **9** as seen down the c axis showing how the alkali polyhedra cluster to form hexagram-shaped channels where the Ce(IV) atoms sit.

Crystal Structures of $(A)_7Ce_6F_{31}$ ($A = NH_4$ (**7**), **K** (**10**), **Na** (**12**))

*Crystal Structures of $(NH_4)_7Ce_6F_{31}$ (**7**) and $K_7Ce_6F_{31}$ (**10**)*

Crystallographic data for compounds **7**, **10**, and **12** are shown in Table 4.9 and selected bond distances are shown in Table 4.10. This structure type crystallizes in the trigonal space group $R\bar{3}$ (No. 148). Only a few isostructural analogs of this class of compounds have previously been reported, including $Na_7Th_6F_{31}$ as a powder,¹² and $K_7Th_6F_{31}$ ^{15,46} and $Na_7Zr_6F_{31}$ ⁴⁷ as single crystals. For this set of compounds A2 ($A = NH_4$, K, Na/Ce) sits on a $\bar{3}$ symmetry site, and the other atom in a special position, F6, happens to sit on a 3-fold rotation symmetry site. The crystallography of **7** and **10** closely resembles that of $(NH_4)_7Th_6F_{31}$ and $Rb_7Th_6F_{31}$, which is discussed in detail (see Chapter 3, compounds **12** and **10**, respectively).

Comparing compounds **7** and **10** to their thorium analogs, both show consistent contraction of their unit cell parameters, with $\Delta a \sim 0.35 \text{ \AA}$ and $\Delta c \sim 0.20 \text{ \AA}$ for each set of

Table 4.9. Crystallographic Data for Structures **7**, **10**, and **12**

	7	10	12
Chemical Formula	(NH ₄) ₇ Ce ₆ F ₃₁	K ₇ Ce ₆ F ₃₁	Na ₇ Ce ₆ F ₃₁
F.W. (g/mol)	1527.79	1703.42	4745.15
Space group	R $\bar{3}$	R $\bar{3}$	R $\bar{3}$
Temp./K	293±2	293±2	293±2
Crystal system	Trigonal	Trigonal	Trigonal
a, Å	15.232 (2)	15.013 (2)	14.567 (2)
c, Å	10.749 (2)	10.295 (2)	9.6921 (19)
V, Å ³	2159.8 (8)	2009.6 (6)	1781.1 (5)
Z	3	3	3
D _{cal} , Mg/m ³	3.524	4.223	4.424
Indices (min)	[-18, -17, -13]	[-18, -18, -12]	[-17, -17, -11]
(max)	[18, 18, 13]	[18, 18, 12]	[17, 17, 11]
Parameters	70	70	69
F(000)	2028	2280	2100
μ, mm ⁻¹	9.492	11.278	11.458
2θ range, °	2.67 – 26.10	2.52 – 26.30	2.65 – 25.17
Collected reflections	6009	6209	4884
Unique reflections	953	910	710
Final R (obs. data), ^a	0.0431	0.0206	0.0401
wR ₂	0.1032	0.0474	0.1063
Final R (all data), R ₁	0.0445	0.0213	0.0419
wR ₂	0.1035	0.0479	0.1079
Goodness of fit (S)	1.111	1.121	1.154
Extinction coefficient	0.000867 (3)	0.00029 (3)	0.00052 (10)
Largest diff. peak	2.706	0.533	2.437
Largest diff. hole	-1.489	-1.475	-1.785

$$^a R_1 = [\sum||F_o| - |F_c||] / \sum|F_o|; wR_2 = \{[\sum w[(F_o)^2 - (F_c)^2]^2]\}^{1/2}$$

compounds. This is surprising, considering the behavior of the thermal parameters of their respective F6 atoms in which their electron density is being distributed in different planes of the unit cell (refer to Chapter 3 for more details). This consistent contraction shows that the unit cell size is dictated by the monovalent atoms that constitute the ends of the pores in which the F6 atoms sit, since the M-F (M = Th, Ce) bond distances are similar for both the potassium and ammonium analogs (average Th-F bond distance of

2.333(4) and 2.337(7) Å for $K_7Th_6F_{31}$ ⁴⁶ and $(NH_4)_7Th_6F_{31}$, respectively, and average Ce-F bond distances of 2.267 (2) and 2.268 (4) Å for compounds **7** and **10**, respectively).

Table 4.10. Selected Bond Distances (Å) with esds for Compounds **7**, **10**, and **12**

$(NH_4)_7Ce_6F_{31}$ (7)		$K_7Ce_6F_{31}$ (10)		$Na_7Ce_6F_{31}$ (12)	
Bond Distances (Å)		Bond Distances (Å)		Bond Distances (Å)	
Ce1—F1	2.1511 (4)	Ce1—F1	2.151 (2)	Ce1/Na1—F1	2.188(5)
Ce1—F2	2.1713 (5)	Ce1—F2	2.152 (2)	Ce1/Na1—F2	2.182 (6)
Ce1—F3	2.3304 (3)	Ce1—F3	2.336 (2)	Ce1/Na1—F3	2.330 (5)
Ce1—F3	2.3669 (4)	Ce1—F3	2.352 (2)	Ce1/Na1—F3	2.336 (5)
Ce1—F4	2.2868 (4)	Ce1—F4	2.285 (2)	Ce1/Na1—F4	2.224 (6)
Ce1—F4	2.2901 (4)	Ce1—F4	2.309 (2)	Ce1/Na1—F4	2.27 (6)
Ce1—F5	2.2700 (4)	Ce1—F5	2.274 (2)	Ce1/Na1—F5	2.222 (6)
Ce1—F5	2.2762 (4)	Ce1—F5	2.276 (2)	Ce1/Na1—F5	2.255 (7)
		Ce1—F6	2.786 (8)	Ce1/Na1—F6	2.687 (7)
		K1—F1	2.633 (2)	Na2/Ce2—F1	2.399 (6)
		K1—F1	2.670 (2)	Na2/Ce2—F1	2.453 (6)
		K1—F1	2.698 (2)	Na2/Ce2—F1	2.614 (7)
		K1—F2	2.659 (2)	Na2/Ce2—F2	2.406 (6)
		K1—F2	2.766 (2)	Na2/Ce2—F2	2.447 (6)
		K1—F3	2.717 (2)	Na2/Ce2—F3	2.498 (6)
		K1—F3	2.720 (2)	Na2/Ce2—F3	2.590 (6)
		K2—F2 (x6)	2.699 (2)	Na3/Ce3—F2 (x6)	2.572 (6)

*Crystal Structure of $Na_7Ce_6F_{31}$ (**12**)*

This is the first instance where disordering of the univalent ion and the tetravalent ion occurs in the formulation $A_7B_6F_{31}$. However, sodium-cerium disorder has been reported for $Na_{0.57}Ce_{0.81}Cl_3$,⁴⁸ $Na_{1.14}Ce_{1.62}Cl_6$,⁴⁹ and Na_2CeO_3 .⁵⁰ For **12**, F6 still sits on a 3-fold rotation symmetry site, but disordered Z3 (Z = Na, Ce) sits on a $\bar{3}$ symmetry site.

The structure for compound **12** is similar to compounds **7** and **10**. The fundamental building block consists of clusters of three eight-coordinate cerium and sodium atoms in a pseudo-square antiprismatic geometry. The cerium and sodium polyhedra within each cluster corner share with one another through F5, and the clusters connect to each other by edge sharing through F4 pairs. Two cerium clusters are sandwiched between layers of disordered cerium and sodium polyhedra (Z2 and Z3), with each layer consisting of six Z2 surrounding one Z3. Unlike the other compounds with this formulation, compound **12** has two F6 that do *not* possess extremely high thermal parameters, that is, they do not widely distribute their electron densities throughout the pore (see Figure 4.5).

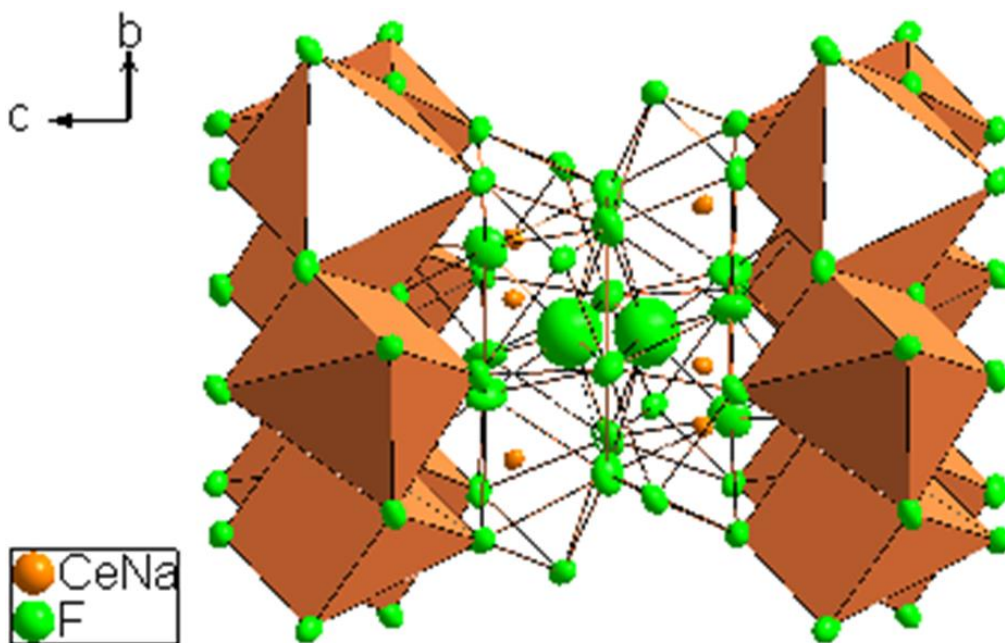


Figure 4.5. The cage-like structure of compound **5**, as viewed down the a axis. The atoms are shown as thermal ellipsoids to demonstrate the thermal parameter of F6. The thorium polyhedra are open-faced for clarity.

A small percentage of disordering is observed between the cerium and sodium atoms in **5** at the 3a and 18f Wyckoff sites. At Z1 (the site where the tetravalent ion is normally fully occupied), there is 87% occupancy of cerium atoms and 13% occupancy of sodium atoms. This causes the pore to be considerably shorter in length (9.6921 (19) Å) compared to its potassium analog (10.295 (2) Å) that exhibits full occupation of the cerium site. At Z2 and Z3 (the site where the monovalent ion is normally fully occupied) the disorder is less pronounced, with average occupancy of 94% sodium atoms and 6% cerium atoms. Since there is not as much disorder at Z2 and Z3 compared to Z1, the pore size is only slightly shorter (5.144 (10) Å) compared to its potassium analog (5.398 (4) Å).

Lithium-Containing Cerium(IV) Fluorides

Crystal Structure of LiCeF₅ (13)

Crystallographic data for compounds **13** and **14** are shown in Table 4.11 and selected bond distances are shown in Table 4.12. Compound **13** crystallizes in the tetragonal space group $I4_1/a$ (No. 88). This solid was found to crystallize similarly to the isostructural analog LiUF₅ synthesized by Brunton.⁵¹ For this compound, none of the unique atoms sit on a special position; all the atoms sit on Wyckoff general position 16f. The fundamental building block of compound **13** consists of clusters of four nine-coordinate cerium(IV) atoms in a slightly distorted monocapped square antiprismatic geometry. The cerium(IV) polyhedra within each cluster corner share with one another through F2. The clusters corner share with each other through F2 to form left-handed

helices that extend through the c axis. The helices are stabilized by six-coordinate lithium atoms in distorted octahedral geometry via corner sharing through F4 and edge sharing through F3 and F5. Each helix forms a small square-shaped channel that runs through the c axis and measures 0.7049 (1) Å on each side dictated by corners of F2 (see Figure 4.6). The helices result in a framework structure that connect via the corner sharing through F1 between each cerium(IV) polyhedral and the edge sharing of two F4 between each lithium polyhedral (see Figure 4.7).

Crystal Structure of Li_4CeF_8 (14)

Compound **14** crystallizes in the orthorhombic space group $Pnma$ (No. 62, see Table 4.2). All of the lithium atoms had to be refined using an ISOR restraint to prevent their principal mean square atomic displacements from being non-positive definite. Only a couple of isostructural analogs of this compound have previously been reported, specifically Li_4UF_8 ⁵² and Li_4TbF_8 ⁵³ as single crystals. The crystallographically unique sites consist of eight-coordinate cerium atoms as $[\text{CeF}_8]^{4-}$ units conforming to a distorted monocapped square prismatic geometry, with average Ce-F distances of 2.256 (6) Å for Ce1, which agrees with the Ce-F bond distance calculations by Shannon.³⁸ Atoms Ce1, F1, and F5 all sit on a special position where they possess a mirror plane on the b axis.

Similar to what was seen with hexagonal $(A)_2\text{CeF}_6$ compounds **9** and **11**, the framework is formed by the alkali metal. The fundamental building block of compound **14** consists of clusters of two six-coordinate lithium atoms in a slightly distorted octahedral geometry. Two of these polyhedral are joined by edge sharing

Table 4.11. Crystallographic Data for Structures **13** and **14**

	13	14
Chemical Formula	F ₅ CeLi	F ₈ CeLi ₄
F.W. (g/mol)	484.12	319.88
Space group	I4 ₁ /a	Pnma
Temp./K	293±2	293±2
Crystal system	Tetragonal	Orthorhombic
a, Å	14.716 (2)	9.936 (2)
b, Å		9.814 (2)
c, Å	6.5060 (13)	5.9344 (12)
V, Å ³	1408.9 (4)	578.7 (2)
Z	8	4
D _{cal} , Mg/m ³	4.565	3.672
Indices (min)	[-17, -17, -7]	[-11, -11, -7]
(max)	[17, 17, 8]	[11, 11, 7]
Parameters	65	83
F(000)	1696	568
μ, mm ⁻¹	12.901	7.964
2θ range, °	2.77 – 26.00	4.00 – 25.06
Collected reflections	4580	4341
Unique reflections	616	542
Final R (obs. data), ^a R ₁	0.0256	0.0316
wR ₂	0.0546	0.0808
Final R (all data), R ₁	0.0276	0.0321
wR ₂	0.0558	0.0810
Goodness of fit (S)	1.211	1.271
Extinction coefficient	0.00060 (8)	0.0186 (15)
Largest diff. peak	1.044	1.171
Largest diff. hole	-0.878	-1.300

$$^aR_1 = [\sum||F_o| - |F_c||] / \sum|F_o|; wR_2 = \{[\sum w[(F_o)^2 - (F_c)^2]^2]\}^{1/2}$$

through F2 and F4 atoms. The clusters alternate by a 180° rotation along the *a* axis and join together by corner sharing through a pair of F3 atoms. This forms a zigzag layer that runs through the *ab* plane. Another layer of alternating clusters (differing by a 65° rotation about the *c* axis) connects to the zigzag layer by corner sharing F1 atoms to create a network that runs along [110].

Table 4.12. Selected Bond Distances (Å) with esds for Compounds **13** and **14**

LiCeF ₅ (13)		Li ₄ CeF ₈ (14)	
Bond Distances (Å)		Bond Distances (Å)	
Ce1—F1 ⁱ	2.172 (4)	Ce1—F1	2.183 (7)
Ce1—F1 ⁱⁱ	2.674 (4)	Ce1—F2 (x2)	2.241 (5)
Ce1—F2 ⁱⁱⁱ	2.214 (4)	Ce1—F3 (x2)	2.358 (5)
Ce1—F2	2.301 (4)	Ce1—F4 (x2)	2.229 (5)
Ce1—F3 ^{iv}	2.276 (4)	Ce1—F5	2.211 (7)
Ce1—F3	2.314 (3)	Li1—F2 ^{ix}	2.00 (3)
Ce1—F4 ^v	2.228 (4)	Li1—F2 ^x	2.12 (3)
Ce1—F5 ^{vi}	2.276 (4)	Li1—F3 ^{xi}	2.01 (3)
Ce1—F5	2.453 (4)	Li1—F3 ^{xii}	2.06 (3)
Li1—F3 ⁱⁱ	2.098 (13)	Li1—F4 ^x	2.19 (3)
Li1—F4 ^{vii}	1.898 (13)	Li1—F5	2.03 (3)
Li1—F4 ^{viii}	1.969 (13)	Li2—F1 ^{xi}	2.01 (3)
Li1—F4 ^v	2.333 (15)	Li2—F2 ^{xiii}	2.02 (3)
Li1—F5 ^{iv}	1.870 (13)	Li2—F3 ^{xi}	2.24 (3)
		Li2—F3 ^{xiv}	2.27 (3)
		Li2—F4 ^{xv}	1.98 (3)
		Li2—F4 ^x	2.07 (3)

Symmetry codes: (i) $x+1/2, y, -z-1/2$; (ii) $-x, -y+1/2, z$; (iii) $-y+3/4, x+1/4, z+1/4$; (iv) $-y+1/4, x+1/4, -z+1/4$; (v) $y-1/4, -x+3/4, z-1/4$; (vi) $-x+1/2, -y+1/2, -z+1/2$; (vii) $x-1/2, y, -z-1/2$; (viii) $-y+1/4, x-1/4, z-1/4$; (ix) $-x+1/2, -y, z-1/2$; (x) $x+1/2, y, -z+1/2$; (xi) $x, -y+1/2, z$; (xii) $-x+1/2, y-1/2, z-1/2$; (xiii) $x+1/2, y, -z+3/2$; (xiv) $-x+1/2, y-1/2, z+1/2$; (xv) $-x+1/2, -y, z+1/2$.

The networking layer along [110] joins to adjacent layers by edge sharing through F2 and F3 on Li1 and F3 and F4 on Li2 to forms large distorted triangular-shaped channels that run through the *c* axis where the cerium(IV) polyhedra sit. The large channels measure 5.157 (1) by 4.269 (7) Å at their widest points, leaving ample room for cerium(IV) polyhedral to sit (see Figure 4.8a). It is interesting to note that an open isosceles triangular-shaped channel still exists, since the cerium(IV) polyhedra does not occupy the entire space. The open space measures 3.066 (8) by 2.571 (7) Å, or 2.655 (7) Å across at its widest point (see Figure 4.8b).

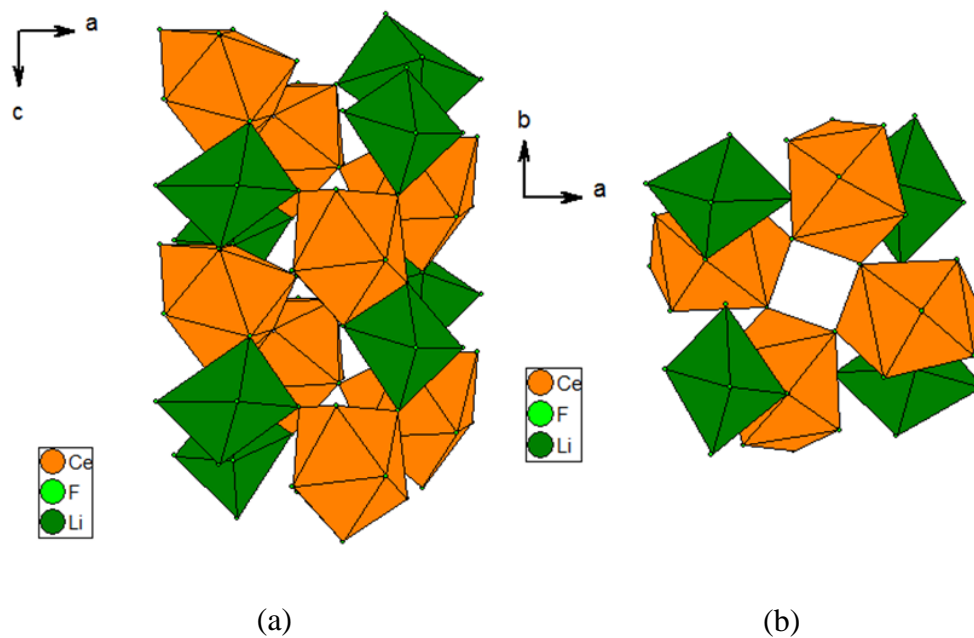


Figure 4.6. (a) Helical building block of **13** as seen down the *b* axis. (b) Said helix as seen down the *c* axis, showing the square-shaped channel.

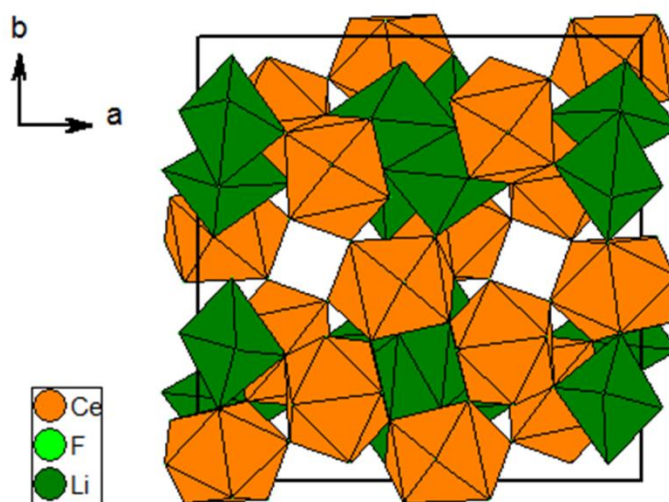


Figure 4.7. The framework structure of **13** as seen down the *c* axis, showing two helical units per unit cell.

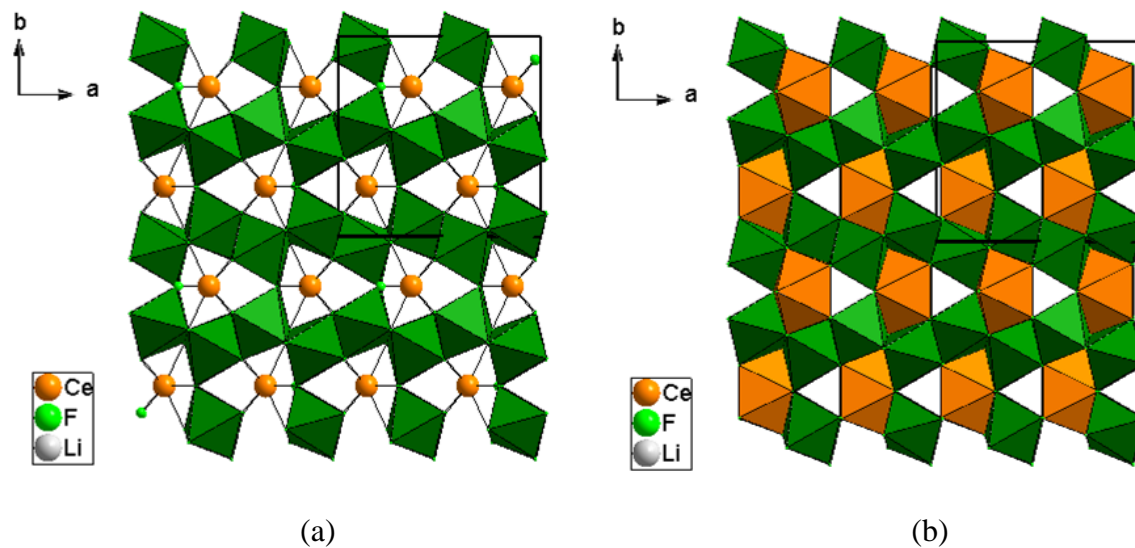


Figure 4.8. (a) Compound **14** as seen down [001], showing the large triangular-shaped channels. The cerium(IV) polyhedra are open for clarity. (b) Compound **14** in the same viewpoint, only with the cerium(IV) polyhedra to show the smaller triangular-shaped channel that exists.

CONCLUSIONS

It was found that hydrothermal synthesis of monovalent cerium(IV) fluorides using CeF_4 and monovalent fluoride mineralizers yielded a wider variety of products than the thorium fluoride system, including the first fully characterized monovalent cerium fluorides (Figure 4.9). All of the formulations reported earlier were not previously characterized by single crystal diffraction due to the lack of exploration of the phase space. Though there is some CeF_3 powder in the reactions, the compounds reported

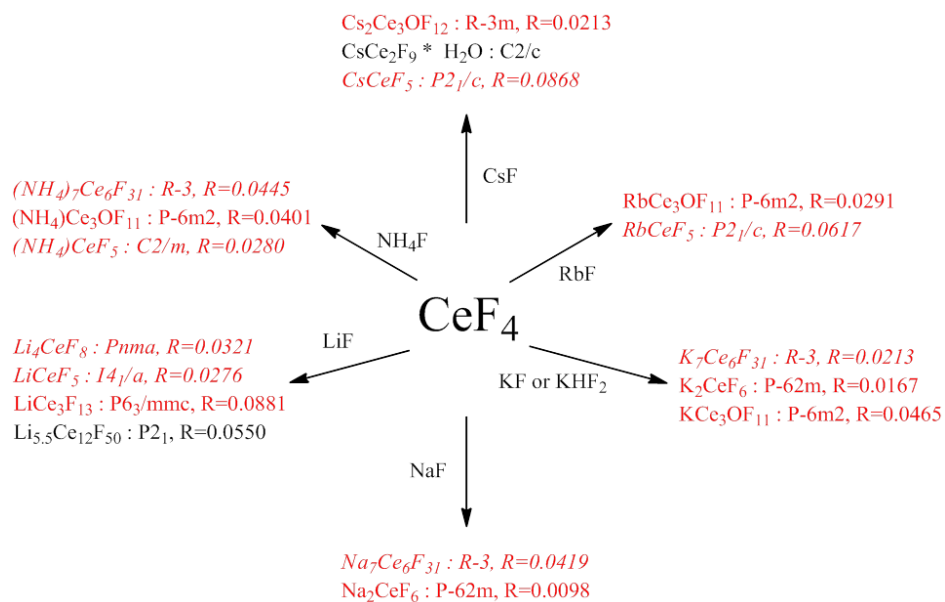


Figure 4.9. Overview of the monovalent cerium(IV) fluorides synthesized using our hydrothermal method. The compounds in black are reported single crystal structures and the compounds in red are new structures. Any compounds in italics have previously-reported powder patterns that were used to confirm the identity of the new materials.

herein can be prepared as phase pure crystals. Many of the compounds grow in a variety of polymorphs that are isostructural to both the thorium and hafnium fluoride systems, acting as a “crystallographic bridge” between the two systems. The identity of the species seems to be primarily dependent on the concentration of the fluoride mineralizer used in their syntheses and lower reaction temperatures. Especially interesting is that an alkali cerium(IV) fluoride that is isostructural for all three K, Rb and Cs phases has not yet identified, similar to what was determined for the thorium fluoride system. The facile growth of these stable monovalent cerium(IV) fluorides is an encouraging sign, and has

opened up the possibility for further development of this virtually unexplored phase space.

REFERENCES

- (1) Mann, M.; Thompson, D.; Serivalsatit, K.; Tritt, T. M.; Ballato, J.; Kolis, J. W. *Cryst. Growth Des.* **2010**, *10*, 2146-2151.
- (2) Underwood, C. C.; Mann, M.; McMillen, C. D.; Kolis, J. W. *Inorg. Chem.* **2011**, *50*, 11825-11831.
- (3) Underwood, C. C.; Mann, M.; McMillen, C. D.; Musgraves, J. D.; Kolis, J. W., *Solid St. Sci.* **2012**, *14*, 574-579.
- (4) Underwood, C. C.; McMillen, C.; Kolis, J. W. *J. Chem. Crystallogr.* **2012**, *42*, 606-610.
- (5) Brunton, G. D.; Insley, H.; McVay, T. N.; Thoma, R. E. *Crystallographic Data for Some Metal Fluorides, Chlorides, and Oxides*; ORNL-3761; U.S. Government Printing Office: Washington, D.C., 1965.
- (6) Thoma, R. E.; Carlton, T. S. *J. Inorg. Nucl. Chem.* **1961**, *17*, 88-95.
- (7) Harris, L. A.; White, G. D.; Thoma, R. E. *J. Phys. Chem.* **1959**, *63*, 1974-1975.
- (8) Asker, W. J.; Segnit, E. R.; Wylie, A. W. *J. Chem. Soc.* **1952**, 4470-4479.
- (9) Thoma, R. E. *Phase Diagrams of Nuclear Reactor Materials*; ORNL-2548; U.S. Government Printing Office: Washington, DC, 1959.
- (10) Derganov, E. P.; Bergman, A. G. *Dokl. Akad. Nauk.* **1948**, *60*, 391.
- (11) Thoma, R. E.; Insley, H.; Landau, B. S.; Friedman, H. A.; Grimes, W. R. *J. Phys. Chem.* **1959**, *63*, 1266-1274.
- (12) Thoma, R. E.; Insley, H.; Herbert, G. M.; Friedman, H. A.; Weaver, C. F. *J. Am. Ceram. Soc.* **1963**, *46*, 37-42.
- (13) Harris, L. A. *Acta Crystallogr.* **1960**, *13*, 502.

- (14) Brunton, G. D. *Acta Crystallogr. B* **1971**, *B27*, 1823-1826.
- (15) Brunton, G. D. *Acta Crystallogr. B* **1971**, *B27*, 2290-2292.
- (16) Ryan, R. R.; Penneman, R. A. *Acta Crystallogr. B* **1971**, *B27*, 829-833.
- (17) Brunton, G. D. *Acta Crystallogr. B* **1972**, *B28*, 144-147.
- (18) Zachariasen, W. H. *J. Am. Chem. Soc.* **1948**, *70*, 2147-2151.
- (19) Grzechnik, A.; Fechtelkord, M.; Morgenroth, W.; Posse, J. M.; Friese, K. *J. Phys. Condens. Matter* **2007**, *19*, 266219.
- (20) Zachariasen, W. H. *Acta Crystallogr.* **1949**, *2*, 390-393.
- (21) Grzechnik, A.; Morgenroth, W.; Friese, K. *J. Solid Chem.* **2008**, *181*, 971-975.
- (22) Cousson, A.; Pagès, M. *Acta Crystallogr. B.* **1978**, *B34*, 1776-1778.
- (23) Pulcinelli, S. H.; de Almeida Santos, R. H.; Senegas, J. *J. Fluorine Chem.* **1989**, *42*, 41-50.
- (24) Laligant, Y.; LeBail, A.; Avignat, D.; Cousseins, J. C.; Ferey, G. *J. Solid St. Chem.* **1989**, *80*, 206-212.
- (25) Laligant, Y.; Ferey, G.; El Ghoszi, M.; Avignat, D. *Eur. J. Solid St. Inorg. Chem.* **1992**, *29*, 497-504.
- (26) Ryan, R. R.; Penneman, R. A.; Rosenzweig, A. *Acta Crystallogr. B* **1969**, *B25*, 1958-1962.
- (27) Penneman, R. A.; Ryan, R. R.; Kressin, I. K. *Acta Crystallogr. B* **1971**, *B27*, 2279-2283.
- (28) Gaumet, V.; El Ghoszi, M.; Avignat, D. *Eur. J. Solid St. Inorg. Chem.* **1995**, *32*, 893-905.
- (29) Brunton, G. D. *Acta Crystallogr. B* **1970**, *B26*, 1185-1187.

- (30) Brunton, G. D.; Sears, D. R. *Acta Crystallogr. B* **1969**, *B25*, 2519-2527.
- (31) Zachariasen, W. H. *Acta Crystallogr.* **1948**, *1*, 265-269.
- (32) Zachariasen, W. H. *Acta Crystallogr.* **1949**, *2*, 388-391.
- (33) Delaigue, A.; Cousseins, J.-C. *Rev. Chim. Min.* **1972**, *9*, 789-798.
- (34) Hoppe, R.; Rödder, K.-M. *Z. Anorg. Allg. Chem.* **1961**, *313*, 154-160.
- (35) Brunton, G. *Acta Crystallogr. B*, **1969**, *B25*, 600-602.
- (36) Renaudin, G.; Dieudonné, B.; Avignant, D.; Mapemba, E.; El-Ghozzi, M.; Fleutot, S.; Martinez, H.; Černý, R.; Dubois, M. *Inorg. Chem.* **2009**, *49*, 686-694.
- (37) Rouse, J.; Weller, M. T. *Dalton Trans.* **2009**, 10330-10337.
- (38) Shannon, R. D. *Acta Crystallogr. A* **1976**, *A32*, 751.
- (39) Koller, D.; Müller, B. G. *Z. Anorg. Allg. Chem.* **2002**, *628*, 575-579.
- (40) Mansouri, I.; Avignant, D. *J. Solid St. Chem.* **1984**, *51*, 91-99.
- (41) Saada, M. A.; Hemon-Ribaud, A.; Maisonneuve, V.; Smiri, L. S.; Leblanc, M. *Acta Crystallogr.* **2003**, *E59*, i131-i133.
- (42) Underwood, C. C.; McMillen, C. D.; Kolis, J. W. *Inorg. Chem.* **2013**, *52*, 237-244.
- (43) Hamilton, W. C. *Acta Crystallogr.* **1965**, *18*, 502-510.
- (44) Plitzko, C.; Meyer, G. *Z. Anorg. Allg. Chem.* **1998**, *624*, 169-170.
- (45) Koller, D.; Müller, B. G. *Z. Anorg. Allg. Chem.* **2002**, *628*, 575-579.
- (46) Grzechnik, A.; Underwood, C. C.; Kolis, J. W.; Friese, K. *J. Fluorine Chem.* **2013**, *150*, 8-13.
- (47) Burns, J. H.; Ellison, R. D.; Levy, H. A. *Acta Crystallogr. B* **1968**, *B24*, 230-237.
- (48) Krämer, K.; Meyer, G. *Z. Anorg. Allg. Chem.* **1990**, *589*, 96-100.

- (49) Lissner, F.; Krämer, K.; Schleid, T.; Meyer, G.; Hu, Z.; Kaindl, G. *Z. Anorg. Allg. Chem.* **1994**, 620, 444-450.
- (50) Zintl, E.; Morawietz, W. *Z. Anorg. Allg. Chem.* **1940**, 245, 26-31.
- (51) Brunton, G. *Acta Crystallogr.* **1966**, 21, 814-817.
- (52) Brunton, G. *J. Inorg. Nucl. Chem.* **1967**, 29, 1631-1636.
- (53) El Ghozzi, M.; Avignant, D.; Cousseins, J. C. *Eur. J. Solid St. Inorg. Chem.* **1992**, 29, 981-992.

CHAPTER FIVE

HYDROTHERMAL CHEMISTRY, STRUCTURES, AND LUMINESCENCE STUDIES OF HAFNIUM FLUORIDES CONTAINING MONOVALENT IONS

INTRODUCTION

Compared to other Group 4 elements, the fundamental inorganic chemistry of hafnium is somewhat underexplored. Hafnium was not discovered until the 1920s,¹ and the descriptive chemistry of solid-state hafnium compounds has not received as much attention as its homologs. Since the discovery that the neutron-capture cross section of hafnium is 600 times that of its sister element zirconium,² its use has grown as an effective control rod in nuclear reactors (including molten fluoride-based reactors) even though the isolation of hafnium from zircon is quite expensive. Limited previous work was done primarily in molten alkali fluoride salts and led to a variety of alkali metal hafnium fluorides. Several ternary $A_x\text{Hf}_y\text{F}_z$ compounds were characterized, mostly by either powder or single crystal diffraction,³⁻¹⁵ with a majority of these phases being potassium hafnium fluorides. Most of the single crystal structural characterization has centered on the $A_2\text{HfF}_6$ phases ($A = \text{K}, \text{Rb}, \text{Cs}$; see Figure 5.1). Given the renewed interest in nuclear reactor safety, the fundamental descriptive chemistry of hafnium fluorides is worthy of investigation.

By way of comparison, our group recently found that an extensive series of alkali thorium fluorides can be grown in hydrothermal fluids.¹⁶⁻¹⁸ We previously found that the chemistry of the thorium fluorides is both extensive and interesting, and a number of long

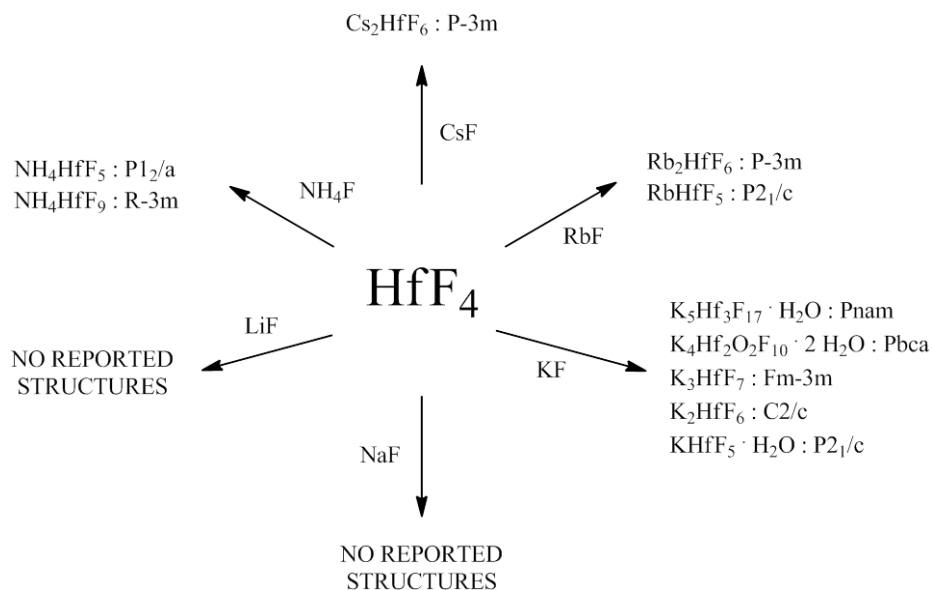


Figure 5.1. Overview of the reported monovalent alkali and pseudo-alkali hafnium fluorides single crystals.

standing issues with the compounds were clarified by the isolation of a number of unusual compounds as high quality single crystals. Given this interesting behavior of the alkali thorium fluorides in hydrothermal fluids and the continued technological interest in hafnium chemistry, a new study of hafnium fluorides in hydrothermal fluids was undertaken to compare the chemistry of the two tetravalent metal fluorides. It was found that the reaction of HfF_4 with alkali fluorides in hydrothermal fluids does lead to a wide variety of new alkali metal hafnium fluoride compounds. Systematic exploration of the phase space reveals a number of compounds that reflect the size and stoichiometry of the alkali ion, as our group also observed with thorium fluorides.¹⁶⁻¹⁸ In contrast to the

thorium fluoride system, in which our group never observed any hydrolysis in hydrothermal fluids even above 600 °C, some hydrolytic reactions with hafnium fluorides were observed to form several oxyfluorides.

In this Chapter, efforts are reported for the exploration of the alkali hafnium fluoride phase space in hydrothermal fluids. The chemistry and structures of a series of new alkali hafnium fluorides and oxyfluorides grown from hydrothermal solutions, including the first ternary sodium and lithium hafnium fluorides to be characterized by single crystal X-ray diffraction are described. Since earlier work with a variety of alkali zirconium oxyfluoride powders showed that they exhibit interesting X-ray luminescent properties,¹⁹ the X-ray and visible luminescent properties of the new compounds were also measured.

RESULTS AND DISCUSSION

Descriptive Synthetic Chemistry

Reactions were investigated by differing temperature, reaction time, and ratios of A:Hf (A = Li – Cs, NH₄) as a means to explore this phase space and identify any trends in compound formation (see Table 5.1). It is interesting to note that the most common formulation of alkali hafnium fluorides encountered in this study is A₂HfF₆. For reactions involving lithium this was the only phase obtained. However, this phase was not obtained for A = Na under any of our conditions, and a greater variety of chemistry is observed, producing crystals of Na₅Hf₂F₁₃ and Na₃HfF₇ (conditions 4 and 5). Ratios of Na:Hf below 4:1 (not included in Table 5.1) under similar reaction conditions repeatedly

produced powders matching a powder pattern for Na_3HfF_7 ¹² accompanied by NaF crystals. Curiously, the formulation Na_2HfF_6 has not been observed by any other investigation. The formula A_2HfF_6 is not isostructural across the various alkali ions. Furthermore, the structure of Li_2HfF_6 is different from that of K_2HfF_6 , which is different from the Rb and Cs analogs (*vide infra*), so perhaps it is not surprising that there is not an apparent stable lattice for the Na analog.

A number of potassium hafnium fluorides resulted from reactions that are varied over a range of stoichiometry and temperature (conditions 6-14) in Table 5.1. In these cases, the products especially tend to be sensitive toward the acidity of the mineralizer, the reaction temperature, and the K:Hf ratio in the reaction. This sensitivity is reflected in the chemical formulae of the products and is not entirely surprising since the mineralizer serves as both the solvent and the sole source of the alkali metal ions. When an acidic mineralizer (such as KHF_2) is used, the oxyfluoride compound $\text{K}_2\text{Hf}_3\text{OF}_{12}$ (**3**) is synthesized, but it only forms from the lowest mineralizer concentrations (K:Hf < 1:1). Potassium-richer phases such as K_2HfF_6 and K_3HfF_7 were synthesized as phase pure products from K:Hf ratios of 2:1 to 9:1, and K:Hf > 9:1, respectively. In contrast, mineralizing with KF (conditions 9-14) leads to a different set of compounds with sensitivity toward reaction temperature. At 400 °C (conditions 12-14), the oxyfluoride elpasolite phase K_3HfOF_5 (**4**) is the one that forms regardless of the K:Hf ratio. When the same reactions are performed at 575 °C (conditions 9-11), anhydrous K_2HfF_6 forms from K:Hf < 1:1 and K_3HfF_7 forms at K:Hf ratios above 6:1.

Table 5.1. Specific reaction conditions for the syntheses of some alkali hafnium fluorides

Condition	Temp. (°C)	Mineralizer	Alkali:Hf Ratio	Pressure (kbar)	Time (days)	Crystal Shape(s)	Compound
1	575	4 M LiF	4.1:1	1.2	6	Plates	Li ₂ HfF ₆ ($P\bar{3}1m$) (1)
2	400	4 M LiF	4.1:1	0.10	5	Plates	1
3	400	9 M LiF	9.2:1	0.10	3	Plates	1
4	400	4 M NaF	4.1:1	0.10	6	Plates, Polyhedra	Na ₅ Hf ₂ F ₁₃ ($C2/m$) (2), Na ₃ HfF ₇ ($Fm\bar{3}m$)
5	400	9 M NaF	9.2:1	0.10	3	Plates, Polyhedra	2 , Na ₃ HfF ₇ ($Fm\bar{3}m$)
6	400	1 M KHF ₂	1:1	0.10	5	Polyhedra	K ₂ Hf ₃ O ₁₂ ($R\bar{3}m$) (3)
7	400	2 M KHF ₂	2:1	0.10	4	Square Rods	K ₂ HfF ₆ ($C2/c$)
8	400	9 M KHF ₂	9.2:1	0.10	1	Square Rods, Polyhedra	K ₂ HfF ₆ ($C2/c$), K ₃ HfF ₇ ($Fm\bar{3}m$)
9	575	1 M KF	1:1	1.2	5	Needles	K ₂ HfF ₆ ($Cmcm$)
10	575	6 M KF	6.1:1	1.2	7	Polyhedra	K ₃ HfF ₇ ($Fm\bar{3}m$)
11	575	9 M KF	9.2:1	1.2	1	Polyhedra	K ₃ HfF ₇ ($Fm\bar{3}m$)
12	400	1 M KF	1:1	0.10	3	Polyhedra	K ₃ HfO ₅ ($Fm\bar{3}m$) (4)
13	400	6 M KF	6.1:1	0.10	6	Polyhedra	4
14	400	9 M KF	9.2:1	0.10	3	Polyhedra	4
15	400	1 M RbF	1:1	0.10	3	Hex. Rods, Polyhedra	Rb ₅ Hf ₄ F ₂₁ •3H ₂ O ($C2/c$), Rb ₂ HfF ₆ ($P\bar{3}m1$)
16	400	2 M RbF	2:1	0.10	7	Polyhedra	Rb ₂ HfF ₆ ($P\bar{3}m1$)
17	575	2 M CsF	2:1	1.2	4	Hex. Rods, Plates	Cs ₂ HfF ₆ ($P\bar{3}m1$)
18	575	6 M CsF	6.1:1	1.2	5	Hex. Rods	Cs ₂ HfF ₆ ($P\bar{3}m1$)
19	400	6 M CsF	6.1:1	0.10	5	Hex. Rods, Plates	Cs ₂ HfF ₆ ($P\bar{3}m1$)
20	400	1 M NH ₄ F	1:1	0.10	3	Polyhedra	(NH ₄) ₃ HfO ₅ ($Fm\bar{3}m$) (5)
21	575	1 M NH ₄ F	1:1	1.2	4	Polyhedra	5
22	575	6 M NH ₄ F	6.1:1	1.2	5	Polyhedra	5
23	400	6 M NH ₄ F	6.1:1	0.10	4	Polyhedra	5
24	400	9 M NH ₄ F	9.2:1	0.10	3	Polyhedra	5

The formation of rubidium hafnium fluorides seems to be largely affected by adjusting the concentration of the mineralizer (conditions 15 and 16). Rb:Hf ratios smaller than 1:1 indicate favorable formation of the hydrated phase $\text{Rb}_5\text{Hf}_4\text{F}_{21}\cdot 3\text{H}_2\text{O}$, whereas Rb:Hf ratios of 1:1 and larger are favorable for the formation of trigonal Rb_2HfF_6 . Much like the potassium-hafnium system the relative ratio of Rb:Hf in the reaction is reflected in the final products in this system as well. The cesium and ammonium hafnium fluorides systems did not exhibit such variety and appear unaffected by changes in reaction temperature or mineralizer concentrations. Regardless of the reaction conditions, only Cs_2HfF_6 and $(\text{NH}_4)_3\text{HfOF}_5$ have been observed in our study.

Crystal Structure Discussion

Data from the single crystal structure refinements of new hafnium fluoride materials are given in Table 5.2 and their selected bond distances are listed in Table 5.3. The following is a discussion of these new hafnium fluorides.

*Crystal Structure of Li_2HfF_6 (**1**)*

Among the alkali hafnium fluorides having the A_2HfF_6 formulation synthesized during this study we emphasize the structure of Li_2HfF_6 (**1**) since this work represents to our knowledge the first single crystal structure determination of a ternary lithium hafnium fluoride. Like the isostructural zirconium fluoride,²⁰ the structure of **1** was determined in space group $\text{P}\bar{3}1m$ (no. 162) as opposed to $\text{P}\bar{3}m1$ (no. 164) in which the A_2HfF_6 structures based on Rb and Cs crystallize, or any of the several space groups (including

$\bar{P}3m1$) adopted by the polymorphs of K_2HfF_6 .¹⁰ All atoms are located on special positions, with Hf1 having $\bar{3}1m$ symmetry, Li1 having 312 symmetry and F1 having m symmetry.

Table 5.2. Crystallographic Data for Structures **1 – 5**

	1	2	3	4	5
Chemical Formula	Li_2HfF_6	$Na_5Hf_2F_{13}$	$K_2Hf_3OF_{12}$	K_3HfOF_5	$(NH_4)_3HfOF_5$
F.W. (g/mol)	306.37	718.93	857.67	1626.92	1325.84
Space group	$\bar{P}31m$	$C2/m$	$R\bar{3}m$	$Fm\bar{3}m$	$Fm\bar{3}m$
Temp./K	293±2	293±2	293±2	293±2	293±2
Crystal system	Trigonal	Monoclinic	Trigonal	Cubic	Cubic
a, Å	4.9748 (7)	11.627 (2)	7.6486 (11)	8.9766 (10)	9.4144 (11)
b, Å		5.5159 (11)			
c, Å	4.6449 (9)	8.4317 (17)	28.802 (6)		
β , °		97.46 (3)			
V, Å ³	99.55 (3)	536.19 (19)	1459.2 (4)	723.33 (14)	834.41 (17)
Z	1	2	6	1	1
D _{cal} , Mg/m ³	5.110	4.453	5.856	3.735	2.639
Indices (min)	[-5, -6, -5]	[-14, -6, -10]	[-9, -9, -35]	[-9, -10, -11]	[-11, -11, -11]
(max)	[6, 5, 5]	[14, 6, 10]	[9, 9, 35]	[10, 10, 10]	[11, 11, 11]
Parameters	12	55	41	8	8
F(000)	132	632	2220	728	584
μ , mm ⁻¹	26.231	19.713	32.956	16.170	12.535
2 θ range, °	4.39 – 26.30	2.44 – 26.33	3.16 – 26.32	3.93 – 26.04	3.75 – 26.12
Collected Reflns.	935	2418	4618	1616	1929
Unique Reflns.	89	597	414	56	66
Final R (obs. data), ^a	0.0319	0.0181	0.0269	0.0290	0.0259
wR ₂	0.0770	0.0449	0.0694	0.0833	0.0619
Final R (all data), R ₁	0.0319	0.0184	0.0271	0.0290	0.0259
wR ₂	0.0770	0.0451	0.0695	0.0833	0.0619
Goodness of fit (S)	1.215	1.164	1.294	1.386	1.291
Extinction Coeff.	0.23 (6)	0.0210 (9)	0.00046 (5)	0.0026 (11)	0.058 (12)
Largest diff. peak	3.008	1.233	3.137	1.500	0.997
Largest diff. hole	-2.662	-1.447	-2.926	-0.986	-0.522

$$^a R_1 = [\sum ||F_o| - |F_c||] / \sum |F_o|; wR_2 = \{[\sum w[(F_o)^2 - (F_c)^2]^2]\}^{1/2}$$

The structure consists of hexagonal closest packing of F⁻ with Li⁺ and Hf⁴⁺ occupying octahedral holes between every other layer in a 2:1 ratio, which forms a three

Table 5.3. Selected Bond Distances (Å) with esds for Compound **1** – **5**

Li ₂ HfF ₆ (1)		Na ₅ Hf ₂ F ₁₃ (2)		K ₂ Hf ₃ OF ₁₂ (3)	
Bond Distances (Å)		Bond Distances (Å)		Bond Distances (Å)	
Hf1—F1 (x6)	2.017 (9)	Hf1—F1 (x2)	2.059 (3)	Hf1—F1 (x2)	2.187 (4)
Li1—F1 (x6)	2.022 (6)	Hf1—F2 (x2)	2.045 (3)	Hf1—F2 (x2)	2.133 (3)
		Hf1—F3 (x2)	2.031 (3)	Hf1—F3 (x2)	2.1321 (14)
		Hf1—F4	2.1070 (6)	Hf1—F4	1.975 (7)
		Na1—F1 (x2)	2.410 (4)	Hf1—O1	2.053 (2)
		Na1—F2 (x2)	2.394 (4)	K1—F1 (x3)	2.788 (7)
		Na1—F2 (x2)	2.440 (4)	K1—F4 (x3)	2.679 (7)
		Na1—F3 (x2)	2.516 (4)	K2—F3 (x6)	3.057 (6)
		Na2—F2 (x4)	2.302 (3)	K2—F4 (x6)	2.698 (7)
		Na2—F3 (x4)	2.600 (3)	K3—F1 (x6)	3.079 (7)
		Na3—F1 (x2)	2.301 (4)	K3—F2 (x6)	2.678 (6)
		Na3—F1 (x2)	2.389 (4)		
		Na3—F3 (x2)	2.301 (4)		
K ₃ HfOF ₅ (4)		(NH ₄) ₃ HfOF ₅ (5)			
Bond Distances (Å)		Bond Distances (Å)			
Hf1—F1 (x5)	1.953 (19)	Hf1—F1 (x5)	1.957 (14)		
Hf1—O1	1.953 (19)	Hf1—O1	1.957 (14)		
K1—F1 (x5)	2.535 (19)	N1—F1 (x5)	2.750 (19)		
K1—O1	2.535 (19)	N1—O1	2.750 (19)		
K2—F1 (x10)	3.1870 (18)	N2—F1 (x10)	3.352 (18)		
K2—O1 (x2)	3.1870 (18)	N2—O1 (x2)	3.352 (18)		

dimensional layered framework of [LiF₆]⁵⁻ and [HfF₆]²⁻ octahedra. Only small angular departures from an ideal octahedron are present, with F-Li-F angles ranging from 87.8 (7) – 91.2 (4)° and F-Hf-F angles ranging from 89.3 (5) – 90.7 (5)°. The lithium fluoride octahedra propagate by edge sharing and form sheets perpendicular to the *c* axis. The sheets contain hexagonal gaps with which isolated [HfF₆]²⁻ octahedra are aligned (Figure 5.2a) in another layer. These isolated hafnium atoms are located in a separate layer sandwiched between lithium fluoride sheets (Figure 5.3a). The two layers are connected by corner sharing of fluoride ions. There is only a small difference in the unit cell parameters of **1** (vol. = 99.37 (3) Å³) compared to the zirconium analog (vol. = 99.77 Å³), with a 0.4% contraction along the *c* axis differentiating the lithium hafnium fluoride.

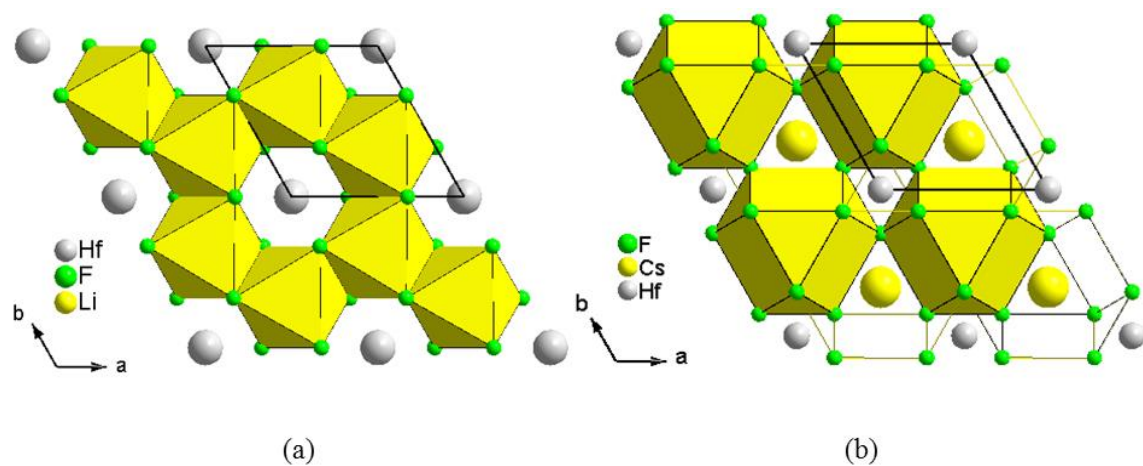


Figure 5.2. Structure of Li_2HfF_6 (a) as compared to Cs_2HfF_6 (b) viewed along $[001]$, with some Cs polyhedra removed for clarity. Li atoms form $[\text{LiF}_6]^{5-}$ polyhedra, whereas Cs atoms form $[\text{CsF}_{12}]^{11-}$ polyhedra.

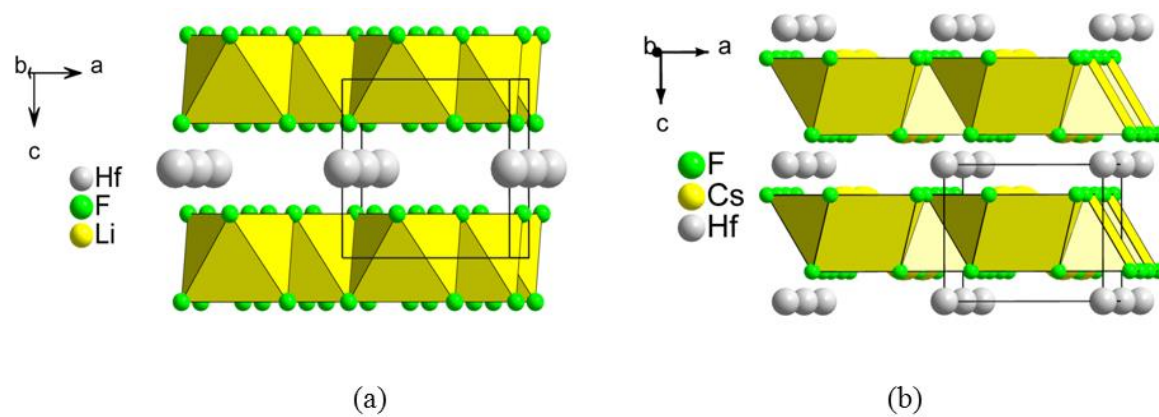


Figure 5.3. Layers of hafnium atoms sandwiched between $[\text{LiF}_6]^{5-}$ polyhedra in Li_2HfF_6 (a) and $[\text{CsF}_{12}]^{11-}$ polyhedra in Cs_2HfF_6 (b) viewed off $[010]$.

As previously reported by Bode and Teufer,⁴ the heavier alkali hafnium and alkali zirconium fluorides based on Rb and Cs have a different structure type than their lithium counterparts, crystallizing in space group $P\bar{3}m1$. The present work has confirmed these structure determinations using our own crystals, and these data are reported as supporting information (Appendix B), as improved R_1 values of 0.0368 (Rb_2HfF_6) and 0.0421 (Cs_2HfF_6) compared to their reports ($R_1 = 0.102$ for both Rb_2HfF_6 and Cs_2HfF_6) have been obtained. While it is not surprising that the Rb and Cs structures have a different layer arrangement than **1** {considering both have a mixed AF_3 (A = Cs, Rb) layer packing, stacking in the cubic closest fashion with one sixth of the Hf^{4+} occupying the octahedral holes to form sheets of $[\text{AF}_{12}]^{11-}$ polyhedra in a layered structure with isolated $[\text{HfF}_6]^{2-}$ octahedra, see Figure 1} it is interesting to note that the trend of lattice contraction for Li_2HfF_6 relative to Li_2ZrF_6 is mirrored in Rb_2HfF_6 and Cs_2HfF_6 relative to their zirconium analogs. In those systems the unit cell volumes of the hafnium analogs are contracted by 0.6% relative to the zirconium compounds.

*Crystal Structure of $\text{Na}_5\text{Hf}_2\text{F}_{13}$ (**2**)*

Compound **2** crystallizes in the monoclinic space group $C2/m$ (No. 12). Powder X-ray data simulated from our structure determination match a previously reported powder pattern for which no space group was determined. The material for the original powder pattern was assigned a nominal formulation of $2 \text{HfF}_4 \cdot 5 \text{NaF}$ based on the melt composition from which it was prepared.¹⁵ The structure of **2** is also isostructural to a formulation of $\text{Na}_5\text{Zr}_2\text{F}_{13}$ that was found to crystallize in the same space group.²¹

However, this is believed to be the first single crystal structure determination performed on a ternary sodium hafnium fluoride (the structure of Na_3HfF_7 was previously derived from X-ray powder films).¹² The crystallographically unique hafnium atom forms a seven-coordinate slightly distorted square face monocapped trigonal prism with average Hf-F distances of 2.054 (3) Å for Hf1, which correlates well with the expected value predicted by Shannon.²² The occurrence of seven-coordinate hafnium atoms tends to be limited to pentagonal bipyramidal geometries in other alkali hafnium fluorides.^{6,8} This phase contains Hf1, Na1, Na2, Na3, and F4 atoms in special positions; Hf1, Na1, and Na3 have *m* symmetry and both Na2 and F4 have *2/m* symmetry.

In compound **2**, pairs of seven-coordinate hafnium atoms are arranged where their caps face each other, and they corner share F4 to form a $[\text{Hf}_2\text{F}_{13}]^{5-}$ arrangement (see Figure 5.4). Bonds to the bridging atom F4 are slightly elongated (2.1070 (6) Å), compared to the average of the other Hf-F bonds which bridge to Na atoms (2.045 (3) Å). The pairs of Hf-F polyhedra are both edge and corner sharing with Na-F polyhedra that form a channel containing the Hf-F polyhedra. This channel is different from those of the recently reported alkali thorium fluorides¹⁶⁻¹⁸ in that the tetravalent Hf, rather than the alkali metal, is contained by the channel. It may be that the smaller radius of Na (and its similar radius to Th) compared to Rb and Cs in the thorium fluorides lends itself more toward formation of the framework. The channel is shaped like an elongated hexagon when viewed along the *b* axis (Figure 5.4b), measuring 7.48 (9) Å in length and 3.05 (2) Å in diameter. Thus the $[\text{Hf}_2\text{F}_{13}]^{5-}$ units are a rather snug fit in the channel. A three dimensional framework of Na-F bonding fills out the remainder of the space in the

structure and serves to connect the $[\text{Hf}_2\text{F}_{13}]^{5-}$ units. Three unique sodium atoms exist: Na1 and Na2 are distorted square prisms, while Na3 is in a six-coordinate trigonal prismatic coordination. The edges of the distorted square prisms range from 2.542 (16) Å to 3.02 (3) Å in length for Na1, and 2.55 (4) Å to 3.05 (2) Å in length for Na2. Comparison to the analogous zirconium structure^{21,23} indicates slightly longer unit cell axes and larger cell volume for **2**, which is to be expected considering the small difference in atomic diameter between zirconium (1.80 Å) and hafnium (1.84 Å) as described by Shannon.²²

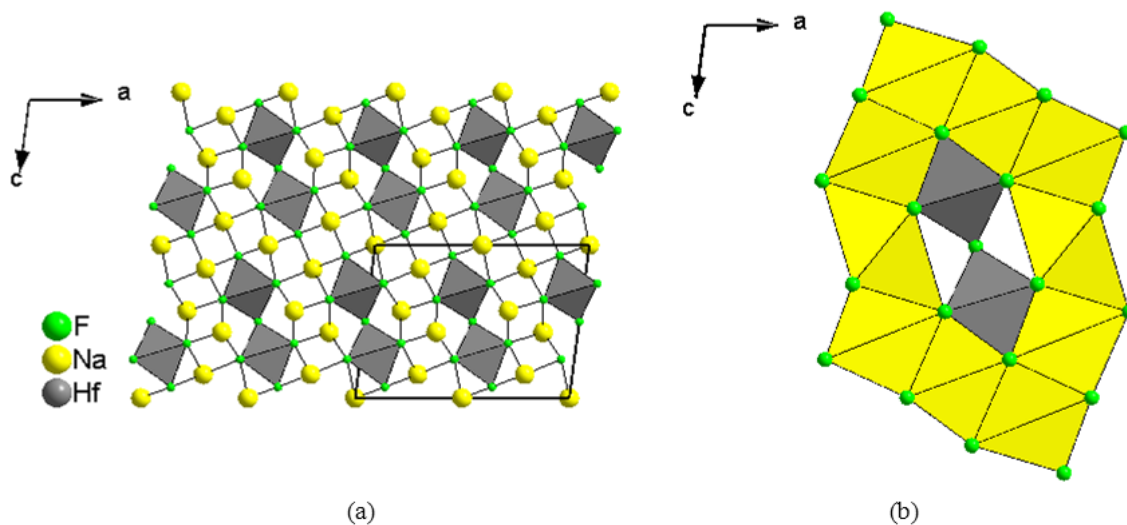


Figure 5.4. (a) Structure of $\text{Na}_5\text{Hf}_2\text{F}_{13}$ viewed along $[010]$. (b) Space filling polyhedral view of an isolated $[\text{Hf}_2\text{F}_{13}]^{5-}$ unit surrounded by a channel of sodium fluoride polyhedra.

*Crystal Structure of $\text{K}_2\text{Hf}_3\text{OF}_{12}$ (**3**)*

Compound **3** crystallizes in the trigonal space group $R\bar{3}m$ (No. 166). It is also isostructural to $\text{Rb}_2\text{Zr}_3\text{OF}_{12}$ and $\text{Rb}_2\text{Hf}_3\text{OF}_{12}$ previously found to grow from fluxes of

RbF and HfF₄ in an atmosphere of Ar/HF,⁵ as well as Tl₂Zr₃OF₁₂ grown from a melt of TlF, ZrF₄, and ZrO₂²⁴ and K₂Zr₃OF₁₂ grown by microwave-assisted hydrothermal synthesis from ZrF₄ and KOH.²⁵ The crystallographically unique sites consist of eight-coordinate hafnium atoms as [HfOF₇]⁵⁻ units conforming to a distorted square antiprism geometry, with average Hf-F distances of 2.126 (7) Å and a Hf-O distance of 2.053 (2) Å for Hf1. All the crystallographically unique atoms are in special positions; Hf1, F2, F3, and F4 have a mirror plane on the *c* axis, K1 and O1 have 3*m* symmetry, K2 and K3 have $\bar{3}m$ symmetry, and F1 has two-fold rotational symmetry about the *c* axis.

Three [HfOF₇]⁵⁻ polyhedra share F4-O1 edges to form [Hf₃OF₁₈] clusters. All three polyhedra in the cluster share the central O1 atom, and thus the observed Hf-O bond distance is slightly shorter (2.053 (2) Å) than one may expect due to this geometrical restriction. The triangular central oxygen atom is just slightly out of plane with the hafnium atoms allowing Hf-O-Hf angles to be slightly distorted at 115 (2)°. Clusters propagate by corner sharing of F3 atoms to form hafnium oxyfluoride layers in the *ab* plane. A second series of hafnium oxyfluoride clusters is joined to this first series along the *c* axis in staggered fashion by edge sharing pairs of F1 atoms, making the hafnium oxyfluoride layer two polyhedra thick along [001] (see Figure 5.5). The staggered arrangement creates gaps within these layers that are occupied by 12-coordinate K3 atoms. This arrangement of clusters is shown in Figure 5.6. Here K3 exhibits six longer (3.089 (7) Å) and six shorter (2.678 (6) Å) bonds to F1 and F2, respectively. The K3 atoms in these gaps are not completely enclosed by hafnium oxyfluoride polyhedra, as

K3 is face sharing with K1 atoms above and below the hafnium oxyfluoride layer through the long bonds to F1 atoms.

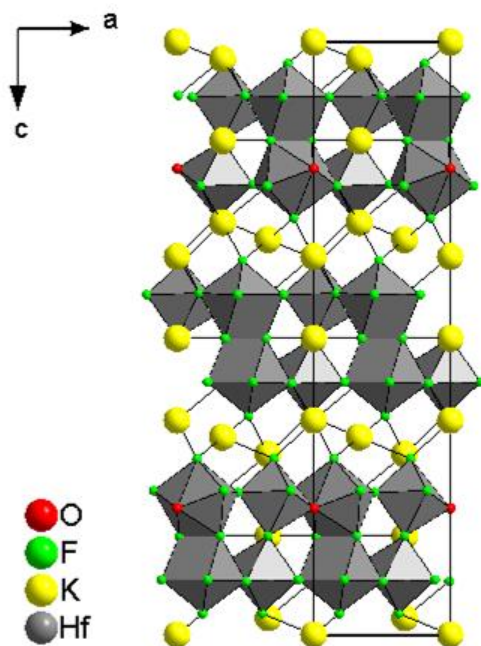


Figure 5.5. Layered structure of $K_2Hf_3OF_{12}$ viewed along $[010]$.

Sandwiched between the hafnium oxyfluoride layers are K1 and K2 atoms. These potassium atoms form their own layer (see Figures 5.5 and 5.6) that propagates by corner sharing of F4 atoms. Atoms F1, F3 and F4 connect K1 and K2 to hafnium atoms by corner sharing of F1 and F4 for K1 and by two F3 and one F4 atoms in face sharing fashion for K2. Thus atom F4 is centered about a planar triangle, making connections to laterally propagate the K1/K2 layer, while also connecting this layer to the hafnium oxyfluoride layer. At 1.975 (7) Å the Hf1-F4 bond is slightly shorter than usual, but similar in length to the connecting bonds in $Rb_2Zr_3OF_{12}$ and $Rb_2Hf_3OF_{12}$. In general the

hafnium oxyfluoride network appears to be quite rigid as there is very little difference between Hf-O and Hf-F bonding in **3** and the analogous $\text{Rb}_2\text{Hf}_3\text{OF}_{12}$. As a result, only about a 1% shortening of the alkali-fluoride bond distances at the K3 site in **3** occur compared to the analogous Rb site in $\text{Rb}_2\text{Hf}_3\text{OF}_{12}$ since this site is confined within the hafnium oxyfluoride layers. The K1 and K2 sites however exhibit a 4% shortening of the alkali-fluoride bond distances compared to the analogous Rb sites, as these serve primarily as spacers for the hafnium oxyfluoride layers. This also accounts for the uneven contraction of the unit cell, where the *a* and *b* axes are contracted by 0.6% (7.648 (1) vs. 7.692 (1) Å), whereas the *c* axis (being more influenced by the spacing between hafnium oxyfluoride layers), is contracted by about 3.5% (28.802 (6) vs. 29.861 (6) Å) for **3** compared to $\text{Rb}_2\text{Hf}_3\text{OF}_{12}$.

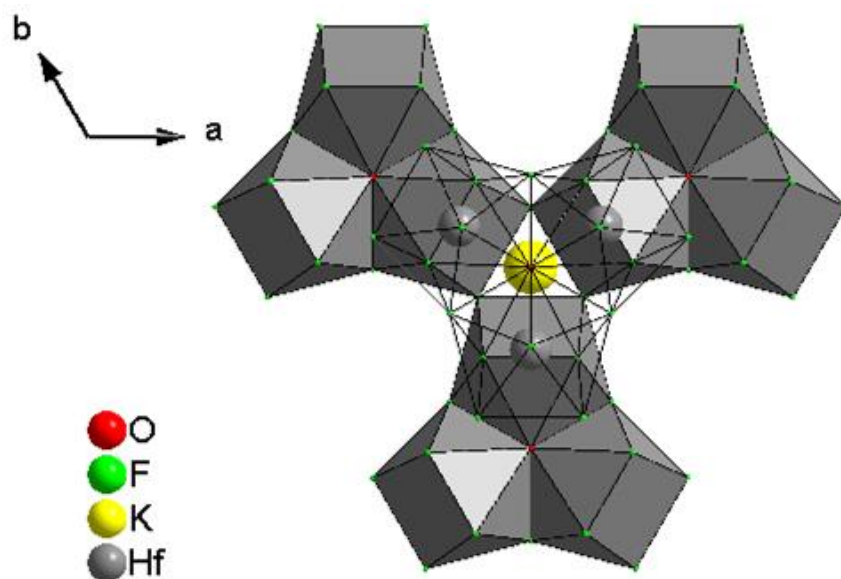


Figure 5.6. Staggered arrangement of $[\text{Hf}_3\text{OF}_{18}]$ clusters with gaps accommodating K3 atoms in $\text{K}_2\text{Hf}_3\text{OF}_{12}$.

Crystal Structures of K_3HfOF_5 (4) and $(NH_4)_3HfOF_5$ (5)

Another interesting class of oxyfluoride crystals is those crystallizing in the cubic elpasolite structure (space group $Fm\bar{3}m$). Titanium- and zirconium-based compounds of this type have been previously explored,²⁶⁻²⁹ but to our knowledge no structures of any hafnium-based oxyfluoride elpasolites have been reported. The elpasolite structure, based on the mineral K_2NaAlF_6 , is a versatile structure type which commonly supports a variety of chemical substitution at the alkali metal and aluminum sites, and fluoroelpasolites are known to crystallize from hydrothermal solutions.^{29,30} In the present study of new hafnium containing elpasolites, EDX was first used to distinguish the composition of the crystals obtained from those of the disordered fluoride K_3HfF_7 , having a related structure with two fluoride ions partially occupying 96j sites.⁸ Elemental analysis always indicated the presence of oxygen at 6.5-9.1 at.% and fluorine present at 51.0-53.6 at.% supporting a composition of A_3HfOF_5 rather than A_3HfF_7 . It should be noted that attempts to solve the structures as A_3HfF_7 resulted in R_1 values as low as 0.0103, but consecutive refinements do not converge. In light of this, the structures were treated as oxyfluoride elpasolites.

A number of different crystallographic models have been determined for the titanium and zirconium oxyfluorides and peroxyfluorides of this structure type, where substitution of a tetravalent ion at the trivalent site in elpasolite requires oxygen substitution for fluorine to maintain charge balance. The first model is a simple substitutional disorder where the fluorine site (Wyckoff 24e) is $5/6$ occupied by fluorine and $1/6$ occupied by oxygen.^{28,31} Models involving more complex orientational disorder

(having partially occupied fluorine atoms at 24e and 96j sites with substitutional oxygen disorder at one or both of those sites) have also been used to describe the structures of $(\text{NH}_4)_3\text{TiOF}_5$ and $\text{Rb}_2\text{KTiOF}_5$.^{26,27} These models sometimes also involve disorder and partial occupancy at the alkali metal site. In another disordered structure type, the oxygen atom is assigned $1/12$ occupancy at a 96k or 96j site different from any of the fluorine sites in the structure. This occupancy and arrangement corresponds to a peroxy group with O-O separation of 1.5 - 1.7 Å, resulting in a formula of $\text{K}_3\text{Ti}(\text{O}_2)\text{F}_5$, for example.³²⁻³⁴ These related peroxyfluoro-elpasolites are also distinguishable by slightly larger unit cell parameters than the similar oxyfluoro-elpasolites.

The potassium and ammonium ions in **4** and **5** were observed to be fully-ordered at 4b and 8c Wyckoff sites, having $m\bar{3}m$ and $\bar{4}3m$ site symmetries, respectively. The fluorine atom is present at the 24e site. Using the substitutional model ($5/6$ F and $1/6$ O at the 24e site) the R_1 values were 0.0289 and 0.0259 for the potassium and ammonium analogs, respectively. Any residual electron density appears concentrated at a 48i position 1.56 Å away from the 24e position. While a scheme of $1/12$ O occupancy at 48i and $5/6$ F occupancy at 24e satisfies charge balance and lowers the R_1 values (0.0197 and 0.0176 for K_3HfOF_5 and $(\text{NH}_4)_3\text{HfOF}_5$, respectively), it results in seven-coordinate K1 and eleven-coordinate K2 atoms in addition to the close O-F contact. Thus the model of $5/6$ fluorine and $1/6$ oxygen occupancy at the 24e site appears to make the most chemical sense for the data collected and corresponding elemental analysis. The structures could be refined where potassium or ammonium ions were subject to partial occupancy at lower symmetry sites (as described by Udovenko and coworkers^{26,27}), but the resulting R_1

values were slightly higher than when atoms were assigned full occupancy in the higher symmetry sites. Disordering of the fluorine and oxygen occupancies was also attempted between the 24e site and a 96j site (also described by Udovenko and coworkers^{26,27}), but these refinements were unsuccessful. The resulting elpasolite structures feature six-coordinate hafnium atoms having identical bond distances (within the esd) for both the potassium and ammonium analogs. The monovalent cations are both six- and twelve-coordinate.

IR Spectroscopy

IR spectra were obtained for the hafnium fluorides synthesized in this study to confirm the solutions for the title compounds and determine their Hf⁴⁺ coordination environments. Figure 5.7 displays the trends that were observed for these compounds. A broad stretch was observed between 3200-3500 cm⁻¹ for Rb₅Hf₄F₂₁•3H₂O, confirming the presence of a hydrated species in the compound (see Figure 5.8). The absence of a broad stretch between 3200-3500 cm⁻¹ for oxyfluorides **3**, **4**, and **5** confirms the lack of hydroxides in their structures. All the compounds display Hf-F stretches between 460-480 cm⁻¹, as was observed for other alkali hafnium fluorides.³⁵ Upon closer inspection, longer Hf-F bond distances result in lower stretching energy as is seen with Rb₂HfF₆ where $\nu = 487$ cm⁻¹ (Figure 5.7(a), Hf-F bond distance of 2.01 Å) and Na₅Hf₂F₁₃ where $\nu = 468$ cm⁻¹ (**2**, Figure 5.7(b), Hf-F bond distance of 2.03-2.11 Å). The oxyfluorides also displayed typical Hf-O stretches that have been reported for hafnium oxides.³⁶ K₂Hf₃OF₁₂ (**3**, Figure 5.7(c)) shows all the distinctive Hf-O stretches: $\nu = 792, 692, 554,$

and 421 cm^{-1} . Fluoroelpasolites **4** and **5** show a separate Hf-O stretch around 430 cm^{-1} (similar to Figure 5.7(d)), further confirming their structure solutions. The other Hf-O stretches are not observed due to the oxygen and fluorine substitutional disorder of the fluoroelpasolite structure. Fluoroelpasolite **5** also displayed stretches ~ 1400 and 3100 cm^{-1} , typically seen for NH_4^+ -containing compounds (see Figure 5.7(d)).

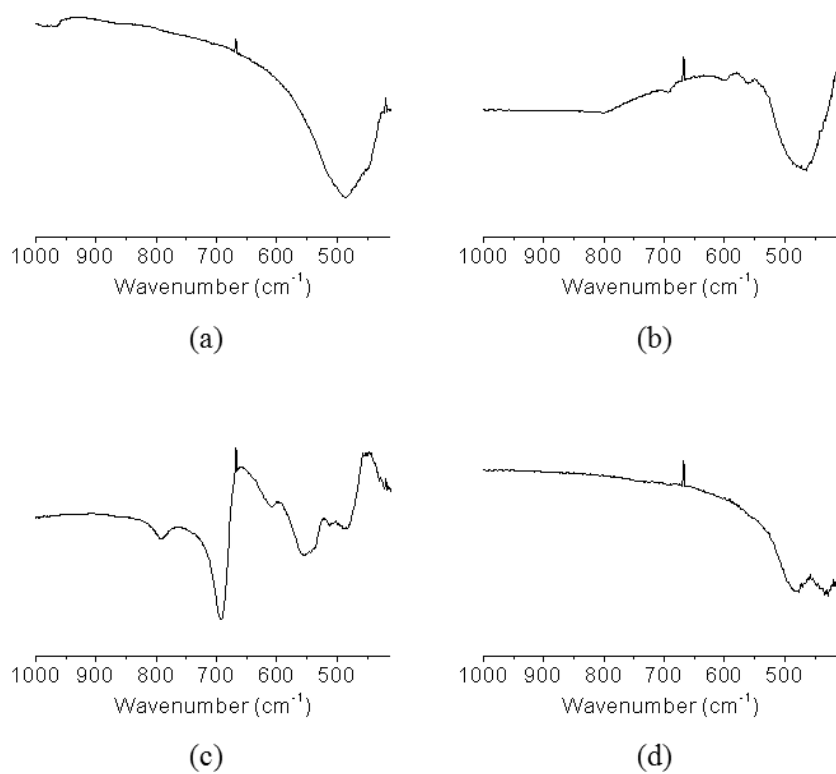


Figure 5.7. IR spectra of (a) Rb_2HfF_6 , (b) compound **2**, (c) compound **3**, and (d) compound **5**.

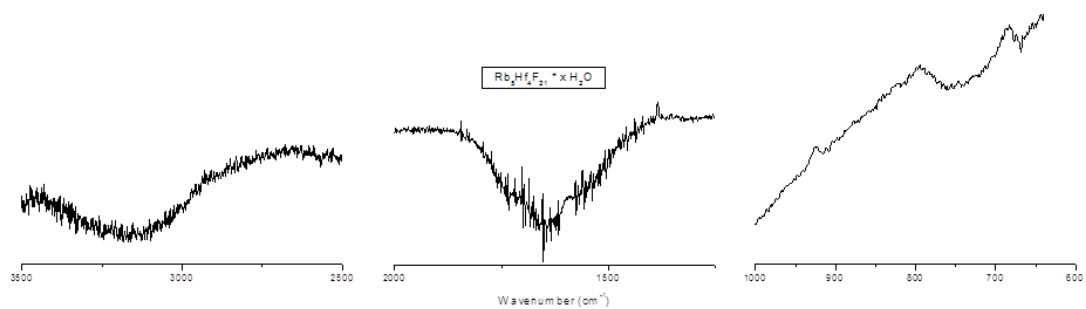


Figure 5.8. IR spectrum of $\text{Rb}_5\text{Hf}_4\text{F}_{21} \cdot 3\text{H}_2\text{O}$.

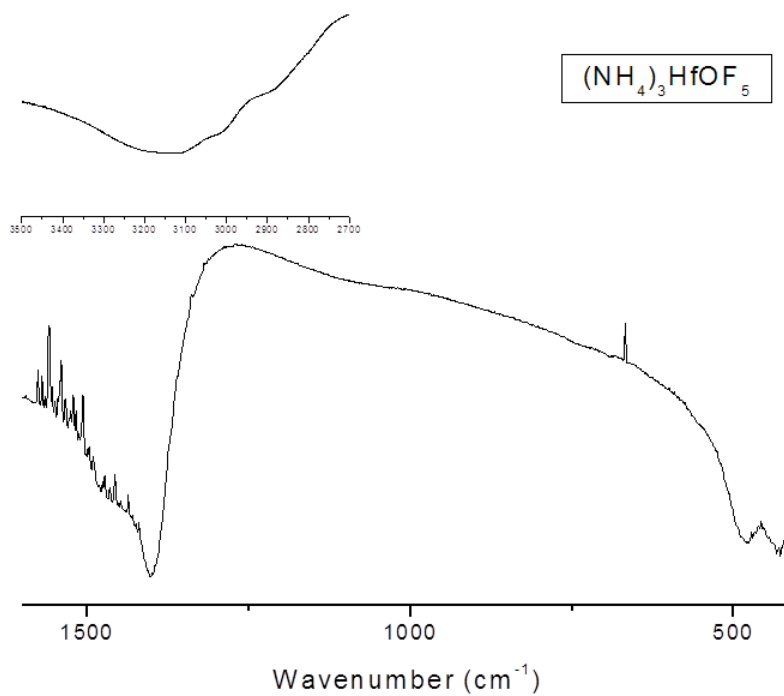


Figure 5.9. Expanded IR spectrum of compound **5**.

X-ray Luminescence Studies

X-ray luminescence studies were also conducted for the alkali hafnium fluorides synthesized in this study. Previous studies showed that hydrated alkali zirconium fluorides and oxyfluorides exhibited strong X-ray luminescence due to the excitation of their luminescent centers to excited states F^* and O^* .¹⁹ Figure 5.10 shows the X-ray luminescence of a number of compounds prepared in this study. Broad luminescence maxima were typically observed. The hafnium-based systems seem to differ significantly from the zirconium-based systems in that the hafnium oxyfluoride, $K_2Hf_3OF_{12}$, exhibits significantly higher luminescence intensity (maximum at 410 nm) than any of the pure fluoride compounds. Interestingly, in the zirconium system intense luminescence was observed for $Rb_2Zr_3OF_{12}$ (at 330 nm), but not $K_2Zr_3OF_{12}$. Luminescence maxima could still be identified in the comparatively weak luminescence data for $Rb_5Hf_4F_{21} \cdot 3H_2O$ (460 nm), Li_2HfF_6 (740 nm), Rb_2HfF_6 (470 nm) and Cs_2HfF_6 (410 nm). We do note that the X-ray source in this study (Ag) is different from that used by Godneva and coworkers (Mo).

As postulated in the previous work¹⁹ the structural complexity in the number of different types of bridging bonds is a likely contributor to their luminescence. This could explain why $K_2Hf_3OF_{12}$, with four types of bridging oxide and fluoride bonds creating a continuous hafnium oxyfluoride layer has a relatively strong X-ray luminescence. As a secondary contributor, coordination number (CN) about the hafnium atoms may also play a role. We note marginally higher luminescence intensities from $Rb_5Hf_4F_{21} \cdot 3H_2O$ which

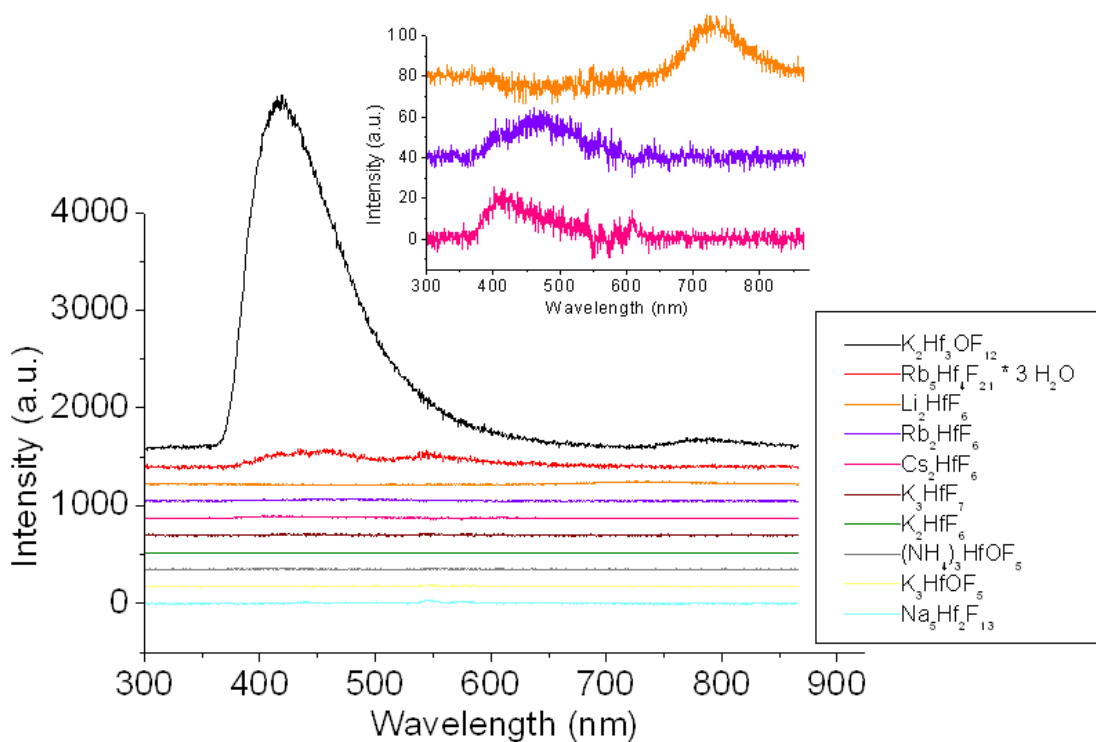


Figure 5.10. X-ray luminescence of the title compounds. The compounds are listed in the order of intensity (most to least) from top to bottom. The spectra were displaced vertically to facilitate their comparison.

contains both $[\text{HfF}_7\text{OH}_2]^{3-}$ and $[\text{HfF}_7]^{3-}$ polyhedra. Those compounds with six-coordinate hafnium (as $[\text{HfOF}_5]^{3-}$ or $[\text{HfF}_6]^{2-}$) exhibited very weak, or no luminescence. $\text{Na}_5\text{Hf}_2\text{F}_{13}$, having seven-coordinate hafnium atoms connected by a single Hf-F-Hf bridge (the $[\text{Hf}_2\text{F}_{13}]^{5-}$ unit) likewise elicited only a weak signal.

A comparison of the A_2HfF_6 compounds also gave us insight into the effects that both alkali metal size and crystallographic symmetry played in X-ray luminescence. The inset in Figure 5.10 displays a comparison between compound Li_2HfF_6 , Rb_2HfF_6 , and Cs_2HfF_6 , which shows that the luminescence maxima shift to lower energies with

decreasing alkali metal size. However, Li_2HfF_6 exhibits slightly greater luminescence intensity than its Cs and Rb counterparts. This is perhaps due to the crystallographic differences between them; Cs_2HfF_6 and Rb_2HfF_6 contain $[\text{CsF}_{12}]^{11-}$ and $[\text{RbF}_{12}]^{11-}$ polyhedra in a layered structure with $[\text{HfF}_6]^{2-}$ octahedra as compared to the layered framework of $[\text{LiF}_6]^{5-}$ and $[\text{HfF}_6]^{2-}$ octahedra in compound Li_2HfF_6 . Comparing the luminescence of the three trigonal compounds to the negligible luminescence from orthorhombic K_2HfF_6 could indicate improved luminescence with higher symmetry in this particular family of compounds.

Visible Luminescence Studies

Visible luminescence studies were also conducted for the alkali hafnium fluorides synthesized in this study. Previous studies showed that hafnium compounds of the type Cs_2HfX_6 ($\text{X} = \text{Cl}, \text{Br}, \text{I}$) exhibit significant luminescence in the visible region,³⁷ while a related hafnium oxide, Li_2HfO_3 , exhibits luminescence in the UV range.³⁸ Figure 5.11 shows the luminescence of a number of compounds prepared in this study using visible excitation. Similarly to the X-ray luminescence, broad emission maxima were typically observed; they are based on the electronic transition of $\text{A}_{1g} \rightarrow \text{T}_{1u}$ that Ackerman observed for his luminescence measurements of alkali hafnium halides at room temperature.³⁷

Comparison of the 2-1-6 structure types shows that trigonal compounds **1**, Rb_2HfF_6 , and Cs_2HfF_6 exhibit both increased luminescence and maxima shifts to higher energies with the decreasing size of the alkali metal. Similar to the observations with

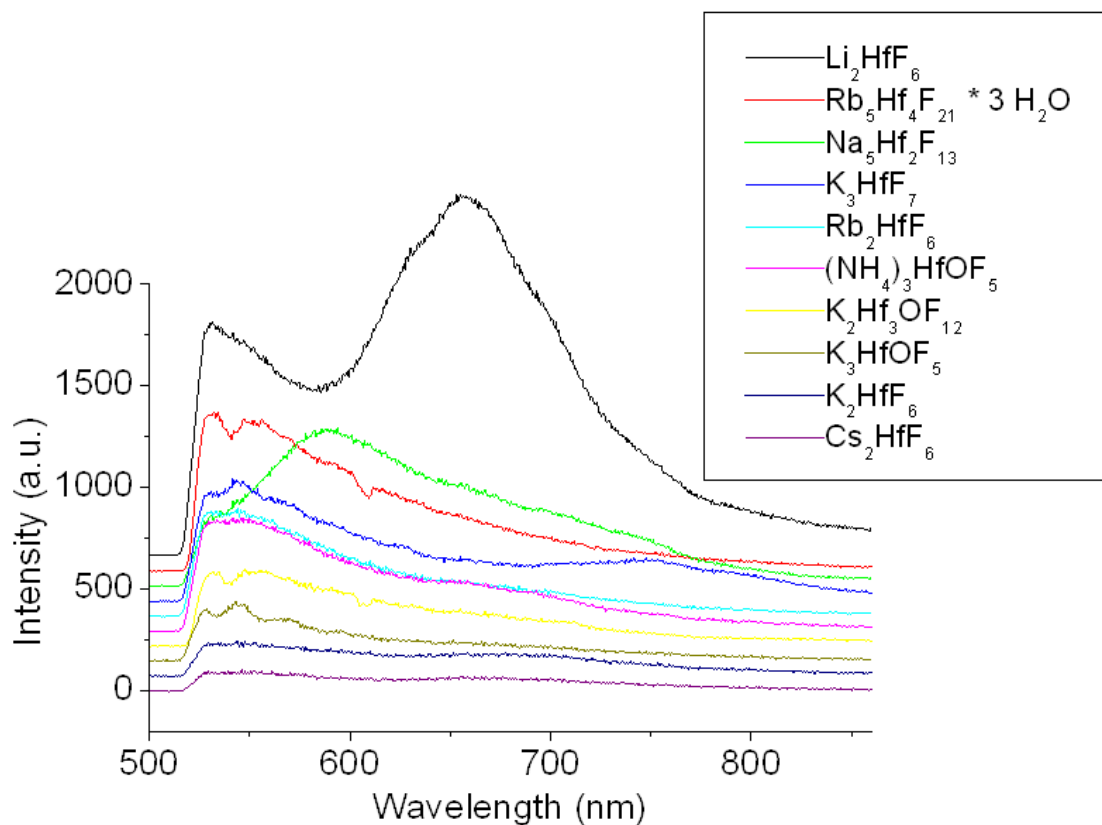


Figure 5.11. Visible fluorescence spectra of the title compounds. The compounds are listed in the order of intensity (most to least) from top to bottom. Emission wavelengths less than 515 nm were cut off with a long pass emission filter. The spectra were displaced vertically to facilitate their comparison.

their X-ray luminescence, compound **1** displays more luminescence than its Cs and Rb counterparts (perhaps again due to the same crystallographic differences described in the previous section) and the intensity of the luminescence tends to increase with decreasing alkali metal size. When comparing these three trigonal compounds to orthorhombic K_2HfF_6 , it also shows that the coordination environment around Hf^{4+} must also be taken

into consideration ($[\text{HfF}_6]^{2-}$ for the trigonal formulations compared to $[\text{HfF}_7]^{3-}$ for the orthorhombic formulation¹⁰), though it may not affect luminescence as significantly. We must note again that we have only seen this trend apply to compounds of the same formulation. Comparing oxygen-containing compounds **3**, **4**, **5**, and $\text{Rb}_5\text{Hf}_4\text{F}_{21}\cdot 3\text{H}_2\text{O}$ shows that only the hydrated compound has significantly more luminescence. The fact that $\text{Rb}_5\text{Hf}_4\text{F}_{21}\cdot 3\text{H}_2\text{O}$ also contains mixed coordination environments for Hf^{4+} ($[\text{HfF}_7]^{3-}$ and $[\text{HfF}_8]^{4-}$) may also factor into its luminescence. Though the coordination environments around the Hf^{4+} for the oxyfluorides differ (disordered $[\text{HfOF}_5]^{3-}$ for **4** and **5**, $[\text{HfOF}_7]^{5-}$ for **3**), it does not seem to affect luminescence. The unexpectedly high luminescence of **2** can also be explained by its Hf^{4+} coordination environment. Of all the alkali hafnium fluorides investigated, only **2** contains corner-sharing $[\text{HfF}_6]^{2-}$ polyhedra, which may drastically alter the luminescence of these compounds. When comparing the luminescence of all the alkali hafnium fluorides used in this study, there does not seem to be a correlation between the group symmetry of the compounds and their luminescence.

CONCLUSIONS

In this Chapter, a variety of diverse chemical results all related to the monovalent hafnium fluorides are described. All the products and chemistry that were elucidated results from hydrothermal reactions. The reactions were performed over a range of stoichiometries and temperatures in an attempt to cover a broad region of phase space. New hafnium fluorides were characterized for all the alkali metals as well as for NH_4^+ (see Figure 5.12). The majority of products were characterized as high quality single

crystals and these provided comparative examples to zirconium where appropriate. In some cases the products are new structures and in others they were reported previously as powder samples made from melts and the single crystal determination is provided here.

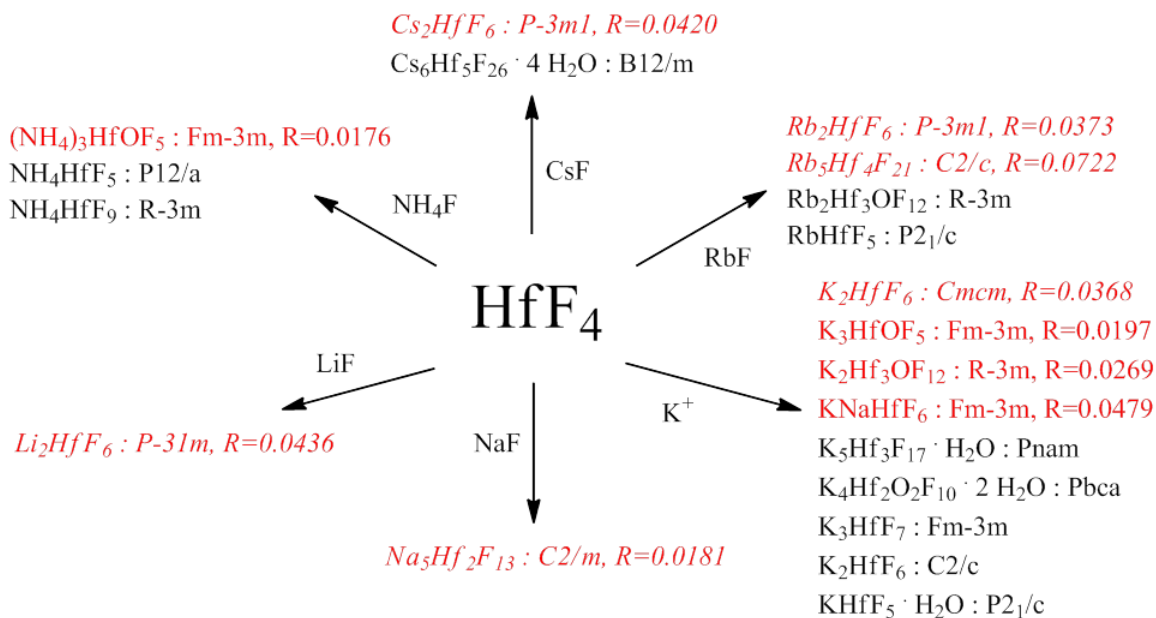


Figure 5.12. Overview of the monovalent hafnium fluorides synthesized using our hydrothermal method. The compounds in black are reported single crystal structures and the compounds in red are new structures. Any compounds in italics have previously-reported powder patterns that were used to confirm the identity of the new materials.

A number of members of the A₂HfF₆ formulation including Li₂HfF₆, which represents to our knowledge the first example of a structure of Li containing hafnium fluoride, were isolated. Interestingly, the isolation of any example of the unknown Na₂HfF₆ formula has shown to be elusive. The heavier analogs of A₂HfF₆ (A = K, Rb,

Cs) were isolated in good yield and are structurally analogous to the previously reported melt reactions. A number of more structurally complex alkali hafnium fluorides such as $\text{Na}_5\text{Hf}_2\text{F}_{13}$ and K_3HfF_7 were also isolated. Although the metal fluoride structural chemistry is not as subtle and complex as our group observed previously in the thorium fluoride system, the chemistry is somewhat richer in the sense that some new hydrolytic oxyfluoride products are observed (such as $\text{K}_2\text{Hf}_3\text{OF}_{12}$, K_3HfOF_5 and $(\text{NH}_4)_3\text{HfOF}_5$) in the hafnium system as well as a known hydrated species ($\text{Rb}_5\text{Hf}_4\text{F}_{21}\cdot 3\text{H}_2\text{O}$). No such oxygen containing examples were observed by our group in the thorium system. In general, the alkali fluoride chemistry is more similar to that of zirconium than thorium.

Given the previous observation that alkali zirconium oxyfluorides demonstrate bright X-ray luminescence, X-ray luminescence was performed on these compounds and also observed bright luminescence for the oxyfluoride $\text{K}_2\text{Hf}_3\text{OF}_{12}$. This is somewhat reminiscent of the observation of bright luminescence of $\text{Rb}_2\text{Zr}_3\text{OF}_{12}$ although the emission is somewhat red shifted for our material (440 nm) vs. 330 nm for the zirconium material. Based on previous observations of visible luminescence for other alkali hafnium halides, visible luminescence studies were also conducted on our compounds, and it was found that Li_2HfF_6 exhibits bright luminescence compared to the other compounds in the study. This shows that changing the alkali metal can also affect both visible luminescence intensity and maxima instead of only changing the halide. The initial luminescence spectroscopy conducted on hafnium fluorides lead to my comparative spectroscopy work with acentric metal borates that are discussed in the next two chapters.

REFERENCES

- (1) Coster, D.; v. Hevesy, G. *Naturwissenschaften* **1923**, *11*, 133-133.
- (2) Itkin, I. Analysis of the Neutron Capture Cross Section and Resonance Integral of Hafnium. In U.S. Government Printing Office: Washington, DC, 1962; Vol. WAPD-TM-324.
- (3) Gerasimenko, A. V.; Bukvetskii, B. V.; Logvinova, V. B.; Davidovich, R. L. *Russ. J. Coord. Chem.* **1991**, *17*, 793-796.
- (4) Bode, H.; Teufer, G. *Z. Anorg. Allg. Chem.* **1956**, *283*, 18-25.
- (5) Koller, D.; Müller, B. G. *Z. Anorg. Allg. Chem.* **2002**, *628*, 575-579.
- (6) Gusev, A. I.; Chuklanova, E. B.; Kuznetsov, V. Y.; Rogachev, D. L. *Russ. J. Inorg. Chem.* **1991**, *36*, 937-938.
- (7) Chernyshov, B. N.; Didenko, N. A.; Bakeeva, N. G.; Bukvetskii, B. V.; Gerasimenko, A. V. *J. Struct. Chem.* **1991**, *36*, 1112-1116.
- (8) Granzin, J.; Saalfeld, H. *Z. Kristallogr.* **1988**, *183*, 71-76.
- (9) Neumann, C.; Saalfeld, H.; Gerdau, E.; Guse, W. *Z. Kristallogr.* **1986**, *175*, 159-164.
- (10) Saalfeld, H.; Guse, W. *Neues Jahr. Miner. Abhand.* **1983**, *146*, 29-40.
- (11) Neumann, C.; Granzin, J.; Saalfeld, H. *Z. Kristallogr.* **1988**, *184*, 221-227.
- (12) Harris, L. *Acta Crystallogr.* **1959**, *12*, 172.
- (13) Plitzko, C.; Meyer, G. *Z. Anorg. Allg. Chem.* **1998**, *624*, 169-170.
- (14) Plitzko, C., Ph.D. Dissertation, Hannover University, Hannover, Germany, 1999.
- (15) Thoma, R. E. Phase Diagrams of Nuclear Reactor Materials. In U.S. Government Printing Office: Washington, DC, 1959; Vol. ORNL-2548.
- (16) Underwood, C. C.; Mann, M.; McMillen, C. D.; Kolis, J. W. *Inorg. Chem.* **2011**, *50*, 11825-11831.
- (17) Underwood, C. C.; Mann, M.; McMillen, C. D.; Musgraves, J. D.; Kolis, J. W. *Solid St. Sci.* **2012**, *14*, 574-579.

- (18) Underwood, C.; McMillen, C.; Kolis, J. *J. Chem. Crystallogr.* **2012**, *42*, 606-610.
- (19) Godneva, M. M.; Motov, D. L.; Boroznovskaya, N. N.; Klimkin, V. M. *Russ. J. Inorg. Chem.* **2007**, *52*, 661-666.
- (20) Hoppe, R.; Dähne, W. *Naturwissenschaften* **1960**, *47*, 397-397.
- (21) Herak, R. M.; Malčić, S. S.; Manojlović, L. M. *Acta Crystallogr.* **1965**, *18*, 520-522.
- (22) Shannon, R. *Acta Crystallogr.* **1976**, *A32*, 751-767.
- (23) Shaoya, M.; Youjun, K.; Jinxiao, M.; Manrong, L.; Zanbin, W.; Xueyan, W.; Thai, Z. J. *Jiegon Huaxue* **2006**, *25*, 173-179.
- (24) Mansouri, I.; Avignant, D. *J. Solid St. Chem.* **1984**, *51*, 91-99.
- (25) Saada, M. A.; Hemon-Ribaud, A.; Maisonneuve, V.; Smiri, L. S.; Leblanc, M. *Acta Crystallogr.* **2003**, *E59*, i131-i133.
- (26) Udovenko, A. A.; Laptash, N. M.; Maslennikova, I. G. *J. Fluorine Chem.* **2003**, *124*, 5-15.
- (27) Udovenko, A. A.; Laptash, N. M. *Acta Crystallogr.* **2011**, *B67*, 447-454.
- (28) Vedrine, A.; Belin, D.; Besse, J. P. *Bull. Soc. Chim. Fr.* **1972**, *1972*, 76-78.
- (29) Goryunov, A. V.; Popov, A. I.; Khajdukov, N. M.; Fedorov, P. P. *Mater. Res. Bull.* **1992**, *27*, 213-220.
- (30) da Fonseca, R. J. M.; Tavares Jr, A. D.; Silva, P. S.; Abritta, T.; Khaidukov, N. M. *Solid St. Comm.* **1999**, *110*, 519-524.
- (31) Pausewang, G.; Rüdorff, W. *Z. Anorg. Allg. Chem.* **1969**, *364*, 69-87.
- (32) Massa, W.; Pausewang, G. *Mater. Res. Bull.* **1978**, *13*, 361-368.
- (33) Schmidt, R.; Pausewang, G. *Z. Anorg. Allg. Chem.* **1986**, *537*, 175-188.
- (34) Schmidt, R.; Pausewang, G.; Massa, W. *Z. Anorg. Allg. Chem.* **1986**, *535*, 135-142.
- (35) Antokhina, T. F.; Ignat'eva, L. N.; Kaidalova, T. A.; Savchenko, N. N. *Russ. J. Coord. Chem.* **2003**, *29*, 157-162.

- (36) Neumayer, D. A.; Cartier, E. *J. Appl. Phys.* **2001**, *90*, 1801-1808.
- (37) Ackerman, J. F. *Mater. Res. Bull.* **1984**, *19*, 783-791.
- (38) Schipper, W. J.; Piet, J. J.; De Jager, H. J.; Blasse, G. *Mater. Res. Bull.* **1994**, *29*, 23-30.

CHAPTER SIX

HYDROTHERMAL GROWTH AND SPECTROSCOPY OF RARE EARTH DOPED ACENTRIC YTTRIUM ORTHOBORATES ($\text{Ln}^{3+}:\text{YBO}_3$ ($\text{Ln} = \text{Nd}, \text{Er}, \text{Yb}$))

INTRODUCTION

The ability of lasers to generate coherent light has led to its many applications; however, the full potential of lasers has yet to be exploited due to limited emission wavelengths. For example, standard lasers such as Nd:YAG (neodymium-doped yttrium aluminum garnet) primarily emit light at 1064 nm, with much weaker emissions at 1052, 1074, 1112, and 1319 nm.¹ Other laser hosts such as sapphire incorporate transition metal ions like Ti^{3+} and Cr^{3+} , giving them the advantage of emitting over a wider range of wavelengths. Known as tunable lasers, the stimulated emission is coupled with the phonon modes of the crystalline lattice, which creates various vibrational sublevels or bands.² This results in the emission of light over much of the infrared spectrum, but the shortest wavelength achieved is approximately 640 nm using Ti:sapphire, leaving the remaining wavelengths in the visible and ultraviolet (UV) region inaccessible. This is unfortunate because shorter wavelengths are critical for many medical, lithographical, and holographic applications.

The use of nonlinear crystals has been well established to reach these shorter wavelengths.² Specifically, second harmonic generation (SHG) is the desired non-linear property used to generate visible and UV wavelengths (see Chapter 1 for a detailed description of SHG). One criteria for a crystal to possess nonlinear properties is its

crystallization in an acentric or non-centrosymmetric space group.^{3,4} Unfortunately, crystals typically adopt structures with a center of symmetry. Of those that do possess acentric symmetry, only a few are actually useful for frequency doubling (i.e., KTiOPO₄ or KTP)⁵ since most have very poor SHG efficiency or exhibit structural deterioration when subjected to intense laser light.

Borates are a common class of laser hosts due to their excellent nonlinear optical (NLO) elements and ultraviolet optics,⁶⁻⁸ the most notable of these materials being β -BaB₂O₄ (BBO) and LiB₃O₅ (LBO), respectively. The NLO properties of BBO arise from the π -conjugation of the trigonal [B₃O₆]³⁻ units in its crystal structure, providing for high polarizability, and the ultraviolet optical elements of LBO are derived from the [B₃O₇]⁵⁻ group that contains both trigonal and tetrahedral coordinate boron with oxygen,⁹ which promotes an opening of the bandgap.¹⁰ It would be desirable to learn how to control the crystal growth of these materials so that they possess multiple functionalities such as light emission and NLO behavior and ultraviolet transparency. This will be critical for the continued miniaturization of future optical components.

One intriguing class of potential hosts is the (RE)BO₃ crystals (RE = Gd³⁺, Y³⁺, Lu³⁺). Much debate has occurred when it comes to the absolute determination of the crystal structure of YBO₃. Initially, Newnham *et al.* obtained PXRD data that showed it was similar to the CaCO₃ vaterite structure, crystallizing in either P6₃/mmc or P6₃/mcm, both centrosymmetric space groups.¹¹ Shortly thereafter, Bradley *et al.* re-determined the same PXRD data to show that YBO₃ crystallizes in the acentric space group P $\bar{6}c2$, a slight modification of P6₃/mcm, but still possessing some vaterite-type characteristics.¹²

More recently, Chadeyron *et al.* was the first to report single crystal data on YBO₃; he claimed that it crystallized in the centrosymmetric space group P6₃/m, similar to what was found by Newnham.¹³ Shortly thereafter, Ren *et al.* obtained PXRD data and re-determined YBO₃ to crystallize in the acentric space group R32.¹⁴ To settle the debate, Giesber *et al.* grew single crystals of YBO₃ and obtained detailed PXRD that agreed with Ren's assessment (s.g. R32).¹⁵ This was further confirmed when single crystals were subjected to the Kurtz experiment¹⁶ and exhibited SHG, indicating NLO properties. Ren's detailed infrared (IR) spectroscopy study of YBO₃ also indicated that the borate building block is composed of [B₃O₉]⁹⁻ groups that contain both trigonal and tetrahedral borates,¹⁴ indicating possible ultraviolet optical behavior.

The approach used in the Kolis group to synthesize crystalline materials involves the use of supercritical water, which is known as an excellent medium for the single crystal growth of new oxides for optoelectronics.¹⁷⁻¹⁹ The relatively low growth temperatures and ability to control crystal growth gives one the luxury to design syntheses for a wide variety of potentially useful optical materials.²⁰ Our group recently explored the use of supercritical aqueous base as a route to large single crystals of new metal borates and found that they exhibit highly favorable chemistries for growth in supercritical water. Thus, one can prepare a wide variety of newly doped yttrium orthoborates as large high quality single crystals from aqueous base under supercritical conditions (T > 375 °C, P > 225 bar). In this paper we report the synthesis and spectroscopy of a series of lanthanide-doped orthoborates from supercritical water under

basic conditions. These crystals are known to grow as hexagonal plates whose growth is primarily along [110].

RESULTS AND DISCUSSION

Synthesis of Rare Earth (RE)-Doped YBO₃

Solid State Synthesis of RE-Doped YBO₃

Previous studies by Giesber showed that an effective synthetic route for producing quality YBO₃ crystals was by first performing a solid-state synthesis of Y₂O₃ and B₂O₃ in a 1:2 ratio, respectively, at 900 °C for 12 h to obtain a microcrystalline feedstock. This feedstock could then be used to grow crystals by spontaneous nucleation (SN) in hydrothermal synthesis.¹⁵ A similar synthetic pathway was utilized, and it was modified by substituting some of the Y₂O₃ with stoichiometric equivalents of the oxides of the desired RE dopants, which in this case was either Nd(III), Er(III), or Yb(III). PXRD patterns of the RE-doped YBO₃ feedstocks were compared to a known powder pattern of acentric YBO₃¹⁴ to confirm the synthesis of the feedstock.

First Nd:YBO₃ feedstock was synthesized with 0.5, 1, and 5% doping, percentages commonly used in laser hosts. It must be noted that previous growth reaction of various host crystals using Nd³⁺ as a doping agent in the Kolis group has generally shown that twice the stoichiometric equivalents of neodymium must be used to obtain the desired doping percentage in the final crystal, especially if the host is the somewhat smaller Y³⁺ or Lu³⁺. Figure 6.1 shows the PXRD patterns obtained for 0.5, 1, and 5% doping. As is expected, the peaks shift to slightly lower angles as the doping

percentage increases, since Nd^{3+} (crystal radius of 1.249 Å according to Shannon)²¹ is larger than Y^{3+} (crystal radius of 1.159 Å) and would cause the unit cell to expand.

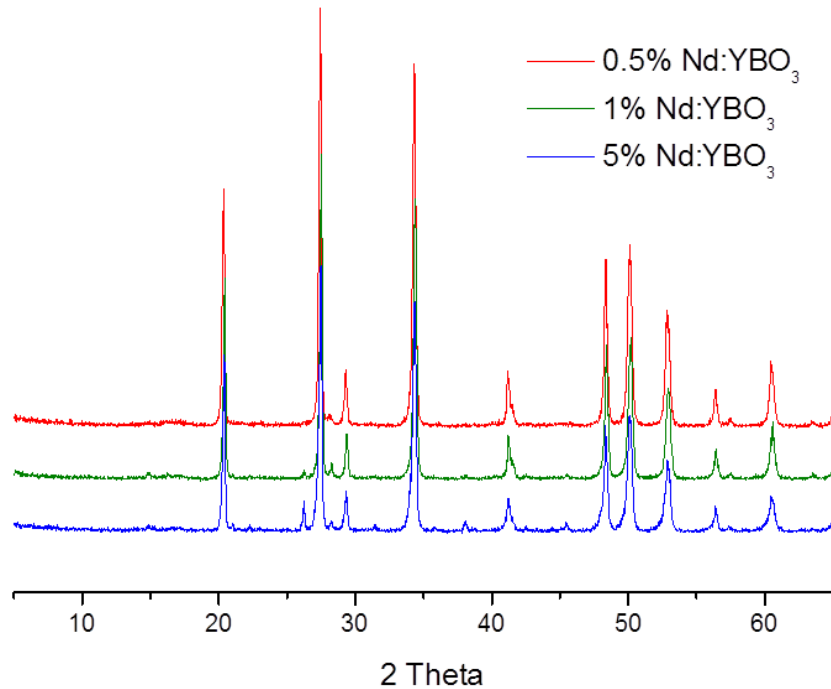


Figure 6.1. PXRd patterns for 0.5, 1, and 5% Nd:YBO₃.

Er:YBO₃ (1, 3, and 5% doping) and Yb:YBO₃ (1, 5, and 10% doping) feedstocks were also synthesized, again using percentages commonly used in laser hosts. Figures 6.2 and 6.3 show the PXRd patterns obtained for said doping. The peaks expectedly shifted to slightly higher angles as the doping percentage increases, since both Er^{3+} (ionic radius of 1.144 Å)²¹ and Yb^{3+} (ionic radius of 1.125 Å) are smaller than Y^{3+} and would cause the unit cell to shrink.

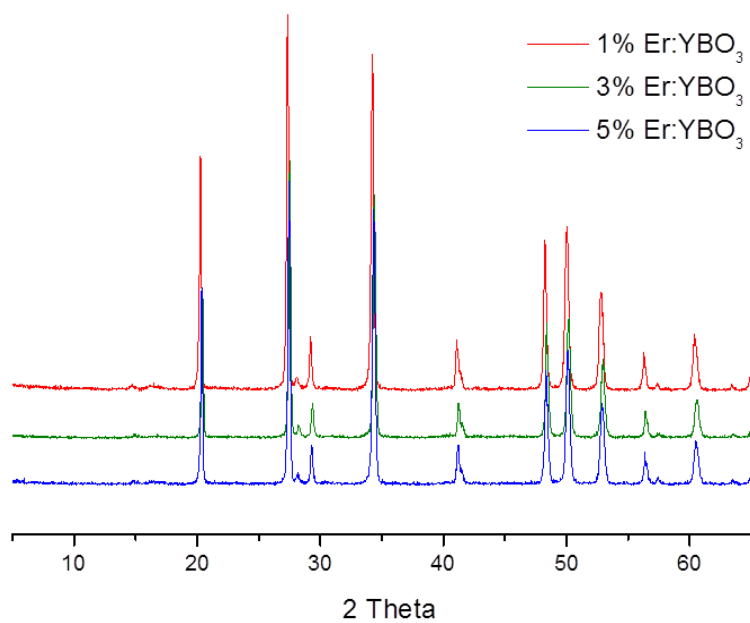


Figure 6.2. PXRD patterns for 1, 3, and 5% Er:YBO₃.

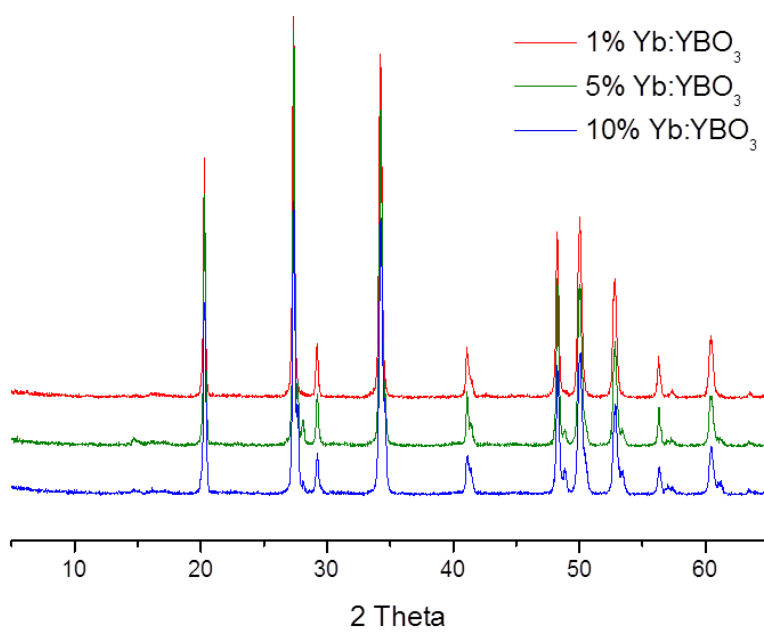


Figure 6.3. PXRD patterns for 1, 5, and 10% Yb:YBO₃.

Spontaneous Nucleation of RE-Doped YBO₃ Crystals

Giesber previously showed that hydrothermal treatment of YBO₃ feedstocks produced via solid state reactions at 600 °C for seven days using 10 M NaOH as the mineralizer yield large single crystals as hexagonal plates with good clarity via SN.¹⁵ It must be noted that these reactions were performed in vertical box furnaces, which have been shown by subsequent members of the Kolis group to heat an autoclave unevenly, developing a temperature gradient of up to 75 °C between the “hot zone” and the “cold zone” (see Chapter 2 for a detailed discussion). Since the current reactions are performed using band heaters (giving better control of temperature gradient), it was decided to set the hot zone at 600 °C and the cold zone at 550 °C.

When the Nd:YBO₃ feedstocks were hydrothermally treated as described above, large hexagonal plates with a bluish hue were obtained. EDX analysis showed that crystals from the reactions containing 0.5, 1, and 5% stoichiometric doping averaged 0.79, 2.35, and 6.00% ± 1% doping, respectively. What was most surprising was that the size of crystals grown from SN after only seven days; the largest crystal grew 7.57 mm x 8.12 mm x 1.75 mm thick, and the average crystal size was 4 mm x 4 mm x 1 mm thick. The crystals grew the largest of the three dopants investigated, but also produced the poorest quality in terms of total clarity and epitaxial growth (see Figure 6.4). Increasing the dopant percentage predictably yielded crystals with darker bluish hues, but surprisingly had no effect on SN growth size and quality.

The Er:YBO₃ feedstocks yielded small hexagonal plates with a pinkish hue after the same hydrothermally treatment. EDX analysis showed that crystals from the

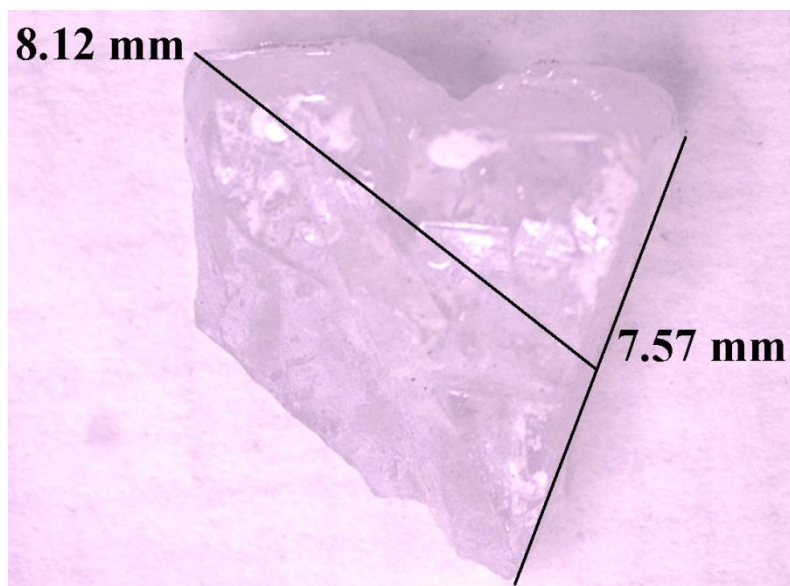


Figure 6.4. Crystal of 1% Nd:YBO₃ grown from SN by hydrothermal treatment.

reactions containing 1, 3, and 5% stoichiometric doping averaged 1.73, 4.19, and 7.63% \pm 1% doping, respectively. The size of crystals grown from SN were again surprising after only seven days, as the largest crystal grew 2.39 mm x 1.92 mm x 0.25 mm thick, and the average crystal size was 1.5 mm x 1.5 mm x 0.20 mm thick. The crystals grew the smallest of the three dopants investigated, but also produced the best quality with excellent clarity and noticeable facets are observed in its epitaxial growth (see Figure 6.5). Increasing the dopant percentage predictably yielded crystals with darker pinkish hues, but again had no effect on SN growth size and quality.

Hydrothermal treatment of the Yb:YBO₃ feedstocks yielded colorless hexagonal plates. EDX analysis showed that crystals from the reactions containing 1, 5, and 10% stoichiometric doping averaged 1.59, 7.93, and 12.57% \pm 1% doping, respectively. The size of crystals grown from SN were again surprising after only seven

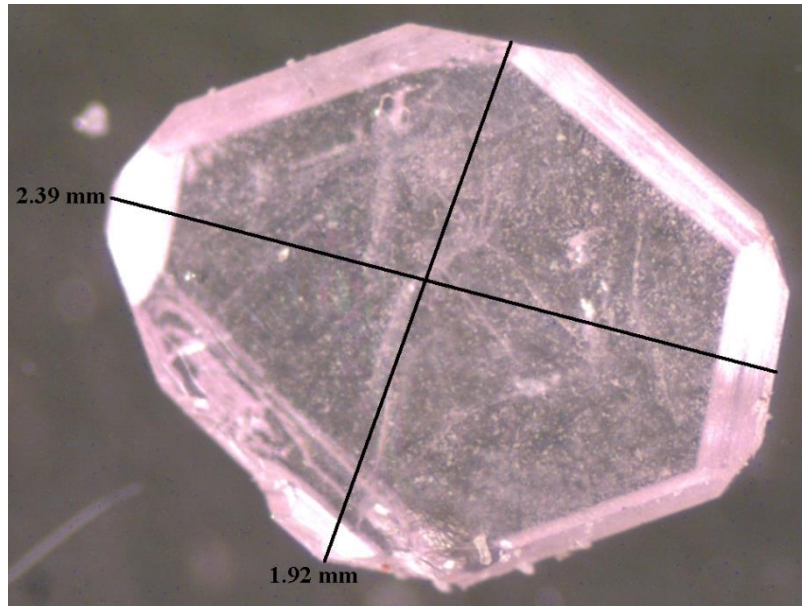


Figure 6.5. Crystal of 5% Er:YBO₃ grown from SN by hydrothermal treatment.

days, as the largest crystal grew 6.49 mm x 5.23 mm x 1.18 mm thick, and the average crystal size was 4 mm x 4 mm x 0.90 mm thick. These crystals yielded both excellent growth and quality with good clarity and noticeable facets observed in its epitaxial growth (see Figure 6.6). Increasing the dopant percentage predictably had no effect on SN growth size and quality, as was seen for the other dopants.

Overall, it was surprising to obtain crystals of such large size and acceptable clarity from solely SN via hydrothermal treatment. Most good quality crystals grown in the Kolis lab are usually obtained through controlled crystal growth using a smaller temperature gradient (10 °C average) and much longer reaction times (between 3-8 weeks). As was observed for crystal growth of undoped YBO₃, most of the growth occurred along [110]. It must be noted that a pitfall to growing YBO₃ in this fashion is

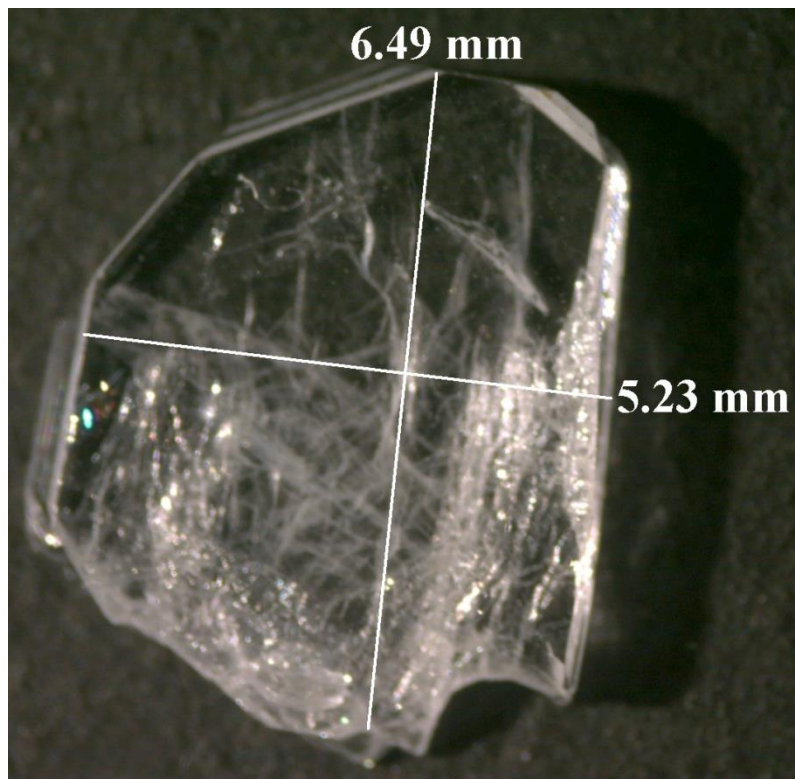


Figure 6.6. Crystal of 1% Yb:YBO₃ grown from SN by hydrothermal treatment.

the difficulty in controlling the plate “stacking” that commonly occurs with this crystal morphology. The plates grow quickly along [110], but growth along [001] is much slower and cannot keep up with [110] growth and uneven stacking occurs (see Figure 6.7). This can affect the alignment of the trigonal and tetrahedral borates, thus reducing its capability to generate efficient NLO response and good SHG.

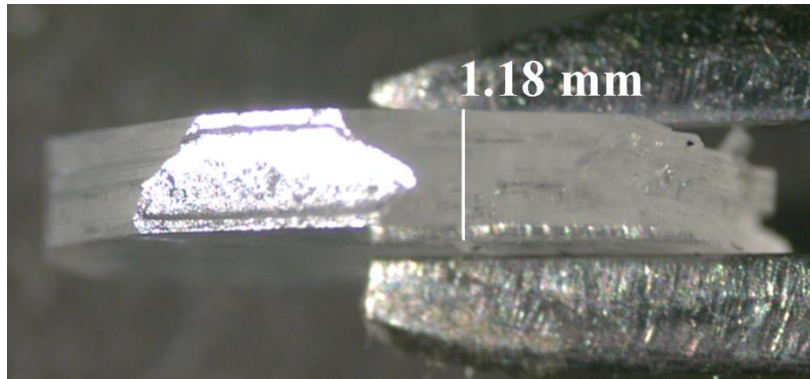


Figure 6.7. Crystal of 1% Yb:YBO₃ shows the uneven plate “stacking” on the facets.

Absorption/Emission Spectroscopy of Rare Earth (RE)-Doped YBO₃

Neodymium-Doped YBO₃

Figure 6.8 shows the absorption spectra obtained for samples of 0.5, 1, and 5% Nd:YBO₃. The significant peaks are similar to what is seen for both neodymium-doped yttrium aluminum garnet (Nd:YAG) and Nd:YVO₄, commonly-used laser host crystals,²² with the peak centered around 800 nm being the most-commonly used for lasing. It must be noted that the peaks are slightly blue-shifted compared to Nd:YAG and Nd:YVO₄ by around 5 nm, and (not surprisingly) increased dopant percentages led to stronger absorption. The transitions that exhibited the most absorption are ${}^4I_{9/2} \rightarrow ({}^4G_{5/2}, {}^2G_{7/2})$; centered around 589 nm), (${}^4S_{3/2}, {}^4F_{7/2}$; centered around 734 nm), and (${}^4F_{5/2}$; centered around 803 nm).

The Nd:YBO₃ samples were then subjected to NIR emission measurements. Figure 6.9 shows the emission spectra that resulted when the Nd:YBO₃ samples were excited with the three wavelengths of energy that exhibited the most absorption: 589, 734, and 803 nm. Each excitation wavelength gave emissions that correspond to ${}^4I_{9/2} \rightarrow$

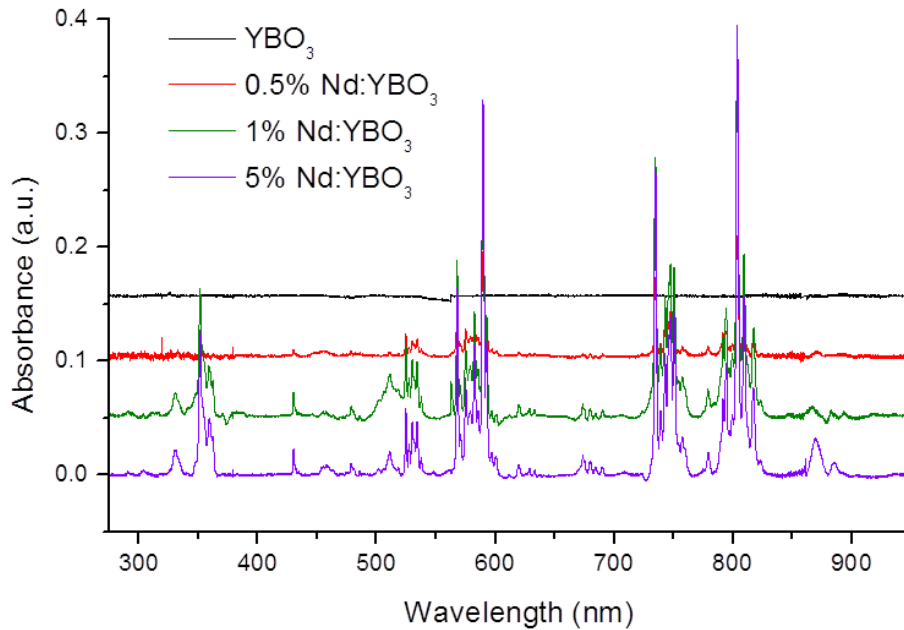
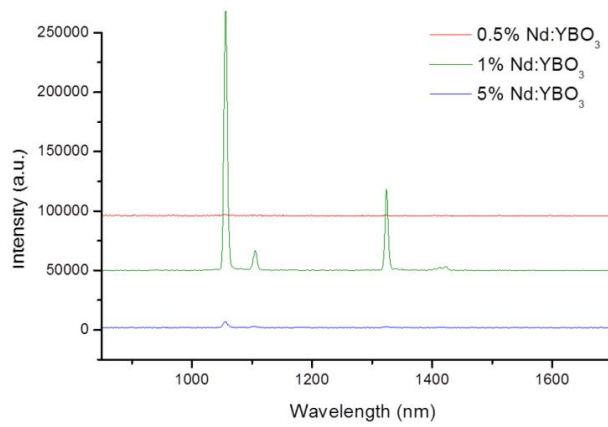
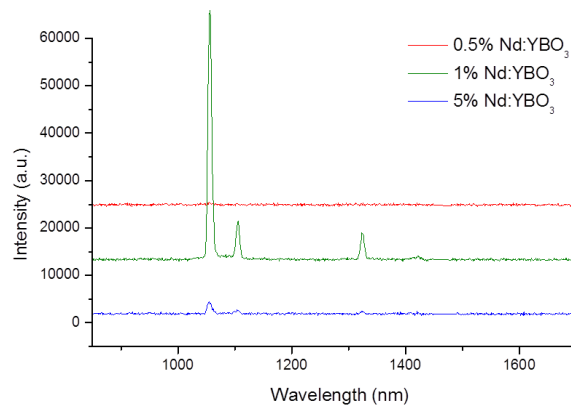


Figure 6.8. Absorption spectra of 0.5, 1, and 5% Nd-doped YBO_3 as compared to YBO_3 .

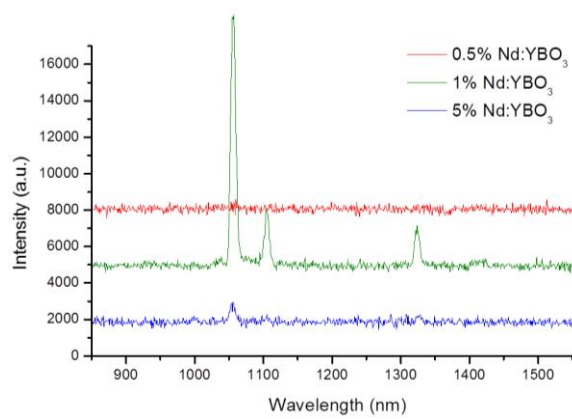
$^4\text{I}_{11/2}$ (1057 nm and 1107 nm) and $^4\text{I}_{13/2}$ (1325 nm), with the band at 1057 nm (predictably) being the most intense band. What is most interesting is significant response of emission compared to the subtle change in doping percentage. An amount of 0.5% doping seems to elicit no emission response, but just a 0.5% increase in dopant (to 1%) yielded the most intense emissions, regardless of excitation wavelength. However, 5% doping yields significantly less intense emission, suggesting that self-quenching occurs between 1 – 5% doping. It is noted that self-quenching of Nd^{3+} ions in crystal lattices is well known in the solid state laser literature.² A comparison of the emission spectra of 1% Nd:YBO₃ shows that excitation at 589 nm surprisingly elicits the most intense emissions, whereas excitation at 803 nm yields the weakest emission (see Figure 6.10). This indicates that obtaining maximum efficiency with a neodymium-doped YBO₃



(a)



(b)



(c)

Figure 6.9. Emission spectra of Nd:YBO₃, excitation at (a) 589, (b) 734, and (c) 803 nm.

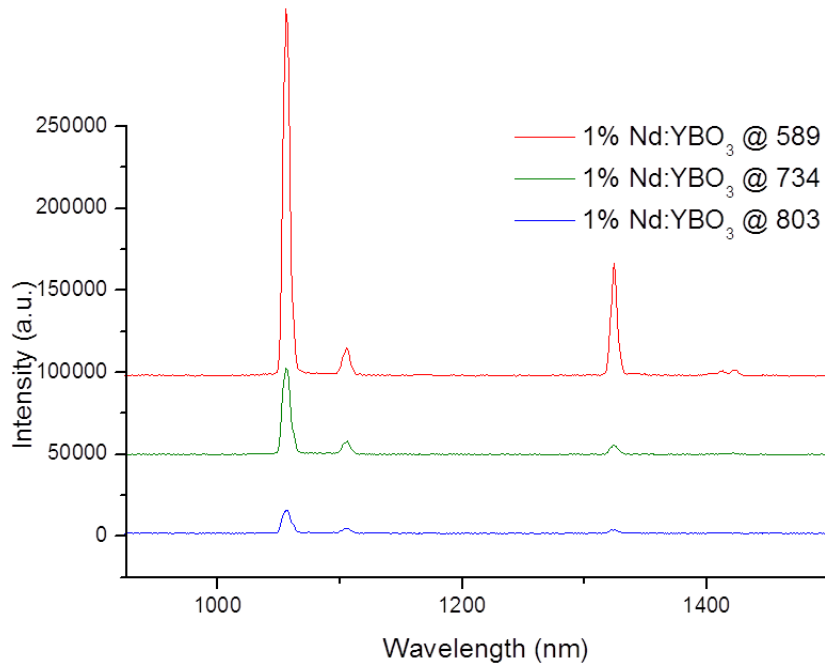


Figure 6.10. NIR emission spectra of 1% Nd:YBO₃ excited at 589, 734, and 803 nm.

crystal requires the use of a 1% Nd:YBO₃ crystal excited at 589 nm to yield 1057 nm light.

Erbium-Doped YBO₃

Figure 6.11 shows the absorption spectra obtained for samples of 1, 3, and 5% Er:YBO₃. The spectra are quite complex, and significant peaks are similar to what is seen for both Er:YAG,²³ with the group of peaks centered around 968 nm being the most commonly used for lasing. It must be noted that the peaks are again slightly blue-shifted compared to Er:YAG by close to 10 nm, and again (not surprisingly) increased dopant percentages led to stronger absorption. The transitions that exhibited the most absorption are $^4I_{15/2} \rightarrow ^4G_{5/2}$ (centered around 365 nm), ($^4S_{3/2}, ^2H_{11/2}$; centered around 511 nm), $^4F_{9/2}$

(centered around 635 nm), $^4F_{9/2}$ (centered around 961 nm), and $^4I_{13/2}$ (centered around 1490 nm). It is well known for Er^{3+} that the absorption peaks around 960 nm are best for eliciting an emission around 1550 nm for lasing.

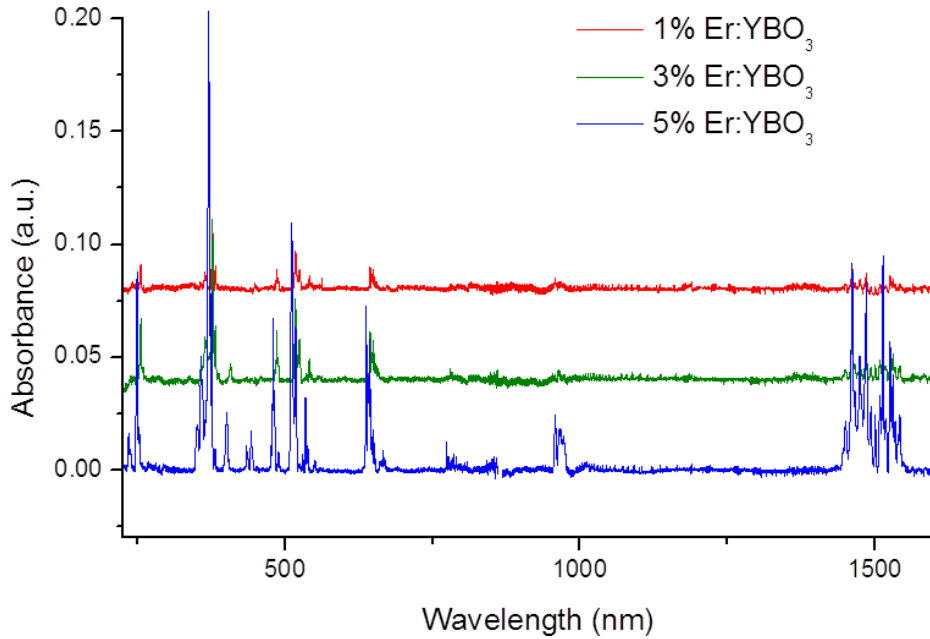


Figure 6.11. Absorption spectra of 1, 3, and 5% Er-doped YBO_3 .

The Er:YBO_3 samples were also subjected to NIR emission measurements. The emission spectra that resulted when the Er:YBO_3 samples were excited using 957, 966, and 972 nm as the excitation wavelengths to obtain the $^4I_{15/2} \rightarrow ^4I_{13/2}$ transition. It was surprising to observe that only the 5% Er:YBO_3 sample yielded a response, a group of small peaks centered around 1530 nm, though Er(III) is known to elicit a poor emission around 1550 nm (as Er:YAG) when using 980 nm excitation. A comparison of the emission spectra of 5% Er:YBO_3 shows that points used from the broad absorption area

(957 – 972 nm) elicits similar weak emissions (see Figure 6.12). This indicates that using erbium as a dopant in YBO_3 may not give as good a response as other alternative lasing hosts.

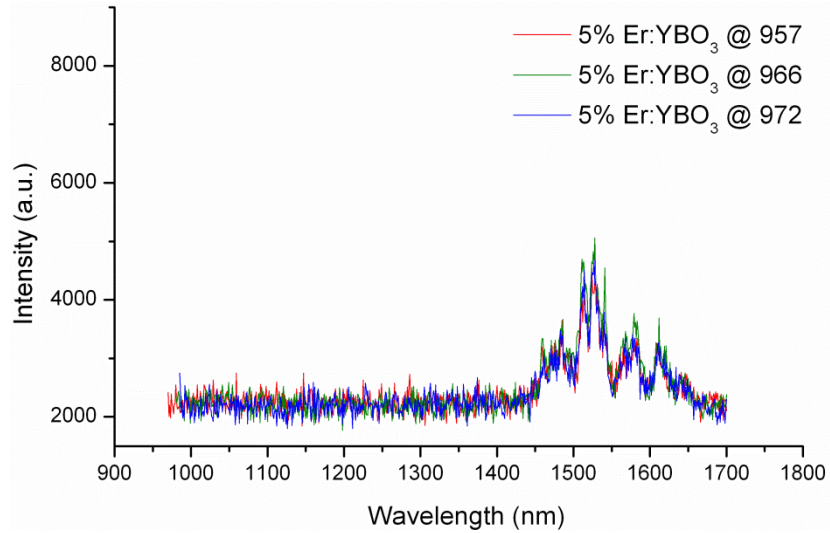


Figure 6.12. NIR emission spectra of 5% Er:YBO₃ excited at 957, 966, and 972 nm.

Ytterbium-Doped YBO₃

Figure 6.13 shows the absorption spectra obtained for samples of 1, 5, and 10% Yb:YBO₃. The spectra is quite simple, with its significant peak similar to what is seen for Yb:YAG,²³ centered around 925 – 971 nm. It must be noted that the major peaks are again slightly blue-shifted compared to Yb:YAG by close to 10 nm, and again (not surprisingly) increased dopant percentages led to stronger absorption. The transition of importance is $^2F_{5/2} \rightarrow ^2F_{7/2}$ (centered around 971 nm). It is well known for Yb³⁺ that the absorption peaks around 980 nm are best for eliciting an emission around 1040 nm for lasing.

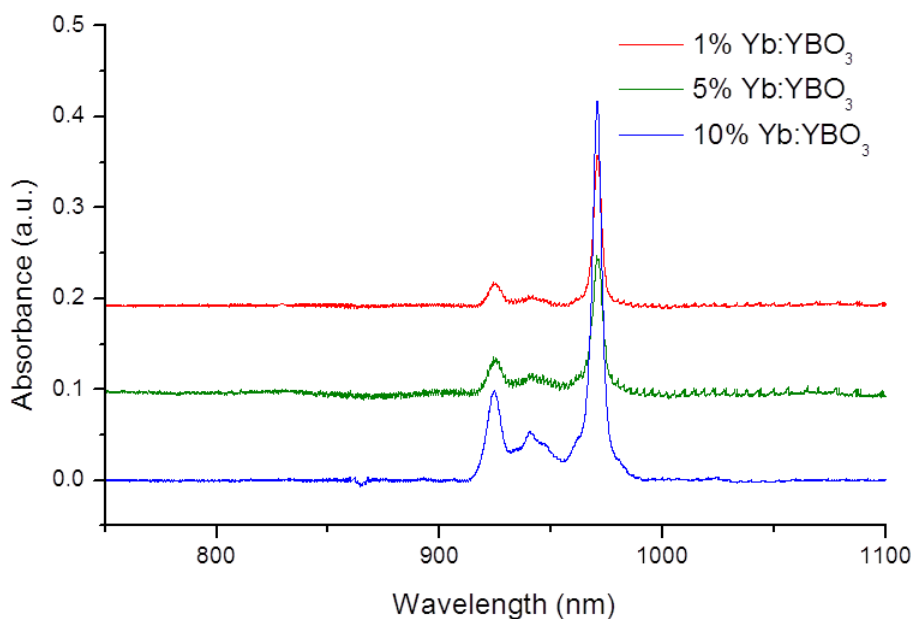
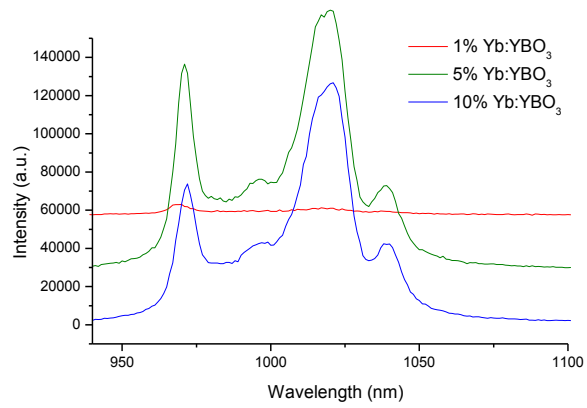
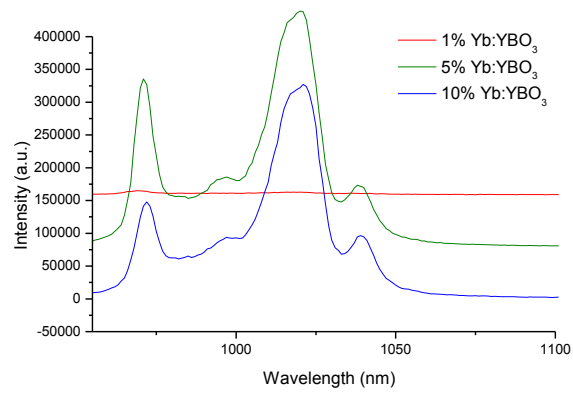


Figure 6.13. Absorption spectra of 1, 5, and 10% Yb-doped YBO₃.

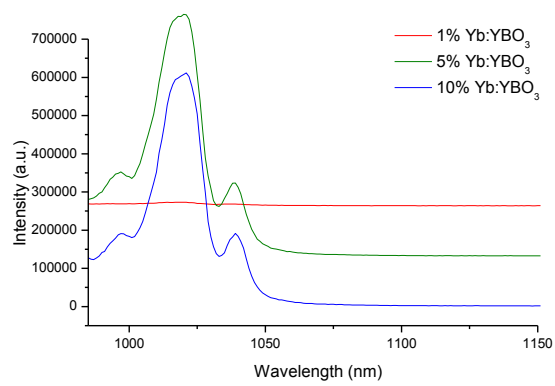
The Yb:YBO₃ samples were also subjected to NIR emission measurements. Figure 6.14 shows the emission spectra that resulted when the Yb:YBO₃ samples were excited with three wavelengths of energy that exhibited the most absorption in the cluster: 925, 941, and 971 nm, with the band at 971 nm (predictably) being the most intense band. What is most interesting is the significant response of emission compared to the subtle change in doping percentage, not unlike with neodymium. A 1% doping concentration seems to elicit no emission response, but an increase to 5% yields the most intense emissions, regardless of excitation wavelength. However, 10% doping yields slightly less intense emission, suggesting that some self-quenching occurs between 5 – 10% doping. A comparison of this data to the emission spectra of 5% Yb:YBO₃ shows



(a)



(b)



(c)

Figure 6.14. Emission spectra of Yb:YBO₃, excitation at (a) 925, (b) 941, and (c) 971 nm.

that excitation at 971 nm expectedly elicits the most intense emissions, but a precipitous drop does not occur in emission intensity when using excitations of 925 and 941 nm (see Figure 6.15). This indicates that obtaining maximum efficiency with a ytterbium-doped YBO₃ crystal requires the use of a 5% Yb:YBO₃ crystal, but does not require a small excitation window like Nd:YBO₃. A larger excitation window allows for more flexibility in terms of the laser tunability.

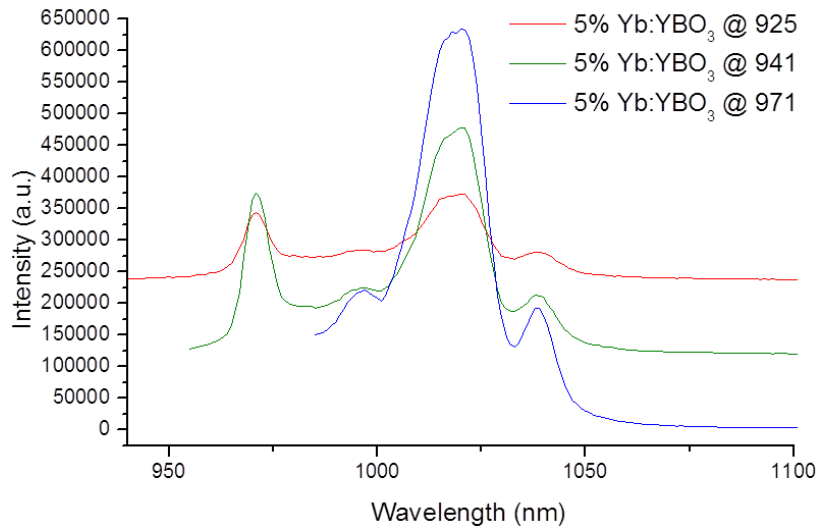


Figure 6.15. NIR emission spectra of 5% Yb:YBO₃ excited at 925, 941, and 971 nm.

CONCLUSIONS

In this Chapter, doped YBO₃ samples were found to show great promise as materials that possess numerous useful optical functionalities. Emissions from Nd³⁺, Er³⁺, and Yb³⁺ doped samples were observed and clearly linked to both dopant and the

acentric structure of the host. The ability to grow these crystals of sufficient size for use in a commercial device has been realized using supercritical hydrothermal approaches via spontaneous nucleation. However, future crystal growth studies of lanthanide-doped YBO₃ need to overcome the uneven stacking that plagues its epitaxial growth. The combination of favorable emission characteristics and an acentric crystal structure clearly marks these materials as multifunctional and of interest for applications utilizing nonlinear optical phenomena, light emission, or ultraviolet transparency.

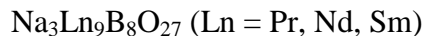
REFERENCES

- (1) Koechner, W. *Solid-State Laser Engineering*, 2nd edn., Berlin, New York: Springer-Verlag, 1996.
- (2) Koechner, W. *Solid-State Laser Engineering*, 6th edn., New York: Springer, 2006.
- (3) Halasyamani, P. S.; Poepelmeier K. P. *Chem. Mater.* **1998**, 10, 2753-2769.
- (4) Hulme, K. F. *Oxides in Non-Linear Optics, Modern Oxide Materials*, Cockayne, B.; Jones, D. W., Eds.; Academic Press: New York, NY, 1996, p. 53.
- (5) Tordjman, I.; Masse, R.; Guitel, J. C. *Z. Kristallogr., Kristallgeom., Kristallphys., Kristallchem.* **1974**, 139, 103-115.
- (6) Keszler, D. A. *Curr. Opin. Solid St. Mater. Sci.* **1996**, 1, 204-211.
- (7) Keszler, D. A. *Curr. Opin. Solid St. Mater. Sci.* **1999**, 4, 155-162.
- (8) Chen, C.; Lui, G. *Ann. Ret. Mater. Sci.* **1986**, 16, 203-243.
- (9) Agulló-López, P.; Cabrera, J.; Agulló-Rueda, F. *Electro-optics, Phenomena, Materials, and Applications*; Academic Press, New York, 1994.
- (10) French, R.; Ling, J.; Okuchi, F.; Chen, C. *Phys. Ret. B* **1991**, 44, 8496-8502.

- (11) Newnham, R. E., Redman, M. J., Santoro, R. P. *J. Am. Ceram. Soc.* **1963**, *46*, 253-256.
- (12) Bradley, W. F., Graf, D. L., Roth, R. S. *Acta Cryst.* **1966**, *20*, 283-287.
- (13) Chadeyron, G., El-Ghozzi, M., Arbus, A., Cousseins, J. C. *J. Solid St. Chem.* **1997**, *128*, 261-266.
- (14) Ren, M., Lin, J. H., Dong, Y., Yang, L. Q., Su, M. Z. *Chem. Mater.* **1999**, *11*, 1576-1580.
- (15) Giesber, H. G.; Ballato, J.; Pennington, W. T.; Kolis, J. W.; Dejneka, M. *Glass Technol.* **2003**, *44*, 42-45.
- (16) Kurtz, S., Perry, T. *J. Appl. Phys.* **1968**, *39*, 3798-3813.
- (17) Laudise, R. A.; Nielson, W. *Solid St. Phys.* **1961**, *12*, 149-222.
- (18) Laudise, R. A. *Crystal Growth of Electronic Materials*. Gilman J. J., Ed.; Amsterdam: Elsevier Science, 1985. Ch. 13.
- (19) Laudise, R. A. *Prog. Inorg. Chem.* **1962**, *3*, 1-47.
- (20) Kolis, J. W.; Korzenski, M. B. *Chemical Synthesis Using Supercritical Fluids*. Jessop, P.G.; Leitner, W., Eds.; New York: Wiley-VCH, 1999. pp. 213-242.
- (21) Shannon, R. D. *Acta Crystallogr.* **1976**, *A32*, 751.
- (22) Holgado, W.; Sola, I. J.; Jarque, E. C.; Jarabo, S.; Roso, L. *Eur. J. Phys.* **2012**, *33*, 265-278.
- (23) Le Quang, A. Q.; Zyss, J.; Ledoux, I.; Truong, V. G.; Jurdyc, A.-M.; Jacquier, B.; Le, D. H.; Gibaud, A. *Chem. Phys.* **2005**, *318*, 33-43.

CHAPTER SEVEN

HYDROTHERMAL CHEMISTRY, STRUCTURES, AND SPECTROSCOPY OF NON-CENTROSYMMETRIC LANTHANIDE BORATES OF FORMULA



INTRODUCTION

It was noted in the previous chapter that borates are a common class of laser hosts due to their excellent nonlinear optical (NLO) elements and ultraviolet optics¹⁻³ due to the π -conjugation of the trigonal $[\text{B}_3\text{O}_6]^{3-}$ units or $[\text{B}_3\text{O}_7]^{5-}$ groups⁴ that are usually found in acentric borates. One acentric borate in particular, $\text{Na}_3\text{La}_9\text{O}_3(\text{BO}_3)_8$, showed promise as an alternative frequency-doubling host, exhibiting a second-harmonic generation (SHG) effect that was three to five times that of a commonly-used host KH_2PO_4 (KDP).^{5,6} Unfortunately, these experiments were conducted on powder samples, since crystals of this material were too small to analyze. It would be desirable to learn how to control the crystal growth of this material to take advantage of their NLO and ultraviolet transparency.

It was shown in Chapter 6 that the use of supercritical aqueous base on acentric borate powders or raw material feedstock with a temperature gradient is a route to large single crystals of new metal borates. Thus, one can prepare a wide variety of new acentric lanthanide borates as large high quality single crystals from aqueous base under supercritical conditions ($T > 375 \text{ }^\circ\text{C}$, $P > 225 \text{ bar}$). In this Chapter, the synthesis and spectroscopy of a series of acentric lanthanide borates from supercritical water under

basic conditions are reported. These crystals are known to grow as trigonal prisms whose growth is primarily along [110].

RESULTS AND DISCUSSION

Synthesis of Compounds 1 – 3

The synthesis of compounds **1** – **3** is a modification of the synthesis of $\text{Na}_3\text{La}_9\text{O}_3(\text{BO}_3)_8$,⁷ where stoichiometric equivalents of the starting materials are reacted in a solid state reaction to yield a crude flux, followed by treatment of the flux via hydrothermal method. A starting material was created making a flux containing $1.5 \text{ Na}_2\text{CO}_3 + 4.5 \text{ Ln}_2\text{O}_3 + 8 \text{ H}_3\text{BO}_3$ by heating at 1000 °C for 12 h. It must be noted that the reaction is only successful when Ln = Pr, Nd, and Sm; the use of other lanthanides (e.g., Eu and Gd) led to powder patterns that closely matched LnBO_3 . The resulting crude flux yielded a mixture of both $\text{Na}_3\text{Ln}_9\text{O}_3(\text{BO}_3)_8$ and $\text{Na}_3\text{Ln}_2(\text{BO}_3)_3$, a “parasitic” species that was described by Peshev *et al.* in the solid state synthesis of $\text{Na}_3\text{La}_9\text{O}_3(\text{BO}_3)_8$.⁵ Figure 7.1 shows a PXRD pattern depicting this mixture, with peak shifts taken into consideration.

The crude flux was hydrothermally treated using 10 M NaOH as the mineralizer. The mixture was heated using a temperature gradient of 550 – 600 °C for 4 days to yield trigonal prisms and polyhedral that SXRD proved to be the target compound, $\text{Na}_3\text{Ln}_9\text{B}_8\text{O}_{27}$ (see Figure 7.2 for an example). The procedure also yielded polyhedra that turned out to be LnBO_3 (Ln = Pr, Nd) in $Pnma$ ^{8,9} upon SXRD analysis, but not with the Sm analog. The average yield of the target compound to LnBO_3 is estimated to be 80:20.

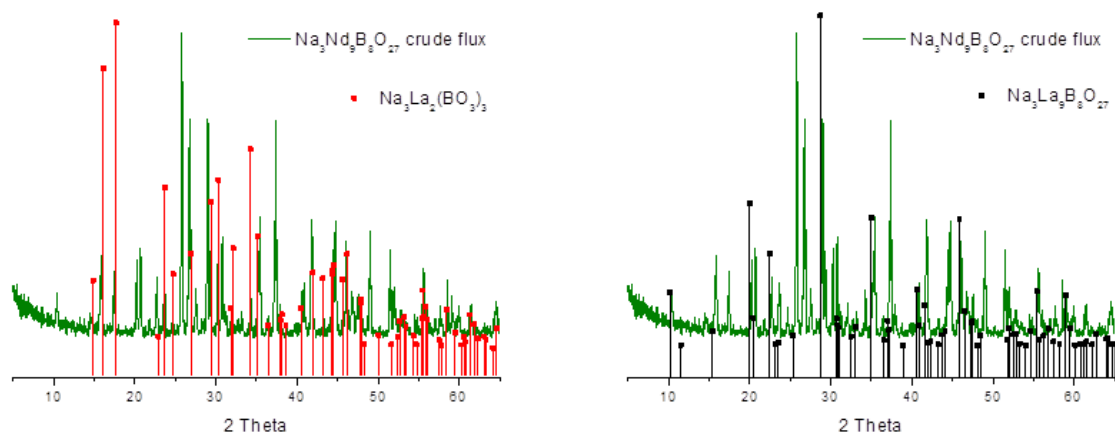


Figure 7.1. PXR D comparison of $\text{Na}_3\text{Nd}_9\text{B}_8\text{O}_{27}$ flux to reported PXR D patterns for $\text{Na}_3\text{La}_2(\text{BO}_3)_3$ (left) and $\text{Na}_3\text{La}_9\text{B}_8\text{O}_{27}$ (right).

It was surprising to observe the absence of the “parasitic” phase $\text{Na}_3\text{Ln}_2(\text{BO}_3)_3$; perhaps the use of concentrated base allows for preferential formation of the target compound over the “parasitic” phase.

Crude fluxes of $\text{Na}_3\text{La}_9\text{B}_8\text{O}_{27}$, $\text{Na}_3\text{Gd}_9\text{B}_8\text{O}_{27}$, and $\text{Na}_3\text{Y}_9\text{B}_8\text{O}_{27}$ were attempted to obtain single crystals of materials that would be spectroscopically silent, ones that would give the capability of doping lasing materials in small percentages. In the case of $\text{Na}_3\text{La}_9\text{B}_8\text{O}_{27}$, the crude flux was confirmed to be the target material, but subsequent hydrothermal treatment gave only LaBO_3 in the *Pnma* space group.¹⁰ Attempts at preparing crude fluxes of $\text{Na}_3\text{Gd}_9\text{B}_8\text{O}_{27}$ and $\text{Na}_3\text{Y}_9\text{B}_8\text{O}_{27}$ only yielded GdBO_3 and YBO_3 , respectively, both in the space group *R32*, which was confirmed by PXR D.

Crystal Structure of Compounds 1 – 3

Crystallographic data for compounds 1 – 3 are shown in Table 7.1 and selected



Figure 7.2. Photo depicting the trigonal prismatic and polyhedral morphologies of $\text{Na}_3\text{Nd}_9\text{B}_8\text{O}_{27}$.

bond distances are shown in Table 7.2. Compounds **1** – **3** crystallize in the hexagonal space group $\text{P}\bar{6}2m$ (No. 189). Unfortunately, all of the atoms save Na1 for compound **3** had to be refined using an ISOR restraint to prevent their principal mean square atomic displacements from being non-positive definite (though Sm1, Sm2, and B2 still remained non-positive definite and were refined isotropically). Atom O2 on both compounds **1** and **2** also had to be refined using an ISOR restraint. However, the structures makes good chemical sense, especially since Gravereau *et al.* characterized $\text{Na}_3\text{La}_9\text{O}_3(\text{BO}_3)_8$ in the same space group and the atomic positions for each atom closely resembles the structure solution reported herein.⁷

Table 7.1. Crystallographic Data for Structures **1 - 3**

	1	2	3
Chemical Formula	Na ₃ Pr ₉ B ₈ O ₂₇	Na ₃ Nd ₉ B ₈ O ₂₇	Na ₃ Sm ₉ B ₈ O ₂₇
F.W. (g/mol)	1855.64	1885.61	1940.69
Space group	P $\bar{6}2m$	P $\bar{6}2m$	P $\bar{6}2m$
Temp./K	293±2	293±2	293±2
Crystal system	Hexagonal	Hexagonal	Hexagonal
a, Å	8.7905 (12)	8.7406 (12)	8.7043 (12)
c, Å	8.5066 (17)	8.4543 (17)	8.3530 (17)
V, Å ³	569.26 (16)	559.4 (2)	548.1 (2)
Z	1	1	1
D _{cal.} , Mg/m ³	5.413	5.597	5.880
Indices (min)	[-10, -10, -10]	[-10, -10, -10]	[-10, -10, -10]
(max)	[10, 9, 10]	[10, 10, 10]	[10, 10, 10]
Parameters	48	48	49
F(000)	820	829	847
μ, mm ⁻¹	9.492	20.661	23.879
2θ range, °	2.39 – 26.01	2.41 – 26.02	2.70 – 25.13
Collected reflections	5320	5212	5047
Unique reflections	452	446	439
Final R (obs. data), ^a	0.0227	0.0305	0.0326
wR ₂	0.0566	0.0812	0.0735
Final R (all data), R ₁	0.0228	0.0309	0.0326
wR ₂	0.0567	0.0814	0.0735
Goodness of fit (S)	1.241	1.236	1.131
Extinction coefficient			0.011997 (7)
Largest diff. peak	1.335	3.561	4.101
Largest diff. hole	-1.535	-2.317	-4.304

$$^a R_1 = [\sum |F_o| - |F_c|] / \sum |F_o|; wR_2 = \{[\sum w[(F_o)^2 - (F_c)^2]^2]\}^{1/2}$$

This new compound consists of alternating layers (along [001]) of eight- and nine-coordinate lanthanide atoms and sodium ions. The lanthanide atoms adopt distorted monocapped square prismatic and tricapped trigonal prismatic geometry for eight- and nine-coordinate, respectively. The average Ln-O bond distances are: 2.456 (6) and 2.560 (6) Å for Pr1 and Pr2, respectively, 2.433 (9) and 2.545 (9) Å for Nd1 and Nd2, respectively, and 2.410 (4) and 2.522 (4) Å for Sm1 and Sm2, respectively (see Table 7.2), agreeing with bond calculations presented by Shannon.¹¹ In the single crystal

structure determination of the present study, only O3 sits on a general position, Wyckoff position $12I$; Ln1, Na1, and O4 have $m2m$ symmetry, Ln2 and O1 possess a mirror plane on the c axis, O2 possesses a mirror plane on the a axis, B1 possesses both three-fold rotational symmetry on the a axis and a mirror plane on the c axis, B2 has $\bar{6}$ symmetry on the a axis, and B3 has three-fold rotational symmetry on the a axis.

Table 7.2. Selected Bond Distances (Å) with esds for Compounds **1** – **3**

Na ₃ Pr ₉ B ₈ O ₂₇ (1)		Na ₃ Nd ₉ B ₈ O ₂₇ (2)		Na ₃ Sm ₉ B ₈ O ₂₇ (3)	
Bond Distances (Å)		Bond Distances (Å)		Bond Distances (Å)	
Pr1—O1 (x2)	2.668 (8)	Nd1—O1 (x2)	2.640 (10)	Sm1—O1 (x2)	2.585 (5)
Pr1—O3 (x4)	2.397 (6)	Nd1—O3 (x4)	2.376 (9)	Sm1—O3 (x4)	2.360 (3)
Pr1—O4 (x2)	2.362 (5)	Nd1—O4 (x2)	2.340 (7)	Sm1—O4 (x2)	2.336 (3)
Pr2—O1 (x2)	2.662 (9)	Nd2—O1 (x2)	2.645 (15)	Sm2—O1 (x2)	2.639 (4)
Pr2—O2 (x2)	2.492 (5)	Nd2—O2 (x2)	2.476 (7)	Sm2—O2 (x2)	2.435 (4)
Pr2—O3 (x2)	2.532 (5)	Nd2—O3 (x2)	2.511 (7)	Sm2—O3 (x2)	2.489 (3)
Pr2—O3 (x2)	2.638 (5)	Nd2—O3 (x2)	2.630 (7)	Sm2—O3 (x2)	2.612 (4)
Pr2—O4	2.396 (4)	Nd2—O4	2.379 (6)	Sm2—O4	2.351 (4)
Na1—O1 (x2)	2.402 (8)	Na1—O1 (x2)	2.396 (11)	Na1—O1 (x2)	2.394 (3)
Na1—O2 (x2)	2.457 (7)	Na1—O2 (x2)	2.443 (10)	Na1—O2 (x2)	2.448 (4)
Na1—O2 (x2)	2.613 (9)	Na1—O2 (x2)	2.591 (12)	Na1—O2 (x2)	2.556 (4)
B1—O1 (x3)	1.375 (8)	B1—O1 (x3)	1.371 (10)	B1—O1 (x3)	1.3761 (2)
B2—O2 (x3)	1.402 (8)	B2—O2 (x3)	1.406 (12)	B2—O2 (x3)	1.4235 (2)
B3—O3 (x3)	1.360 (6)	B3—O3 (x3)	1.360 (9)	B3—O3 (x3)	1.3671 (2)

This set of compounds consists of nine-coordinate lanthanide atoms (Ln2) that join to two eight-coordinate lanthanide atoms (2-Ln1), one through face sharing a triangle consisting of the O1, O3, and O4 atoms, and the other through the edge-sharing of two O3 atoms. Seven of these lanthanide polyhedra alternate and form a zigzag pattern that runs through $[110]$. Every seventh polyhedra on each chain join through the aforementioned face-sharing to form the fundamental building block (FBB) of this

structural type. The FBBs forms triangular-shaped cavities where five trigonal planar $[\text{BO}_3]^{3-}$ units sit (see Figure 7.3a). The five borate units consist of one B1 and two B2 atoms where the B2 atoms are in the same orientation on the ab plane, whereas the B1 sits rotated 60° about the c axis. A peculiar structure feature to the FBB of these structures is that two the B3 atoms sit directly underneath the two B2 atoms, also rotated 60° about the c axis like the B1 atoms; however, no borate units are found to sit directly beneath the B1 atoms (see Figure 7.3b).

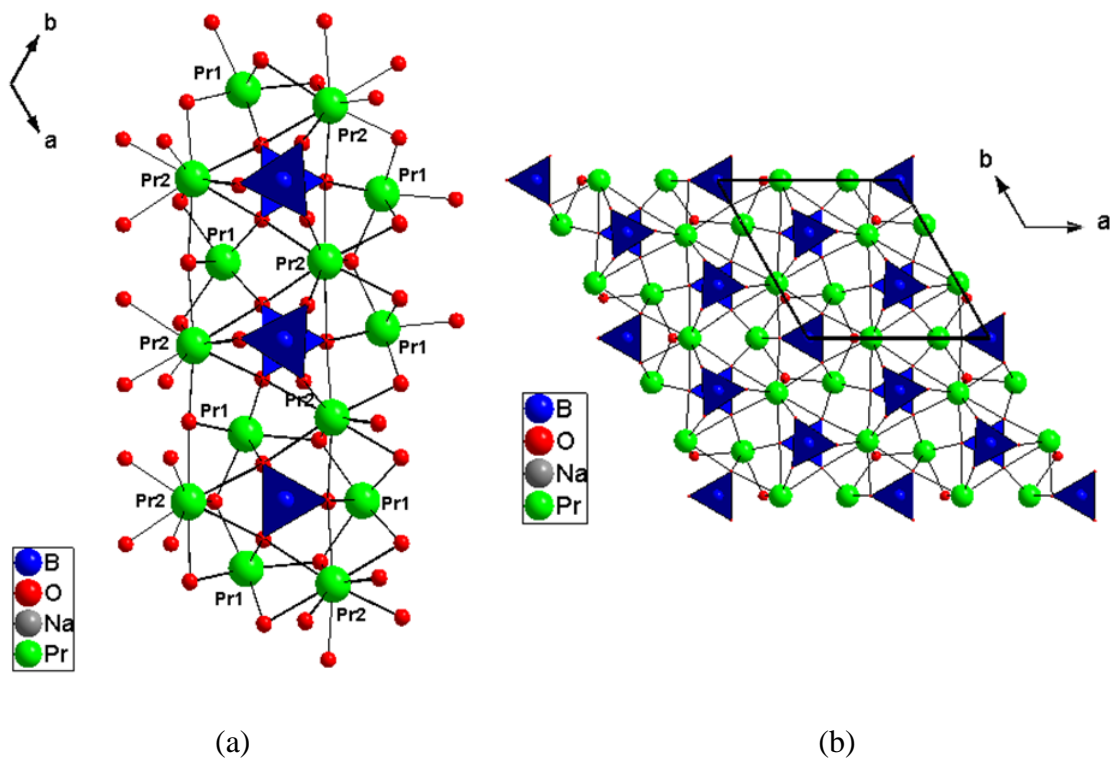


Figure 7.3. (a) The fundamental building block (FBB) of compound **1** as seen down $[001]$. (b) The arrangement of the planar $[\text{BO}_3]^{3-}$ units in compound **1** as seen down $[001]$. The sodium polyhedra are removed for clarity.

The FBBs are joined together through the face-sharing Ln1-Ln2 pairs that cap the ends of the clusters and form a network that runs through [110] (see Figure 7.4a). One layer of FBBs attach to two staggered layers of other FBBs through alternating face-sharing Ln1-Ln2 and edge-sharing Ln1-Ln2 pairs that stack through [001]. The three layer sets of FBBs are separated by a layer of six-coordinate sodium atoms that adopt a highly distorted octahedral geometry. The sodium polyhedra form their layer through the joining of three polyhedra by the $[\text{BO}_3]^{3-}$ units of B2 (see Figure 7.4b). The resulting structure consists of uneven layers that stack in an ABAB fashion through [001].

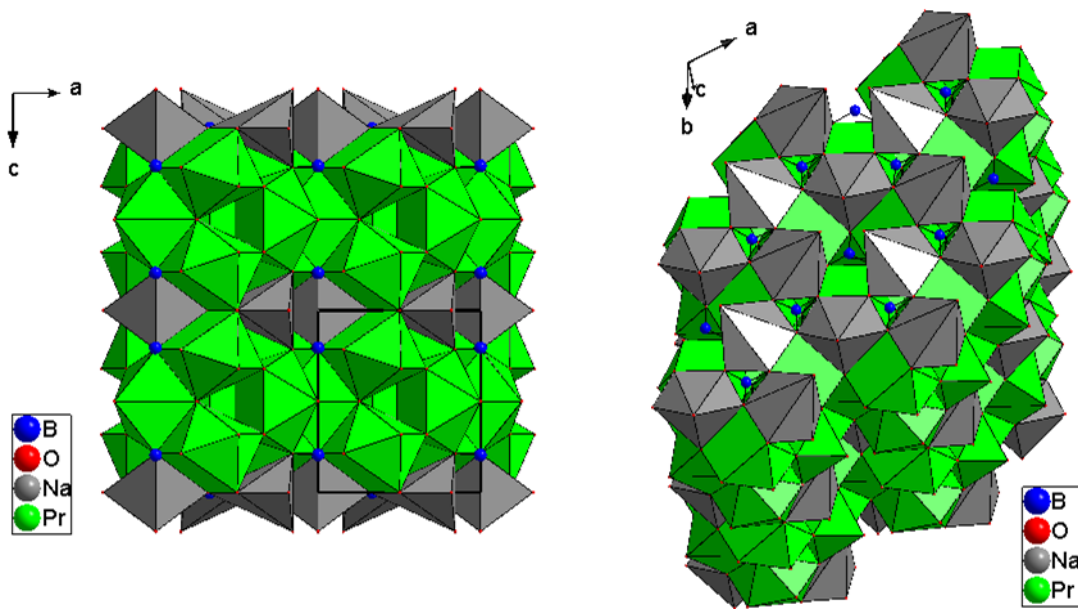


Figure 7.4. (a) The layering of compound **1** as seen down [010]. (b) Off-axis view of the arrangement of the sodium polyhedra in compound **1**. The borate polyhedra are removed for clarity.

Absorption Spectroscopy of Acentric Borates 1 – 3

Given that the title compounds have a high percentage of lanthanide atoms, they may not be useful as laser hosts due to self-quenching mechanisms, but they could be used as possible scintillator hosts due to the sensitivity of lanthanide ions such as Pr(III), Nd(III), and Sm(III) to ionizing radiation. Diffuse reflectance absorption spectroscopy was conducted on the title compounds. Figure 7.5 shows the absorption spectra obtained for samples of compound **1**. The spectrum is comparable to what has been seen for Pr(III)-doped $\text{Li}_2\text{B}_4\text{O}_7$ (LTB), a known NLO material used in acoustic wave devices.¹² It must be noted that the peaks are blue-shifted compared to LTB by around 50 nm. The transitions that exhibited the most absorption are $^3\text{P}_2$, $^3\text{P}_1$, $^3\text{P}_0$ (centered around 440 nm), $^1\text{D}_2$, (centered around 600 nm), $^1\text{G}_4$ (centered around 1050 nm), $^3\text{F}_4$ (centered around 1420 nm), and $^3\text{F}_3$ (centered around 1575 nm). One peak of interest is the one around 440 nm, for that excitation wavelength has been shown to yield an excellent $^1\text{D}_2 \rightarrow ^3\text{H}_4$ emission around 600 nm due its strong 5d-4f transition, especially in Pr-doped lutetium aluminum garnet (Pr:LuAG).¹³ The peak around 300 nm is especially interesting because this band is usually only seen in Pr-doped materials that are incorporated into a lattice that includes d-block elements, of which this class of materials lacks.

Figure 7.6 shows the absorption spectra obtained for samples of compound **2**. Each spectrum is comparable to what has been seen for both Nd:YAG,¹⁴ and Nd:YBO₃ (see Chapter 6). It must be noted that the peaks are again blue-shifted compared to Nd:YAG by around 10 nm. The transitions that exhibited the most absorption are $^4\text{G}_{5/2}$, $^2\text{G}_{7/2}$ (centered around 590 nm), $^4\text{S}_{3/2}$, $^4\text{F}_{7/2}$ (centered around 770 nm), and $^4\text{F}_{5/2}$ (centered

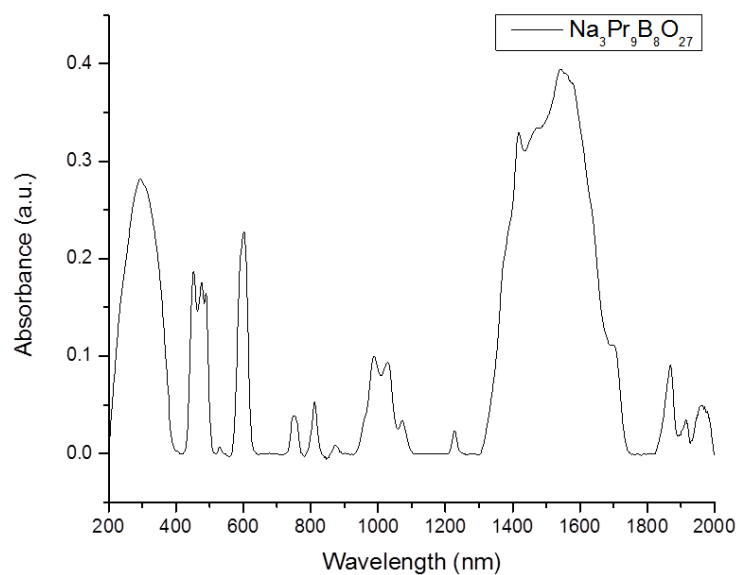


Figure 7.5. Absorption spectrum of compound 1.

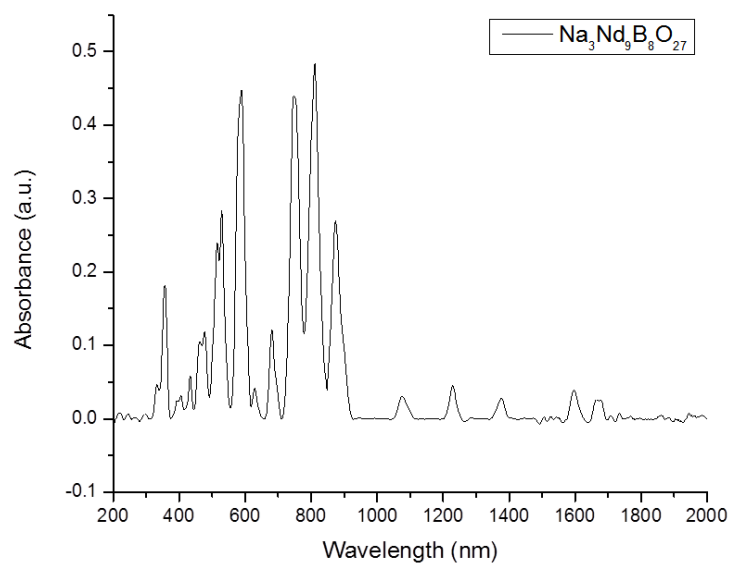


Figure 7.6. Absorption spectrum of compound 2.

around 800 nm). One peak of interest is the one around 800 nm, for that excitation wavelength has been shown to yield light around 1060 nm, a commonly-used wavelength for neodymium-doped laser hosts.¹⁴

Figure 7.7 shows the absorption spectra obtained for samples of compound **3**. The spectrum is comparable to what has been seen for Sm-doped materials such as Sm-doped KLu(WO₄)₂.¹⁵ It must be noted that the peaks are again blue-shifted compared to Nd:YAG by around 10 nm. The transitions that exhibited the most absorption are ⁴K_{11/2} (centered around 400 nm), ⁴G_{5/2} (centered around 470 nm), ⁶F_{11/2} (centered around 900 nm), ⁶F_{9/2} (centered around 1070 nm), ⁶F_{7/2} (centered around 1250 nm), ⁶F_{5/2} (centered around 1375 nm), and ⁶H_{15/2}, ⁶F_{3/2}, ⁶F_{1/2} (centered around 1500 nm). One peak of interest is the one around 470 nm, for that excitation wavelength has been shown to yield light around 650 nm, which is the only observable Stark level for Sm-doped materials.¹⁶

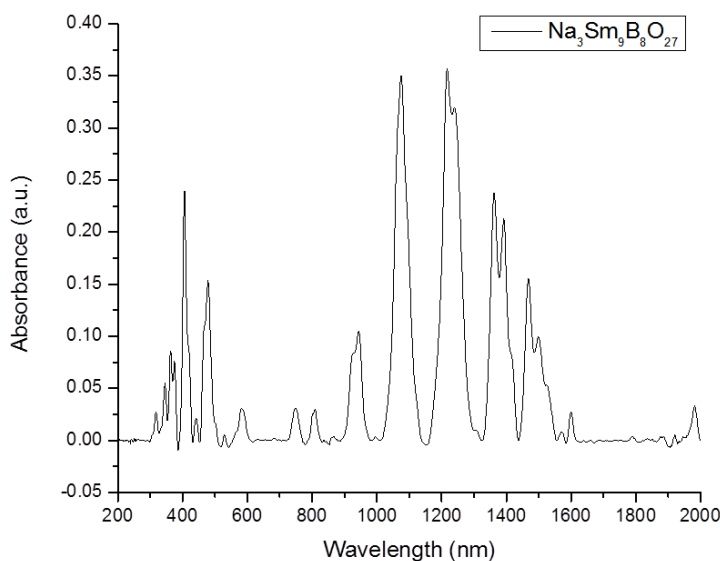


Figure 7.7. Absorption spectrum of compound **3**.

CONCLUSIONS

In this Chapter, a little-explored class of acentric borates of the formula $\text{Na}_3\text{Ln}_9\text{O}_3(\text{BO}_3)_8$ was investigated in a preliminary fashion, and these samples have shown promise as materials with optical functionalities. Absorption spectra from Pr(III), Nd(III), and Sm(III) analogs were obtained and showed excellent absorption at transitions typically observed for materials doped with these lanthanides. The ability to grow these crystals using supercritical fluids via spontaneous nucleation gives the opportunity for future investigation into this phase space, such as the synthesis of other lanthanide analogs and conducting emission spectroscopy on said materials. The combination of favorable absorption characteristics and an acentric crystal structure clearly pique interest for applications utilizing nonlinear optical phenomena and light emission.

REFERENCES

- (1) Keszler, D. A. *Curr. Opin. Solid St. Mater. Sci.* **1996**, *1*, 204-211.
- (2) Keszler, D. A. *Curr. Opin. Solid St. Mater. Sci.* **1999**, *4*, 155-162.
- (3) Chen, C.; Lui, G. *Ann. Ret. Mater. Sci.* **1986**, *16*, 203-243.
- (4) Agulló-López, P.; Cabrera, J.; Agulló-Rueda, F. *Electro-optics, Phenomena, Materials, and Applications*. Academic Press, New York, 1994.
- (5) Peshev, P.; Pechev, S.; Nikolov, V.; Gravereau, P.; Chaminade, J.-P.; Binev, D.; Ivanova, D. *J. Solid St. Chem.* **2006**, *179*, 2834-2849.
- (6) Zhang, G.; Wu, Y.; Li, Y.; Chang, F.; Pan, S.; Fu, P.; Chen, C. *J. Cryst. Growth* **2005**, *275*, e1997–e2001.
- (7) Gravereau, P.; Chaminade, J. -P.; Pechev, S.; Nikolov, V.; Ivanova, D.; Peshev, P. *Solid St. Sci.* **2002**, *4*, 993-998.

- (8) Haberer, A.; Kaindl, R.; Huppertz, H. *Z. Naturforsch. B* **2010**, *65*, 1206-1212.
- (9) Mueller-Bunz, H.; Nikelski, T.; Schleid, T. *Z. Naturforsch. B* **2003**, *58*, 375-380.
- (10) Abdullaev, G. K.; Dzhafarov, G. G.; Mamedov, K. S. *Azerb. Khim. Zh.* **1976**, 117-120.
- (11) Shannon, R. D. *Acta Crystallogr.* **1976**, *A32*, 751.
- (12) Voda, M.; Balda, R.; Al-Saleh, M.; Sáez de Ocáriz, I.; Cano, M.; Lobera, G.; Macho, E.; Fernández, J. *J. Alloys Comp.* **2001**, *323-324*, 250-254.
- (13) Ogiegło, J. M.; Zych, A.; Jüstel, T.; Meijerink, A.; Ronda, C. R. *Opt. Mater.* **2013**, *35*, 322-331.
- (14) Holgado, W.; Sola, I. J.; Jarque, E. C.; Jarabo, S.; Roso, L. *Eur. J. Phys.* **2012**, *33*, 265-278.
- (15) Wang, K.; Zhang, J.; Wang, J.; Yu, W.; Zhang, H.; Wang, Z.; Shao, Z. *Mater. Res. Bull.* **2006**, *41*, 1695-1700.
- (16) Karthikeyan, B. *Chem. Phys. Lett.* **2006**, *432*, 513-517.

CHAPTER EIGHT

SUMMARY AND PERSPECTIVE

The ability to easily grow crystals that can lead to new materials and to help understand a phase space that was otherwise not well known is a powerful tool to crystal growers. The ability to grow large, high-quality, single crystals with interesting optical properties using the same technique puts forth a substantial argument toward being the ideal means to grow most crystals. So it is surprising that crystal growth using hydrothermal techniques is often passed over in favor of classical melt techniques, though melts are known to incorporate inclusions and promote thermal strain and cracking. This dissertation both demonstrates the ease of synthesizing crystals for exploratory purposes and also addresses the need to explore and understand alternative crystal growing techniques in order to further develop the growth of crystals used in optical technology. It has been shown that hydrothermal crystal growth is an excellent method for growing both monovalent ion thorium, cerium(IV), and hafnium fluoride crystals of single crystal X-ray quality and acentric lanthanide-doped YBO_3 with potential as a solid state laser host.

First, the hydrothermal synthesis of monovalent thorium fluorides using ThF_4 and monovalent fluoride mineralizers was found to yield a wide variety of products, including the first fully characterized cesium thorium fluorides. Many of the formulations reported earlier were not previously characterized by single crystal diffraction due to the lack of suitably high quality crystals, and many of the compounds reported herein can be prepared as phase pure materials. A high percentage of the compounds grow in a variety

of polymorphs indicating the subtlety and richness of this phase space. The identity of the species seems to be primarily dependent on the concentration of the fluoride mineralizer used in their syntheses. The facile growth of these stable alkali thorium fluorides is an encouraging sign, and may be useful if thorium is to be developed as a safe alternative nuclear fuel source in the future.

Next, a variety of alkali ion hafnium fluorides were synthesized from hydrothermal reactions. The reactions were carried out over a range of stoichiometries and temperatures in an attempt to cover a broad region of phase space. In some cases the products are new structures, while in others they were reported previously as powder samples made from melts. A number of members of the A_2HfF_6 formulation including Li_2HfF_6 , which represents to our knowledge the first example of a structure of Li containing hafnium fluoride, were isolated. A number of more structurally complex alkali hafnium fluorides such as $Na_5Hf_2F_{13}$ and K_3HfF_7 were also isolated. Although the metal fluoride structural chemistry is not as subtle and complex as our group observed previously in the thorium fluoride system, the chemistry is somewhat richer in the sense that some new hydrolytic oxyfluoride products (such as $K_2Hf_3OF_{12}$, K_3HfOF_5 and $(NH_4)_3HfOF_5$) are observed in the hafnium system as well as a known hydrated species ($Rb_5Hf_4F_{21} \cdot 3H_2O$). In general, the alkali fluoride chemistry appeared to be more similar to that of zirconium than thorium. Luminescence studies were also carried out on the samples obtained from this phase space, and it was found that the oxyfluorides gave the brightest X-ray luminescence, whereas the smaller monovalent ion hafnium fluorides yielded the brightest visible luminescence. These studies also showed that the size of the

monovalent ion was a driving force in both X-ray and visible luminescence. This was valuable experience and knowledge to gain for when the crystal growth of borates was explored.

The hydrothermal synthesis of alkali metal cerium(IV) fluorides using CeF_4 and alkali fluoride mineralizers yielded a wider variety of products than the thorium fluoride system. The reactions were generally performed at the relatively low temperature of 200 °C, as all reactions performed at higher temperatures (500 °C) invariably led to reduction of the cerium and formation of CeF_3 . All of the formulations reported earlier were not previously characterized by single crystal X-ray diffraction due to the lack of exploration of the phase space. Though some CeF_3 powder exists in product mixture of these reactions, the compounds reported herein can be prepared as phase pure crystals. Many of the compounds grow in a variety of polymorphs that are isostructural to both the thorium and hafnium fluoride systems, acting as a “crystallographic bridge” between the two systems. The identity of the species seems to be primarily dependent on the concentration of the fluoride mineralizer used in their syntheses and lower reaction temperatures. Especially interesting is the fact that an alkali cerium(IV) fluoride has not yet been identified that is isostructural for all three K, Rb, and Cs phases, similar to what was determined for the thorium fluoride system. The facile growth of these stable monovalent cerium(IV) fluorides is an encouraging sign, and this has opened up the possibility for further development of this virtually unexplored phase space.

In a foray into borates, lanthanide-doped YBO_3 crystals were successfully grown via the hydrothermal method, and these crystals were found to show great promise as

materials with numerous useful optical functionalities. Emissions from Nd^{3+} , Er^{3+} , and Yb^{3+} doped samples were observed and clearly linked to both dopant and the acentric structure of the host. The ability to grow these crystals of sufficient size for use in a commercial device has been realized using supercritical hydrothermal approaches via spontaneous nucleation. However, future crystal growth studies of lanthanide-doped YBO_3 need to overcome the uneven stacking that plagues its epitaxial growth. The combination of favorable emission characteristics and an acentric crystal structure clearly marks these materials as multifunctional and of interest for application utilizing nonlinear optical phenomena, light emission, or ultraviolet transparency. The extension of the host chemistry to LuBO_3 is especially promising.

Serendipitously, a little-explored class of acentric borates of the formula $\text{Na}_3\text{Ln}_9\text{O}_3(\text{BO}_3)_8$ was discovered during the crystal growth of lanthanide-doped YBO_3 . This class of borates also showed to have promise as materials with optical functionalities. Absorption spectra from Pr^{3+} , Nd^{3+} , and Sm^{3+} analogs were obtained and showed excellent absorption at transitions typically observed for materials doped with these lanthanides. Unfortunately, a suitable host system has yet to be prepared as La, Gd, Y and Lu ions all lead only to $(\text{RE})\text{BO}_3$ phases. However the presence of two different metal sites in the lattice provides the potential to mix and match various ion sizes to lead to possible new hosts. The ability to grow these crystals using supercritical fluids via spontaneous nucleation gives the opportunity for future investigation into this phase space, such as the synthesis of other lanthanide analogs and conducting emission spectroscopy on said materials. The combination of favorable absorption characteristics

and an acentric crystal structure clearly pique interest for application utilizing nonlinear optical phenomena and light emission.

APPENDICES

Appendix A

Copyright Releases



Title: Hydrothermal Descriptive Chemistry and Single Crystal Structure Determination of Cesium and Rubidium Thorium Fluorides

Author: Christopher C. Underwood, Matthew Mann, Colin D. McMillen, and Joseph W. Kolis

Publication: Inorganic Chemistry

Publisher: American Chemical Society

Date: Nov 1, 2011

Logged in as:
Christopher Underwood
Account #:
3000324056

LOGOUT

Copyright © 2011, American Chemical Society

PERMISSION/LICENSE IS GRANTED FOR YOUR ORDER AT NO CHARGE

This type of permission/license, instead of the standard Terms & Conditions, is sent to you because no fee is being charged for your order. Please note the following:

- Permission is granted for your request in both print and electronic formats, and translations.
- If figures and/or tables were requested, they may be adapted or used in part.
- Please print this page for your records and send a copy of it to your publisher/graduate school.
- Appropriate credit for the requested material should be given as follows: "Reprinted (adapted) with permission from (COMPLETE REFERENCE CITATION). Copyright (YEAR) American Chemical Society." Insert appropriate information in place of the capitalized words.
- One-time permission is granted only for the use specified in your request. No additional uses are granted (such as derivative works or other editions). For any other uses, please submit a new request.

Copyright © 2013 [Copyright Clearance Center, Inc.](#) All Rights Reserved. [Privacy statement](#).
Comments? We would like to hear from you. E-mail us at customercare@copyright.com

Figure A-1: *Inorg. Chem.* **2011**, *50*, 11825-11831.

Dear Christopher Underwood,

Thank you for your permission request.

Please note that, as one of the Authors of this article, you retain the right to include the journal article, in full or in part, in a thesis or dissertation. On condition that you fully cite the source and the copyright, you should not need formal permission. Of course, if any part of the material to be used (for example, figures) has appeared in our publication with credit or acknowledgement to another source, permission must also be sought from that source (if such permission is not obtained then that material may not be included in your publication/copies).

For full details of your rights as a Journal Author, please visit:

<http://www.elsevier.com/wps/find/authorsview.authors/copyright#whatrights>

Your retained rights allow you to submit your article in electronic format and to post this Elsevier article online if it is embedded within your thesis. You are also permitted to post your Author Accepted Manuscript online, however posting of the final published article is prohibited.

Please refer to Elsevier's Posting Policy for further information:

<http://www.elsevier.com/wps/find/authors.authors/postingpolicy>

Best regards,

Charlotte PECCIA-GALLETTO


Legal department

Elsevier Masson

62, rue Camille Desmoulins

92442 Issy les Moulineaux cedex France

Figure A-2: *Solid St. Sci.* **2012**, *14*, 574-579.

- **Order detail ID:**63630219
- **Article Title:**The Crystal Structures of CsTh6F25 and NaTh3F13
- **Author(s):**Underwood, Christopher C. ; McMillen, Colin D. ; Kolis, Joseph W.
- **DOI:**10.1007/S10870-012-0289-6
- **Date:**Jan 01, 2012
- **ISSN:**1074-1542
- **Publication Type:**Journal
- **Volume:**42
- **Issue:**6
- **Start page:**606
- **Publisher:**SPRINGER NEW YORK LLC
- **Permission Status:**  **Granted**
- **Permission type:**Republish or display content
- **Type of use:**use in a thesis/dissertation

Order License Id: 3140220748082

- [Hide details](#)

○

Portion	Full text
Number of copies	1
Author of this Springer article	Yes and you are the sole author of the new work
Title of your thesis / dissertation	HYDROTHERMAL CHEMISTRY, CRYSTAL STRUCTURES, AND SPECTROSCOPY OF NOVEL FLUORIDES AND BORATES
Expected completion date	Aug 2013
Estimated size(pages)	250

Figure A-3: *J. Chem. Crystallogr.* **2012**, 42, 606-610



ACS Publications Title: Hydrothermal Chemistry, Structures, and Luminescence Studies of Alkali Hafnium Fluorides

Author: Christopher C. Underwood, Colin D. McMillen, Hongyu Chen, Jeffery N. Anker, and Joseph W. Kolis

Publication: Inorganic Chemistry

Publisher: American Chemical Society

Date: Jan 1, 2013

Copyright © 2013, American Chemical Society

Logged in as:

Christopher Underwood

Account #:
3000324056

LOGOUT


PERMISSION/LICENSE IS GRANTED FOR YOUR ORDER AT NO CHARGE

This type of permission/license, instead of the standard Terms & Conditions, is sent to you because no fee is being charged for your order. Please note the following:

- Permission is granted for your request in both print and electronic formats, and translations.
- If figures and/or tables were requested, they may be adapted or used in part.
- Please print this page for your records and send a copy of it to your publisher/graduate school.
- Appropriate credit for the requested material should be given as follows: "Reprinted (adapted) with permission from (COMPLETE REFERENCE CITATION). Copyright (YEAR) American Chemical Society." Insert appropriate information in place of the capitalized words.
- One-time permission is granted only for the use specified in your request. No additional uses are granted (such as derivative works or other editions). For any other uses, please submit a new request.

Copyright © 2013 [Copyright Clearance Center, Inc.](#) All Rights Reserved. [Privacy statement.](#)
Comments? We would like to hear from you. E-mail us at customercare@copyright.com

Figure A-4: *Inorg. Chem.* **2013**, 52, 237-244.

- **Order detail ID:**63630213
- **Article Title:**Crystal structures and stability of K₂ThF₆ and K₇Th₆F₃₁ on compression
- **Author(s):**Grzechnik, Andrzej ; et al
- **DOI:**10.1016/J.JFLUCHEM.2013.02.024
- **Date:**Jan 01, 2013
- **ISSN:**0022-1139
- **Publication Type:**Journal
- **Volume:**150
- **Issue:**
- **Start page:**8
- **Publisher:**ELSEVIER S.A.
- **Permission Status:**  **Granted**
- **Permission type:**Republish or display content
- **Type of use:**reuse in a thesis/dissertation
-

Order License Id: 3140220743076

- [Hide details](#)

○

Number of pages	6
Portion	full article
Format	both print and electronic
Are you the author of this Elsevier article?	Yes
Will you be translating?	No
Order reference number	
Title of your thesis/dissertation	HYDROTHERMAL CHEMISTRY, CRYSTAL STRUCTURES, AND SPECTROSCOPY OF NOVEL FLUORIDES AND BORATES
Expected completion date	Aug 2013
Estimated size (number of pages)	250
Elsevier VAT number	GB 494 6272 12
Permissions price	0.00 USD
VAT/Local Sales Tax	0.00 USD

Figure A-5: *J. Fluorine Chem.* **2013**, *150*, 8-13.

Appendix B

Crystallographic Data for Cs₂HfF₆ and Rb₂HfF₆

Table B-1: Crystallographic Data for Cs₂HfF₆ and Rb₂HfF₆

Chemical Formula	Cs ₂ HfF ₆	Rb ₂ HfF ₆
F.W. (g/mol)	306.37	463.43
Space group	<i>P-3m1</i>	<i>P-3m1</i>
Temp./K	293±2	293±2
Crystal system	Trigonal	Trigonal
a, Å	6.3876(9)	6.1364(9)
b, Å		
c, Å	5.0133(10)	4.8265(10)
V, Å ³	177.15(5)	157.39(5)
Z	1	1
D _{cal} , Mg/m ³	5.234	4.889
Indices (min)	[-7, -7, -6]	[-7, -7, -5]
(max)	[7, 7, 6]	[7, 7, 5]
Parameters	13	13
F(000)	236	200
μ, mm ⁻¹	24.877	31.964
2θ range, °	3.68 – 26.42	3.83 – 26.28
Collected Reflns.	1575	1366
Unique Reflns.	160	139
Final R (obs. data), ^a	0.0420	0.0359
wR ₂	0.1141	0.0842
Final R (all data), R ₁	0.0421	0.0368
wR ₂	0.1146	0.0848
Goodness of fit (S)	1.188	1.138
Extinction Coeff.	0.018(7)	0.0096(15)
Largest diff. peak	2.652	2.292
Largest diff. hole	-2.434	-1.626

Appendix C

Tables of Fractional Coordinates

Table C-1: Fractional Atomic Coordinates of α -CsThF₅.

	x	y	z
Th1	0.2500	0.2500	0.4554 (2)
Cs1	0.7500	0.2500	0.0000
F1	0.2500	0.2500	0.148 (4)
F2	0.542 (3)	0.085 (3)	0.648 (2)

Table C-2: Fractional Atomic Coordinates of β -CsThF₅.

	x	y	z
Th1	0.92417 (5)	0.15325 (6)	0.14281 (5)
Cs1	0.43112 (11)	0.10336 (15)	-0.33681 (11)
F1	1.1593 (10)	0.0711 (10)	0.0726 (8)
F2	0.8365 (10)	-0.1423 (9)	0.2111 (9)
F3	0.8767 (10)	0.2004 (11)	0.3834 (9)
F4	1.1505 (10)	-0.0296 (9)	0.3525 (8)
F5	1.3718 (10)	-0.3206 (11)	0.4793 (10)

Table C-3: Fractional Atomic Coordinates of γ -CsThF₅.

	x	y	z
Th1	0.02314 (8)	0.24728 (3)	0.07961 (9)
Th2	0.45227 (8)	0.24793 (3)	-0.04666 (8)
Cs1	-0.28246 (14)	0.01803 (8)	0.27858 (15)
Cs2	-0.77299 (15)	-0.01867 (8)	0.23839 (15)
F1	-0.0604 (12)	0.1059 (7)	0.1002 (13)
F2	0.4919 (14)	0.3974 (7)	-0.0081 (15)
F3	-0.0132 (13)	0.3960 (8)	0.0526 (14)
F4	0.5377 (13)	0.1083 (8)	-0.0763 (14)
F5	-0.0730 (13)	0.2102 (9)	-0.1890 (13)
F6	0.5436 (13)	0.2034 (9)	0.2230 (12)
F7	0.2372 (11)	0.1555 (7)	0.0104 (13)
F8	-0.2650 (15)	0.2646 (9)	0.0164 (15)
F9	0.2943 (11)	0.3088 (6)	0.1800 (11)
F10	0.1817 (12)	0.3115 (6)	-0.1527 (13)

Table C-4: Fractional Atomic Coordinates of α -CsTh₃F₁₃.

	x	y	z
Th1	-0.5000	-0.5000	0.26590 (10)
Cs1	0.0000	0.0000	0.5000
Cs2	0.0000	0.0000	0.0000
F1	-0.6495 (16)	-0.6495 (16)	0.5000
F2	-0.6667	-0.3333	0.346 (3)
F3	-0.632 (3)	-0.8161 (15)	0.196 (2)
F4	-0.5000	-0.5000	0.0000

Table C-5: Fractional Atomic Coordinates of β -CsTh₃F₁₃.

	X	y	z
Th1	0.5000	0.38981 (17)	0.58555 (12)
Th2	0.24847 (14)	0.10581 (8)	0.92314 (12)
Cs1	0.0000	0.6073 (3)	0.7932 (2)
F1	0.0000	-0.057 (2)	0.9389 (16)
F2	0.5000	0.133 (2)	0.765 (2)
F3	0.2473 (14)	0.3233 (17)	0.7292 (16)
F4	0.1989 (15)	0.0470 (15)	1.1853 (14)
F5	0.5000	0.112 (2)	1.0557 (19)
F6	0.0000	0.268 (2)	0.9512 (16)
F7	0.3322 (16)	-0.1866 (17)	0.9527 (12)
F8	0.6936 (15)	0.6134 (15)	0.5417 (13)
F9	0.5000	0.467 (3)	0.323 (2)

Table C-6: Fractional Atomic Coordinates of CsTh₆F₂₅.

	x	y	z
Th1	0.33407 (8)	0.16704 (4)	0.11268 (4)
Cs1	0.3333	0.6667	0.2500
F1	0.308 (2)	0.1539 (12)	0.2500
F2	0.1489 (7)	-0.1489 (7)	0.1487 (7)
F3	0.3230 (12)	0.3230 (12)	0.0000
F4	0.5332 (8)	0.4668 (8)	0.1600 (7)
F5	0.0000	0.0000	0.0741 (9)
F6	0.6667	0.3333	0.0599 (13)

Table C-7: Fractional Atomic Coordinates of RbTh₂F₉.

	x	y	z
Th1	0.32503 (6)	0.44883 (5)	0.34817 (7)
Rb1	0.4662 (3)	0.2500	0.8608 (3)
F1	-0.0063 (9)	0.5960 (8)	0.0736 (12)
F2	0.2862 (11)	0.0935 (8)	0.0333 (12)
F3	0.2790 (13)	0.6035 (9)	0.1473 (10)
F4	0.0625 (10)	0.4202 (8)	0.3044 (15)
F5	0.3221 (14)	0.2500	0.3386 (18)

Table C-8: Fractional Atomic Coordinates of RbTh₃F₁₃.

	x	y	z
Th2	0.5000	0.60789 (13)	0.41293 (3)
Th1	0.75307 (8)	0.89648 (6)	0.07900 (16)
Rb1	1.0000	0.3950 (4)	0.2205 (3)
F1	1.0000	1.0613 (16)	0.0646 (17)
F2	0.5000	0.8635 (18)	0.2353 (19)
F3	0.7544 (10)	0.6739 (12)	0.2711 (13)
F4	0.8009 (11)	0.9523 (12)	-0.1845 (12)
F5	0.5000	0.895 (2)	-0.0485 (16)
F6	1.0000	0.7292 (16)	0.0504 (17)
F7	0.6706 (11)	1.1926 (12)	0.0477 (11)
F8	0.3045 (11)	0.3830 (13)	0.4560 (11)
F9	0.5000	0.531 (2)	0.672 (2)

Table C-9: Fractional Atomic Coordinates of Rb₇Th₆F₃₁.

	x	y	z
Th1	0.53301 (3)	0.14541 (3)	0.00432 (3)
Rb1	0.35755 (8)	0.10684 (8)	0.32740 (9)
Rb2	0.6667	0.3333	0.3333
F1	0.3798 (5)	0.0985 (5)	0.0674 (6)
F2	0.5428 (5)	0.1543 (5)	0.2101 (6)
F3	0.5718 (5)	0.0224 (4)	0.0717 (6)
F4	0.8741 (6)	0.4943 (5)	-0.1632 (6)
F5	0.5783 (5)	0.2082 (6)	0.6207 (7)
F6	0.6667	0.3333	1.3 (8)

Table C-10: Fractional Atomic Coordinates of Tl₇Th₆F₃₁.

	x	y	z
Th1	0.534440 (1)	0.146232 (1)	0.002401 (2)
Tl1	0.361456 (1)	0.108295 (2)	0.325015 (2)
Tl2	0.6667	0.3333	0.3333
F1	0.37945 (3)	0.09489 (3)	0.06789 (4)
F2	0.54302 (2)	0.15435 (2)	0.21071 (4)
F3	0.57093 (2)	0.02192 (2)	0.07225 (3)
F4	0.87386 (3)	0.49550 (2)	-0.16316 (4)
F5	0.57890 (2)	0.20865 (3)	0.61965 (4)
F6	0.6667	0.3333	-4.0000 (12)

Table C-11: Fractional Atomic Coordinates of $(\text{NH}_4)_7\text{Th}_6\text{F}_{31}$.

	x	y	z
Th1	0.610653 (2)	0.144824 (2)	0.000690 (3)
N1	0.69484 (4)	-0.08020 (4)	-0.00569 (6)
N2	0.6667	0.3333	0.3333
F1	0.71717 (4)	0.09872 (4)	0.06873 (6)
F2	0.61007 (4)	0.15619 (4)	0.20568 (6)
F3	0.44985 (3)	0.02205 (3)	0.07025 (5)
F4	0.50369 (4)	0.12442 (5)	-0.16350 (6)
F5	0.75339 (5)	0.29652 (5)	0.03969 (7)
F6	0.6667	0.3333	0.1439 (19)

Table C-12: Fractional Atomic Coordinates of $\text{NaTh}_3\text{F}_{13}$.

	x	y	z
Th1	0.32404 (8)	0.16202 (4)	0.11323 (4)
Na1	0.3333	0.6667	0.1013 (11)
F1	0.1681 (6)	-0.1681 (6)	0.1446 (7)
F2	0.5391 (7)	0.4609 (7)	0.1609 (6)
F3	0.3278 (12)	0.0000	0.0000
F4	0.277 (2)	0.1385 (11)	0.2500
F5	0.0000	0.0000	0.0878 (15)
F6	0.6667	0.3333	0.0515 (10)
F7	0.3333	0.6667	0.2500

Table C-13: Fractional Atomic Coordinates of CsCeF₅.

	x	y	z
Ce1	0.017256 (17)	0.244489 (9)	0.110604 (18)
Ce2	0.442458 (16)	0.246839 (8)	-0.032944 (18)
Cs1	-0.27849 (2)	0.024176 (11)	0.29713 (2)
Cs2	-0.75978 (2)	-0.024056 (12)	0.21589 (2)
F1	-0.0555 (2)	0.10179 (10)	0.11416 (19)
F2	0.49299 (19)	0.39242 (10)	0.01537 (19)
F3	-0.02390 (18)	0.38953 (11)	0.0759 (2)
F4	0.51667 (18)	0.10594 (11)	-0.0477 (2)
F5	-0.0721 (2)	0.22249 (13)	-0.1689 (2)
F6	0.52438 (18)	0.21218 (11)	0.23630 (17)
F7	0.22379 (18)	0.16336 (11)	0.0183 (2)
F8	-0.2688 (2)	0.25438 (11)	0.0394 (2)
F9	0.27224 (18)	0.31514 (11)	0.2035 (2)
F10	0.19363 (19)	0.32375 (11)	-0.1481 (2)

Table C-14: Fractional Atomic Coordinates of Cs₂Ce₃OF₁₂.

	x	y	z
Ce1	0.81809 (3)	0.18191 (3)	0.105745 (10)
Cs1	0.6667	0.3333	-0.03053 (3)
Cs2	1.0000	0.0000	0.0000
Cs3	0.6667	0.3333	-0.1667
F1	0.4989 (3)	-0.0022 (6)	0.09243 (12)
F2	0.6881 (5)	0.0214 (5)	0.1667
F3	1.1108 (3)	0.2216 (6)	0.09369 (13)
F4	0.8103 (3)	0.1897 (3)	0.03959 (12)
O1	0.6667	0.3333	0.1189 (2)

Table C-15: Fractional Atomic Coordinates of RbCe₃OF₁₁.

	x	y	z
Ce1	0.35259 (12)	0.17630 (6)	0.26792 (6)
Rb1	0.3333	0.6667	0.0000
Rb2	0.3333	0.6667	0.5000
F1	0.3935 (12)	0.1968 (6)	0.0000
F2	0.4947 (6)	-0.0105 (12)	0.2147 (10)
F3	0.1206 (8)	-0.1206 (8)	0.1917 (15)
F4	0.3356 (11)	0.3183 (8)	0.5000
F5	0.6667	0.3333	0.3084 (18)
O1	0.0000	0.0000	0.375 (4)
O2	0.6667	0.3333	0.3084 (18)

Table C-16: Fractional Atomic Coordinates of RbCeF₅.

	x	y	z
Ce1	0.01473 (2)	0.242444 (13)	0.10860 (3)
Ce2	0.44151 (3)	0.246512 (12)	-0.03088 (3)
Rb1	-0.27781 (5)	0.02208 (3)	0.30211 (5)
Rb2	-0.76388 (5)	-0.02495 (3)	0.21514 (5)
F1	-0.0656 (3)	0.09331 (16)	0.1137 (3)
F2	0.4954 (3)	0.39691 (16)	0.0282 (3)
F3	-0.0305 (3)	0.39657 (17)	0.0740 (3)
F4	0.5187 (3)	0.10197 (17)	-0.0672 (3)
F5	-0.0777 (3)	0.2216 (2)	-0.1646 (3)
F6	0.5232 (3)	0.19891 (17)	0.2401 (3)
F7	0.2189 (2)	0.15560 (16)	0.0160 (2)
F8	-0.2727 (3)	0.25537 (18)	0.0393 (3)
F9	0.2753 (3)	0.31489 (15)	0.1954 (3)
F10	0.1893 (3)	0.32717 (16)	-0.1470 (3)

Table C-17: Fractional Atomic Coordinates of $K_7Ce_6F_{31}$.

	x	y	z
Ce1	0.864621 (16)	0.053050 (14)	0.17590 (2)
K1	0.56199 (6)	-0.02024 (7)	0.16271 (7)
K2	0.3333	-0.3333	0.1667
F1	0.71024 (17)	-0.05420 (18)	0.2371 (2)
F2	0.87307 (17)	0.05473 (16)	0.3846 (2)
F3	0.75943 (16)	0.11445 (15)	0.0929 (2)
F4	0.79327 (19)	-0.04730 (17)	-0.0037 (2)
F5	0.8744 (2)	-0.0902 (2)	0.2206 (3)
F6	1.0000	0.0000	0.0620 (18)

Table C-18: Fractional Atomic Coordinates of K_2CeF_6 .

	x	y	z
Ce1	1.0000	1.0000	1.0000
K1	0.3333	0.6667	0.5000
F1	0.6637 (7)	0.6637 (7)	1.0000
F2	1.0000	0.7745 (7)	0.5000

Table C-19: Fractional Atomic Coordinates of $\text{KCe}_3\text{OF}_{11}$.

	x	y	z
Ce1	0.3507 (3)	0.17536 (13)	0.26723 (11)
K1	0.3333	0.6667	0.0000
K2	0.3333	0.6667	0.5000
F1	0.397 (2)	0.1983 (12)	0.0000
F2	0.4943 (9)	-0.0115 (18)	0.214 (2)
F3	0.1199 (14)	-0.1199 (14)	0.192 (3)
F4	0.335 (3)	0.322 (2)	0.5000
F5	0.6667	0.3333	0.310 (4)
O1	0.0000	0.0000	0.385 (8)
O2	0.6667	0.3333	0.310 (4)

Table C-20: Fractional Atomic Coordinates of $(\text{NH}_4)\text{CeF}_5$.

	x	y	z
Ce1	0.21424 (5)	0.5000	0.37091 (11)
N1	0.0000	0.2298 (7)	0.0000
F1	0.5000	0.5000	0.5000
F2	0.0000	0.4036 (7)	0.5000
F3	0.2783 (9)	0.3525 (4)	0.376 (2)
F4	0.3038 (11)	0.4572 (7)	-0.0931 (18)
F5	0.0494 (9)	0.4346 (5)	0.8352 (18)

Table C-21: Fractional Atomic Coordinates of $(\text{NH}_4)\text{Ce}_3\text{OF}_{11}$.

	x	y	z
Ce1	0.6476 (2)	0.82382 (10)	0.73201 (8)
N1	0.6667	0.3333	1.0000
N2	0.6667	0.3333	0.5000
F1	0.6048 (14)	0.8024 (7)	1.0000
F2	0.5052 (8)	1.0104 (17)	0.7851 (18)
F3	0.8776 (10)	1.1224 (10)	0.8099 (17)
F4	0.6644 (13)	0.6798 (8)	0.5000
F5	0.3333	0.6667	0.685 (4)
O1	1.0000	1.0000	0.627 (7)
O2	0.3333	0.6667	0.685 (4)

Table C-22: Fractional Atomic Coordinates of $(\text{NH}_4)_7\text{Ce}_6\text{OF}_{31}$.

	x	y	z
Ce1	0.609508 (1)	0.145576 (1)	-0.001553 (2)
N1	0.693599 (19)	-0.082537 (19)	-0.00676 (2)
N2	0.6667	0.3333	0.3333
F1	0.713503 (14)	0.099138 (14)	0.06405 (2)
F2	0.610311 (14)	0.157132 (14)	0.19982 (2)
F3	0.450935 (13)	0.022478 (12)	0.071093 (19)
F4	0.503170 (15)	0.125725 (16)	-0.16320 (2)
F5	0.752251 (18)	0.296190 (16)	0.03780 (2)
F6	0.6667	0.3333	0.1489 (8)

Table C-23: Fractional Atomic Coordinates of Na₂CeF₆.

	x	y	z
Ce1	0.0000	1.0000	0.0000
Na1	0.3333	0.6667	-0.5000
F1	0.3666 (6)	0.3666 (6)	0.0000
F2	0.0000	0.2490 (5)	0.5000

Table C-24: Fractional Atomic Coordinates of Na₇Ce₆F₃₁.

	x	y	z
Ce1	0.04968 (4)	0.86056 (4)	0.31685 (5)
Ce2	-0.02908 (19)	0.56175 (18)	0.3355 (2)
Ce3	0.0000	1.0000	0.0000
Na1	0.04968 (4)	0.86056 (4)	0.31685 (5)
Na2	-0.02908 (19)	0.56175 (18)	0.3355 (2)
Na3	0.0000	1.0000	0.0000
F1	-0.0641 (5)	0.6996 (4)	0.2493 (6)
F2	0.0558 (4)	0.8695 (4)	0.0920 (6)
F3	0.2245 (4)	0.9144 (4)	0.2553 (6)
F4	-0.0538 (5)	0.7892 (6)	0.5003 (7)
F5	-0.0912 (5)	0.8746 (6)	0.2640 (8)
F6	0.0000	1.0000	0.4252

Table C-25: Fractional Atomic Coordinates of LiCeF₅.

	x	y	z
Ce1	0.19378 (2)	0.31286 (2)	0.00681 (5)
Li1	-0.0692 (10)	0.3347 (9)	-0.233 (2)
F1	-0.2117 (3)	0.3270 (3)	-0.2524 (6)
F2	0.1577 (3)	0.4567 (2)	-0.1053 (6)
F3	0.1103 (2)	0.1828 (2)	0.0735 (6)
F4	0.4518 (2)	0.3351 (2)	0.0206 (6)
F5	0.1983 (2)	0.2856 (2)	0.3787 (6)

Table C-26: Fractional Atomic Coordinates of Li₄CeF₈.

	x	y	z
Ce1	0.13975 (6)	0.2500	0.36609 (10)
Li1	0.374 (3)	0.056 (3)	0.125 (4)
Li2	0.399 (3)	0.077 (3)	0.633 (5)
Li3	0.403 (3)	-0.023 (3)	0.346 (5)
Li4	0.338 (3)	0.135 (3)	0.869 (5)
F1	0.2907 (7)	0.2500	0.6333 (11)
F2	0.0242 (5)	0.1190 (5)	0.6075 (8)
F3	0.2404 (5)	0.4675 (5)	0.3752 (8)
F4	0.0298 (5)	0.1118 (5)	0.1315 (8)
F5	0.3040 (7)	0.2500	0.1147 (11)

Table C-27: Fractional Atomic Coordinates of K_3HfOF_5 .

	x	y	z
Hf1	0.0000	0.0000	0.0000
K1	0.5000	0.5000	0.5000
K2	0.2500	0.2500	0.2500
F1	0.0000	0.782 (2)	0.0000
O1	0.0000	0.782 (2)	0.0000

Table C-28: Fractional Atomic Coordinates of $K_2Hf_3OF_{12}$.

	x	y	z
Hf1	0.81806 (3)	0.18194 (3)	0.104603 (13)
K1	0.6667	0.3333	-0.02853 (15)
K2	1.0000	0.0000	0.0000
K3	0.6667	0.3333	-0.1667
F1	1.0087 (10)	0.5044 (5)	0.0902 (2)
F2	0.6835 (8)	0.0168 (8)	0.1667
F3	0.7767 (10)	-0.1116 (5)	0.0929 (2)
F4	0.8121 (5)	0.1879 (5)	0.0361 (2)
O1	0.6667	0.3333	0.1198 (4)

Table C-29: Fractional Atomic Coordinates of $(\text{NH}_4)_3\text{HfOF}_5$.

	x	y	z
Hf1	0.0000	0.0000	0.0000
N1	0.5000	0.5000	0.5000
N2	0.2500	0.2500	0.2500
F1	0.0000	0.7921 (15)	0.0000
O1	0.0000	0.7921 (15)	0.0000

Table C-30: Fractional Atomic Coordinates of $\text{Na}_5\text{Hf}_2\text{F}_{13}$.

	x	y	z
Hf1	0.42742 (2)	0.5000	0.25766 (3)
Na1	0.2230 (2)	0.0000	0.1544 (4)
Na2	0.0000	0.5000	0.0000
Na3	0.1623 (3)	0.5000	0.4302 (3)
F1	0.3195 (3)	0.2644 (6)	0.3570 (3)
F2	0.3677 (2)	0.7233 (6)	0.0715 (3)
F3	0.5610 (2)	0.2640 (7)	0.2524 (3)
F4	0.5000	0.5000	0.5000

Table C-31: Fractional Atomic Coordinates of Li_2HfF_6 .

	x	y	z
Hf1	0.0000	0.0000	0.0000
Li1	0.3333	0.6667	0.5000
F1	1.0000	0.3278 (19)	0.2554 (17)

Table C-32: Fractional Atomic Coordinates of Na₃Pr₉B₈O₂₇.

	x	y	z
Pr1	0.28137 (10)	0.28137 (10)	0.5000
Pr2	0.34818 (6)	0.0000	0.23578 (6)
Na1	0.3342 (7)	0.3342 (7)	0.0000
O1	0.1562 (9)	0.1562 (9)	0.2142 (9)
O2	0.5022 (11)	0.1795 (10)	0.0000
O3	0.5121 (8)	0.3335 (7)	0.3198 (6)
O4	0.2539 (12)	0.0000	0.5000
B1	0.0000	0.0000	0.206 (2)
B2	0.6667	0.3333	0.0000
B3	0.6667	0.3333	0.326 (2)

Table C-33: Fractional Atomic Coordinates of Na₃Nd₉B₈O₂₇.

	x	y	z
Nd1	0.28098 (16)	0.28098 (16)	0.5000
Nd2	0.34802 (8)	0.0000	0.23664 (9)
Na1	0.3351 (9)	0.3351 (9)	0.0000
O1	0.1568 (12)	0.1568 (12)	0.2153 (12)
O2	0.5007 (15)	0.1781 (14)	0.0000
O3	0.5117 (12)	0.3345 (9)	0.3205 (9)
O4	0.2522 (18)	0.0000	0.5000
B1	0.0000	0.0000	0.211 (4)
B2	0.6667	0.3333	0.0000
B3	0.6667	0.3333	0.326 (3)

Table C-34: Fractional Atomic Coordinates of Na₃Sm₉B₈O₂₇.

	x	y	z
Sm1	0.719226 (1)	0.719226 (1)	0.5000
Sm2	0.651016 (1)	1.0000	0.763496 (1)
Na1	0.663732 (11)	0.663732 (11)	1.0000
O1	0.841960 (15)	0.841960 (15)	0.781756 (14)
O2	0.501020 (14)	0.825717 (14)	1.0000
O3	0.489903 (12)	0.665754 (10)	0.681500 (11)
O4	0.74597 (2)	1.0000	0.5000
B1	1.0000	1.0000	0.78618 (5)
B2	0.3333	0.6667	1.0000
B3	0.3333	0.6667	0.67792 (4)